| REPORT DOCUMENTATION PAGE | Form Approved OMB NO. 0704-0188 |
|---|---|

Public reporting burden for this collection of information is estimated to average 1 hour per response, including the time for reviewing instructions, searching existing data sources, gathering and maintaining the data needed, and completing and reviewing the collection of information. Send comment regarding this burden estimates or any other aspect of this collection of information, including suggestions for reducing this burden, to Washington Headquarters Services, Directorate for information Operations and Reports, 1215 Jefferson Davis Highway, Suite 1204, Arlington, VA 22202-4302, and to the Office of Management and Budget, Paperwork Reduction Project (0704-0188), Washington, DC 20503.

| 1. AGENCY USE ONLY (Leave blank) | 2. REPORT DATE 20th June 98 | 3. REPORT TYPE AND DATES COVERED Final Technical Rept. 1 July 97 - 20 June 98 |
|---|---|---|

| 4. TITLE AND SUBTITLE | 5. FUNDING NUMBERS |
|---|---|
| Optical Pulse Coding for Maximum Data Rate | DAAG55-97-C-0043 |
| **6. AUTHOR(S)** Terence W. Barrett, Ph.D. | |

| 7. PERFORMING ORGANIZATION NAMES(S) AND ADDRESS(ES) **Reproduced From Best Available Copy** BSEI 1453 Beulah Road Vienna, VA 22182 | 8. PERFORMING ORGANIZATION REPORT NUMBER 12 |
|---|---|

| 9. SPONSORING / MONITORING AGENCY NAME(S) AND ADDRESS(ES) U.S. Army Research Office P.O. Box 12211 Research Triangle Park,, NC 27709-2211  **DTIC QUALITY INSPECTED 3** | 10. SPONSORING / MONITORING AGENCY REPORT NUMBER ARO 37516.1-MA-SDI |
|---|---|

**11. SUPPLEMENTARY NOTES**

The views, opinions and/or findings contained in this report are those of the author(s) and should not be construed as an official Department of the Army position, policy or decision, unless so designated by other documentation.

| 12a. DISTRIBUTION / AVAILABILITY STATEMENT | 12b. DISTRIBUTION CODE |
|---|---|
| Approved for public release;  distribution unlimited. | 19981223 122 |

**13. ABSTRACT (Maximum 200 words)**

This study shows the benefit of a *two-stage hierarchy* of coding schemes for achieving maximum data rate transmission in optical fiber communications. A first matched filter identifies the code/microchannel *orthogonal code* and a second matched filter identifies the data either *BPSQ'd* or *pulse-position-modulated* with error correction. The novel achievements of this study are: (1) the introduction of group theory (Young frame and tableaux methods) in characterizing code properties for optimum code design with optimum auto- and cross-correlation properties; (2) the development of Lexicographic-Greedy code algorithms for perfect codes and orthogonal codes; (3) the demonstration of orthogonal codes as extended Reed-Solomon codes and their implementation; (4) the implementation of Zech logarithmic code constructions; (5) the application of optical Fourier methods implementing matched filters in optical hub systems; (6) the analysis of code properties in terms of underlying group symmetry structure; (7) the confirmation of the utility of shepherding pulse techniques in bit parallel wavelength division multiplexing (BPWD) for maintaining pulse alignment; and (8) bit error analysis - all addressed in order to achieve the goal of the maximum in high data rate optical fiber communications commensurate with available device technology.

| 14. SUBJECT TERMS Optical Communications, Optical Orthogonal Codes, Auto- and Cross-Correlation Properties, Bit Parallel Wavelength Division, Shepherding Pulse. | 15. NUMBER IF PAGES 218 |
|---|---|
| | 16. PRICE CODE |

| 17. SECURITY CLASSIFICATION OR REPORT UNCLASSIFIED | 18. SECURITY CLASSIFICATION OF THIS PAGE UNCLASSIFIED | 19. SECURITY CLASSIFICATION OF ABSTRACT UNCLASSIFIED | 20. LIMITATION OF ABSTRACT UL |
|---|---|---|---|

ARO Contract DAAG55-97-C-0043
Effective Date 1 July 1997
Requisition: P-34591-MA-SDI
TITLE: OPTICAL PULSE CODING FOR HIGH DATA RATE

US Army Research Office
ATTN: AMXRO-ICA (Johnson)
P.O. Box 1211 Research Triangle Park, NC 27709-2211

COR: US Army Research Office
ATTN: Dr. Jagdish Chandra
Mathematical and Computer Sciences Division
P.O. Box 12211
Research Triangle Park, NC 27709-2211

FINAL TECHNICAL REPORT

Terence W. Barrett, Ph.D., BSEI, 1453 Beulah Road, Vienna, VA 22182
Tel: 703-759-4518; E-Mail: barrett506@aol.com

**June 20th, 1998**

*Contents:*

# 1.0 Preliminaries

## 1.1 Definition of Scientific Problem:

Given state-of-the-art device and material capabilities in wavelength and timing diversity for optical fiber communications, how can the data rate be maximized, so that large arrays, images., etc. can be transmitted in a timely fashion to the maximum number of users at acceptable probability of error, and real time (> 30 fps) and interactive video be achieved?

## 1.2 The Aim

The discussion of the results to follow is facilitated by use of the following nomenclature. Referring to Fig. 1.2.1, orthogonal codes are defined over a superframe of slots. A single pulse occurs only once per frame and the complete pulse code sequence is transmitted over the total time of the superframe of frames.

Slot Size = $\tau$

Frame Length
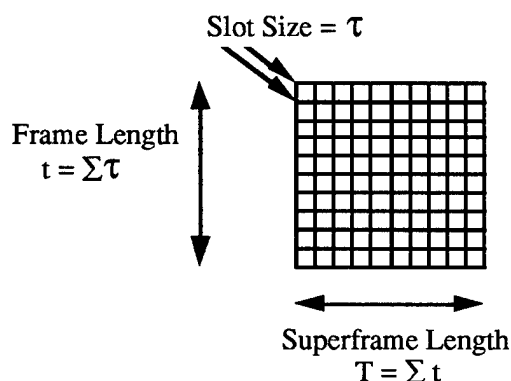$t = \Sigma \tau$

Superframe Length
$T = \Sigma t$

Fig. 1.2.1 Orthogonal codes are defined over a superframe of frames. A pulse of each orthogonal code occurs only once per frame and the total code sequence of pulses occurs completely over the superframe time. In this example, the frame size is 10 slots and there are 10 frames, so the size of the superframe is 100 slots. Therefore a complete orthogonal code is 10 pulses spread over the superframe time.
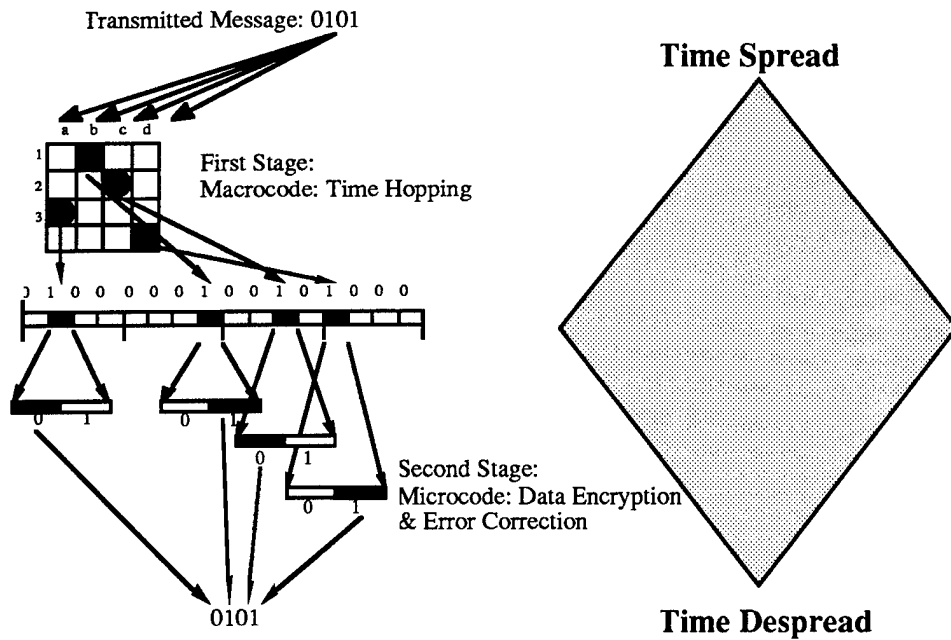
# Spread Time Technique



Fig. 1.2.2. Graphical representation of the Spread Time Technique with coding at a first stage identifying the channel and coding at a second stage by, e.g., BPSK, pulse-position modulation, etc. providing data encoding and error-correction. Here, pulse-position modulation is shown.

Two major types of codes will be discussed below: (1) orthogonal codes; and (2) error-correcting codes. The orthogonal codes are generated over a matrix field and are transferred to a time hopping representation by the method shown in Fig. 1.2.3, where a number of frames of a superframe are shown. The *spread time technique* reduces noise during the transmission phase (as does the spread spectrum technique). because after removal of the spreading code the data is recovered but the noise remains spread.

The work over the past 12 months has confirmed the benefit of a *two-stage hierarchy* of codes. In this scheme, the *orthogonal codes* define the microchannel or user, and, once a code is identified by a first matched filter, a second matched filter identifies the data encoded by, e.g., BPSK, pulse-position-modulation, etc., with error correction, hence *error-correcting codes* are required for the second stage. The two stages are represented in Fig. 1.2.3.
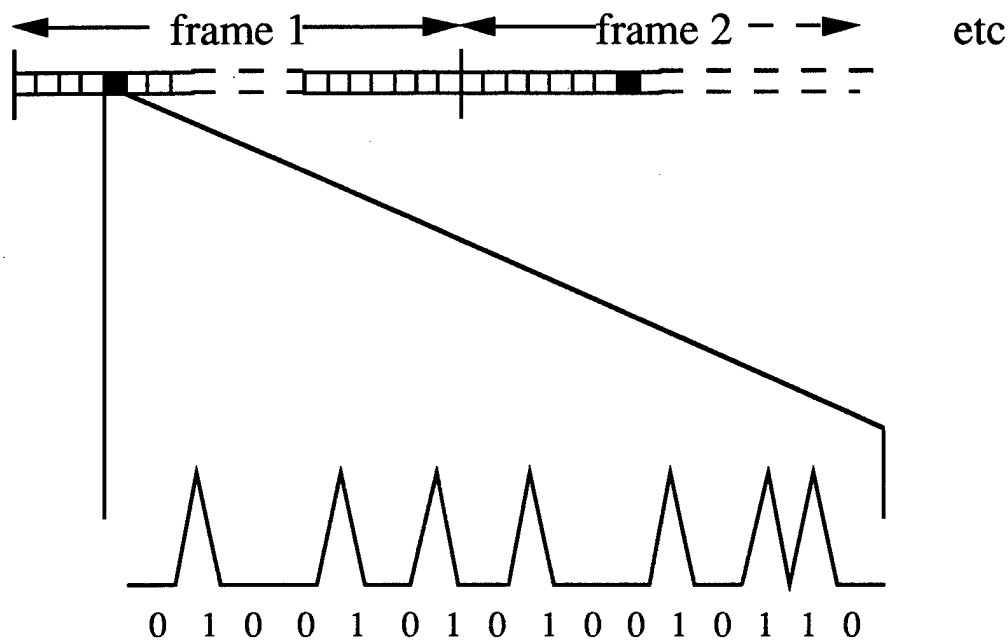
3

Fig. 1.2.3. Two-stage encoding. The user, or channel is defined by an orthogonal code. A second matched filter, positioned behind the first, decodes data and applies error-correction. Hence error-correcting codes are required for the second stage. The word size of the second stage is dependent upon the availability of optical devices capable of providing, e.g., BPSK or pulse position modulation (PPM), etc., representing $n$-bit words. Here, a 16-bit word is shown.

Using the two-stage principle of encoding as well as multidimensional coding, and presuming device capabilities which are either available now, or being tested in the laboratory, or might be in the future, predictions can be made concerning the data rate achievable for high data rate channels. Table 1.2.1 provides those predictions.

The aim of this research is illustrated in the data rates of the following Table 1.2.1 showing channel data rate estimates with two-level coding & devices and input-output capability assumed§.

**Table 1.2.1:** An Example Algorithm - Channel Data Rate Estimate with Two-Level Coding & Devices and Input-Output Capability Assumed§

| | | 2-bit word | 4-bit word | 8-bit word | 16-bit word† | 32-bit word† |
|---|---|---|---|---|---|---|
| One Code (*MicroChannel*) | | | | | | |
| Min. MicroPulse Durat. Assumed | | 100 femtosec. | | | | |
| MacroPulse & MacroSlot Duration | | 1 picosecond | | | | |
| MacroSlot Repetition Frequency | | 1 TeraHertz | | | | |
| One Code/MicroChannel Data Rate | | 2 Gigabits/s. | 4 Gigabits/s | 8 Gigabits/s. | 16 Gigabits/s | 32 Gigabits/s. |
| | | | | | | |
| *MacroChannel* | | | | | | |
| For a 1021 x 1021 length code: | | | | | | |
| MacroSlot Rate | | 1 TeraHertz | | | | |
| Frame Rate | | 1 GigaHertz | | | | |
| SuperFrame Rate | | 1 MegaHertz | | | | |
| MicroSlot Duration | | 500 femtos. | 250 femtos. | 125 femtos. | 62.5 femtos. | 31.25 femtos. |
| Timing Accuracy Required | | ±250 femtos. | ±125 femtos. | ± 62.5 femtos. | ± 31.25 femtos. | ± 15.625 femtos. |
| One Code/MicroChannel Data Rate | | 2 Gigabits/s/ | 4 Gigabits/s. | 8 Gigabits/s. | 16 Gigabits/s. | 32 Gigabits/s. |
| 1021 Code/MacroChannel | | 2 Terabits/s. | 4 Terabits/s. | 8 Terabits/s. | 16 Terabits/s. | 32 Terabits/s. |
| Wavelengths Available (Now) | 4 | 4 Terabits/sec. | 16 Terabits/sec. | 32 Terabits/sec. | 64 Terabits/sec. | 128 Terabits/sec. |
| Wavelengths Available (Future) | 8 | 8 Terabits/sec. | 32 Terabits/sec. | 64 Terabits/sec. | 128 Terabits/sec. | 256 Terabits/sec. |

§ A minimum resolvable micropulse duration of 100 femtoseconds is assumed.
† Shaded columns assume a minimum resolvable micropulse duration of less than 100 femtoseconds.

## 1.3 State of the Art Benchmark from which BSEI Research Proceeds

The state of the art is to utilize wavelength division multiplexing (WDM) to provide separate communications channels; and code division multiple access (CDMA) together with time hopping (TH) to provide multiple access using orthogonal codes.

## 1.4 Deficiencies in State of the Art Addressed by BSEI Research:

• Good orthogonal codes must possess both good autocorrelation properties (for code lock-on) and also good crosscorrelation properties (for minimum multiuser crosstalk). These two necessary properties are in a tradeoff relationship, e.g., some codes possess one without the other. There is presently no understanding of this tradeoff so that the design of good orthogonal codes with both desirable properties is presently an empirical pursuit.

• Good error-correcting codes are also required at a second level in order to provide reliable communications. Although perfect (because able to correct error patterns at a stipulated distance) codes are available, they are rare, and those in common use have limitations. There is presently a need to extend the foundations of error correcting codes so that the design of perfect codes can be advanced.

• Although WDM has become available, there has been no extension of spread spectrum techniques to joint time-frequency schemes (i.e., both time and frequency hopping). As in all spread spectrum techniques, a time-frequency spread spectrum coding would reduce the probability of error.

• New device technology permits the implementation of new coding schemes, but new coding schemes justify new device technology. Both the device technology and code possibilities justify approaches to more efficient communications backbone schemes. This mutual "cross-fertilization" between device and coding capabilities has not occurred to any degree.

• Both new hopping codes and device technologies require new device approaches to timing control and code identification.

## 1.5 Implementation by BMDO

• In any ballistic missile defense scenario, high data rate communications supporting real-time interactive imagery are required by Command & Control. Given a physical infrastructure, the highest data rates can be achieved only by efficient coding techniques.

• In any BMDO test-bed scenario, the test and showcasing of technologies ready for transition will be dependent upon high data rate communications. Again, given a physical infrastructure, the highest data rates can be achieved only by efficient coding techniques.

• Dual use: the medical profession is moving from a photographic data capture to an electronic data capture environment, e.g., the Army's "All Digital Hospital" concept. Transmission of medical images and large data arrays will test the performance of communications channels. Therefore high data rates are required and so, again, given a physical infrastructure, the highest data rates can be achieved only by efficient coding techniques.

## 1.6 What is new, innovative in BSEI's research results and what are the implications?

### 1.6.1 New and Innovative:

BSEI has

- implemented group theory (Young frame and tableaux) in characterizing code properties and has used these methods in optimum code design.
- developed a Lexicographic-Greedy Code algorithm for code generation - Lexicographic-Greedy codes provide perfect codes.
- implemented Lexicographic constructions for optimum orthogonal codes, not just error correcting codes.
- demonstrated:
  - orthogonal codes as extended cyclic Reed-Solomon an increase in the number of usable codes (More codes, means higher aggregate data rate).
  - inverse constructions extending number of usable codes.
  - constructions from a Young tableau diagram formalism for designing optimum properties
  - conjugate constructions using Young tableaux to extend the number of usable codes
  - codes formulated in group symmetry form for attainment of optimum correlation properties
  - application of Lexicographic ordering for achieving optimum orthogonal codes

- utilized the Zech Logarithmic constructions with the normal constructions as basis, by a new method of deriving a GF(11) field from the $GF(2^4)$ field. To our knowledge the generation of codes by these construction methods is original and unique. The number of codes with good autocorrelation and crosscorrelation properties can be increased by the use of the Zech Logarithm construction. These new methods provide a fruitful way of doubling the number of usable codes. As each code provides another user, or channel, their use will increase the available data rate of information transmission.

- applied optical, analog, Fourier transform principles to determine whether all-optical methods can be implemented to rapidly detect time hopping codes in optical fibers. The results obtained are clear-cut. The optical (analog) method according to the results obtained provides signal-to-noise levels equal to that of electronic (digital) methods. In the case of the two codes, the Hyperbolic Congruence and the Quadratic Congruence, the results are superior for both auto- and cross-correlation detection. Furthermore, the cross-correlation (but not the auto-correlation) of the Welch-Costas codes is known to be inferior, and this is clearly detected. We also demonstrated that although optical methods can be used to identify codes in noise, e.g., the noise from other codes, the hub system is ultimately overwhelmed by that noise. This is because optical methods provide *a global (in time) matched filter* which is open to noise interference. An electronic matched filter, on the other hand, provides *local (in time) matched filters* which are masked from the noise caused by the presence of other codes by electronic switching. An electronic matched filter would provide better performance in the presence of noise due to other codes.

- addressed the underlying group structure of the orthogonal codes: the hyperbolic congruence, the quadratic congruence, and the Welch-Costas codes. Excellent performance in the case of one attribute, e.g., auto-correlation, is sometimes associated with poor performance in the other attribute, e.g., cross-correlation; and reported the *Mathematica* algorithmsfor demonstrating the differences in group structure between three types of

7

orthogonal codes. The superiority of the hyperbolic and quadratic congruence codes in both auto- and cross-correlation properties, as compared with the superiority of the Welch-Costas codes in auto-correlation properties, but poor performance in cross-correlation properties, is clearly mirrored in the lack of symmetry shown by the Welch-Costas codes by this form of analysis.

• addressed the possibility of increasing data rate in optical fiber communications by using the method of bit parallel wavelength division (BPWD) which, among other techniques, utilizes the "shepherding pulse" technique to maintain pulse alignment. Both method and technique are due to Yeh & Bergman and is based on the cross-phase modulation effect. Simulation of this technique involves the numerical evaluation of simultaneous coupled nonlinear Schrödinger equations. These investigators used the split-Fourier method but we were able to solve the coupled equations using approximation methods. Although limitations in computer memory precluding our simulating over optical fiber distances greater than 10 km, we were able to confirm their results.

## 1.6.2 Implications of this research

• BSEI's work has confirmed the benefit of a two-stage hierarchy of codes. At the first stage, orthogonal codes define the microchannel or user, identified by a first (temporal) matched filter. Once a code is identified by this filter, a second (temporal) matched filter identifies the pulse-position-modulated data with error correction, hence error-correcting codes are required for the second stage. BSEI has shown that congruence codes have the best properties for use as orthogonal codes (hyperbolic, quadratic, cubic and quartic) and Lexicographic codes for error correcting codes.

• Besides a hierarchical backbone topology, a multidimensional coding scheme intermixing CMDA, TDMA and WDM provides the possibility of the highest data rates.

• These recommended techniques provide signal spreading techniques, but they are spread time techniques, as opposed to spread spectrum techniques.

• A major part of this study has addressed the impact of symmetry principles on code design to achieve optimum properties. BSEI has provided many examples of heretofore unknown symmetries underlying code design. These discoveries impact optimum code design and hence data rate.

## 1.8 Future work

(1) Multi-bit words required from devices and addressed by codes

(2) Extend codes from time hopping to time and frequency hopping.

(3) Extend perfect Lexicographic codes for use in both orthogonal code construction and error correction code construction.

(4) Extend Group theory (Young tableaux approach) constructions into error correcting code design.

## 1.9 Future Needs

Generation of Lexicographic codes of only length 10, takes over 36 hours of continuous run time on a 120 MHz Power Macintosh.

Codes of length 1021 are required, therefore BSEI needs access to more powerful computational capabilities for implementation of these codes.

BSEI has generated many new ideas concerning code constructions for optimum properties. Now collaboration is needed with both coding theorists and new device developers, as well as access to more powerful computational capabilities. Implementation of these ideas should now take place.

## 2.0 Summary of Results:

This report summarizes the major results of the study, and which were reported on a monthly basis throughout the 12-month duration of the contract. Due to the fact that this investigation produced a rich harvest of new approaches and insights, not all the details of the results reported monthly can be encompassed in a single final report. Therefore, we summarize in this section the major results, which are:

**2.0.1** We addressed the maximum number of simultaneous users in multiple access and possible sources of reduction in performance. Using the Gaussian approximation, we showed that pulse-position modulation accommodates a large number of simultaneous users at an excellent error probability. There are indicators that the probability of error for orthogonal codes decreases with (1) an increase in the matched filter threshold and (2) an increase in code length. However, the simple statement that performance is improved by increasing the code length and raising the receiver threshold obscures a more subtle relationship. We showed, in fact, that using more pulses in a code sequence results in reduction in performance unless the receiver threshold is raised. However, using more pulses in a sequence does not result in a reduction in performance if the receiver threshold is raised. We also showed a dramatic degradation in performance of the system when timing errors are introduced.

**2.0.2** We provided an analytical model from the signal processing perspective as a basis for the cross-comparison of the varieties of spread spectrum techniques. The technique we have advocated for use in high data rate optical fiber communications - time hopping CDMA - is shown to be distinctively different from other forms of spread spectrum. Implementation of time hopping at high data rates will be dependent on device hardware capabilities.

**2.0.3** We addressed the generation of more usable codes than can be obtained by normal construction methods and examined the hyperbolic congruence, the quadratic congruence and the Welch-Costas codes. Specifically, we were able to utilize Zech Logarithmic constructions with the normal constructions as basis, by a new method of deriving a $GF(11)$ field from the $GF(2^4)$ field. To our knowledge the generation of codes by these construction methods is original and unique. The major results detected by this form of analysis are: (1) The number of codes with good autocorrelation and crosscorrelation properties can be increased by the use of the Zech Logarithm construction. This increase in usable codes is particularly so in the case of hyperbolic congruence codes, less so in the case of quadratic congruence codes, but not so in the case of Welch-Costas codes. (2) It is significant that the relative merits of the three normal constructions - hyperbolic congruence, quadratic congruence and Welch-Costas - are transferred to the Zech Logarithm constructions of those codes. That is, both the merits and demerits of the normal constructions appear in the Zech Logarithm constructions. These new methods provide a fruitful way of doubling the number of usable codes. As each code provides another user, or channel, their use will increase the available data rate of information transmission.

**2.0.4** We applied optical, analog, Fourier transform principles to determine whether all-optical methods can be implemented to rapidly detect time hopping codes in optical fibers. We address three types of orthogonal codes: Hyperbolic Congruence Codes, $p = 11$; Quadratic Congruence Codes, $p = 11$; Welch-Costas Codes, $p = 11$. A specific objective was to determine whether optical auto- and cross-correlation methods provide sufficient signal-to-noise to compete with electronic digital methods not only in speed but also in accuracy. The results obtained are clear-cut. The optical (analog) method according to the results obtained provides signal-to-noise levels equal to that of electronic (digital) methods.

10

In the case of the two codes, the Hyperbolic Congruence and the Quadratic Congruence, the results are superior for both auto- and cross-correlation detection. Furthermore, the cross-correlation (but not the auto-correlation) of the Welch-Costas codes is known to be inferior, and this is clearly detected. Future work will address implementing these principles in a communications hub system.

**2.0.5** We continued to develop optical, analog, Fourier transform analytical methods to determine whether all-optical methods can be implemented to rapidly detect time hopping codes in optical fibers and specifically in a hub system. We addressed three types of orthogonal codes: Hyperbolic Congruence Codes, $p = 11$; Quadratic Congruence Codes, $p = 11$; Welch-Costas Codes, $p = 11$. A specific objective was to determine whether multiple orthogonal codes can be identified in an all-optical hub filter system. Using 2-D Fourier, 2D-inverse Fourier and filter optics, we show that the optics method performs well in identifying/recognizing 4 or more codes. However, we also demonstrate that although optical methods can be used to identify codes in noise, e.g., the noise from other codes, the hub system is ultimately overwhelmed by that noise. This is because optical methods provide a *global (in time) matched filter* which is open to noise interference. An electronic matched filter, on the other hand, provides *local (in time) matched filters* which are masked from the noise caused by the presence of other codes by electronic switching. An electronic matched filter would provide better performance in the presence of noise due to other codes. We also examined the variables affecting BER in an optical receiver.

**2.0.6** We addressed (1) the trades possible between the bandwidth of a multibit word and the bandwidth of multiple frequency channels (WDM) under Shannon channel capacity theorem limitations; and (2) the trades dictated by the power penalties due to: (i) the extinction ratio; (ii) intensity noise parameter; (iii) timing jitter parameter; (iv) quantum limit; (v) dispersion; (vi) mode-partition noise; (vii) mode suppression; (viii) frequency chirping; (ix) feedback.

**2.0.7** We addressed the problem of determining performance limits on optical communications systems in the presence of both Poisson and Gaussian noise influences. Traditionally the model for detection of the inherently stochastic optical signal is a simple realistic model of a filtered Poisson process in which randomly excited detected photons excite a bandlimited filter. However, there are further stochastic disturbances, e.g., additive Gaussian colored noise introduced by post-detection signal processing circuits. As has been pointed out by O'Reilly and others, the result is a superposition of marked (compound) and filtered process with a colored Gaussian process. This is the mixed compound Poisson plus Gaussian regime. We used moment generating function methods to calculate those influences on receiver performance. We find that although the additive influence do influence optical receivers with no gain, influences on receivers with substantial gain are negligible. In the latter case, although compound influences are present, there appears no real need to take them into consideration.

**2.0.8** We addressed the impact of device capability on data rate and bit error rate, examining chirped Gaussian pulses, dispersion, modulation formats, preamplification and use of soliton pulses. The interaction between dispersion and pulse chirping was explored; the optimal operation of lightwave systems was modeled near the zero-dispersion wavelength of a fiber and by using optical sources with a relatively narrow spectral width; the effect on bit error rate of various modulation formats was modeled; as well as the effect on receiver sensitivity of filter bandwidth at various levels of the noise figure which showed that amplifiers with small noise figure must be used and performance can also be improved by reducing the optical filter bandwidth. As bit rate can also be increased by the use of very short pulses, solitons were modeled with respect to pulse evolution according to the order of the soliton. Other evolutions modeled were: to a "sech" pulse from a

Gaussian input and from a "sech" input of varying order; dark solitons; soliton pairs; and chirped solitons.

**2.0.9** We addressed the underlying group structure of the orthogonal codes: the hyperbolic congruence, the quadratic congruence, and the Welch-Costas codes. Achievement of the highest data rate optical communications - given a defined subcomponent performance - is dependent on achieving orthogonal codes with both excellent auto- and cross-correlation properties. Excellent performance in the case of one attribute, e.g., auto-correlation, is sometimes associated with poor performance in the other attribute, e.g., cross-correlation. To determine the group structure determining performance on both attributes, we initiated a study of the relative incidence of sequence occurrence across codes based on different prime numbers, and for sequences of 2,...., 6. We report the *Mathematica* algorithms and demonstrate the differences in group structure between the three types of orthogonal codes. The superiority of the hyperbolic and quadratic congruence codes in both auto- and cross-correlation properties, as compared with the superiority of the Welch-Costas codes in auto-correlation properties, but poor performance in cross-correlation properties, is mirrored in the lack of symmetry shown by the Welch-Costas codes in the analysis offered here.

**2.0.10** We addressed the possibility of increasing data rate in optical fiber communications by using the method of bit parallel wavelength division (BPWD) which, among other techniques, utilizes the "shepherding pulse" technique to maintain pulse alignment. Both method and technique are due to Yeh & Bergman and is based on the cross-phase modulation effect. The shepherding technique relies on the cross-phase modulation effect. Simulation of this technique involves the numerical evaluation of simultaneous coupled nonlinear Schrödinger equations. Yeh & Bergman used the split-Fourier method but we were able to solve the coupled equations using approximation methods. Although limitations in computer memory precluding our simulating over optical fiber distances greater than 10 km, we were able to confirm that a shepherding pulse will (1) decrease the bandwidth and heighten the amplitude of shepherded pulses; and (2) align to a time slot shepherded pulses propagating before and after that time slot. We also showed that (A) the effect is due to the greater amplitude of the shepherding pulse; (B) a shepherd pulse, although energy will not be exchanged between the beams, will enhance the compression of co-propagating beams at different wavelengths if those beams are in the anomalous dispersion region; (C) unlike SPM and GVD, in the case of CPM, in the presence of a shepherding pulse compression will occur for soliton orders << 1; (D) if the primary pulse is in the normal dispersion region, a dark soliton is generated rather than pulse compression; (E) time-alignment of copropagating beams. Successful generation of time-aligned pulses on BPWD beams is crucial to the realization of ultra-high data rate BPWD single fiber systems.These results are obtained within an analysis of the more general relations of dispersive effects, the nonlinear Schrödinger equation and cross-phase modulation.

## 3.0 Probability of Error

A Gaussian approximation can be used to evaluate the probability of error for time hopping codes[1]. A derivation in Kwong et al[2] gives the following approximation (valid for large values of $N$:

$$P_E = \phi\left(\frac{-P}{\sqrt{N-1}}\right),$$

where

$$\phi = \frac{1}{\sqrt{2\pi}}\int_{-\infty}^{x} exp\left[-\xi^2/2\right]d\xi$$

is the unit normal cumulative distribution function and $P$ is a prime number, as well as the number of codes generated and equal to $\omega$, the number of binary ones per code sequence. Fig.s 1, 2 and 3 show the (log) probability of error versus the number of simultaneous users users as a function of $P$.

logPE
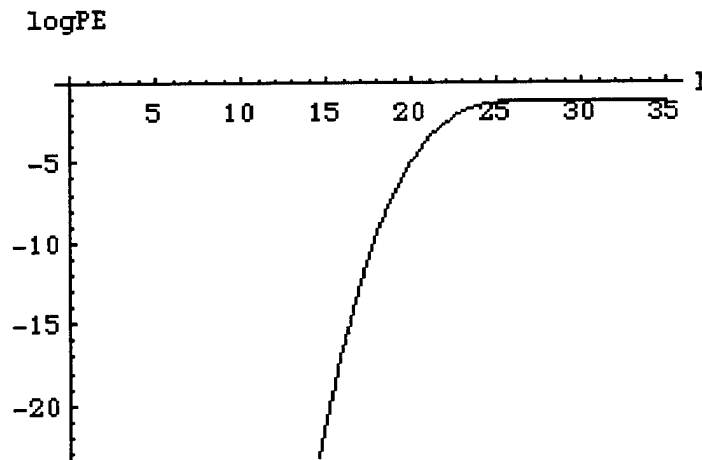


Fig. 3.0.1. Log Probability of error versus the number of simultaneous users for prime number and number of codes = 23. It can be seen that pulse position modulation (PPM) CDMA can accommodate 23 subscribers and 18 simultaneous users with a probability of error less than $10^{-9}$.

[1]Prucnal, P.R., Santoro, M.A. & Fan, T.R., Spread spectrum fiber-optic local area network using optical processing. *J. Lightwave Technology*, LT-4, 547-554, 1986;

Kwong, W.C., Perrier, P.A. & Prucnal, P.R., Performance comparison of asynchronous and synchronous code-division multiple-access techniques for fiber-optic local area networks. *IEEE Trans. Comm.*, 11, 1625-1634, 1991;

Gagliardi, R.M., Mendez, A.J., Dale, M.R. & Park, E., Fiber-optic digital video multiplexing using optical CDMA. J. Lightwave Technology 11, 20-26, 1993;

Gagliardi, R.M., Pulse-coded multiple acces in space optical communications. *IEEE J. Selected Areas in Communications*, 13, 603-608, 1995.

[2]Kwong, W.C., Perrier, P.A. & Prucnal, P.R., Performance comparison of asynchronous and synchronous code-division multiple-access techniques for fiber-optic local area networks. *IEEE Trans. Comm.*, 11, 1625-1634, 1991.

LogPE
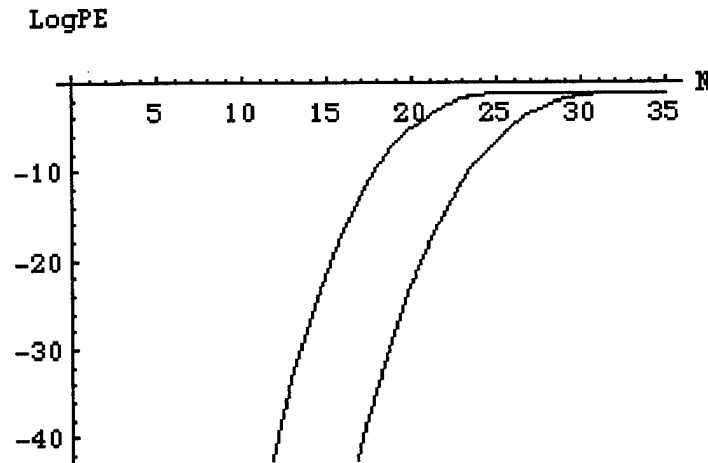


Fig. 3.0.2. Log Probability of error versus the number of simultaneous users for prime numbers and number of codes = 23 and 29. It can be seen that pulse position modulation (PPM) CDMA can accommodate 29 subscribers and 24 simultaneous users with a probability of error less than $10^{-9}$.

logPE
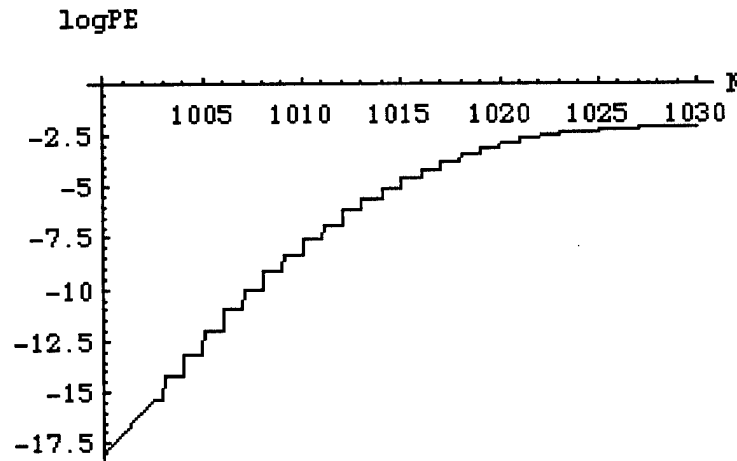


Fig. 3.0.3 Log Probability of error versus the number of simultaneous users for prime number and number of codes = 1021. It can be seen that pulse position modulation (PPM) CDMA can accommodate 1021 subscribers and 1008 simultaneous users with a probability of error less than $10^{-9}$.

Fig.s 3.0.1-3 indicate that time hopping pulse position modulation CDMA can accommodate a large number of simultaneous users at an excellent error probability.

## 3.1 Interference from multiple access and graceful degradation

Other calculations indicate that the probability of error for orthogonal codes decreases with (1) an increase of the matched filter threshold and (2) an increase in code length. For example, Azizoglu et al[3] addressed performance limitations in optical CDMA

[3] Azizoglu, M.Y., Salehi, J.A. & Li, Y., On the performance of fiber-optic CDMA systems. Proc. IEEE GLOBECOM 1990, San Diego, CA, Dec. 1990, pp. 1861-1865;

14

scenarios. Using the primary number 11 as an example, the following variables are defined:

$F$ chips constitute a superframe. In the case of a 10×10 code matrix, $F = 10^2 = 100$. Each of these chips is of duration $\tau_c$ with $T_b = F\tau_c$ being the duration of the superframe. $K$ of the $F$ chips are occupied. In the case of $p = 11$ codes, $K = 11$. The data encoding which Azizoglu et al consider are cases of users in the network sending their data in an on-off modulation format, so that for a "0" bit a user sends nothing and for a "1" bit a temporal signature is sent, but the data encoding could be a pulse-position modulation scheme.

In the case of optical orthogonal codes (OOC), two code words should not overlap at more than one pulse position. As there are $K^2$ ways of pairing the $K$ pulses of two users, the probability that a pulse belonging to a particular user overlapping with one of the pulses of the desired user is:

$$q = \frac{K^2}{2F},$$

where the factor 1/2 is due to the probability that the interferer is transmitting a "1" - i.e., that the first form of informational encoding has been chosen.

If $M$ is the number of users, and $l$ the number of interfering users, the *pattern of interferences* is described by a an interference vector, $\alpha(l)$. Given that there are $i$ interfering users - each interfering at exactly one pulse position - there is a variety of possible interference patterns. Therefore, the vector, $\alpha(l)$, is a $K$-dimensional vector whose $i$th element, $\alpha_i(l)$, represents the number of pulses that overlap with the $i$th pulse of the desired user. *As every interfering user contributes one and only one pulse*[4], the vector satisfies:

$$\sum_{i=1}^{K} \alpha_i(l) = l \quad \alpha_i(l) \in \{0,1,...,l\}.$$

If the receiver is *not* hard-limited, then:

$$\sum_{i=1}^{K} \alpha_i \geq Th,$$

and an error will occur if $l \geq Th$. On the other hand, in the hard-limited case, $Th = K$ and Azizoglu et al show that:

$$P_E = \frac{1}{2}\sum_{i=0}^{K}(-1)^i\binom{K}{i}\left(1-\frac{qi}{K}\right)^{M-1},$$

This probability of error is shown in Fig. 3.1.1 for three values of $M$, the number of users.

---

Azizoglu, M.Y., Salehi, J.A. & Li, Y., Optical CDMA via temporal codes. *IEEE Trans. Comm.*, 40, 1162-1170, 1992.

[4] This assumption is questionable.
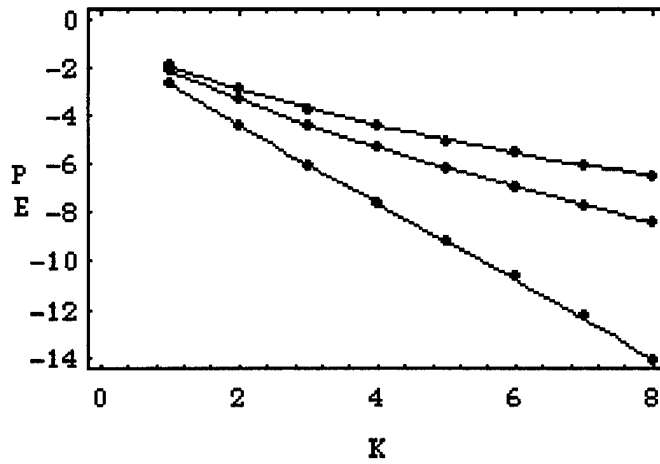
Fig. 3.1.1. Bit error probability for an OOC with F = 1000, M = 10, 30 & 50 (lower to upper) and $K = Th$. After Azizoglu et al[3].

If the restrictions on the auto- and cross-correlations are relaxed from $\lambda = 1$ to $\lambda = 2$, upper and lower bounds can be given to the error probability:

$$lower\ bound : P_E \geq \sum_{i=0}^{K}(-1)^i\binom{K}{i}\left[1-\frac{pi}{K}\left(2-\frac{i}{K}\right)\right]^{M-1},$$

$$upper\ bound : P_E \leq \sum_{i=0}^{K/2}(-1)^i\binom{K}{i}\left[1-\frac{pi}{K}\left(2-\frac{i}{K}\right)\right]^{M-1},$$

where $p = K^2/4F$. Upper and lower bounds are shown in Fig. 3.1.2, for $M = 50$, and Fig. 3.1.3. for $M = 10$.



K   M=50, F=1000 ,
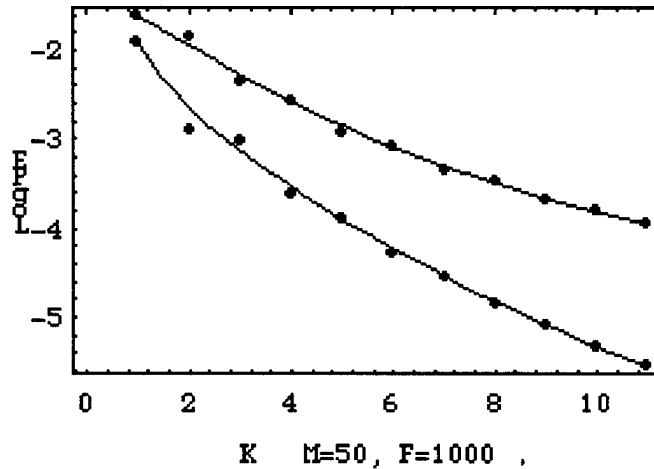
Fig. 3.1.2. Upper and lower bounds to the worst case error probability for the $\lambda$=2 code, $M = 50$. After Azizoglu et al[3].

16
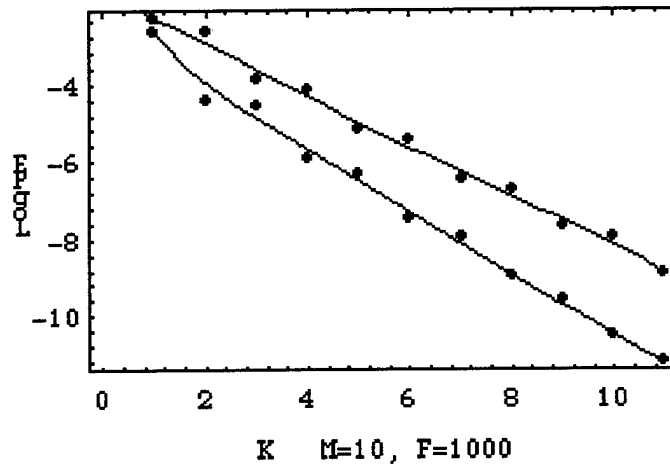
Fig. 3.1.3. Upper and lower bounds to the worst case error probability for the $\lambda = 2$ code, $M = 10$. After Azizoglu et al[3].

Further evidence that the probability of error decreases with an increase of the matched filter threshold and an increase in code length is provided by Kostic and Titlebaum[5]. These authors addressed the problem of error for two sets of quadratic congruence codes defined with respect to the bound on the maximum value of the inner product between two arbitrary sequences being equal to 2 - $C'_{QC}$, or equal to 1 - $C_{QC}$, where $C'_{QC}$ is a time hopping pattern set and $C_{QC}$ is an optical code set[6]. Interference is represented by a probability distribution function ($pdf$) of a random variable, $I$. For the set, $C'_{QC}$ and prime $p$, the $pdf$ is:

$$pdf_{C'_{QC}} = \frac{1}{p+1}\delta(I_n - 0) + \frac{p}{p+1}\delta(I_n - 1), \text{ and}$$

$$E(I_n) = 1, \quad \sigma^2(I_n) = \frac{p-1}{p};$$

and for the set, $C_{QC}$, the $pdf$ is:

$$pdf_{C_{QC}} = \frac{3p-1}{4p}\delta(I_n) + \frac{1}{2p}\delta(I_n - 1) + \frac{p-1}{4p}\delta(I_n - 2), \text{ and}$$

$$E(I_n) = 1, \quad \sigma^2(I_n) = \frac{3p-2}{4p}.$$

With the variables, $A$, $B$ and $C$, defined as:

[5] Kostic, Z. & Titlebaum, E.L., The design and performance analysis for several new classes of codes for optical synchronous CDMA and for arbitrary-medium time-hopping synchronous CDMA communication systems. *IEEE Trans. Comm.*, 42, 2608-2617, 1994.

[6] Sequences from the set $C'_{QC}$ have the bound on the maximum value of the inner product between two arbitrary sequences equal to 2 and the number of code sequences is very large. The code set $C'_{QC}$ can be partitioned into many smaller $C_{QC}$ sets with the bound on the inner product equal to 1. Cf. Kostic, Z. & Titlebaum, E.L., *IEEE Trans. Comm.*, 42, 2608-2617, 1994.

17

$$A = \frac{p-1}{2p}, B = \frac{1}{p}, C = \frac{p-1}{2p},$$

$$A = \frac{3p-1}{4p}, B = \frac{1}{2p}, C = \frac{p-1}{4p}$$

for the sets $C'_{QC}$ and $C_{QC}$, respectively, the error probability is:

$$PE = \frac{1}{2}\left\{ \sum_{i=Th}^{N-2} \sum_{j=\left\lfloor \frac{i+1}{2} \right\rfloor}^{i} A^{N-1-j} B^{2j-i} C^{i-j} \frac{(N-1)!}{(2j-i)!(i-j)!(N-1-j)!} + \right.$$

$$\left. \sum_{i=N-1}^{2(N-1)} \sum_{j=\left\lfloor \frac{i+1}{2} \right\rfloor}^{N-1} A^{N-1-j} B^{2j-i} C^{i-j} \frac{(N-1)!}{(2j-i)!(i-j)!(N-1-j)!} \right\}$$

Fig.s 3.1.4-7 show the (log) error probability versus matched filter threshold for several codes and users. Fig.s 3.1.8-11 show the ratio of the error probability to the number of sequences in a set versus the matched filter threshold for a number of codes and users.
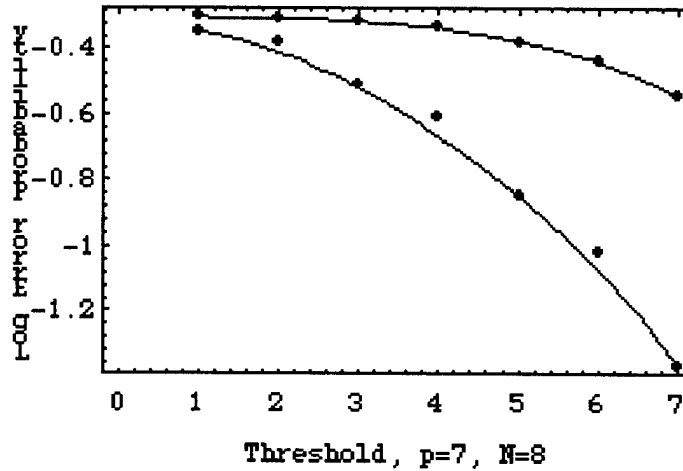


Fig. 3.1.4. Error probability versus matched filter threshold for $p = 7$, $N = 8$. $C_{QC}$ (lower), $C'_{QC}$ (upper). After Kostic & Titlebaum[5].
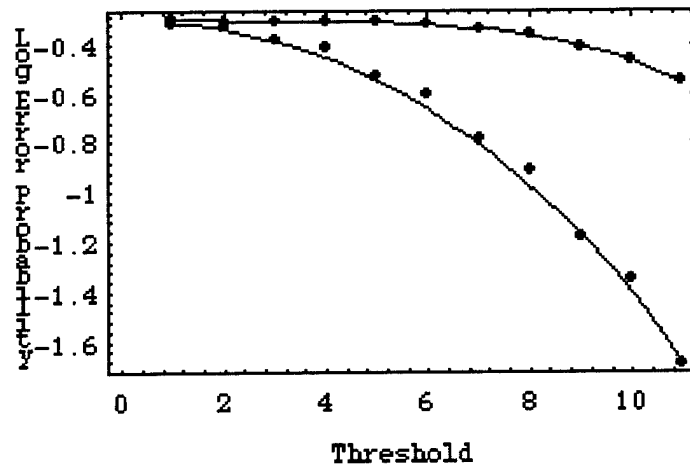
Fig. 3.1.5. Error probability versus matched filter threshold for $p = 11, N = 12$. $C_{QC}$(lower), $C'_{QC}$ (upper). After Kostic & Titlebaum[5].
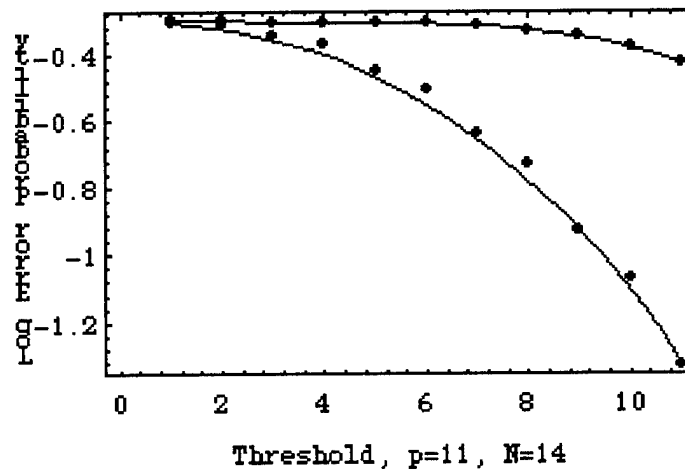


Fig. 3.1.6. Error probability versus matched filter threshold for $p = 11, N = 14$. $C_{QC}$(lower), $C'_{QC}$ (upper). After Kostic & Titlebaum[5].
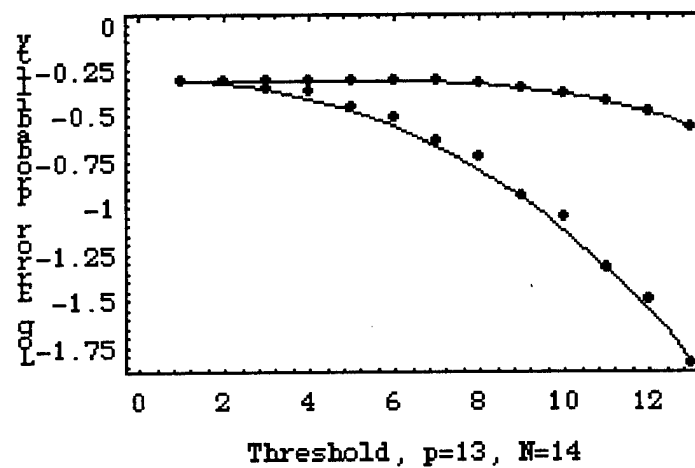


Fig. 3.1.7. Error probability versus matched filter threshold for $p = 13, N = 14$. $C_{QC}$(lower), $C'_{QC}$ (upper). After Kostic & Titlebaum[5].

19
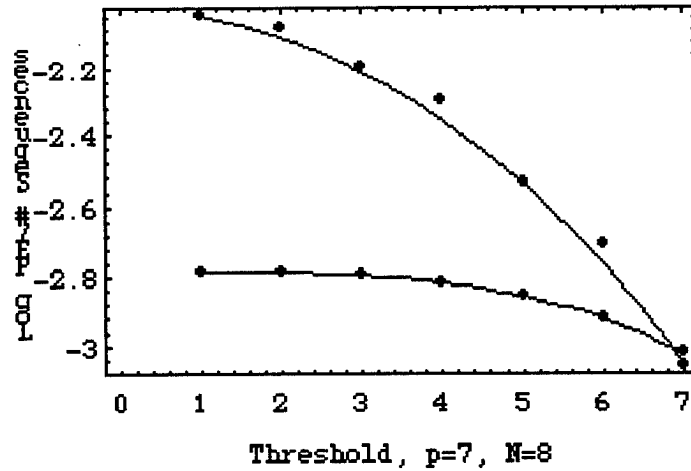
Fig. 3.1.8. Log PE/number of sequences in set as a function of threshold. $p = 7, N = 8$. $C_{QC}$ (upper); $C'_{QC}$ (lower).
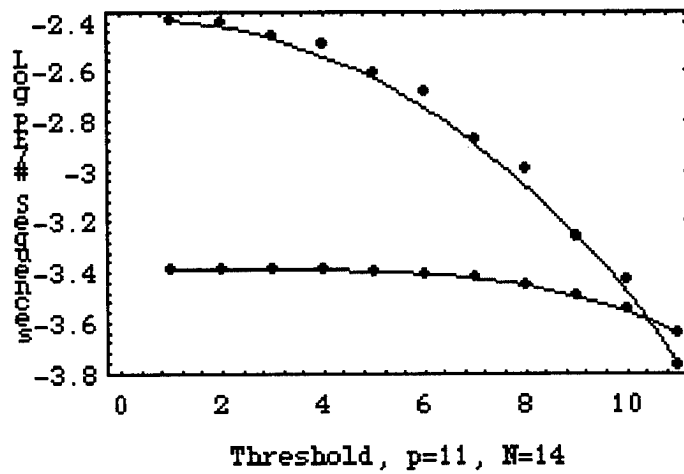


Fig. 3.1.9. Log PE/number of sequences in set as a function of threshold. $p = 11$, $N = 12$. $C_{QC}$ (upper); $C'_{QC}$ (lower).
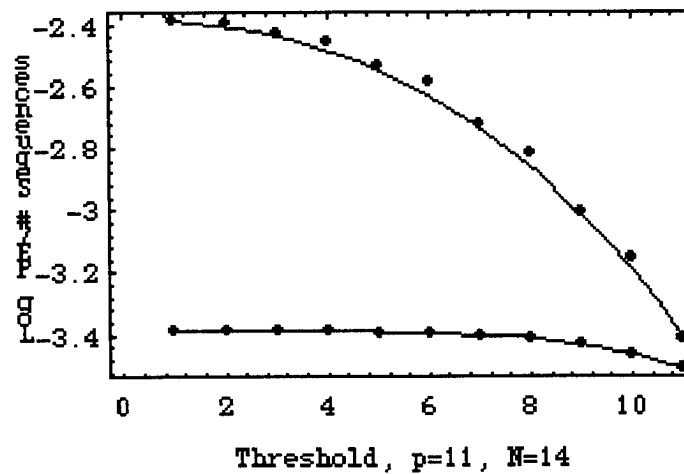


Fig. 3.1.10. Log PE/number of sequences in set as a function of threshold. $p = 11$, $N = 14$. $C_{QC}$ (upper); $C'_{QC}$ (lower). After Kostic & Titlebaum[5].

20
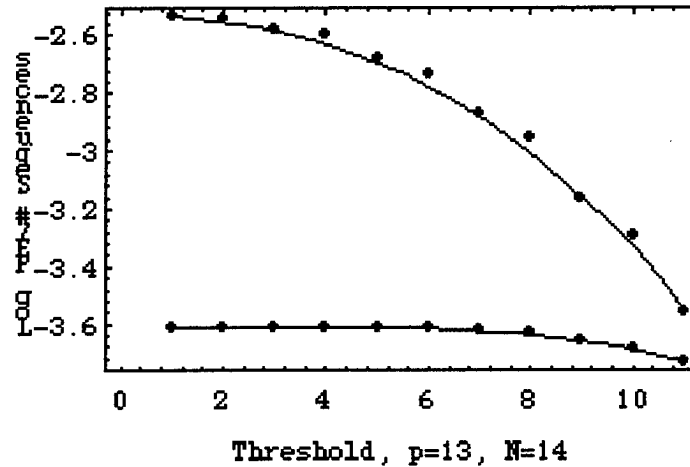
Fig. 3.1.11. Log PE/number of sequences in set as a function of threshold. $p = 13$, $N = 14$. $C_{QC}$ (upper); $C'_{QC}$ (lower).

## 3.2 Reduction in Performance Resulting from More Pulses in a Sequence is Offset by Raising the Threshold of the Receiver

The simple statement that performance is improved by increasing the code length and raising the receiver threshold obscures a more subtle relationship. Using more pulses in a sequence does not result in a reduction in performance *if one can raise the receiver threshold*. In fact, raising the receiver threshold due to the availability of more pulses in the code results in a much greater gain in performance than any reduction in performance due to there being more pulses in the code. However, if the number of pulses in the code were increased and the threshold were kept constant, then the performance *would* degrade.

This can be seen using the method of extended sets of Salehi[7]. By this method, if two codes #1 and #2, e.g., of the cubic congruence code $p = 11$ are considered, then equivalent sets, $A^1$ and $A^2$, are:

$$A^1 = \{17, 7, 14, \ 5, 13, \ 5, 14, 7, 17, 1\},$$

$$A^2 = \{4, \ 11, 16, 8, 9, 8, 16, 11, 4, 13\}.$$

The Salehi extended sets are defined as follows. For any sequences, $x_n$ and $y_n$, of period $F$ and chip size $K$:

$$\left| \sum_{n=0}^{F-1} x_n x_{n+l} \right| = \begin{cases} K & \text{for } l = 0 \\ \leq \lambda_a & \text{for } 1 \leq l \leq F-1 \end{cases},$$

$$\left| \sum_{n=0}^{F-1} x_n y_{n+l} \right| \leq \lambda_c \quad \text{for } \ 0 \leq l \leq F-1 \ .$$

[7] Salehi, J.A., Code division multiple-access techniques in optical fiber networks - Part I: Fundamental principles. *IEEE Trans. Comm.*, 37, 824-833, 1989.

where $\lambda_a$ and $\lambda_c$ are constants. Optical orthogonal codes are defined by the condition: $\lambda_a = \lambda_c = 1$. An extended set, $A^i_{EXT}$, is defined as all linear combinations of jointly connected relative delays, $\tau$, of different lengths, e.g.:

$$A_{EXT} = \left\{ \tau_1, \tau_2, ...\tau_n, \quad \tau_1 + \tau_2, ..., \tau_{n-1} + \tau_n, \quad ... \quad \tau_1 + \tau_2 + ...\tau_{n-1}, ..., \tau_n + \tau_1 + ...\tau_{n-2} \right\}$$

In the case of $A^1$ and $A^2$, the extended sets are:

$A^1_{EXT} =$
{17, 7, 14, 5, 13, 5, 14, 7, 17, 1, 24, 21, 19, 18, 18, 19, 21, 24, 18, 38, 26, 32, 23, 32, 26, 38, 25, 35, 25, 43, 39, 37, 37, 39, 43, 39, 42, 42, 39, 56, 44, 51, 44, 56, 44, 56, 49, 56, 44, 61, 58, 58, 61, 57, 61, 63, 63, 61, 57, 75, 65, 75, 62, 57, 61, 63, 63, 61, 57, 82, 82, 76, 61, 57, 61, 63, 63, 61, 57, 99, 83, 58, 61, 57, 61, 63, 63, 61};

$A^2_{EXT} =$
{4, 11, 16, 8, 9, 8, 16, 11, 4, 13, 15, 27, 24, 17, 17, 24, 27, 15, 17, 17, 31, 35, 33, 25, 33, 35, 31, 28, 21, 28, 39, 44, 41, 41, 44, 39, 44, 32, 32, 44, 48, 52, 57, 52, 48, 52, 48, 43, 48, 52, 56, 68, 68, 56, 61, 56, 59, 59, 56, 61, 72, 79, 72, 69, 61, 56, 59, 59, 56, 61, 83, 83, 85, 56, 61, 56, 61, 56, 59, 59, 56, 61, 87, 96, 68, 56, 61, 56, 59, 59, 56, 61},

where

$$\left| A^i_{EXT} \right| = K(K-1) \quad and \quad for \ K = 10, \ \left| A^i_{EXT} \right| = 90.$$

From the above, we can see that there are elements of both the sets $A^1_{EXT}$ and $A^2_{EXT}$ which are repeated eleven times and that there are common elements between the two sets, e.g., 17, 24, 35, 61. Thus, the above code is not an optical orthogonal code as defined by $\lambda_a = \lambda_c = 1$.

In the case of $N$ codes, the number of optical orthogonal codes are bounded by:

$$N \leq \left\lfloor \frac{F-1}{K(K-1)} \right\rfloor .$$

*For example, with F = 100 and* K = 10, $N \leq 1$, that is, only 1 optical orthogonal code is expected. In fact, the expectancy of an optical code can be predicted from the probability of a hit, or overlap in transmission from multiple users:

$$p = \frac{K^2}{F}.$$

For the codes considered in the tables above, i.e., with $K = 10$ and $F = 100$, $p = 1$. For $p = K^2/F \geq 0.8$ no families of optical orthogonal codes can be constructed other than $K = 2$, $N = 2$ and $F = 5$. (By optical orthogonal code a definition is meant whereby $\lambda_a = \lambda_c = 1$.) In the following, we see that this strict criterion can be relaxed.

## 3.3 Bit Error Analysis

The upper bound of the probability of error for the case of chip synchronous is[8]:

$$PE = \frac{1}{2}\sum_{i=Th}^{N-1}\binom{N-1}{i}\left(\frac{K^2}{2F}\right)^i\left(1-\frac{K^2}{2F}\right)^{N-1-i},$$

where "$Th$" is a correlation receiver threshold, $0 \leq Th \leq K$. Fig. 3.3.1 indicates (a) as expected, a reduction of the number of chips per frame results in a lowering of performance; and (b) as the receiver threshold is raised, the performance improves.
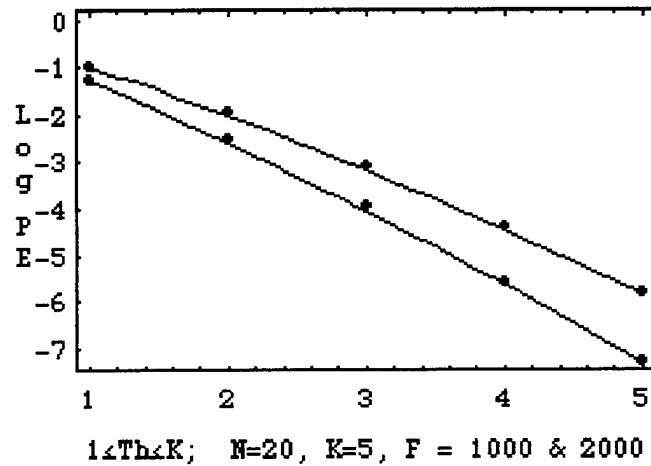


Fig. 3.3.1 Upper bound on bit error rate (chip synchronous): $N = 20$, $K = 5$. Upper, $F = 1000$; Lower, $F = 2000$. A reduction in the total number of chips per frame, $F$, i.e., slots available, results in a reduction in performance. After Ref[8]. Fig. 3(a).



---
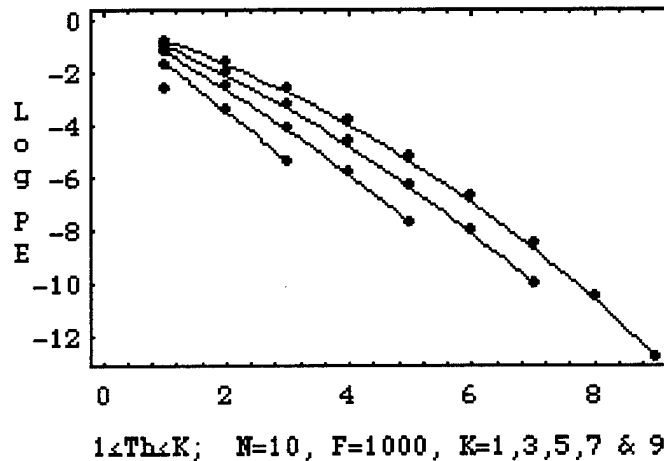
[8] Salehi, J.A. & Brackett, C.A., Code division multiple-access techniques in optical fiber networks - Part II: Systems performance analysis. *IEEE Trans. Comm.*, 37, 834-842, 1989.

Fig. 3.3.2. Upper bound on bit error rate (chip synchronous): $N = 10$, $F = 1000$, $K = 1,3,5,7,9$, left-to-right. Although increasing the number of pulses in the code, $K$, ostensibly results in a reduction in performance, the possibility of raising the receiver threshold actually results in a considerable increase in performance. After Ref[8], Fig. 3(b).

Fig. 3.3.2 on the other hand, indicates that using more pulses in a sequence *does not result in a reduction in performance if one can raise the receiver threshold*. In fact, raising the receiver threshold due to the availability of more pulses in the code *results in a much greater gain in performance than any reduction in performance due to there being more pulses in the code*. However, if the number of pulses in the code were increased and the threshold were kept constant, then the performance *would* degrade.

Fig. 3.3.3 shows the result for the case of the number of slots available in a superframe, $F$, being much larger than the number of users, $N$. In this case, increasing the number of users results in a reduction of performance (increasing $N$ from 10 to 50 is shown). This reduction in performance can be offset by hardlimiting the receiver. An optical hardlimiter, or threshold element, is defined as:

$$g(x) = \begin{cases} 1, & x \geq 1 \\ 0, & 0 \leq x < 1 \end{cases}.$$

That is, if an optical light intensity (x) is greater than, or equal to, one, then hardlimiting gives an output of one; and if the optical light intensity is smaller than one, then the response of the hardlimiter is zero.
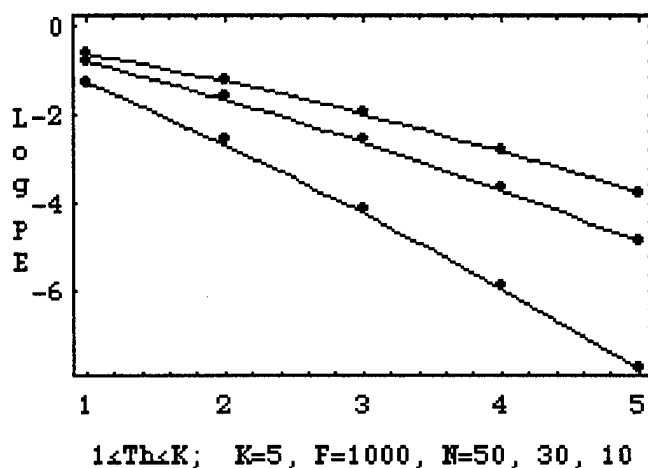


Fig. 3.3.3 Upper bound on bit error rate (chip synchronous): $K = 5, F = 1000, N = 10$, 30 and 50, left-to-right. This is the case of the number of slots in a superframe, $F$, being much larger than the number of users, $N$. In the case, increasing the number of users results in a major reduction in performance. After Ref[8], Fig. 3(c).

If *hard-limiting* is used on a receiver front-end, then the probability of error for the chip synchronous case is:

$$PE \leq \frac{1}{2} \binom{K}{Th} \prod_{m=0}^{Th-1} (1 - q^{N-1-m}); \quad q = 1 - \frac{K}{2F}; \quad p = 1 - q.$$

Fig. 3.3.4 (when compared with Fig. 3.3.2) shows that hard limiting increases performance by approximately 1.5 orders of magnitude. Fig.s 3.3.5 and 3.3.6 (when compared with Fig.s 3.3.1 and 3.3.3) indicate the same level of performance improvement.



1≤Th≤K;  F=1000, N=10, K=7 & 9
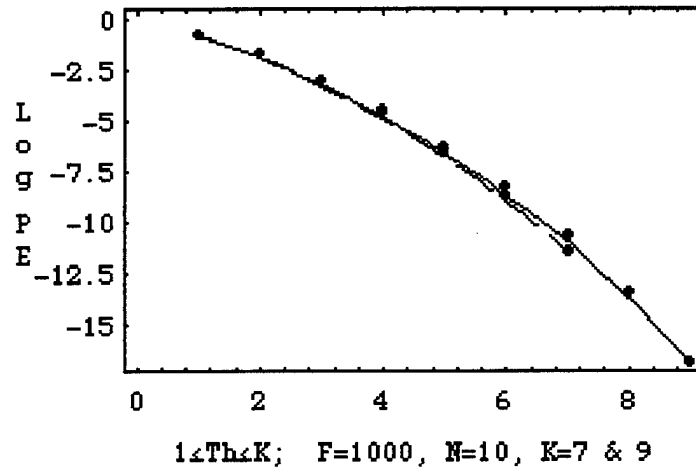
Fig. 3.3.4 Upper bounds on bit error rate (chip synchronous) with optical hard limiter: $F = 1000$, $N = 10$ and $K = 7$ (lower, hatched), $K = 9$ (upper, line, showing that hard-limiting increases performance by approx. 1.5 orders of magnitude. After Ref[8], Fig. 6(b).



1≤Th≤K;  F=1000, N=50,K=5 & N=30,K=6
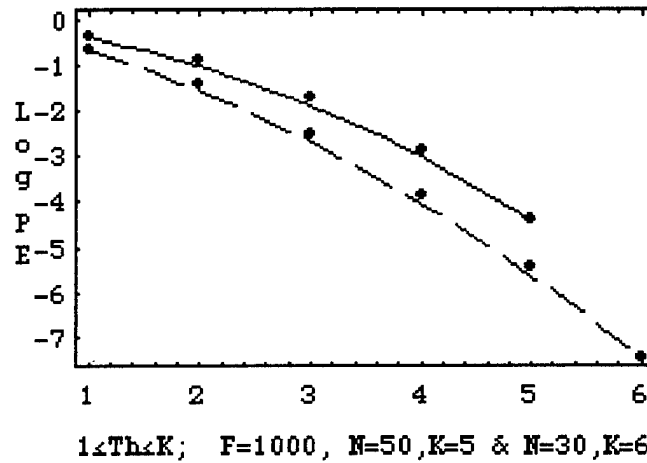
Fig. 3.3.5 Upper bounds on bit error rate (chip synchronous) with optical hard-limiter: $F = 1000$, $N = 50$ and $K = 5$ (upper, line) and $N = 30$ and $K = 6$ (lower, hatched). After Ref[8], Fig. 6(a).

1≤Th≤K;  F=1000, K=5, N=10 & 50
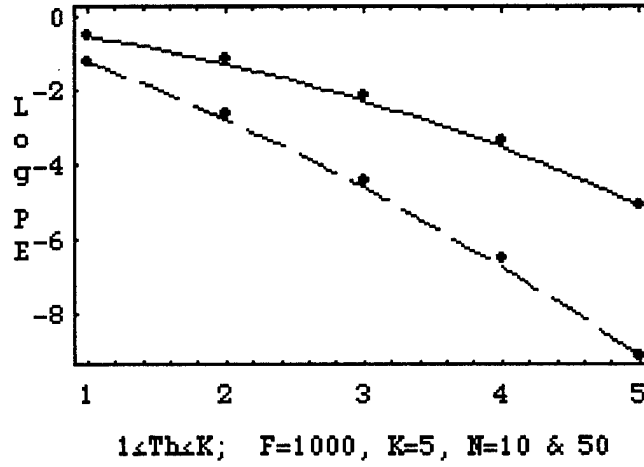
Fig. 3.3.6 Upper bounds on bit error rate (chip synchronous) with optical hard limiter: $F = 1000, K = 5$ and $N = 10$ (lower, hatched), $N = 50$ (upper, line). Compare with Fig. 3.1.3. After Ref[8], Fig. 6(c).

In the case of asynchronous transmission with hard limiting, the probability of error is:

$$PE \le \frac{1}{2}\binom{K}{Th}\prod_{m=0}^{Th-1}\left[1-\left\{q^{N-1-m}+(N-1-m)pq^{N-2-m}+\sum_{i=2}^{N-1-m}\binom{N-1-m}{i}p^i q^{N-1-i-m}\left(1-Q\left(\frac{1-i/2}{\sqrt{i/12}}\right)\right)\right\}\right]$$

where

$$p = \frac{K}{F},$$

$$q = 1-p,$$

$$Q(x) = \frac{1}{\sqrt{2\pi}}\int_x^\infty \exp\left[-\frac{\mu^2}{2}\right]d\mu.$$

Fig. 3.3.7 indicates the improvement of hard-limiting to the asynchronous case. The improvement is about 4-5 orders of magnitude.

26

$1 \le Th \le K; \quad F=1000, \quad K=5, \quad N=10 \ \& \ 50$
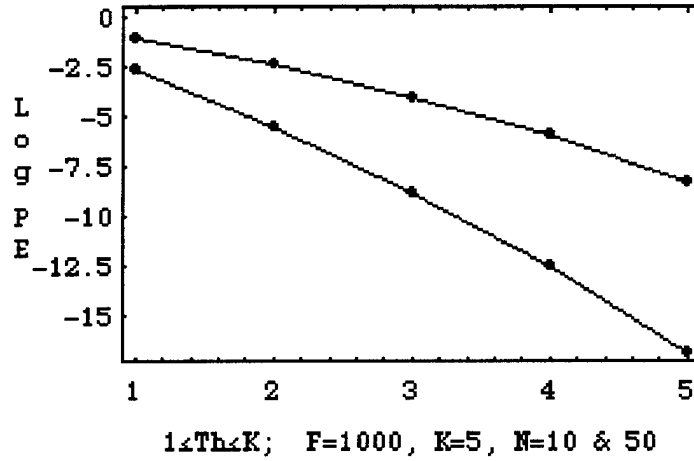
Fig. 3.3.7 (lower line) and $N = 50$ (upper line). With hard-limiting the system performance increases by 4-5 orders of magnitude. After Ref[8], Fig. 7.

Because the number of users is unacceptably low with the criterion $\lambda = 1$, the consequences of raising this criterion to $\lambda = 2$ has been examined. With $l_1$ users interfering at 1 position and $l_2$ users interfering at 2 pulse positions, (giving the total number of interfering pulses $= l_2 + 2l_2$), the error probability is:

$$P_E = \frac{1}{2} \sum_{\substack{l_1 - 2l_2 \ge Th \\ l_1 - l_2 < M}} \Pr(l_1 l_2)$$

with

$$l_1 + l_2 < M,$$

$$M \le \frac{(F-1)(F-2)}{K(K-1)(K-2)} .$$

The probability of error is then:

$$P_E = \frac{1}{2} - \frac{1}{2} \sum_{l_1=0}^{Th-1} \sum_{l_2=0}^{\lfloor (Th-1-l_1)/2 \rfloor} \frac{(M-1)!}{l_1! l_2! (M-1-l_1-l_2)!} q_1^{l_1} q_2^{l_2} (1 - q_1 - q_2)^{M-1-l_1-l_2} .$$

Azizoglu et al[9] have shown that the statistic:

$$c \approx \frac{q_1}{K^2 / 2F}$$

indicates the deviation of a *pde* from the strict orthogonal optical code (OOC) criterion. For $c = 1$ the code is an OOC. For $c = 0$, the code will have 2 overlaps in auto- and cross-correlation (see Note 6). Fig.s 3.3.8 and 3.3.9 show the error probability as a function of $c$

[9] Azizoglu, M., Salehi, J.A. & Li, Y., Optical CDMA via temporal codes. *IEEE Trans. Comm.*, 40, 1162-1169, 1992.

27

for the optimum threshold: $Th = K$, with $F = 1000$ and for the hard-limiting case. These Fig.s show that the error probability increases with decreasing $c$, *but the number of possible users increases.*



C, No Hd Limiting; M=10, F=1000, K=2,4,6,8 & 10
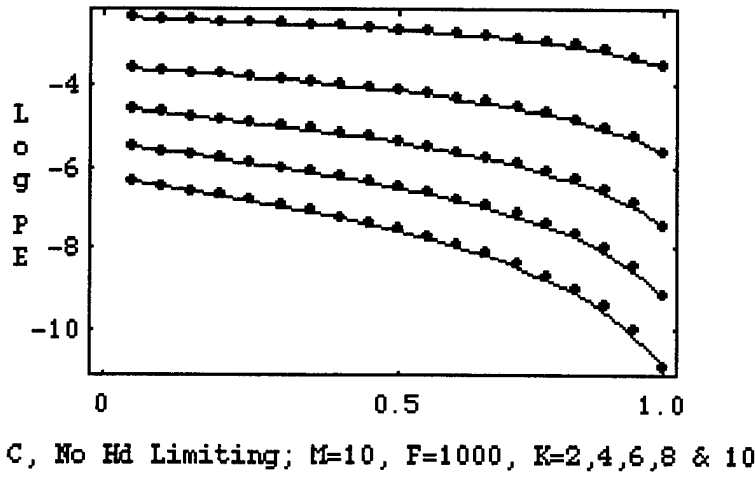
Fig. 3.3.8 $\lambda = 2$, Optical Orthogonal Code, without hard limiting. Dependence of the error probability on the parameter $c = q_1/(K^2/2F)$ and $M \leq [(F-1)(F-2)]/[K(K-1)(K-2)]$. $M = 10, F = 1000, K = 2, 4, 6, 8$ & $10$, top to bottom. After Ref[9], Fig. 4(a).



C, No Hd Limiting; M=10, F=1000, K=2,4,6,8 & 10
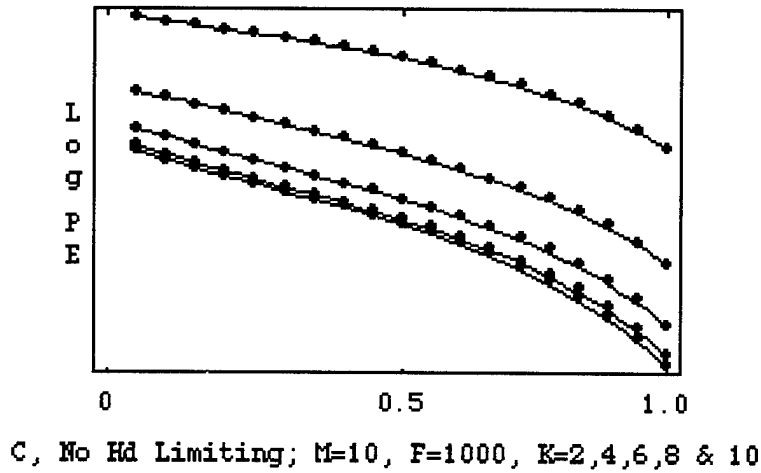
Fig. 3.3.9 $\lambda = 2$, Optical Orthogonal Code, without hard limiting. Dependence of the error probability on the parameter $c = q_1/(K^2/2F)$ and $M \leq [(F-1)(F-2)]/[K(K-1)(K-2)]$. $M = 50, F = 1000, K = 2, 4, 6, 8$ & $10$, top to bottom. After Ref[9], Fig. 4(b).

On introducing hard-limiting to the receiver, and with $\lambda = 2$, the lower bound on the error probability is:

$$P_E \geq \frac{1}{2} \sum_{i=0}^{K} (-1)^i \binom{K}{i} \left[ 1 - \frac{pi}{K} \left( 2 - \frac{i}{K} \right) \right]^{M-1} ,$$

and the upper bound is:

28

$$P_E \leq \frac{1}{2}\sum_{i=0}^{K/2}(-1)^i \binom{K/2}{i}\left(1-\frac{2pi}{K}\right)^{M-1}.$$

The upper and lower bounds are shown in Fig. 3.3.10, for $M = 50$, $F = 1000$, and in Fig. 3.3.11, for $M = 10$, $F = 1000$. A comparison with Fig. 3.3.12, for the $\lambda = 1$ case, indicates that the performance with $\lambda = 2$ is a few orders of magnitude poorer, but as pointed out by Azizoglu et al, more chips, $K$, can be used for the codes, thus giving compensatory performance - as Fig. 3.3.2 clearly shows. Therefore the conclusion must be that $\lambda = 2$ codes may be as good in performance as $\lambda = 1$ codes, while possibly offering the availability of more codes to more users.
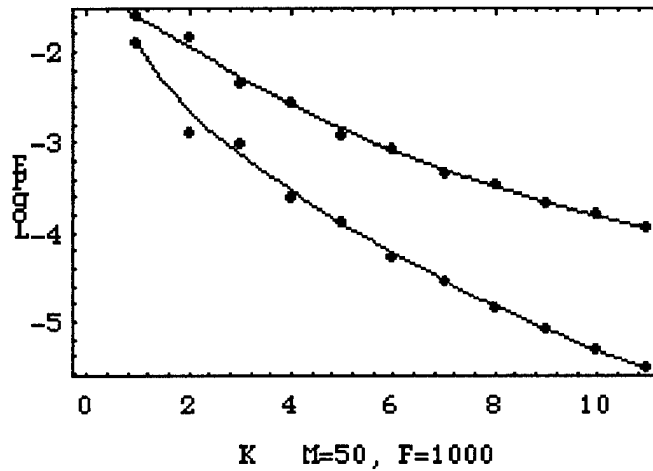
Fig. 3.3.10 Upper and lower bounds to the worst case error probability for the $\lambda = 2$ code, $M = 50$, with hard limiting. After Ref[9], Fig. 5 upper.
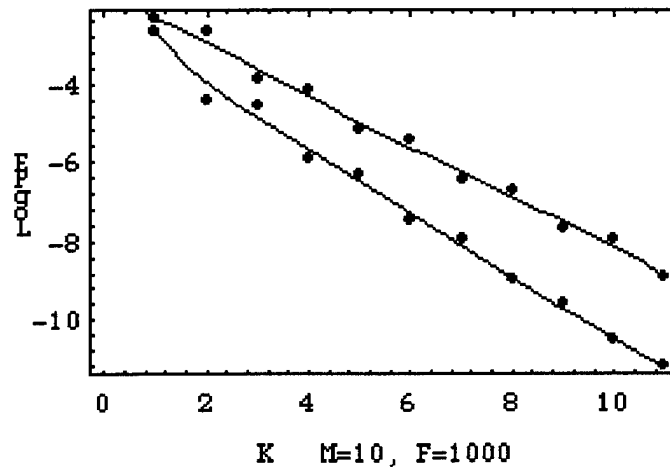
Fig. 3.3.11 Upper and lower bounds to the worst case error probability for the $\lambda = 2$ code, $M = 10$, with hard limiting. After Ref[9], Fig. 5 lower.
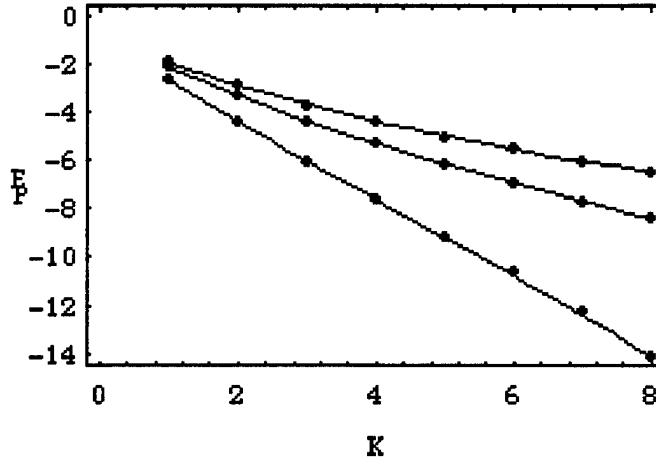
Fig. 3.3.12 Bit error probability for an OOC ($\lambda = 1$) with $F = 1000$, $M = 10,30,50$ (lower to upper) and $K = Th$. After Ref[9], Fig. 2).

## 3.4 Timing Errors

There is a dramatic degradation of the system when timing errors are introduced, indicating the reliance of PPM systems on accurate timing control. Both direct detection and heterodyne detection were examined, as well as the probability of error (PE) and probability of word error (PWE) for PPM. A complex interplay between good PWE and length of superframe size can be demonstrated.

In the shot-noise-limited-ideal-gain case, for a specific bit interval, the output of. e.g., a current bit-time integrator following direct photodetection is the random variable:

$$v = egm,$$

where $m$ is the primary count variable collected from the bit integration, $e$ is the electron charge and $g$ is the gain of the photomultiplier. The probability that $m = k$ is the Poisson probability:

$$\Pr[m = k] = \frac{(K_s + K_b)^k \exp[-(K_s + K_b)]}{k!},$$

where $K_s$ and $K_b$ are the contributions to the average count from the source field and background or input noise, respectively. With respect to the optical pulse power, $P_p$, and the average background power, $P_b$, these are defined as:

$$K_s = \alpha P_p T_b$$

$$K_b = \alpha P_b T_b$$

where $\alpha$ is a proportionality constant.

30

A comparison of $v$ with a set threshold, $v_T$, is equivalent to a comparison of the count variable, $m$, with a threshold $m_T = v_T/eg$. Therefore the decoding bit probability of error (PE) for equally probable bits is:

$$PE = 0.5 \times \Pr[m > m_T \,|\, 0] + 0.5 \times \Pr[m < m_T \,|\, 1].$$

Inserting the Poisson count probabilities gives[10]:

$$PE = 0.5 \times \sum_{k=0}^{m_T} \frac{(K_s + K_b)^k \exp[-(K_s + K_b)]}{k!} + 0.5 \times \sum_{k=m_T}^{\infty} \frac{K_b^k \exp[-K_b]}{k!}.$$

As the threshold can be selected to minimize the PE, a choice is made so that $d\text{PE}/dm_T = 0$, giving a threshold value of:

$$m_T = \frac{K_s}{\log\left(1 + \dfrac{K_s}{K_b}\right)}.$$

Plots of the bit error probability using this value for an on-off keying (OOK) system for several values of $K_b$ are shown in Fig. 3.4.1. These curves provide an estimate of the amount of received pulse power needed to achieve a desired PE with a given amount of background light present.
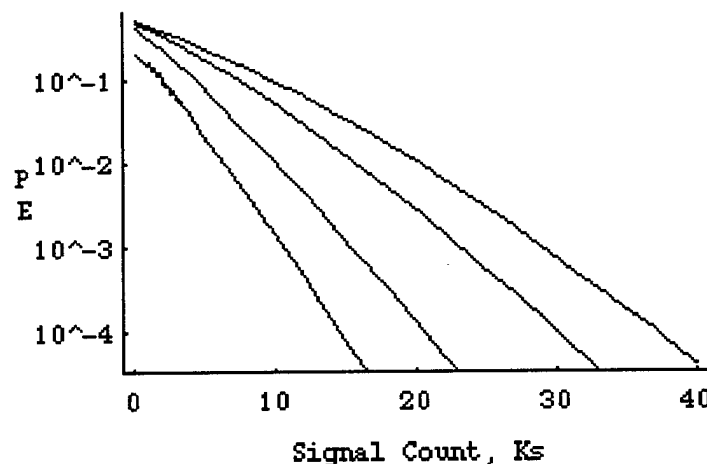


Fig. 3.4.1 Bit error probability, OOK binary system, for various noise counts per bit interval,: 0, 1, 5, 10, left to right.

With an avalanche photodiode (APD), the statistics are changed to account for the receiver containing thermal noise. producing random gain and resulting in Gaussian noise. The integrated detector current has a continuous probability density which is:

---

[10] Pierce, J. Optical channels - practical limits in photon counting. *IEEE Trans. Commun.*, 26, dec., 1968; Karp, S., O'Neill, E. & Gagliardi, Communication theory for the free space optical channel. *Proc. IEEE*, 58, October, 1970;
Gagliardi, R.M. & Karp, S., *Optical Communications*, 2nd Edition, Wiley, 1995.

$$p(v/\bar{k}) = \sum_{k_2=0}^{\infty} P(k_2|\bar{k}) G(v, ek_2, \sigma_n^2)$$

where

$$G(v, a, \sigma_n^2) = \frac{1}{\sqrt{2\pi}\sigma_n} \exp\left[\frac{-(v-a)^2}{2\sigma_n^2}\right],$$

$$\sigma_n^2 = N_{0c} T_b = (2\kappa T^0 / R_L) T_b,$$

$N_{0c}$ is the spectral level,

$T_b$ is the bit field length,

$P(k_2|\bar{k})$ is the discrete APD count probability with primary mean count $\bar{k}$.

As the test is now an *integrated* current threshold test, as opposed to a count test as in the Poisson channel, the probability of bit error is:

$$PE = 0.5 \times \int_0^{v_T} p(v|K_s + K_b) dv + 0.5 \times \int_{v_T}^{\infty} p(v|K_b) dv.$$

with threshold:

$$p(v_T|K_s + K_b) = p(v_T|K_b).$$

Combining these two Eq.s gives:

$$PE = 0.5 + 0.5 \sum_{k_2=0}^{\infty}\left[P(k_2|K_b) - P(k_2|K_s + K_b) Q\left(\frac{v_T - ek_2}{\sigma_n}\right)\right],$$

where

$$Q(x) = \int_x^{\infty} G(v, 0, 1) dv.$$

When the average counts $K_s$ and $K_b$ are high, the discrete APD counting probabilities are approximated by continuous Gaussian densities. With (1,0) subscripts indicating the (on,off) pulse condition, the variable, $v$, is then a Gaussian variate with mean and variance dependent on the "1" and "0" bits.

The OOK bit error probability for the Gaussian model with $v_T$ a decision threshold is:

$$PE = 0.5 \times Q\left(\frac{m_1 - v_T}{\sigma_T}\right) + 0.5 \times Q\left(\frac{v_T - m_0}{\sigma_0}\right) \quad where$$

$$m_1 = \bar{g}e(K_s + K_b),$$

$$m_0 = \bar{g}eK_b,$$

$$\sigma_1^2 = \bar{g}Fe^2(K_s + K_b) + \sigma_n^2,$$

$$\sigma_0^2 = (\bar{g}e)^2 FK_b + \sigma_n^2.$$

with an optimal threshold:

$$v_T = \frac{m_1 + m_0}{\sigma_1 + \sigma_0}.$$

Use of the optimal threshold gives the following PE:

$$PE = Q\left(\frac{m_1 + m_0}{\sigma_1 + \sigma_0}\right) = Q\left(\sqrt{SNR}\right), \quad where$$

$$SNR = \frac{(m_1 + m_2)^2}{(\sigma_1 + \sigma_0)^2} = \frac{(\bar{g}eK_s)^2}{(\sigma_1 + \sigma_0)^2}.$$

Fig. 3.4.2 is a plot of the OOK *PE* versus *SNR*, Gaussian model.
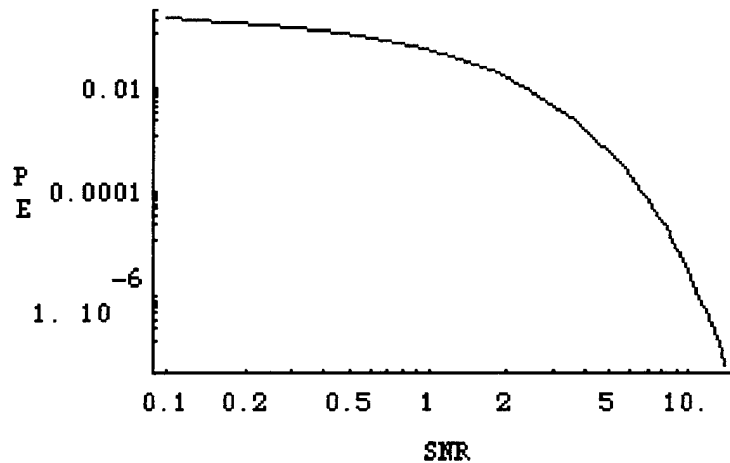


Fig. 3.4.2. OOK bit error probability versus SNR, Gaussian model.

In the case of Manchester coding for the Poisson channel, the bit error is the probability that one Poisson count containing the pulse energy does not exceed another Poisson count containing no pulse:

$$PE = \sum_{k1=0}^{\infty} \sum_{k_2=k_1+1}^{\infty} Pos(k_1,K_s+K_b)Pos(k_2,K_b) + 0.5 \times \sum_{k_1=0}^{\infty} Pos(k_1,K_s+K_b)Pos(k_1,K_b),$$

*where the Poisson probability with level q is :*

$$Pos(p,q) = \frac{q^p Exp[-q]}{p!}$$

Fig. 3.4.3 shows plots of the Manchester Poisson model *PE* in terms of $K_s$ and $K_b$. As the OOK method uses pulses twice as long as the Manchester method, the OOK has a higher noise count, $K_b$. Therefore if the systems are compared at the same $K_s$, the Manchester
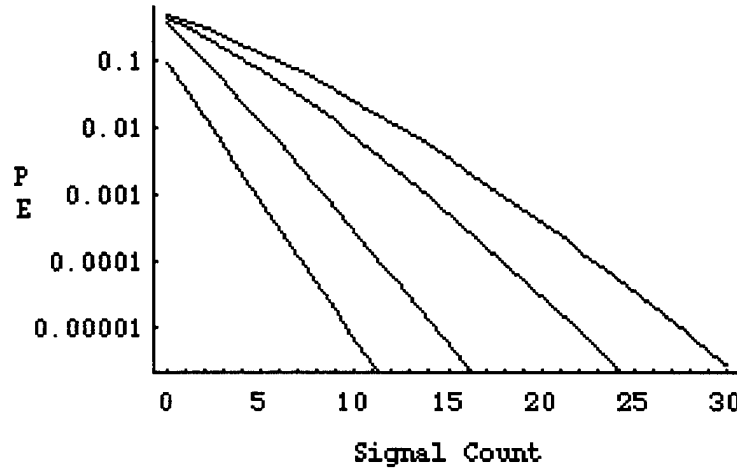


Fig. 3.4.3. Manchester encoding, Poisson channel. Plots are for signal count, $K_s$, at various $K_b$'s: 0, 1, 5, 10, left to right.

coding shows better *PE* performance. However, if systems based on the two methods are compared at the same average signal power, the OOK has twice the signal energy, and therefore the better performance.

The above methods involved direct detection. However, a coherent digital system can be used by encoding digital bits directly on the phase or frequency of the laser carrier. With a heterodyne receiver, the laser carrier can be downconverted to an RF frequency, and the digital modulation treated by RF methods. If a strong laser field is used for the heterodyning, the photodetected mixed field can be modeled as a Gaussian process and the decoding bit error for Gaussian RF channels with BPSK and FSK modulation is:

$$PE = \begin{cases} Q\sqrt{2E_b/N_{od}} & BPSK \\ 0.5 \times exp[-E_b/2N_{od}] & FSK \end{cases}$$

where $E_b/N_{0d}$ is the decoder signal bit energy to noise level ratio, defined:

$$\frac{E_b}{N_{0d}} = \frac{2K_s}{1+\alpha N_0}.$$

Fig. 3.4.4. shows plots of *PE* for BPSK and FSK heterodyne decoding as a function of the parameter $K_s/1+\alpha N_0$.
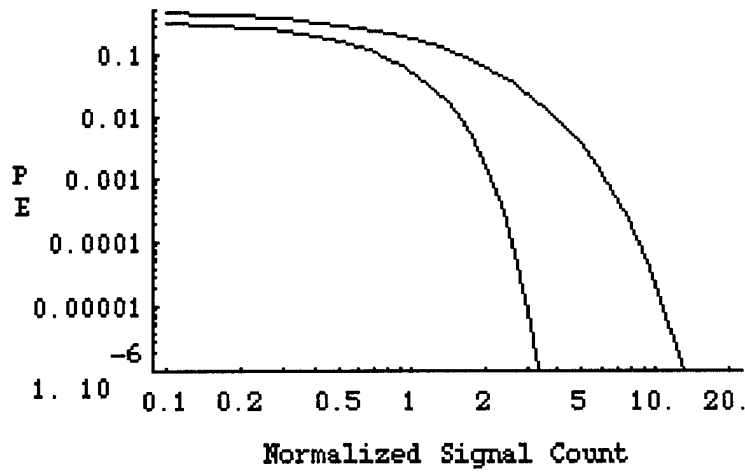
Fig. 3.4.4. Bit error probability vs normalized signal count for heterodyne digital systems. PSK left, FSK, right.

## 3.5 Pulse Position Modulation

An alternative to binary systems is block encoding permitting pulse position modulation (PPM). A decoding word error is made if an incorrect slot produces a higher integration value than the correct slot. As integrations are independent from slot to slot, the probability of word error (PWE) in PPM is:

$$PWE = 1 - \int_0^\infty p(v_1|1)\left[\int_0^{v_1} p(v_2|0)dv_2\right]^{M-1} dv_1$$

where

$p(v|1)$ is the probability density of $v$ for the signal slot, and $p(v|0)$ is that for the incorrect slots.

For the Poisson receiver model, the probability of word error is:

$$PWE = 1 - \frac{\exp[-(K_s + MK_b)]}{M} - \sum_{k_1=1}^{\infty} Pos(k_1, K_s + K_b)\left[\sum_{k_2=1}^{k_1-1} Pos(k_s, K_b)\right]^{M-1}$$

$$- \sum_{r=1}^{M-1}\frac{(M-1)!}{r!(M-1-r)!(r+1)}\sum_{k=1}^{\infty} Pos(k, K_s + K_b)[Pos(k, K_b)]^r\left[\sum_{j=0}^{k-1} Pos(j, K_b)\right]^{M-1-r}$$

where $K_b$ is the noise count per slot level and $K_s$ is the signaling pulse count.

With the Gaussian detector model, the probability densities are:

35

$$p(v|1) = G[v, \overline{g}(K_s + K_b), \sigma_1^2],$$

$$p(v|0) = G(v, \overline{g}eK_b, \sigma_0^2).$$

The PWE is bounded by[11]:

$$PWE \cong (M-1)\Pr[\text{one incorrect slot } v \text{ exceeds the correct slot } v],$$

indicating that the probability in brackets is similar to the Manchester PE. Therefore, the PWE is:

$$PWE \cong (M-1)Q(\sqrt{SNR}).$$

Plots are shown in Fig. 3.5.1 for various values of $M$ with $K_b = 3$.

The appearance in Fig. 3.5.1 of performance worsening as higher frame sizes, $M$, are used is deceptive. $K_s$ and $K_b$ are fixed; the higher $M$ systems are transmitting higher data rates at fixed frame times (i.e., the curves are not rate normalized, and PPM systems convert average laser power to peak power directly proportional to $M$, resulting in the higher $M$ systems operating at higher $K_s$ values. The latter point is manifest when $K_s$ is written in terms of the average laser power, $P_s$:

$$K_s = \alpha P_p T_s$$

$$= \alpha(MP_s)T_s$$
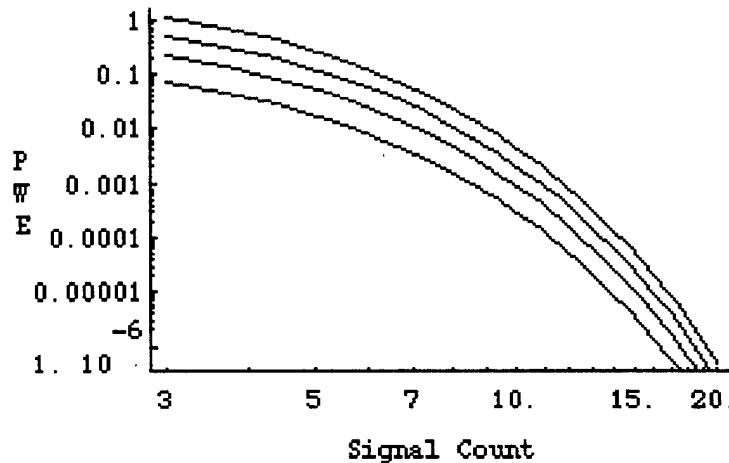


Fig. 3.5.1. Word error probability for M-ary PPM decoding. Gaussian channel. $K_b = 3$ counts/slot. M= 2, 4, 8, 16, left to right.

There is a rapid degradation of the channel as timing errors, $\Delta$, are introduced into a PPM system. This degradation can be described as follows. Defining:

[11] Wozencraft, J. & Jacobs, I., *Principles of Communication Engineering*, Wiley, New York, 1965.

$$K_s = n_s T_b,$$

$$K_s' = n_s(T_b - \Delta),$$

$$K_s'' = n_s\Delta, \quad where$$

$T_b$ is bit time, sec,

$\Delta$ is time offset, sec,

then

$$P(v < v_T \mid K_s') = \sum_{k=0}^{v_T} Pos\big[k, K_s(1-2\varepsilon) + K_b'\big],$$

$$P(v > v_T \mid K_s'') = \sum_{k=v_T}^{\infty} (k, K_b'),$$

where $\varepsilon = \Delta/T_b$. These Eq.s are combined to give the OOK *PE* of a system with the noise count increased from $K_b$ to $K'_b$ and the signal reduced from $K_s$ to $K_s(1\text{-}2\varepsilon)$. For the Poisson channel this is:

$$PE \mid \Delta = 0.5 \times PE(K_s, K_b) + 0.5 \times PE\big[K_s(1-2\varepsilon), K_s\varepsilon + K_b\big].$$

Fig. 3.5.2 plots this *PE* versus the normalized timing error, showing the rapid degradation of the system as the timing error increases.
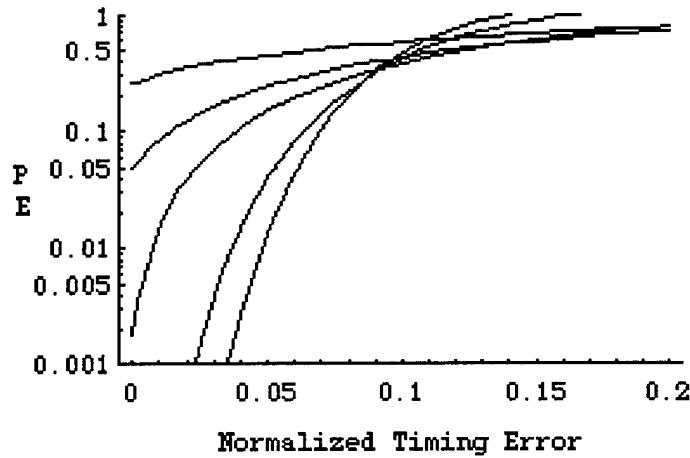


Fig. 3.5.2  OOK decoding versus normalized timing error, $\varepsilon$. Poisson channel. $K_b = 0.01$; $K_s = 2, 5, 10,$ 50, 100.

In the case of the Manchester decoder (Poisson receiver), the PE is:

$$PE \mid \varepsilon = 0.5 \times PE(K_s', K_b') + 0.25 \times PE(K_s'', K_b) + 0.25 \times PE(K_s', K_b'),$$

where

$$K_s' = K_s(1 - 2\varepsilon),$$

$$K_s'' = K_s(1 - \varepsilon),$$

$$K_b' = K_s\varepsilon + K_b$$

Fig. 3.5.3 plots the normalized timing error, ε, against PE, showing, again, that the system performance degrades as the timing error increases.
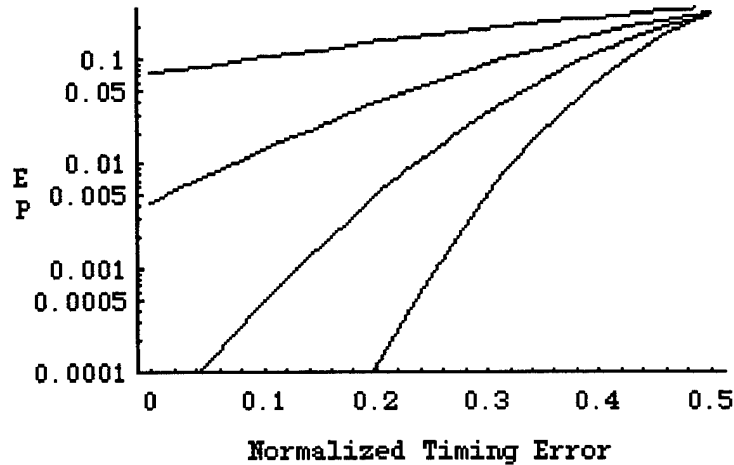


Fig. 3.5.3. Manchester decoding versus normalized timing offset ε. Poisson channel. $K_b = 0.5, K_s = 2, 5,$ 10, 20.

In the case of the Poisson channel, the probability of word error (PWE) is:

$$PWE\big|\, \varepsilon = 1 - \sum_{k=0}^{\infty} Pos\big[k, K_s(1 - \varepsilon) + K_b\big] \sum_{j=0}^{k} Pos(j, K_s\varepsilon + K_b) \left[\sum_{j=0}^{k} Pos(j, K_b)\right]^{M-2}.$$

Fig. 3.5.4 shows plots of *PWE* versus timing error. Again, there is demonstrated a rapid degradation in performance as the timing offset increases.
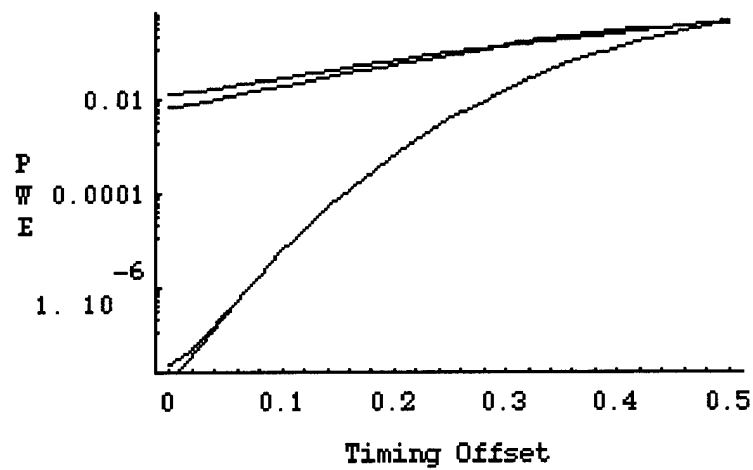
Fig. 3.5.4 *PWE* degradation for PPM versus timing offsets. $Kb = 3$; $Ks = 10$, $M = 8$ & 10 (upper); $Ks = 30$, $M = 4$ & 8 (lower).

## 4.0 Differences between Time Hopping CDMA and other forms of Spread Spectrum Communications:

We address, here, only the first matched filter, which identifies the channel or user code, not the second matched filter, which identifies the information encoded in a pulse-position modulation, or phase-shift keying scheme. We use the terminology introduced by Flikkema[12], except when a departure is called for and such departures are indicated. If

$\{b_m\}$ is the informational sequence, $b_m \in +1 \, or \, 0$

then the received sequence is;

$$r_m = Eb_m + w_m,$$

where $E$ is the energy of the transmitted pulse and $w_m$ is zero-mean additive white Gaussian noise (AWGN) with autocovariance:

$$E[w_m w_{m+1}] = \sigma^2 \delta(l).$$

In the case of time hopping CDMA, for each informational bit, instead of one pulse being transmitted, one pulse within one slot of a frame of slots, e.g., $\{0,0,0,0,1,0,0,0,0,0\}$, is transmitted. If we only consider the transmitted bit, then the subscript $m$ can be dropped and the transmitted signal for every bit over a frame of $N$ slots is:

$$s_n = E_s b, \quad n = 1,.....,N.$$

Thus, 1 discrete-time pulse in one slot positioned (by a code) within a frame of $N$ slots represents a bit of information. Therefore the duration of a data bit is partitioned into $N$ subintervals or slots.

Whereas with other forms of spread spectrum during one subinterval, or slot duration, of one frame, a pulse of energy

$$E_s = E / N$$

is transmitted, in the case of time hopping, only one pulse is transmitted per frame. Therefore

$$E_s = E,$$

and we drop the subscript, $s$, there being no difference between the pulse energy at a particular slot, and the total energy transmitted during a frame (for one code). Each slot or subinterval in a frame is known as a *chip*.

The received sequence for the frame, which represents the bit, is:

---

[12] Flikkema. P.G., Spread-spectrum techniques for wireless communication. *IEEE Signal Processing Magazine*, May, 1997, 26-36.

$$r_n = Eb + w_n, \; n = 1,...,N$$

with noise of variance $E[w_n^2] = \sigma^2 / N$. However, it should be noted that the matched filter is only "open" to receive a signal at one slot or subinterval of the frame time - that subinterval being determined by the code. Therefore, unlike other forms of spread spectrum, the received sequence for the frame is:

$$r = Eb + w$$

and we drop the subscript $n$.

The optimal receiver employs a correlation before the level detector, that correlation being for a code length $N$ over a superframe (of $N \times N = M$ chips) representing $N$ bits. Therefore the decision variable for the superframe, or output from the receiver, is:

$$y = \sum_{n=1}^{N} r_n, \text{ or}$$

$$y = \sum_{n=1}^{N} (Eb + w_n) = NEb + \sum_{n=1}^{N} w_n$$

Thus the decision variable, or receiver output, $y$, has a mean $NEb$ and variance $N\dfrac{\sigma^2}{N} = \sigma^2$, so performance is determined by the ratio $E / \sigma$.

The transmitted signal *per frame* can be written as:

$$s_n = Ebc,$$

where $c = $ *either* 1 *or* 0, *and only one '1' is assigned per frame*; and the transmitted signals *per superframe* can be written as:

$$S_n = \sum_{n=1}^{N} s_n = NEbc_n, \; n = 1,....,N,$$

where $\{c_n\}_{n=1}^{n=N} = 1$, with each *frame* identified with a *unipolar* unitary value (as opposed to each *chip* being identified with a *bipolar* unitary value in conventional spread spectrum). Each frame could be identified with m-ary values, but for ease of exposition unitary values are used here.

Quite apart from the assignment of unipolar unitary values to frames, instead of bipolar unitary values to chips, time hopping spread spectrum differs from other forms of spread spectrum in distinguishing *frame* signals from *superframe* signals.

The spread spectrum property, *for other forms of spread spectrum*, arises from the fact that the *chips,* rather than being identically valued, are drawn from a known (deterministic) binary (+1 or -1) source. In the case of time hopping, the spread spectrum property arises from the fact that it is the value of the *frames* (of chips) which are drawn from a known (deterministic) binary (1 or 0) source. The source in both cases provides the

coding scheme. The sequence of chips, for conventional spread spectrum, or of frames, for time hopping, is known as a *spreading sequence*.

Assuming that the spreading sequence $\{c_n\}$ is defined for all $n$ and has period $N$, i.e., $\sum_{n=1}^{N} c_n c_{n+kN} = N$, for any $k$, then the mean value is unitary (rather than zero - as in the case of other forms of spread spectrum), i.e.:

$$\frac{1}{N} \sum_{n=1}^{N} c_n = 0,$$

and the time autocorrelation (the discrete time periodic autocorrelation) is:

$$\frac{1}{N} \sum_{n=1}^{N} c_n c_{n+i} = \begin{cases} 1, & i = 0 \\ \min, & 0 < |i| < N. \end{cases}$$

The correlation receiver performs the following operation to obtain the decision variable, or correlator output, $y$:

$$y = \sum_{n=1}^{N} r_n c_n = \sum_{n=1}^{N} (Ebc_n + w_n)c_n,$$

or

$$y_n = NEb + \sum_{n=1}^{N} w_n c_n.$$

If an interfering signal, $I$, is added to the received signal, the decision variable for the *unspread system* has a mean of

$$N(Eb + I),$$

rendering it unusable. For the *spread system*, the received sequence is:

$$r_n = Ebc_n + i_n + w_n, \quad n = 1,...N,$$

where $i_n = I$.

The correlation receiver then produces the decision variable:

$$y = \sum_{n=1}^{N} (Ebc_n + i_n + w_n)c_n,$$

which yields:

$$y = NEb + I\sum_{n=1}^{N} c_n + \sum_{n=1}^{N} w_n c_n = NEb + 0 + \sum_{n=1}^{N} w_n c_n.$$

Thus the decision variable has a mean of $Eb$ and a variance of $\sigma^2$, with the interference suppressed by the despreading (correlation) operation.

*Mitigation of Multipath:*

The information sequence is $\{b_m\}_{m=0}^{\infty}$. Following Flikkema[12] but with modifications, the frame energy is incorporated into the bits by setting $b_m = \{Ec\}$.

Considering a simple multipath channel, with a direct path with strength $\alpha$ and a specular (reflected) path that causes another copy of the signal to arrive at delay $l$ with strength $\beta$. The received frames (as opposed to chips) during the $m$th bit interval are:

$$r_n = \begin{cases} \alpha b_m c_n + \beta b_{m-1} c_{N-l+n}, & n = 1,...l-1 \\ \alpha b_m c_n + \beta b_m c_{n-l}, & n = l,...N \end{cases}$$

for $0 < l < N$, i.e., the delay is less than a frame duration.

Therefore:

$$y_m = N\alpha b_m + \beta b_{m-1}\sum_{n=1}^{l-1} c_{N-l+n}c_n + \beta b_m\sum_{n=l}^{N} c_{n-l}c_n + \sum_{n=1}^{N} w_n c_n ,$$

which becomes

$$y_m = N\alpha b_m + 0 + 0 + \sum_{n=1}^{N} w_n c_n$$

and the multipath is suppressed by the despreading.

*Multiple Access:*

With $K$ users and with the $k$th transmitter modulating its output with a spreading sequence $\{c_n^{(k)}\}$, then the members of this set of signature sequences or spreading codes have the crosscorrelation property:

$$\frac{1}{N}\sum_{n=1}^{N} c_n^{(k)} c_{n+i}^{(j)} = \begin{cases} 1, & k = j, i = 0 \\ \min, & k = j, 0 < |i| < N \\ \min, & k \neq j \end{cases}$$

With time synchronization among the signals, and considering signal $k = 1$, the received signal is:

$$y_m^{(1)} = b_m^{(1)} \sum_{n=1}^{N} \left( c_n^{(1)} \right)^2 + \sum_{k=2}^{K} b_m^{(k)} \sum_{n=1}^{N} c_n^{(k)} c_n^{(1)} + \sum_{n=1}^{N} w_n c_n^{(1)}$$

Because of the mutual orthogonality of the sequences, this Eq. simplifies to:

$$y_m^{(1)} = N b_m^{(1)} + 0 + \sum_{n=1}^{N} w_n c_n^{(1)}$$

and simultaneous transmissions in the same channel are permitted.

Defining the signaling pulse:

$$p_T(t) = \begin{cases} 1, & 0 < t < T \\ 0, & otherwise \end{cases}$$

The informational pulse corresponding to bit $m$ is:

$$s_m(t) = b_m c_n p_{T_c}(t - nT_c),$$

and the sequence of pulses corresponding to $N$ bits transmitted over a superframe is:

$$s_N(t) = \sum_{n=1}^{N} b_n c_n p_{T_c}(t - nT_c),$$

where the chip, or slot, energy is $E = A^2 T_c$, $T_c$ is the chip or slot duration, and $T_c^{-1}$ is the *spreading rate*. The frame duration, or bit duration, is then:

$$T_b = NT_c,$$

with the ratio, $N$, being the *processing gain*.

As comparison, the following five *continuous time* systems and time hopping CDMA, a *discrete time* system, are defined:

| Spread Spectrum Variations, with informational pulse corresponding to bit m: $$s_m(t) = b_m c_n p_{T_c}(t - nT_c)$$ | |
|---|---|
| $$s(t) = \sum_{m=0}^{\infty} s_m(t - mT_b)$$ | *Direct Sequencing Spread Spectrum - the spreading sequence $\{c_n\}$ directly modulates the information sequence $\{b_m\}$.* |
| $$s_m(t) = Ab_m \cos(2\pi f_m t) p_{T_b}(t - mT_b)$$ | *Frequency Hopping Spread Spectrum - $f_m$ is chosen from a set of N frequencies selected according to a code sequence. The informational sequence, $b_m$, modulates the phase of the signal, so the signal is a Binary Phase Shift Keyed Signal (FH/BPSK).* |
| $$s_m(t) = A\cos(2\pi(v_m + f_m)t) p_{T_b}(t - mT_b)$$ | *Frequency Hopping Spread Spectrum - the information sequence and also the spreading sequence jointly determine the frequency of the signal, with the information encoded in the frequency $v_m$. This is M-ary Frequency-Shift Keyed FM (FH/MFSK).* |
| *The Fourier Transform of the transmitted pulse in signal interval m is:* $$Q_m(f) = \sum_{k=-N/2}^{N/2-1} \tilde{b}_m(k)\tilde{c}(k) p_{F_c}(f - kF_c)$$ *The Inverse Fourier Transform is:* $$s(t) = \sum_m q(t - mT)w(t - mT)$$ | *Spread Time (ST) Modulation[13]. Direct modulation occurs in the frequency domain.* |
| $$s_m(t) = b_m \sum_{n=1}^{N} c_n \exp[i2\pi nFt/t_b] p_{T_b}(t - mT_b)$$ *and the transmitted signal is:* $$s(t) = \sum_{m=0}^{\infty} s_m(t - mT_b)$$ | *Multicarrier CDMA[14] Spreading sequence is applied in the frequency domain to N carriers with spacing determined by the integer F.* |
| $$s_m(t) = b_m \sum_{n=1}^{N} \exp[i2\pi(t + c_n\tau)/t_c] p_{T_b}(t - mT_b)$$ *and the transmitted signal is:* $$s(t) = \sum_{m=1}^{N} s_m(t - mT_b)$$ | *Time Hopping CDMA. Spreading sequence applied in the time domain to N frames each of duration $T_b$ in which a pulse occurs once in slot time $T_c$ at offsets $c_n\tau$ for N frames or 1 superframe.* |

[13] Crespo, P., Honig, M. & Salehi, J.A., Spread-time code division multiple access. *IEEE Trans. Comm.*, 43, 2139-2148, 1995.

[14] Yee, N., Linnartz, J. & Fettweis, Multi-carrier CDMA in indoor wireless radio networks. *IEICE Transactions on Communications*, Japan, vol. E77-B, pp. 900-904, July 1994.

The actual transmitted signal, $x(t)$, is related to the baseband signal, $s(t)$, by:

$$x(t) = s(t)\cos(2\pi f_c t + \theta),$$

where $\cos(2\pi f_c t + \theta)$ is the carrier and $\theta$ is an arbitrary phase. In the following table, the relation between the three bandwidths: instantaneous, information and spread bandwidth, is shown for the various spread spectrum techniques.

| Relation between instantaneous, information and spread bandwidth | | |
|---|---|---|
| Spread Spectrum Technique | Bandwidths | Relative Bandwidths |
| DS | If $W_l$ is the information bandwidth, then $NW_l$ is the spread bandwidth | Instantaneous bandwidth is equal to the spread bandwidth |
| Slow Frequency Hopping | Maximum bandwidth: $f_c + v_m + f_m$ Signal information bandwidth: $f_c + f_m$ | Instantaneous bandwidth is equal to the information (unspread) bandwidth. |
| Spread Time Modulation | Either of above. | Instantaneous bandwidth can be equal to the spread bandwidth or to the information bandwidth. |
| Time Hopping | $p_{F_c}(f - kF_c)$ | Instantaneous bandwidth is equal to the individual pulse or packet bandwidth |

*Near-Far Problem:*

If $E^{(k)}$ is the received strength of the $k$th signal, then the received signal is:

$$r_n = \sum_{k=1}^{K} E^{(k)} b_m^{(k)} c_n^{(k)} + w_n$$

The decision variable, or correlator output, for a single transmission in the presence of multiple users, all using orthogonal codes, is:

$$y_m^{(1)} = E^{(1)} b_m^{(1)} \sum_{n=1}^{N} (c_n^{(1)})^2 + \sum_{k=2}^{K} E^{(k)} b_m^{(k)} \sum_{n=1}^{N} c_n^{(k)} c_n^{(1)} + \sum_{n=1}^{N} w_n c_n^{(1)}$$

$$= NE^{(1)} b_m^{(1)} - \sum_{k=2}^{K} E^{(k)} b_m^{(k)} + \sum_{n=1}^{N} w_n c_n^{(1)}$$

which shows that if $E^{(k)} \gg E^{(1)}$, the spreading gain, $N$, may be insufficient to suppress the multiuser interference (MUI) - the *near-far problem.* Two approaches are used to attack

46

this problem: (1) power control of the transmitted signal to provide rough equality of received signal strengths; (2) multi-user detection designed for the multiplicity of signals present[15].

*MultiPath Problem:*

The rake receiver is a pre-detection multipath-combining receiver which mitigates multipath in all forms of spread spectrum systems.

[15] Holtzman, J.M., CDMA power control for wireless networks. In *Third Generation Wireless Networks* (S. Nanda & D.J. Goodman, eds.), pp. 299-311, Kluwer Academic, 1992;
S. Ariyavisitakul & L.F. Chang, Signal and interference statistics of a CDMA system with feedback power control. *IEEE Trans. Comm.*, 41, 1626-1634, 1993;
Verdu, S., Recent progress in multi-user detection. In *Advances in Communications and Signal Processing* (W. A. Porter & S.C. Kak, eds.), pp. 15-23, Springer-Verlag, 1989;
Duel-Hallen, A., Holtzman, J. & Zvonar, Z., Multiuser detection in CDMA systems. *IEEE Personal Communications*, 2, 46-58, 1995.

## 5.0 Mathematical Foundations of Orthogonal Codes

We commence with a Galois field of order equal to $2^4$, i.e., $GF(2^4)$. There are then 3 irreducible polynomials, $\pi(x)$, i.e., polynomials which are not divisible by any polynomial over $GF(2)$ up to degree $2/4 = 2$. There are three:

$$1+x+x^4$$
$$1+x^3+x^4, \text{ and}$$
$$1+x+x^2+x^3+x^4.$$

We choose the first:

$$\pi(x) = 1 + x + x^4,$$

and use the primitive element

$$x = 0100$$

$GF(2^4)$ modulo $1 + x + x^4$ is:

| GF(2⁴) modulo $1 + x + x^4$ | | |
|---|---|---|
| power | polynomial | 4-tuple |
| $-\infty$ | 0 | 0000 |
| 0 | 1 | 1000 |
| 1 | $x$ | 0100 |
| 2 | $x^2$ | 0010 |
| 3 | $x^3$ | 0001 |
| 4 | $1+x$ | 1100 |
| 5 | $x+x^2$ | 0110 |
| 6 | $x^2+x^3$ | 0011 |
| 7 | $1+x+x^3$ | 1101 |
| 8 | $1+x^2$ | 1010 |
| 9 | $x+x^3$ | 0101 |
| 10 | $1+x+x^2$ | 1110 |
| 11 | $x+x^2+x^3$ | 0111 |
| 12 | $1+x+x^2+x^3$ | 1111 |
| 13 | $1+x^2+x^3$ | 1011 |
| 14 | $1+x^3$ | 1001 |
| 15 | 1 | 1000 |

As this exercise is for a $GF(p)$ field, where $p = 11$, we require 10, not 15, assigned numbers. To reduce the $GF(2^4)$ field to $GF(11)$, we add modulo 2, the 4-tuples of $x^{11}+....x^{15}$:

0111
1111

48

```
1011
1001
1000
0110
```

obtaining 0110, and substitute the reciprocal, i.e., 1001, for one of the 4-tuples of $x^1....x^{10}$. We choose $x^6$. The GF(11) table is then:

| GF(11) modulo $1 + x + x^4$ | | |
|---|---|---|
| power | polynomial | 4-tuple |
| -∞ | 0 | 0000 |
| 0 | 1 | 1000 |
| 1 | $x$ | 0100 |
| 2 | $x^2$ | 0010 |
| 3 | $x^3$ | 0001 |
| 4 | $1+x$ | 1100 |
| 5 | $x + x^2$ | 0110 |
| 6 | $1 + x^3$ | 1001 |
| 7 | $1 + x + x^3$ | 1101 |
| 8 | $1 + x^2$ | 1010 |
| 9 | $x + x^3$ | 0101 |
| 10 | $1 + x + x^2$ | 1110 |

Now in order to generate more codes, a "perfect" permutation is sought which permutes the "1" positionings of codes, but yet leaves the number of "hits" in the auto- and cross-correlations of those codes relatively unchanged. The Zech logarithm $Z(n)$, defined:

$$2^{Z(n)} := 1 + 2^n$$

achieves that goal. The Zech logarithm permutation on GF(11) is shown in the following table:

| Zech Logarithm conversion | | |
|---|---|---|
| power | 4-tuple | Zech Log 4-tuple = Number |
| 1 | 0100 | 1100 = 4 |
| 2 | 0010 | 1010 = 8 |
| 3 | 0001 | 1001 = 6 |
| 4 | 1100 | 0100 = 1 |
| 5 | 0110 | 1110 = 10 |
| 6 | 1001 | 0001 = 3 |
| 7 | 1101 | 0101 = 9 |
| 8 | 1010 | 0010 = 2 |
| 9 | 0101 | 1101 = 7 |
| 10 | 1110 | 0110 = 5 |

The simplified conversion is thus:

$$1 \rightarrow 4$$
$$2 \rightarrow 8$$
$$3 \rightarrow 6$$
$$4 \rightarrow 1$$
$$5 \rightarrow 10$$
$$6 \rightarrow 3$$
$$7 \rightarrow 9$$
$$8 \rightarrow 2$$
$$9 \rightarrow 7$$
$$10 \rightarrow 5$$

Applying this Zech logarithm conversion to the hyperbolic congruence codes, quadratic congruence codes and Welch-Costas codes, $p = 11$ (Tables 5.0.1, 5.0.3, 5.0.5), gives the corresponding Tables 5.0.2, 5.0.4 and 5.0.5, below.

The hyperbolic congruence codes and their Zech logarithmic construction are shown in Fig.s 5.0.1 and 5.0.2; the quadratic congruence codes and their Zech logarithmic construction in Fig.s 5.0.3 and 5.0.4; and the Welch-Costas codes and their logarithmic construction in Fig.s 5.0.5 and 5.0.6.

The method of displaying code properties involves a 3-dimensional representation which includes one autocorrelation in the middle of a stack of crosscorrelations. For example, in Fig. 5.0.7, is shown the autocorrelation of code #1 of the normal hyperbolic code construction, $p = 11$, preceded by the crosscorrelations with the other 9 codes of the normal construction and succeeded by crosscorrelations with the 10 codes of the Zech Logarithm construction. Fig.s 5.0.8 and 5.0.9 are similar representations for the quadratic congruence codes and the Welch-Costas codes, $p = 11$.

In contrast, Fig.s 5.0.13 shows the autocorrelation of code #1 of the Zech Logarithm construction of the hyperbolic codes, $p = 11$, preceded by the crosscorrelations with the other 10 codes of the normal hyperbolic construction and succeeded by crosscorrelations with the 9 codes of the Zech Logarithm construction. Fig.s 5.0.14 and 5.0.15 are similar representations of the quadratic congruence and the Welch-Costas codes, $p = 11$.

These representations were then simplified by showing only those correlations which exceeded a value of 4, in comparison with a maximum correlation value of 10. Thus Fig. 5.0.10 summarizes the data of Fig.s 5.0.7, 5.0.8 and 5.0.9; and Fig. 5.0.16 summarizes the data of Fig.s 5.0.13, 5.0.14 and 5.0.15.

Fig.s 5.0.11 and 5.0.12 analyze further the correlations of Fig.s 5.0.8 and 5.0.9; and Fig.s 5.0.17, 5.0.18 and 5.0.19 analyze further the correlations of Fig.s 5.0.13, 5.0.14 and 5.0.15.

| | Table 5.0.1 Hyperbolic Congruence Code, p=11, "1" Positionings | | | | | | | | | |
|---|---|---|---|---|---|---|---|---|---|---|
| Frame | #1 | #2 | #3 | #4 | #5 | #6 | #7 | #8 | #9 | #10 |
| 1 | 1 | 2 | 3 | 4 | 5 | 6 | 7 | 8 | 9 | 10 |
| 2 | 6 | 1 | 7 | 2 | 8 | 3 | 9 | 4 | 10 | 5 |
| 3 | 4 | 8 | 1 | 5 | 9 | 2 | 6 | 10 | 3 | 7 |
| 4 | 3 | 6 | 9 | 1 | 4 | 7 | 10 | 2 | 5 | 8 |
| 5 | 9 | 7 | 5 | 3 | 1 | 10 | 8 | 6 | 4 | 2 |
| 6 | 2 | 4 | 6 | 8 | 10 | 1 | 3 | 5 | 7 | 9 |
| 7 | 8 | 5 | 2 | 10 | 7 | 4 | 1 | 9 | 6 | 3 |
| 8 | 7 | 3 | 10 | 6 | 2 | 9 | 5 | 1 | 8 | 4 |
| 9 | 5 | 10 | 4 | 9 | 3 | 8 | 2 | 7 | 1 | 6 |
| 10 | 10 | 9 | 8 | 7 | 6 | 5 | 4 | 3 | 2 | 1 |

| | Table 5.0.2 Zech Logarithm Hyperbolic Congruence Code, p=11, "1" Positionings | | | | | | | | | |
|---|---|---|---|---|---|---|---|---|---|---|
| Frame | #1 | #2 | #3 | #4 | #5 | #6 | #7 | #8 | #9 | #10 |
| 1 | 4 | 8 | 6 | 1 | 10 | 3 | 9 | 2 | 7 | 5 |
| 2 | 3 | 4 | 9 | 8 | 2 | 6 | 7 | 1 | 5 | 10 |
| 3 | 1 | 2 | 4 | 10 | 7 | 8 | 3 | 5 | 6 | 9 |
| 4 | 6 | 3 | 7 | 4 | 1 | 9 | 5 | 8 | 10 | 2 |
| 5 | 7 | 9 | 10 | 6 | 4 | 5 | 2 | 3 | 1 | 8 |
| 6 | 8 | 1 | 3 | 2 | 5 | 4 | 6 | 10 | 9 | 7 |
| 7 | 2 | 10 | 8 | 5 | 9 | 1 | 4 | 7 | 3 | 6 |
| 8 | 9 | 6 | 5 | 3 | 8 | 7 | 10 | 4 | 2 | 1 |
| 9 | 10 | 5 | 1 | 7 | 6 | 2 | 8 | 9 | 4 | 3 |
| 10 | 5 | 7 | 2 | 9 | 3 | 10 | 1 | 6 | 8 | 4 |

| | Table 5.0.3 Quadratic Congruence Code, p=11, "1" Positionings | | | | | | | | | |
|---|---|---|---|---|---|---|---|---|---|---|
| Frame | #1 | #2 | #3 | #4 | #5 | #6 | #7 | #8 | #9 | #10 |
| 1 | 1 | 2 | 3 | 4 | 5 | 6 | 7 | 8 | 9 | 10 |
| 2 | 3 | 6 | 9 | 1 | 4 | 7 | 10 | 2 | 5 | 8 |
| 3 | 6 | 1 | 7 | 2 | 8 | 3 | 9 | 4 | 10 | 5 |
| 4 | 10 | 9 | 8 | 7 | 6 | 5 | 4 | 3 | 2 | 1 |
| 5 | 4 | 8 | 1 | 5 | 9 | 2 | 6 | 10 | 3 | 7 |
| 6 | 10 | 9 | 8 | 7 | 6 | 5 | 4 | 3 | 2 | 1 |
| 7 | 6 | 1 | 7 | 2 | 8 | 3 | 9 | 4 | 10 | 5 |
| 8 | 3 | 6 | 9 | 1 | 4 | 7 | 10 | 2 | 5 | 8 |
| 9 | 1 | 2 | 3 | 4 | 5 | 6 | 7 | 8 | 9 | 10 |

| | Table 5.0.4 Zech Logarithm Quadratic Congruence Code, p=11, "1" Positionings | | | | | | | | | |
|---|---|---|---|---|---|---|---|---|---|---|
| Frame | #1 | #2 | #3 | #4 | #5 | #6 | #7 | #8 | #9 | #10 |
| 1 | 4 | 8 | 6 | 1 | 10 | 3 | 9 | 2 | 7 | 5 |
| 2 | 6 | 3 | 7 | 4 | 1 | 9 | 5 | 8 | 10 | 2 |
| 3 | 3 | 4 | 9 | 8 | 2 | 6 | 7 | 1 | 5 | 10 |
| 4 | 5 | 7 | 2 | 9 | 3 | 10 | 1 | 6 | 8 | 4 |
| 5 | 1 | 2 | 4 | 10 | 7 | 8 | 3 | 5 | 6 | 9 |
| 6 | 5 | 7 | 2 | 9 | 3 | 10 | 1 | 6 | 8 | 4 |
| 7 | 3 | 4 | 9 | 8 | 2 | 6 | 7 | 1 | 5 | 10 |
| 8 | 6 | 3 | 7 | 4 | 1 | 9 | 5 | 8 | 10 | 2 |
| 9 | 4 | 8 | 6 | 1 | 10 | 3 | 9 | 2 | 7 | 5 |

| Frame | #1 | #2 | #3 | #4 | #5 | #6 | #7 | #8 | #9 | #10 |
|-------|-----|-----|-----|-----|-----|-----|-----|-----|-----|------|
| | | | | Table 5.0.5 | | | | | | |
| | | | Welch-Costas Code, p=11, "1" Positionings | | | | | | | |
| 1 | 2 | 4 | 6 | 8 | 10 | 1 | 3 | 5 | 7 | 9 |
| 2 | 4 | 8 | 1 | 5 | 9 | 2 | 6 | 10 | 3 | 7 |
| 3 | 8 | 5 | 2 | 10 | 7 | 4 | 1 | 9 | 6 | 3 |
| 4 | 5 | 10 | 4 | 9 | 3 | 8 | 2 | 7 | 1 | 6 |
| 5 | 10 | 9 | 8 | 7 | 6 | 5 | 4 | 3 | 2 | 1 |
| 6 | 9 | 7 | 5 | 3 | 1 | 10 | 8 | 6 | 4 | 2 |
| 7 | 7 | 3 | 10 | 6 | 2 | 9 | 5 | 1 | 8 | 4 |
| 8 | 3 | 6 | 9 | 1 | 4 | 7 | 10 | 2 | 5 | 8 |
| 9 | 6 | 1 | 7 | 2 | 8 | 3 | 9 | 4 | 10 | 5 |
| 10 | 1 | 2 | 3 | 4 | 5 | 6 | 7 | 8 | 9 | 10 |

**Table 5.0.5**
**Welch-Costas Code, p=11, "1" Positionings**

| Frame | #1 | #2 | #3 | #4 | #5 | #6 | #7 | #8 | #9 | #10 |
|-------|-----|-----|-----|-----|-----|-----|-----|-----|-----|------|
| | | | | Table 5.0.6 | | | | | | |
| | | | Zech Logarithm Welch-Costas Code, p=11, "1" Positionings | | | | | | | |
| 1 | 8 | 1 | 3 | 2 | 5 | 4 | 6 | 10 | 9 | 7 |
| 2 | 1 | 2 | 4 | 10 | 7 | 8 | 3 | 5 | 6 | 9 |
| 3 | 2 | 10 | 8 | 5 | 9 | 1 | 4 | 7 | 3 | 6 |
| 4 | 10 | 5 | 1 | 7 | 6 | 2 | 8 | 9 | 4 | 3 |
| 5 | 5 | 7 | 2 | 9 | 3 | 10 | 1 | 6 | 8 | 4 |
| 6 | 7 | 9 | 10 | 6 | 4 | 5 | 2 | 3 | 1 | 8 |
| 7 | 9 | 6 | 5 | 3 | 8 | 7 | 10 | 4 | 2 | 1 |
| 8 | 6 | 3 | 7 | 4 | 1 | 9 | 5 | 8 | 10 | 2 |
| 9 | 3 | 4 | 9 | 8 | 2 | 6 | 7 | 1 | 5 | 10 |
| 10 | 4 | 8 | 6 | 1 | 10 | 3 | 9 | 2 | 7 | 5 |

**Table 5.0.6**
**Zech Logarithm Welch-Costas Code, p=11, "1" Positionings**

The major results detected by this form of analysis are:

• The number of codes with good autocorrelation and crosscorrelation properties can be increased by the use of the Zech Logarithm construction. This increase in usable codes is particularly so in the case of hyperbolic congruence codes (see Fig. 5.0.10 and 5.0.17), less so in the case of quadratic congruence codes (see Fig. 5.0.11 and 5.0.18), but not so in the case of Welch-Costas codes (see Fig.s 5.0.12 and 5.0.19).

• Although the Welch-Costas codes of both the normal and the Zech Logarithm construction have very poor crosscorrelation properties, these constructions have superior autocorrelation properties. It is known that there is a trade between optimum autocorrelation properties and crosscorrelation properties. The Welch-Costas codes exhibits the case of extremely superior autocorrelation properties, but at the expense of crosscorrelation properties, which are unacceptable.

• It is significant that the relative merits of the three normal constructions - hyperbolic congruence, quadratic congruence and Welch-Costas - are transferred to the Zech Logarithm constructions of those codes. That is, both the merits and demerits of the normal constructions appear in the Zech Logarithm constructions.
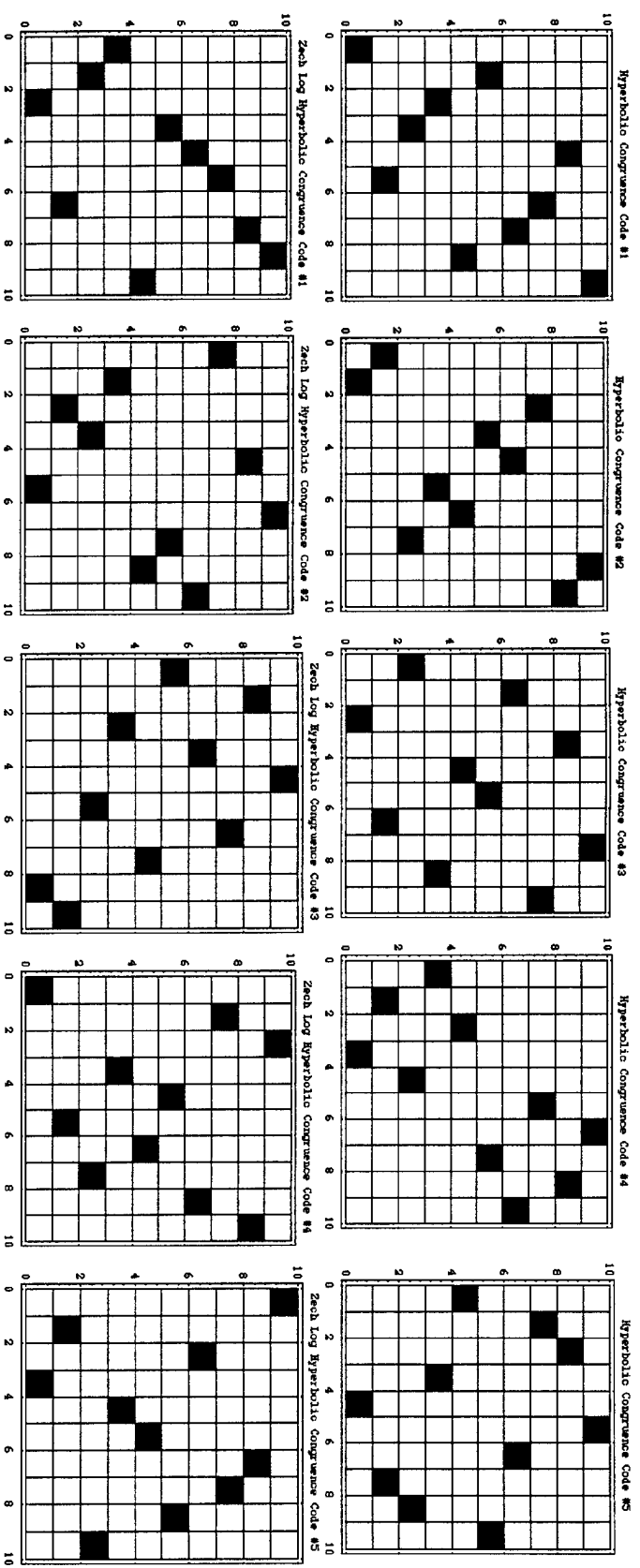
Fig. 5.0.1. Top: Hyperbolic Congruence Codes, $p = 11$, #1-5; Bottom: Zech Logarithm of the top codes.
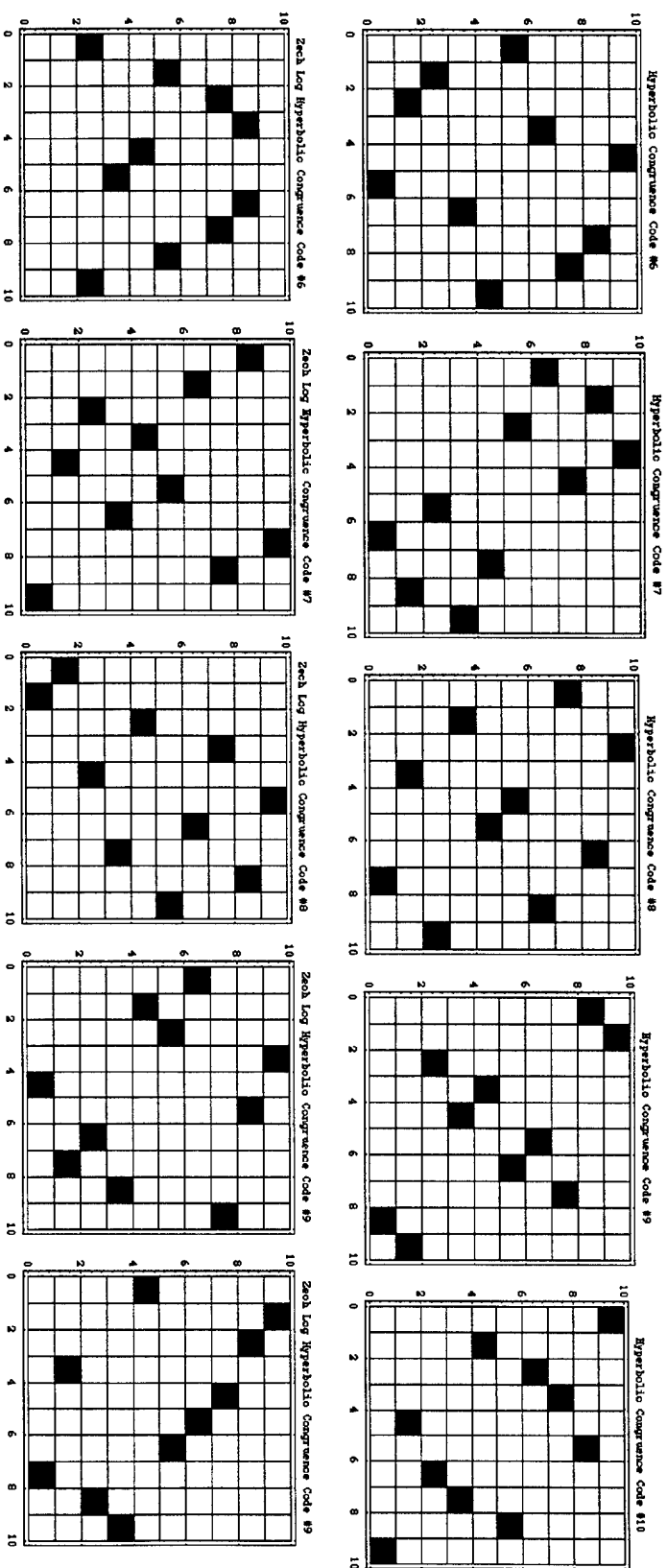
Fig. 5.0.2. Top: Hyperbolic Congruence Codes, $p = 11$, #6-10; Bottom: Zech Logarithm of the top codes.
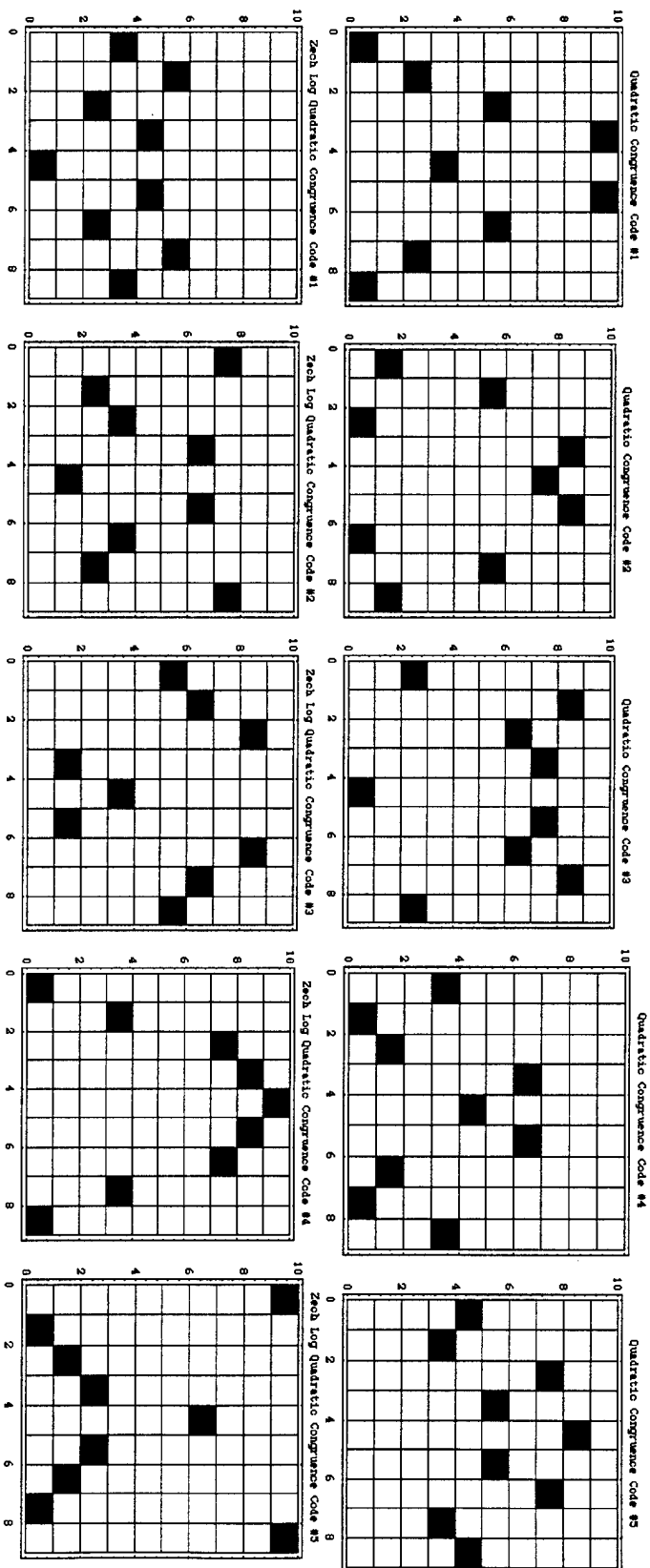
Fig. 5.0.3. Top: Quadratic Congruence Codes, $p = 11$, #1-5; Bottom: Zech Logarithm of the top codes.
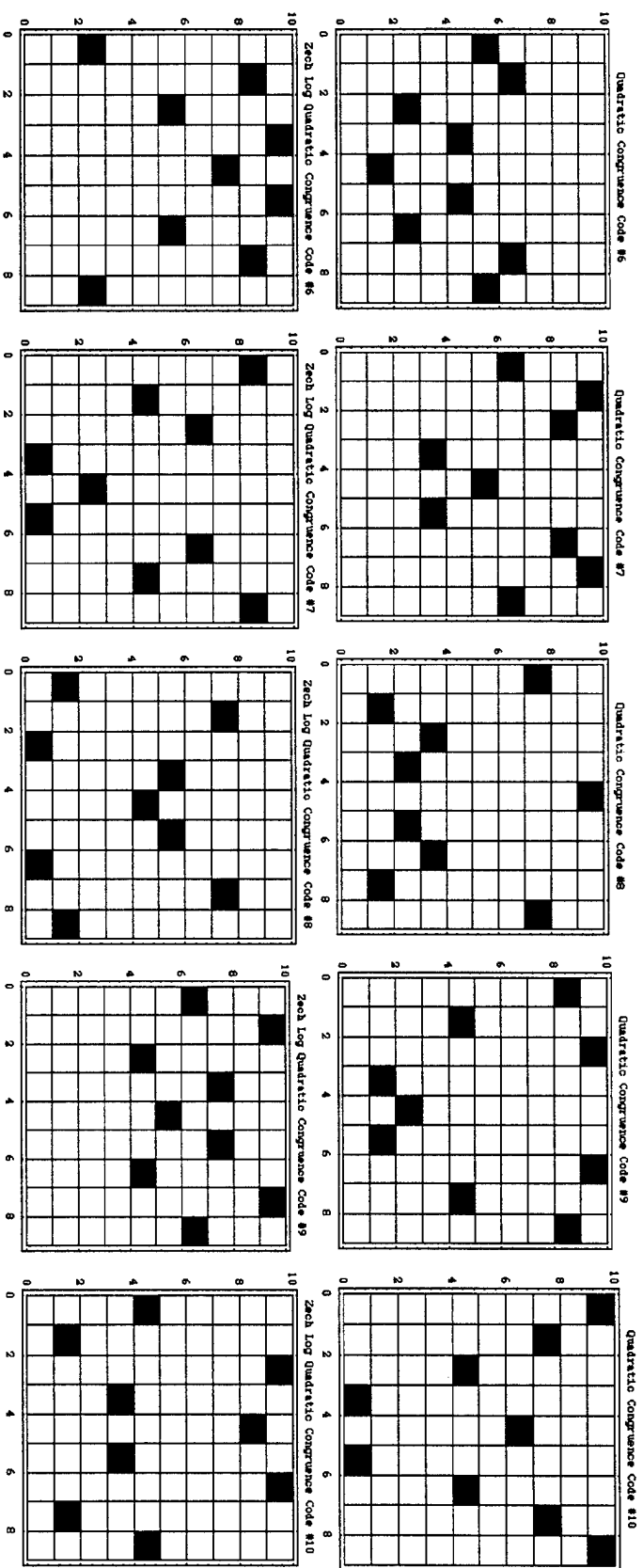
Fig. 5.0.4. Top: Quadratic Congruence Codes, $p = 11$, #6-10; Bottom: Zech Logarithm of the top codes.
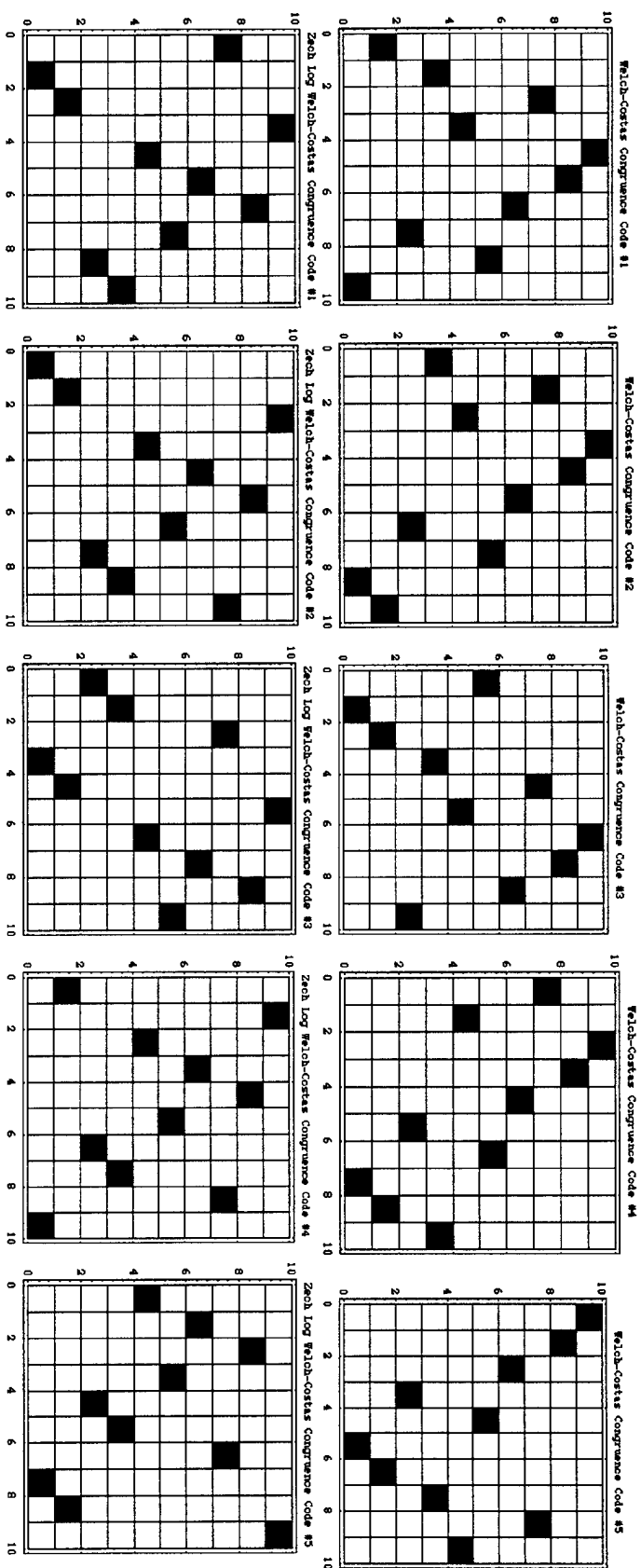
Fig. 5.0.5. Top: Welch-Costas Congruence Codes, $p = 11$, #1-5; Bottom: Zech Logarithm of the top codes.
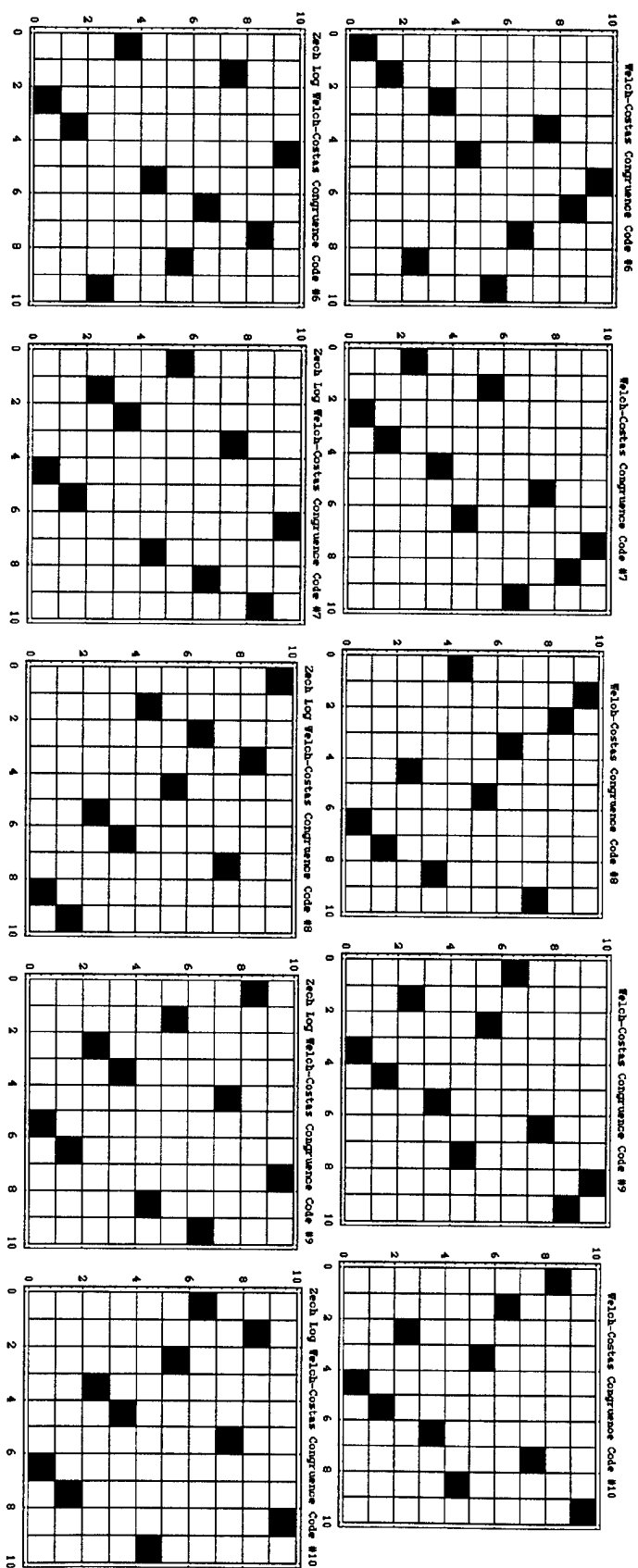
Fig. 5.0.6. Top: Welch-Costas Congruence Codes, $p = 11$, #6-10; Bottom: Zech Logarithm of the top codes.

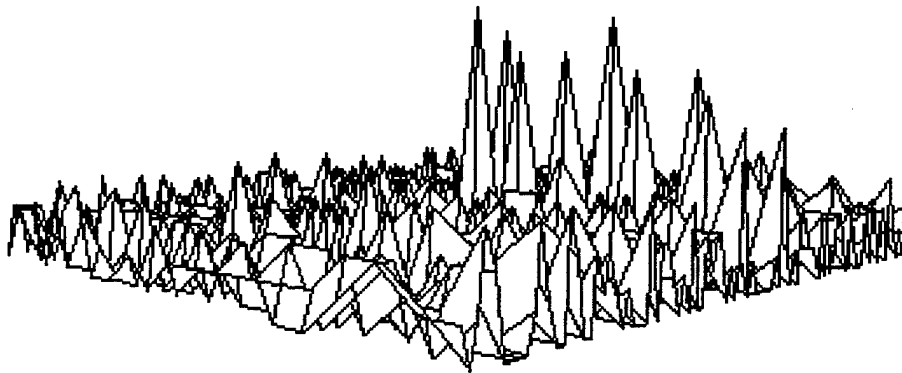Normal vs ZechLog Hyperb.CC, Agnst Normal#1
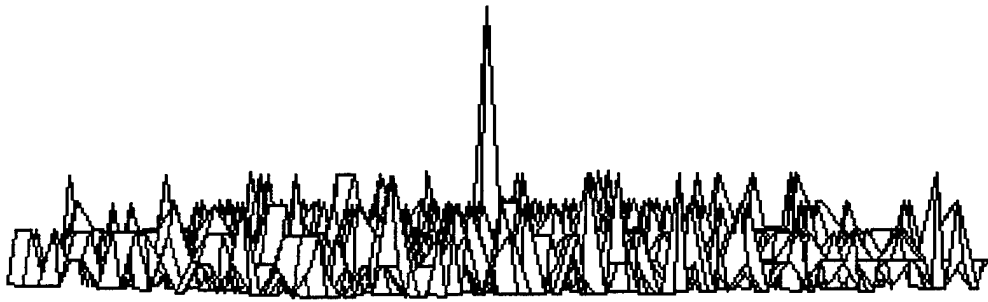
Normal vs ZechLog Hyperb.CC, Agnst Normal#1
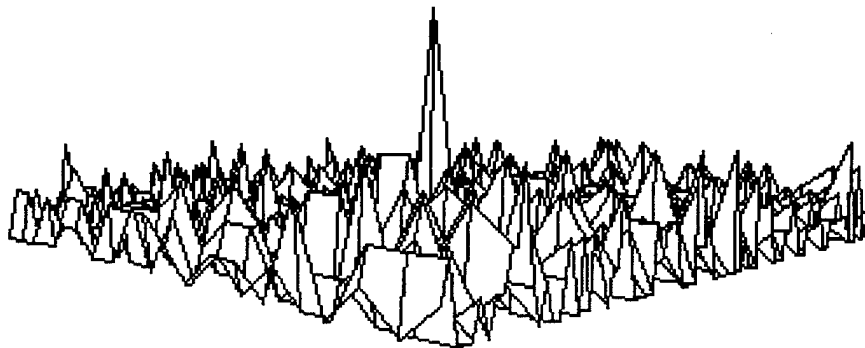
Fig. 5.0.7. These two plots are the plots of the same data, but at two different angles, of the autocorrelation (center) of code #1 of the hyperbolic congruence codes, $p = 11$, using the normal construction, and the crosscorrelations of this code with the 9 other codes of the normal construction and the 10 codes constructed from the Zech Logarithm of these hyperbolic congruence codes.

61

ZechLog & Normal Quadratic Congruence Codes, Against Normal#1
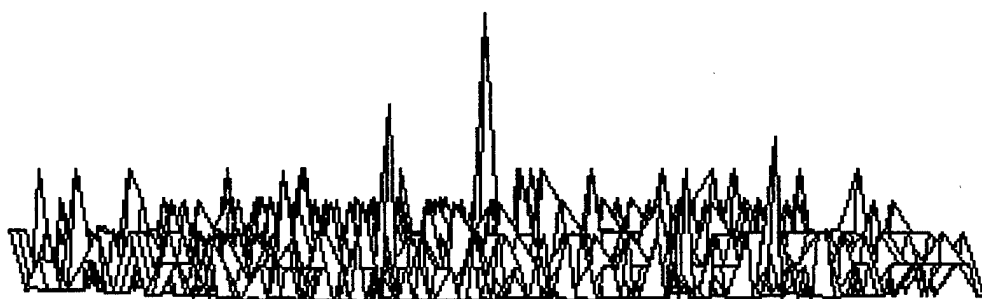
ZechLog & Normal Quadrat. Congr.Codes, Against Normal#1
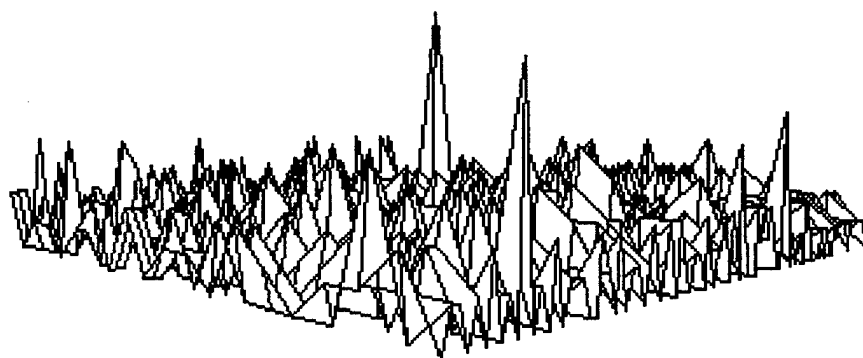


Fig. 5.0.8. These two plots are the plots of the same data, but at two different angles, of the autocorrelation (center) of code #1 of the quadratic congruence codes, $p = 11$, using the normal construction, and the crosscorrelations of this code with the 9 other codes of the normal construction and the 10 codes constructed from the Zech Logarithm of these quadratic congruence codes.

ZechLog&Norm. Welch-Costas Codes, Against Norm#1
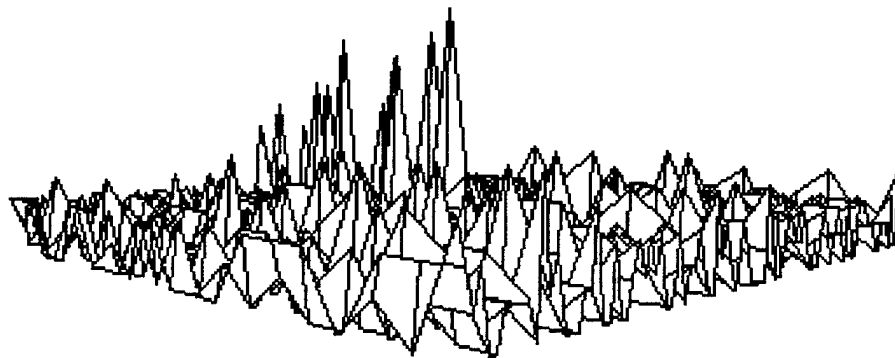


Fig. 5.0.9. These two plots are the plots of the same data, but at two different angles, of the autocorrelation (center) of code #1 of the Welch-Costas congruence codes, $p = 11$, using the normal construction, and the crosscorrelations of this code with the 9 other codes of the normal construction and the 10 codes constructed from the Zech Logarithm of these Welch-Costas congruence codes.

**A.**

Normal vs ZechLog Hyperb.CC, Agnst Normal#1, >4

**B.**
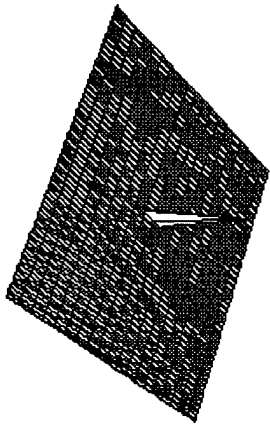
ZechLog & Norm. Quadr.CC, Against Norm#1, >4

**C.**

ZechLog&Norm.Welch-Costas Cs,Against Norm#1, >4



Normal vs ZechLog Hyperb.CC, Agnst Normal#1, >4



ZechLog & Norm. Quadr.CC, Against Norm#1, >4
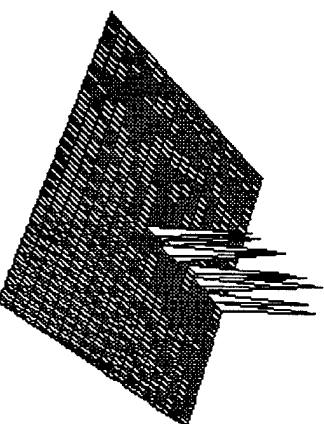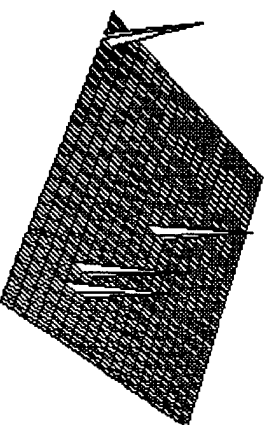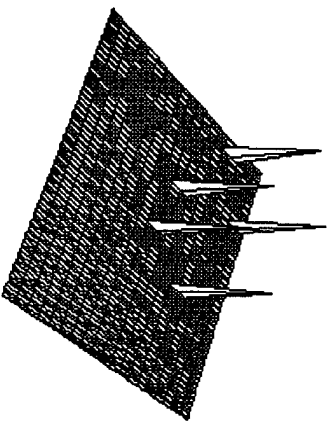


ZechLog&Norm.Welch-Costas Cs,Against Normal#1, >4
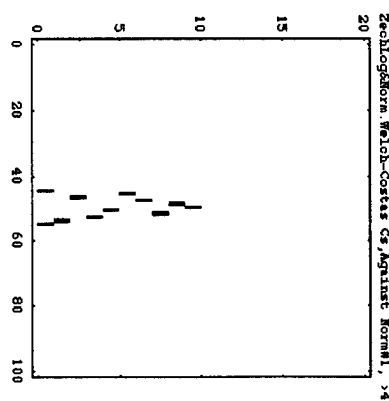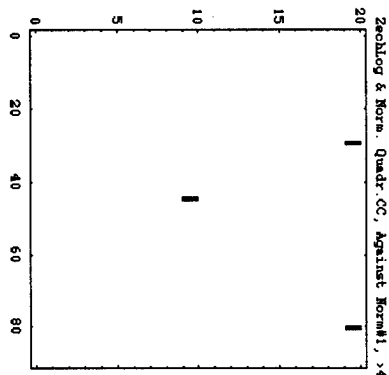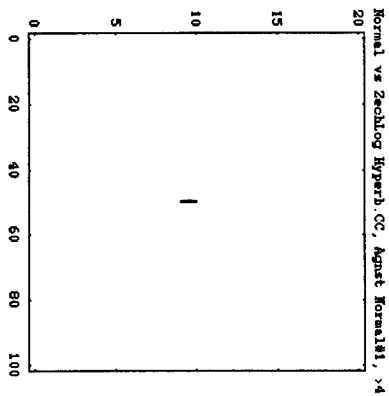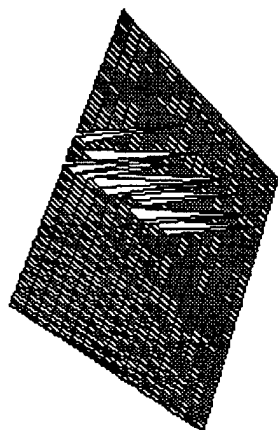
Fig. 5.0.10. These are plot summaries of Fig.s 7, 8 and 9. Top and bottom are 3- and 2-dimensional plots of 1 autocorrelation (#10) of the first code of the normal construction and 9 crosscorrelations of the normal construction (#1-#9) and 10 of the Zech Logarithm of the normal construction (#11-20) for those values greater than 4 (with 10 as maximum). A: hyperbolic codes, $p = 11$, showing an excellent autocorrelation and excellent crosscorrelations for the normal and the Zech Logarithm constructions; B: quadratic congruence codes, $p = 11$, showing an excellent autocorrelation and excellent crosscorrelations for the normal constructions, with largely excellent crosscorrelations except for 1 code; C: Welch-Costas codes, $p = 11$, showing an excellent autocorrelation, poor crosscorrelations for the normal construction and excellent crosscorrelations for the Zech Logarithm constructions.

64

**A.**

ZechLog & Norm. Quadr.CC, Against Norm#1, >4

**B.**

ZechLog & Norm. Quadr.CC, Against Norm#1, >5
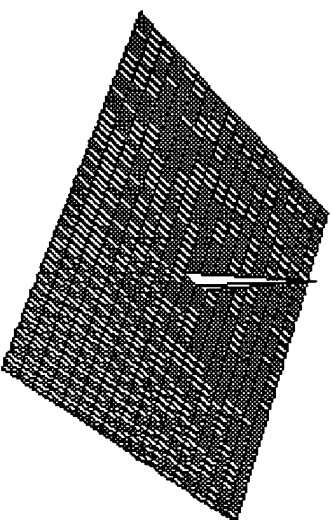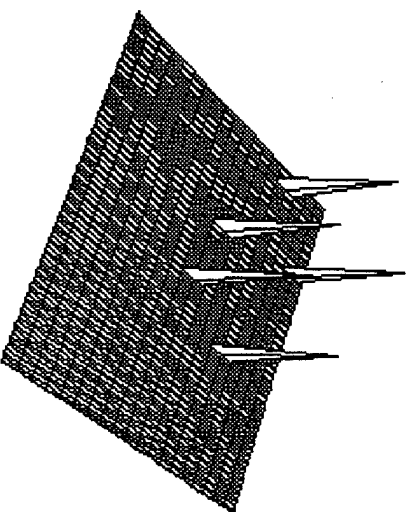
**C.**

ZechLog & Norm. Quadr.CC, Against Norm#1, >6
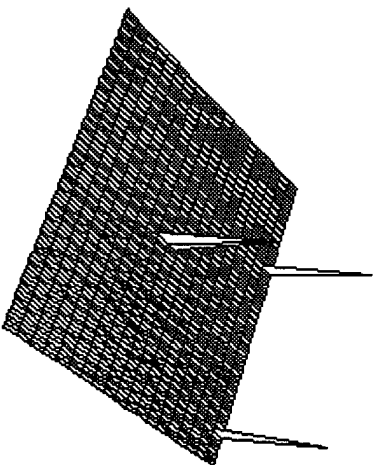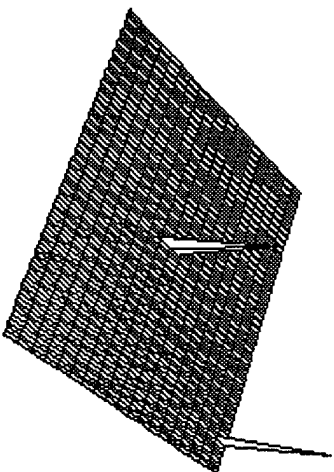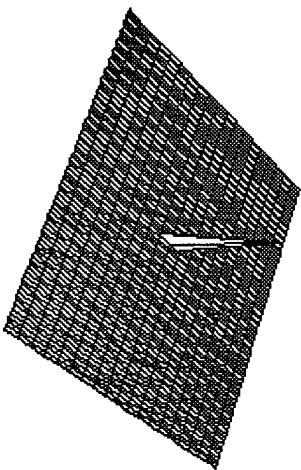


Fig. 5.0.11. These are plot summaries of Fig.s 8, i.e., 3–dimensional plots of 1 autocorrelation (#10) of the first code of the normal construction of the quadratic congruence codes, $p = 11$, and 9 crosscorrelations of the normal construction (#1-#9) and 10 of the Zech Logarithm of the normal construction (#11-20) for those values greater than A: 4, B: 5, and C: 6 (with 10 as maximum). Fig. 11A was shown in Fig. 10B, above. This figure shows that if the interference crosscorrelation criterion is relaxed from 4 to 6, then the Zech Logarithm codes are usable.

**A.**

ZechLog&Norm.Welch-Costas Cs,Against Norm#1, >4ZechLog&Norm.Welch-Costas Cs,Against Norm#1, >5ZechLog&Norm.Welch-Costas Cs,Against Norm#1, >6

**B.**

**C.**

**D.**
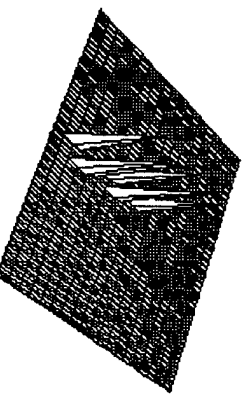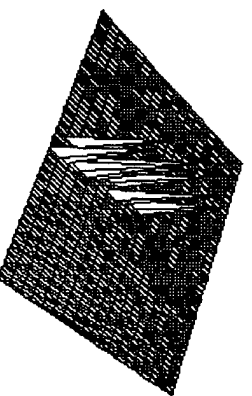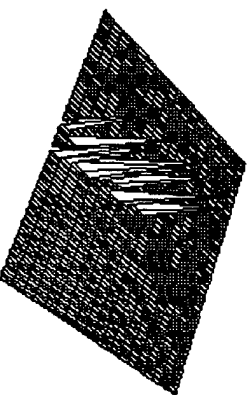
ZechLog&Norm.Welch-Costas Cs,Against Norm#1, >7ZechLog&Norm.Welch-Costas Cs,Against Norm#1, >8ZechLog&Norm.Welch-Costas Cs,Against Norm#1, >9
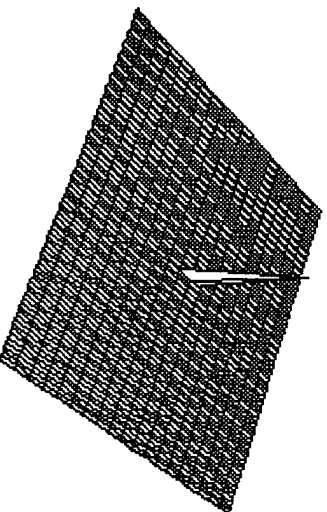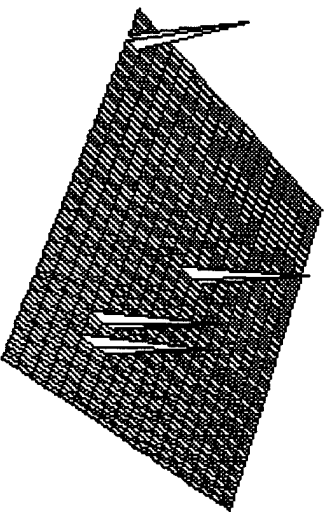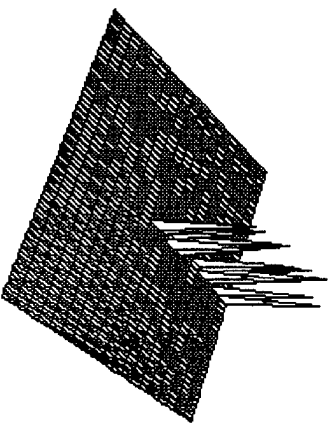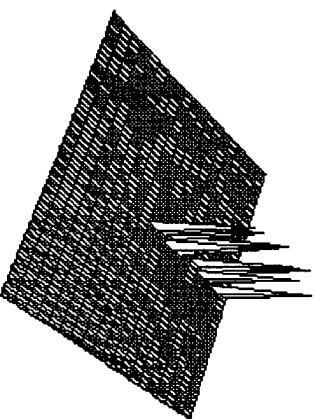
**E.**

**F.**
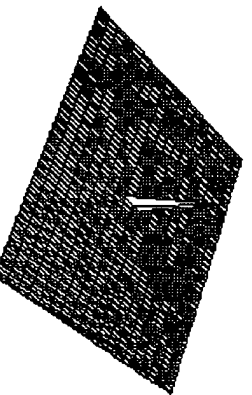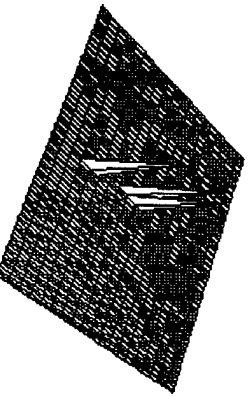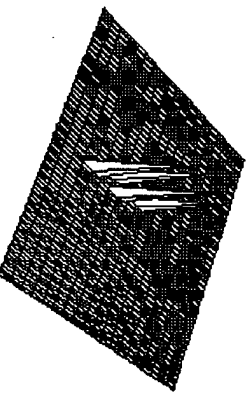
Fig. 5.0.12. These are plot summaries of Fig.s 9, i.e., 3--dimensional plots of 1 autocorrelation (#10) of the first code of the normal construction of the Welch-Costas codes, $p = 11$, and 9 crosscorrelations of the normal construction (#1-#9) and 10 of the Zech Logarithm of the normal construction (#11-20) for those values greater than A: 4, B: 5, C: 6, D: 7, E: 8 and F: 9 (with 10 as maximum). Fig. 12A was shown in Fig. 10C, above. This figure shows that even if the interference crosscorrelation criterion is relaxed from 4 to 9, then theWelch-Costas codes are usable, but the Zech Logarithm of the codes might be. This hope is denied by the analysis to follow.

Normal & ZechLog Hyperb.CC, Agnst ZechLog#1
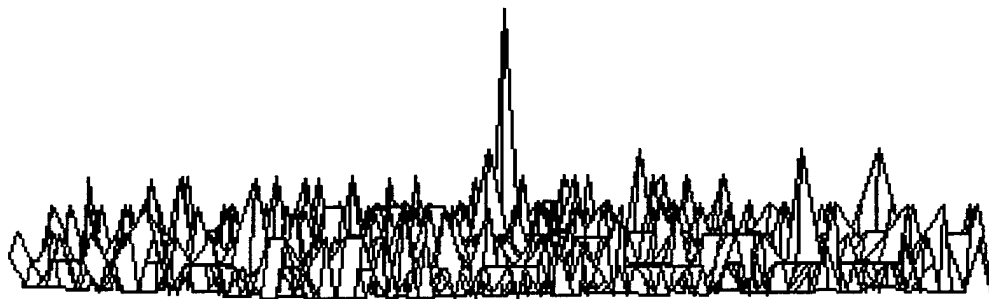


Normal & ZechLog Hyperb.CC, Agnst ZechLog#1
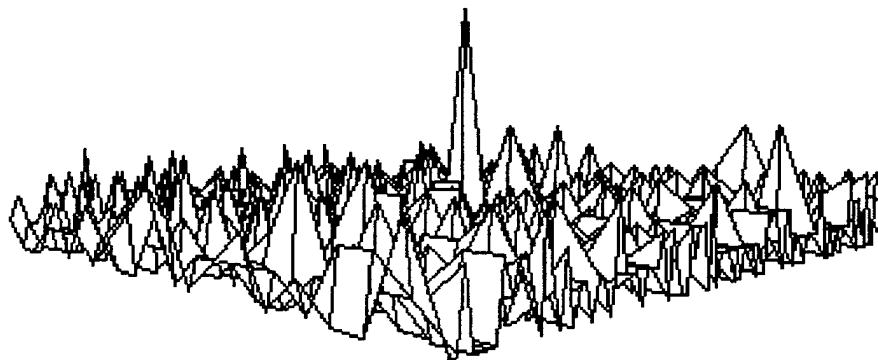


Fig. 5.0.13. These two plots are the plots of the same data, but at two different angles, of the autocorrelation (center) of code #1 of the Zech Logarithm construction of the hyperbolic congruence codes, $p = 11$, and the crosscorrelations of this code with the 9 other codes of the Zech Logarithm construction and the 10 codes of the normal construction for hyperbolic congruence codes.

ZechLog+Normal Quadr.Congr.Codes, Against ZechLog#1
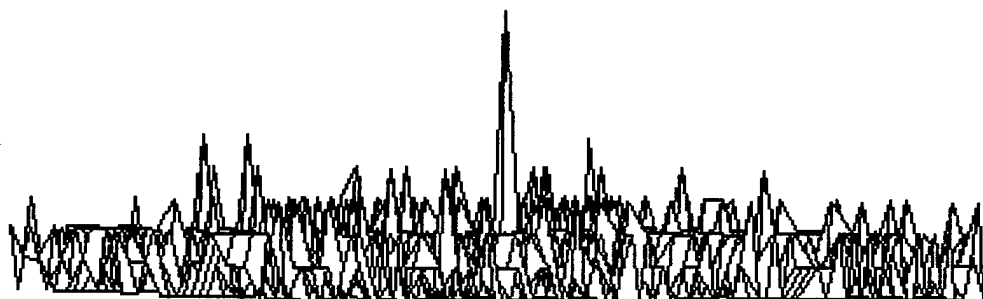
ZechLog+Normal Quadr.Congr.Codes, Against ZechLog#1
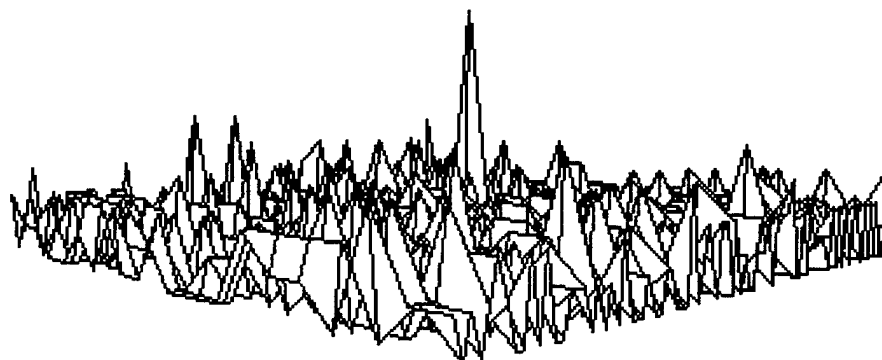
Fig. 5.0.14. These two plots are the plots of the same data, but at two different angles, of the autocorrelation (center) of code #1 of the Zech Logarithm construction of the quadratic congruence codes, $p$ = 11, and the crosscorrelations of this code with the 9 other codes of the Zech Logarithm construction and the 10 codes of the normal construction for quadratic congruence codes.

68

ZechLog&Norm Welch-Costas Codes, Against ZechLog#1
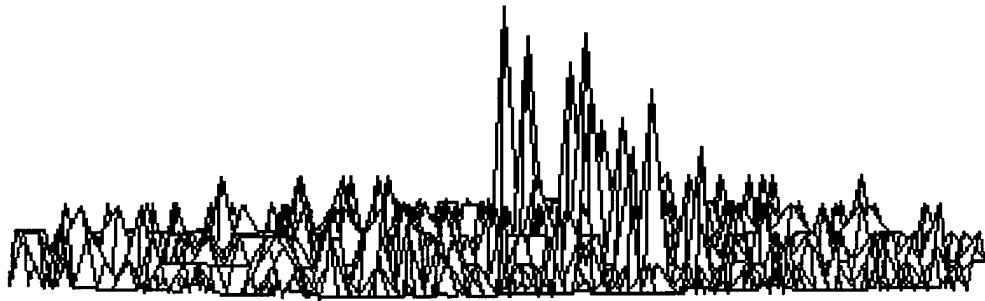


ZechLog&Norm Welch-Costas Codes, Against ZechLog#1



Fig. 5.0.15. These two plots are the plots of the same data, but at two different angles, of the autocorrelation (center) of code #1 of the Zech Logarithm construction of the Welch Costas codes, $p = 11$, and the crosscorrelations of this code with the 9 other codes of the Zech Logarithm construction and the 10 codes of the normal construction for Welch Costas codes.

**A.**

Normal & ZechLog Hyperb.CC, Agnst ZechLog#1, >4   ZechLog+Norm.Quadr.CCs, Against ZechLog#1, >4   ZechLog&Norm Welch-Costas,Against ZechLog#1, >4

**B.**

**C.**
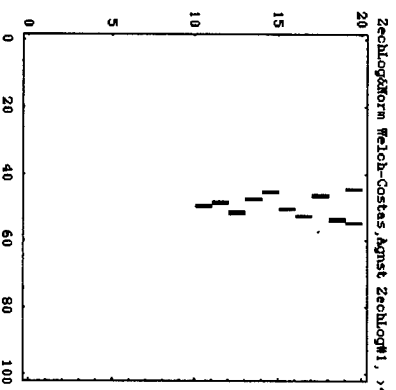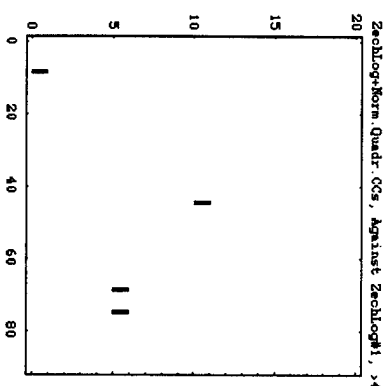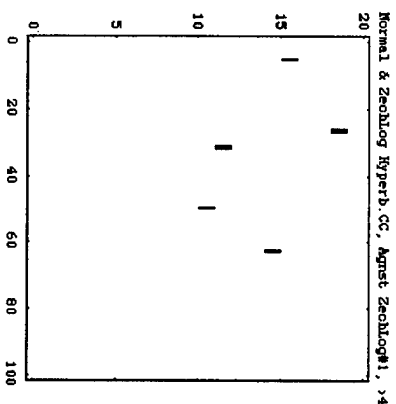


Fig. 5.0.16. These are plot summaries of Fig.s 13, 14 and 15. Top and bottom are 3- and 2-dimensional plots of 1 autocorrelation (#10) of the first code of the Zech Logarithm construction and 9 crosscorrelations of the Zech Logarithm construction (#1-#9) and 10 of the normal construction (#11-20) for those values greater than 4 (with 10 as maximum). A: hyperbolic codes, $p = 11$, showing an excellent autocorrelation and excellent crosscorrelations for the normal, but less optimum for the Zech Logarithm codes; B: quadratic congruence codes, $p = 11$, showing an excellent autocorrelation and excellent crosscorrelations for the normal constructions, buts less than optimum for the Zech Logarithm codes; C: Welch-Costas codes, $p = 11$, showing an excellent autocorrelation, excellent crosscorrelations for the Zech Logarithm constructions and but poor crosscorrelations for the normal constructions.

**A.**

Normal & ZechLog Hyperb.CC, Agnst ZechLog#1, >4

**B.**

Normal & ZechLog Hyperb.CC, Agnst ZechLog#1, >5



Fig. 5.0.17. These are plot summaries of Fig.s 13, i.e., 3–dimensional plots of 1 autocorrelation (#10) of the first code of the Zech Logarithm construction of the hyperbolic congruence codes, $p = 11$, and 9 crosscorrelations of the Zech Logarithm construction (#1-#9) and 10 of the normal construction (#11-20) for those values greater than A: 4, and B: 5 (with 10 as maximum). Fig. 17A was shown in Fig. 16A, above. This figure shows that if the interference crosscorrelation criterion is relaxed from 4 to 5, then the normal codes can be used with the Zech Logarithm codes.

A.

`ZechLog+Norm.Quadr.CCs, Against ZechLog#1, >4`     `ZechLog+Norm.Quadr.CCs, Against ZechLog#1, >5`

B.



Fig. 5.0.18. These are plot summaries of Fig.s 14, i.e., 3–dimensional plots of 1 autocorrelation (#10) of the first code of the Zech Logarithm construction of the quadratic congruence codes, $p = 11$, and 9 crosscorrelations of the Zech Logarithm construction (#1–#9) and 10 of the normal construction (#11-20) for those values greater than A: 4, and B: 5 (with 10 as maximum). Fig. 18A was shown in Fig. 16B, above. This figure shows that if the interference crosscorrelation criterion is relaxed from 4 to 5, then the normal codes can be used with the Zech Logarithm codes.

A.

ZechLog&Norm Welch-Costas,Against ZechLog#1, >4    ZechLog&Norm Welch-Costas,Against ZechLog#1, >5    ZechLog&Norm Welch-Costas,Against ZechLog#1, >6

B.

C.

D.
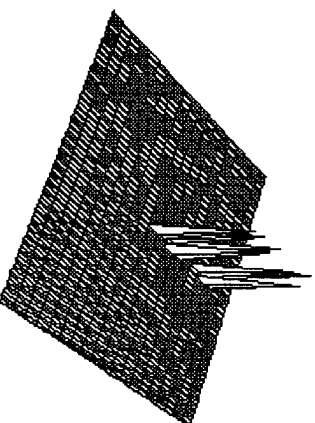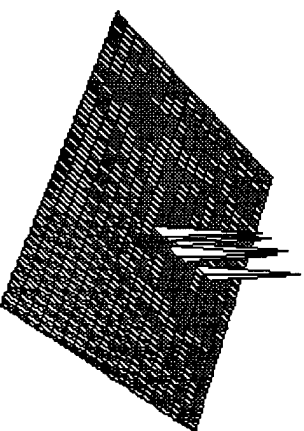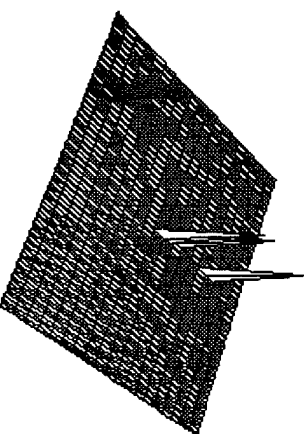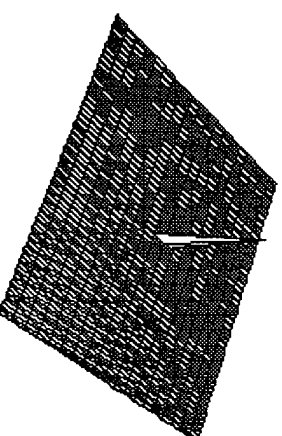
ZechLog&Norm Welch-Costas,Against ZechLog#1, >7    ZechLog&Norm Welch-Costas,Against ZechLog#1, >8    ZechLog&Norm Welch-Costas,Against ZechLog#1, >9

E.

F.

Fig. 5.0.19. These are plot summaries of Fig.s 15, i.e., 3–dimensional plots of 1 autocorrelation (#10) of the first code of the Zech Logarithm construction of the Welch-Costas codes, $p = 11$, and 9 crosscorrelations of the Zech Logarithm construction (#1-#9) and 10 of the normal construction (#11-20) for those values greater than A: 4; B: 5; C: 6; D: 7; E: 8; and F: 9 (with 10 as maximum). Fig. 19A was shown in Fig. 16C, above. This figure shows that even if the interference crosscorrelation criterion is relaxed from 4 to 8, the normal codes cannot be used with the Zech Logarithm codes.

## 6.0 Fourier Analysis Treatment of Orthogonal Codes.

### Introduction:

The goal of achieving extremely high data rate communications transmissions is dependent a great deal on the ability to recognize and lock-on to codes which either define a channel or a user. There are numerous electronic methods for achieving auto- and cross-correlations of superframes of time-hopping pulses, but, in optical communications, the transduction from the optical to the electronic modalities can result in delays, if not bottlenecks. Therefore, the possibility of using optical matched filter methods to achieve code detection should be explored.

The use of optics in communications is not new - for example Ref[1] - and the use of optics in temporal signal processing in radar is well-known[2]. However, here we show that it is possible to take time-hopping codes and achieve optical auto- and cross-correlations the signal-to-noise of which is sufficient for use in communications channels.

The auto-correlation of a function, $s(x,y)$,is defined by:

$$f(x',y') = \int\int_{-\infty}^{+\infty} s(\xi,\eta)s^*(\xi-x',\eta-y')d\xi d\eta.$$

The cross-correlation of two functions, $s(x,y)$ and $g(x,y)$, is:

$$f(x',y') = \int\int_{-\infty}^{+\infty} g(\xi,\eta)s^*(\xi-x',\eta-y')d\xi d\eta.$$

In both cases, the integrals are weighted sums, where one function is used to weight the values of the other. If three functions are related as they are in the auto- and cross-correlation expressions, above, then their respective Fourier transforms are related as follows:

$$F(v_x,v_y) = S(v_x,v_y)S^*(v_x,v_y),$$

$$F(v_x,v_y) = G(v_x,v_y)S^*(v_x,v_y).$$

It is well-known that spherical lenses produce the Fourier transform of an input image at the back focal plane[3]. A frequency-plane correlator utilizes a hologram spatial filter whose transmittance is described by $S^*$ and when light represented by $S$ (for auto-correlation) or $G$ (for cross-correlation) is passed through the filter, it is modulated by $S^*$. A second lens takes the inverse Fourier transform, resulting in $f(x,y)$ at the output plane[4] (Fig. 1). Any bright spot on the output plane indicates a high correlation value[5]. From an

[1] J.W. Goodman, *Introduction to Fourier Optics*, McGraw-Hill, New York, 1968.

[2] Cf. Part III of Horner, J.L. (Ed.) *Optical Signal Processing*, Academic, NY, 1987.

[3] Rhodes, J.E., Analysis and synthesis of optical images. *Am. J. Phys.*, 21, 337-343, 1953.

[4] Cutrona, L.J., Leith, E.N., Palermo, C.J. & Porcello, L.J., Optical data processing and filtering systems. *IEEE Trans. Information Theory*, IT-6, 386-400, 1960;

VanderLugt, A.B., Signal detection by complex spatial filtering. *IEEE Trans. Information Theory*, IT-10, 139-145, 1964;

Kozma, A. & Kelly, D.L., Spatial filtering for detection of signals submerged in noise. *Applied Optics* 4, 387-392, 1965.

VanderLugt, A.B., Coherent optical processing. *Proc. IEEE*, 62, 1300-1319, 1974.

[5] Casasent, D., Coherent optical pattern recognition. *Proc. IEEE*, 67, 813-825, 1979;

optical perspective, both the operations of *correlation* and *convolution* are similar. However, strictly speaking the convolution operation also involves a folding operation, which is not present in the correlation operation[6].

If the input to the correlator is $s(x,y)$, i.e., the input is correlated with the filter, then after modulation by the filter we have $S(v_x,v_y)S*(v_x,v_y)$. But, after passing through a first lens, this is the squared modulus of $S$, which is a real positive value, indicating that the phase across the output beam is constant, i.e., the output from the filter is a plane wave. But a plane wave input to a second lens is focused to a point on the correlation plane. Thus, the effect of this optical analog correlator is to concentrate the energy of a signal correlated with the filter to a point, while leaving the noise smeared, i.e. increasing the signal-to-noise of the correlated signal.

In terms of linear systems, the description is in terms of the impulse response, which is:

$$h(x,y,x',y') = s*(x-x',y-y'),$$

or, simplified:

$$h(x,y) = s*(-x,-y).$$

In this description, the filter is said to be matched to the signal $s$[7].

If an input, $g(x,y)$, is applied to a filter matched to , then the output, is:

$$f(x',y') = \int\int_{-\infty}^{\infty} h(x'-\xi,y-\eta)g(\xi,\eta)d\xi d\eta$$

$$= \int\int_{-\infty}^{\infty} g(\xi,\eta)s*(\xi-x',\eta-y')d\xi d\eta$$

which is the previously stated cross-correlation. It is well-known that, if a signal of known form, buried in "white" noise, is to be detected, then a matched filter provides the linear operation which maximizes the ratio of instantaneous signal power (at a particular time) to average noise power[8].

Goodman, J.W., *Introduction to Fourier Optics*, McGraw-Hill, 1968, p. 179;

Feitelson, D.G., *Optical Computing*, MIT Press, 1988.

[6] Proakis, J.G. & Manolakis, D.G., *Digital Signal Processing Principles, Algorithms and Applications*, Macmillan, New York, 1992.

[7] Turin, G.L., An introduction to matched filters. *IRE Trans. Information Theory*, IT-6, 311-329, 1960; Turin, G.L., An introduction to digital matched filters. *Proc. IEEE* 69, 79-92, 1976.

[8] Elias, P., Optics and Communication Theory, *J. Opt. Soc. Am.*, 43, 229, 1953;

O'Neill, E.L., Spatial filtering in optics. *IRE Trans. Inform. Theory*, IT-2, 56, 1956;

Cutrona, L.J., Leith, E.N., Palermo, C.J. & Porcello, L.J., Optical data processing and filtering systems. *IEEE Trans. Information Theory*, IT-6, 386-400, 1960;

Cutrona, L.J., Leith, E.N., Palermo, C.J. & Porcello, L.J., On the application of coherent optical processing techniques to synthetic-aperture radar. *Proc. IEEE*, 54, 1026, 1966;

Stroke, G.W. & Funkhouser, A.T., Fourier-transform spectroscopy using holographic imaging without computing and with stationary interferometers. *Phys. Lett.*, 16, 272, 1965;

Kovasnay, L.S.G. & Arman, A., Optical autocorrelation measurement of two-dimensional random patterns. *Rev. Sci. Instr.*, 28, 793, 1957;

If a filter is required matched to an input signal, $s(x,y)$, then the required transfer function for a mask is:

$$H(f_x, f_y) = S^*(f_x, f_y).$$

With $s(x,y)$, as input and its Fourier transformation $S^*$ incident on the mask, the output transmitted by the mask is $SS^*$, which is entirely real, i.e., all curvature of the incident wavefront $S$ is canceled. Therefore, as explained before, this plane wavefront can then be brought to a bright focus by a final lens.

On the other hand, if a signal other than $s(x,y)$ is input, e.g., $g(x,y)$, the wavefront curvature will not be canceled by the mask and the wavefront will not be brought to a sharp focus by a final lens. Thus, the presence of the signal, $s(x,y)$, can be detected by measuring the intensity of light at the focal point of a final transforming lens.
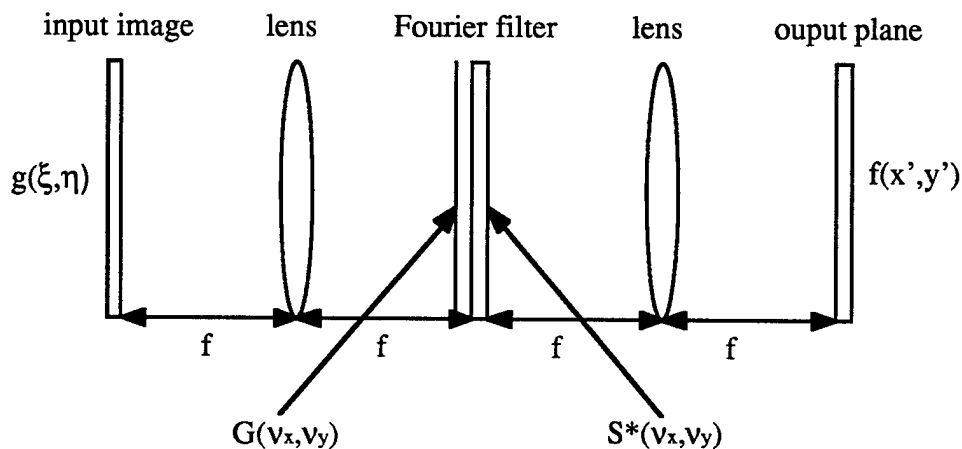


Fig. 6.1. Typical structure of an image correlator. $f$ is the focal length of the lenses. In the case of Fig.s 2, 5 and 8. below, the lenses are 1-D cylindrical. In the case of Fig.s 3, 4, 6, 7, 9 and 10 below, the lenses are 2-D cylindrical.

In the following, we apply these principles to determine whether all-optical methods can be implemented to rapidly detect time hopping codes in optical fibers. We address three types of orthogonal codes:

(1) Hyperbolic Congruence Codes, $p = 11$, (Table 6.1).
(2) Quadratic Congruence Codes, $p = 11$, (Table 6.2).
(3) Welch-Costas Codes, $p = 11$, (Table 6.3).

Trabka, E.A. & Roetling, P.G., Image transformations for pattern recognition using incoherent illumination and bipolar aperture masks. *J. Opt. Soc. Am.*, 54, 1242, 1964;

Armitage, J.D. & Lohmann, A.W., Character recognition by incoherent spatial filtering. *Appl. Opt.*, 4, 461, 1965;

VanderLugt, A.B., Signal detection by complex spatial filtering. *IEEE Trans. Inform. Theory*, IT-10, 2, 1964;

Kozma, A. & Kelly, D.L., Spatial filtering for detection of signals submerged in noise. *Appl. Opt.*, 4, 387, 1965.

A specific objective is to determine whether optical auto- and cross-correlation methods provide sufficient signal-to-noise to compete with electronic digital methods not only in speed but also in accuracy.

| Table 6.1 Hyperbolic Congruence Code, p=11, "1" Positionings | | | | | | | | | | |
| --- | --- | --- | --- | --- | --- | --- | --- | --- | --- | --- |
| Frame | #1 | #2 | #3 | #4 | #5 | #6 | #7 | #8 | #9 | #10 |
| 1 | 1 | 2 | 3 | 4 | 5 | 6 | 7 | 8 | 9 | 10 |
| 2 | 6 | 1 | 7 | 2 | 8 | 3 | 9 | 4 | 10 | 5 |
| 3 | 4 | 8 | 1 | 5 | 9 | 2 | 6 | 10 | 3 | 7 |
| 4 | 3 | 6 | 9 | 1 | 4 | 7 | 10 | 2 | 5 | 8 |
| 5 | 9 | 7 | 5 | 3 | 1 | 10 | 8 | 6 | 4 | 2 |
| 6 | 2 | 4 | 6 | 8 | 10 | 1 | 3 | 5 | 7 | 9 |
| 7 | 8 | 5 | 2 | 10 | 7 | 4 | 1 | 9 | 6 | 3 |
| 8 | 7 | 3 | 10 | 6 | 2 | 9 | 5 | 1 | 8 | 4 |
| 9 | 5 | 10 | 4 | 9 | 3 | 8 | 2 | 7 | 1 | 6 |
| 10 | 10 | 9 | 8 | 7 | 6 | 5 | 4 | 3 | 2 | 1 |

| Table 6.2 Quadratic Congruence Code, p=11, "1" Positionings | | | | | | | | | | |
| --- | --- | --- | --- | --- | --- | --- | --- | --- | --- | --- |
| Frame | #1 | #2 | #3 | #4 | #5 | #6 | #7 | #8 | #9 | #10 |
| 1 | 1 | 2 | 3 | 4 | 5 | 6 | 7 | 8 | 9 | 10 |
| 2 | 3 | 6 | 9 | 1 | 4 | 7 | 10 | 2 | 5 | 8 |
| 3 | 6 | 1 | 7 | 2 | 8 | 3 | 9 | 4 | 10 | 5 |
| 4 | 10 | 9 | 8 | 7 | 6 | 5 | 4 | 3 | 2 | 1 |
| 5 | 4 | 8 | 1 | 5 | 9 | 2 | 6 | 10 | 3 | 7 |
| 6 | 10 | 9 | 8 | 7 | 6 | 5 | 4 | 3 | 2 | 1 |
| 7 | 6 | 1 | 7 | 2 | 8 | 3 | 9 | 4 | 10 | 5 |
| 8 | 3 | 6 | 9 | 1 | 4 | 7 | 10 | 2 | 5 | 8 |
| 9 | 1 | 2 | 3 | 4 | 5 | 6 | 7 | 8 | 9 | 10 |

| Table 6.3 Welch-Costas Code, p=11, "1" Positionings | | | | | | | | | |
| --- | --- | --- | --- | --- | --- | --- | --- | --- | --- |
| Frame | #1 | #2 | #3 | #4 | #5 | #6 | #7 | #8 | #9 | #10 |
| 1 | 2 | 4 | 6 | 8 | 10 | 1 | 3 | 5 | 7 | 9 |
| 2 | 4 | 8 | 1 | 5 | 9 | 2 | 6 | 10 | 3 | 7 |
| 3 | 8 | 5 | 2 | 10 | 7 | 4 | 1 | 9 | 6 | 3 |
| 4 | 5 | 10 | 4 | 9 | 3 | 8 | 2 | 7 | 1 | 6 |
| 5 | 10 | 9 | 8 | 7 | 6 | 5 | 4 | 3 | 2 | 1 |
| 6 | 9 | 7 | 5 | 3 | 1 | 10 | 8 | 6 | 4 | 2 |
| 7 | 7 | 3 | 10 | 6 | 2 | 9 | 5 | 1 | 8 | 4 |
| 8 | 3 | 6 | 9 | 1 | 4 | 7 | 10 | 2 | 5 | 8 |
| 9 | 6 | 1 | 7 | 2 | 8 | 3 | 9 | 4 | 10 | 5 |
| 10 | 1 | 2 | 3 | 4 | 5 | 6 | 7 | 8 | 9 | 10 |

The results are shown in Fig.s 6.2-6.10:

Fig. 6.2 shows the auto- and cross-correlations for Hyperbolic Congruence codes #1 and #2, $p = 11$ using wedge Fourier transforms.

Fig.s 6.3 and 6.4 show the auto- and cross-correlations for Hyperbolic Congruence codes #1 and #2, $p = 11$ using 2D- Fourier transforms.

Fig. 6.5 shows the auto- and cross-correlations for Quadratic Congruence codes #1 and #2, $p = 11$ using wedge Fourier transforms.

Fig.s 6.6 and 6.7 show the auto- and cross-correlations for Quadratic Congruence codes #1 and #2, $p = 11$ using 2D- Fourier transforms.

Fig. 6.8 shows the auto- and cross-correlations for Welch Costas codes #1 and #2, $p = 11$ using wedge Fourier transforms.

Fig.s 6.9 and 6.10 show the auto- and cross-correlations for Welch Costas codes #1 and #2, $p = 11$ using 2D- Fourier transforms.

Clearly, this optical (analog) method according to these results provides signal-to-noise levels equal to that of electronic (digital) methods. The cross-correlation of Welch-Costas codes is known to be inferior, and this is clearly shown in Fig.s 6.8C and 6.10. In the case of the other two codes, the Hyperbolic Congruence and the Quadratic Congruence, the results are superior.
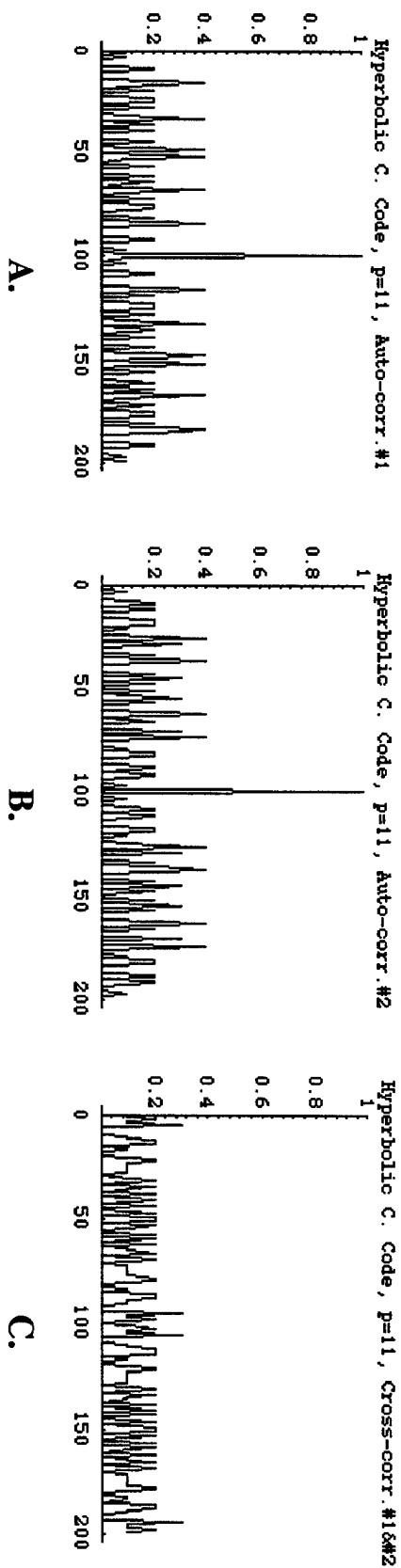
**Fig. 6.2.** A. Auto-correlation of Hyperbolic Congruence Code, $p = 11$, Code #1 using a wedge Fourier Transform and inverse Fourier Transform.
B. Auto-correlation of Hyperbolic Congruence Code, $p = 11$, Code #2 using a wedge Fourier Transform and inverse Fourier Transform.
C. Cross-correlation of Hyperbolic Congruence Code, $p = 11$, Codes #1 & #2 using a wedge Fourier Transform and inverse Fourier Transform.

Auto-Corr.Hyperbolic C.C.p=11, Codes#1&1



**A.**

**B.**

**C.**
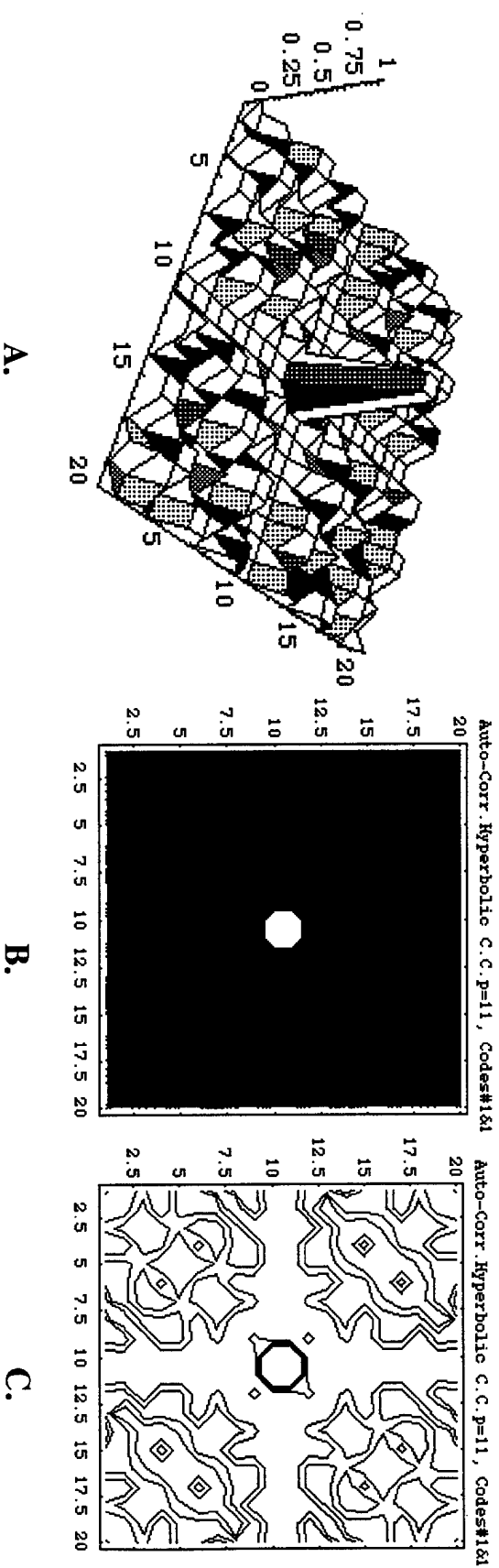
Fig. 6.3.
A. Auto-correlation of Hyperbolic Congruence Code, $p = 11$, Code #1 using a 2D-Fourier Transform (double cylindrical lens) and inverse Fourier Transform.
B. Same data as A, but viewed from above as a contour plot with shading.
C. Same data as A and B, but viewed from above as a contourplot without shading.

Cross-Corr.Hyperbolic C.C.p=11, Codes#1&2

**A.**

**B.**

**C.**
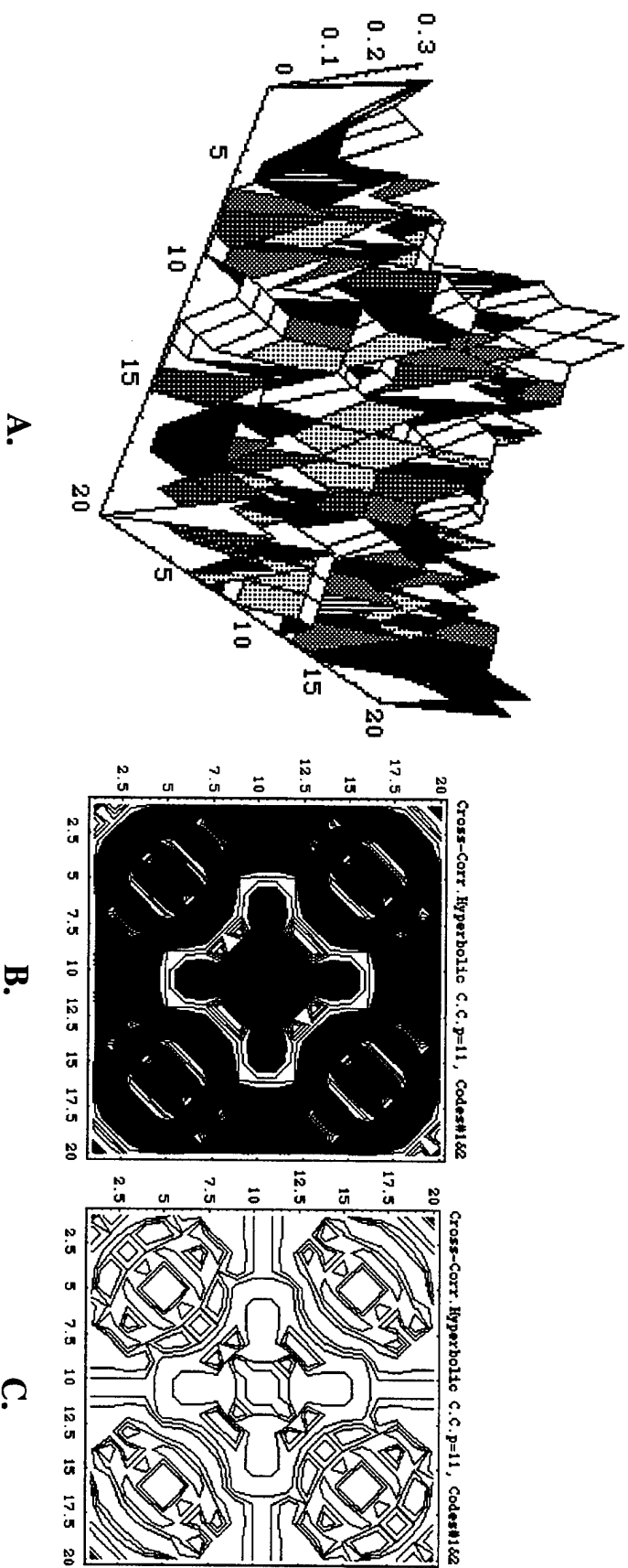
Fig. 6.4.
A. Cross-correlation of Hyperbolic Congruence Code, $p = 11$, Codes #1 and #2 using a 2D-Fourier Transform (double cylindrical lens) and inverse Fourier Transform.
B. Same data as A, but viewed from above as a contour plot with shading.
C. Same data as A and B, but viewed from above as a contourplot without shading.

A.



B.



C.
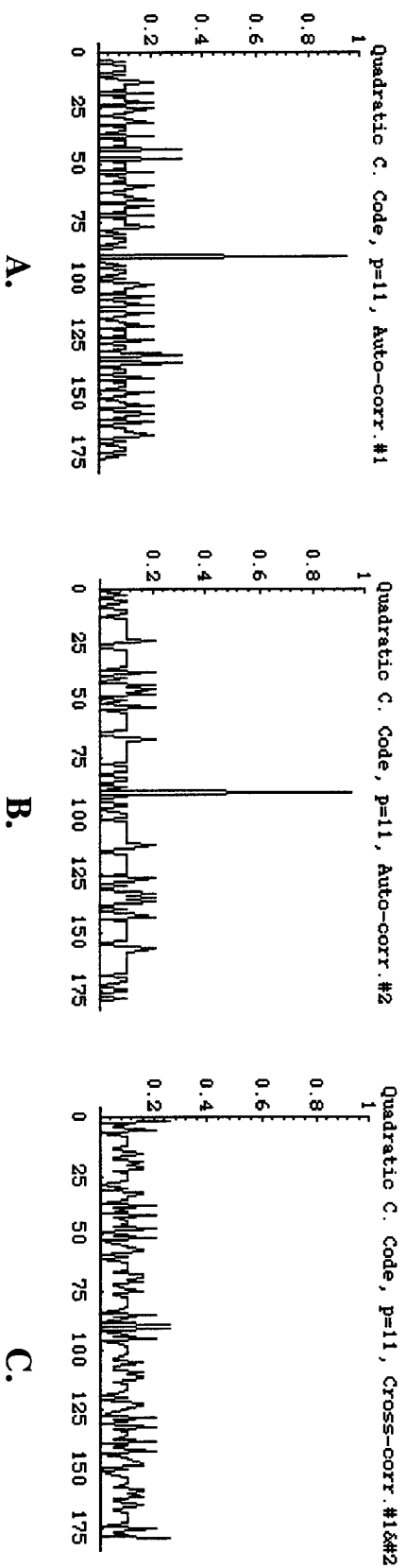
Fig. 6.5. A. Auto-correlation of Quadratic Congruence Code, $p = 11$, Code #1 using a wedge Fourier Transform and inverse Fourier Transform.
B. Auto-correlation of Quadratic Congruence Code, $p = 11$, Code #2 using a wedge Fourier Transform and inverse Fourier Transform.
C. Cross-correlation of Quadratic Congruence Code, $p = 11$, Codes #1 & #2 using a wedge Fourier Transform and inverse Fourier Transform.

83

Auto-Corr. Quadratic C.C. p=11, Codes#1&2
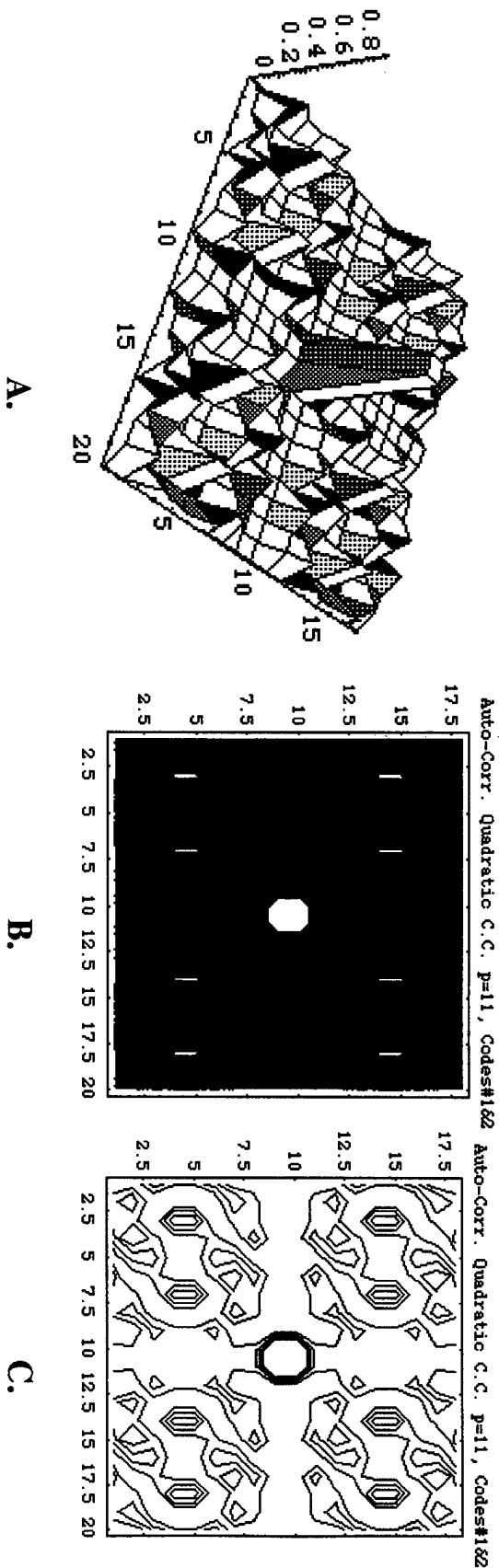


**A.**



**B.**



**C.**

Fig. 6.6
A. Auto-correlation of Quadratic Congruence Code, $p = 11$, Code #1 using a 2D- Fourier Transform (double cylindrical lens) and inverse Fourier Transform.
B. Same data as A, but viewed from above as a contour plot with shading.
C. Same data as A and B, but viewed from above as a contourplot without shading.

84

Cross-Corr. Quadratic C.C. p=11, Codes#1&2

A.

Cross-Corr. Quadratic C.C. p=11, Codes#1&2

B.

Cross-Corr. Quadratic C.C. p=11, Codes#1&2
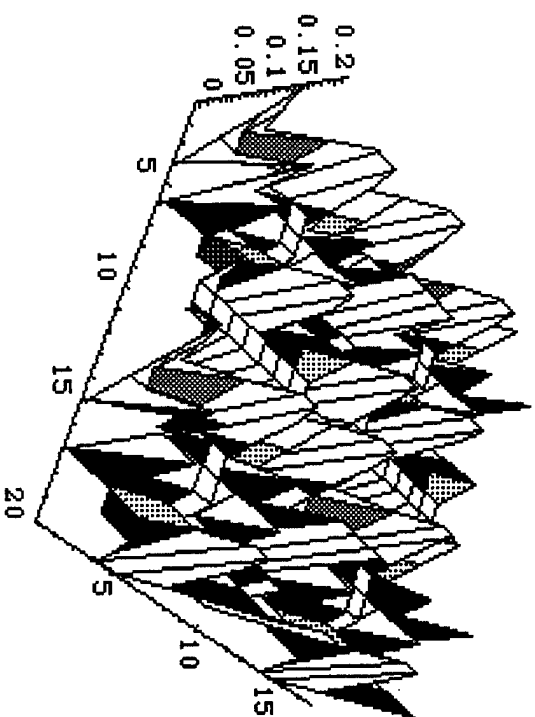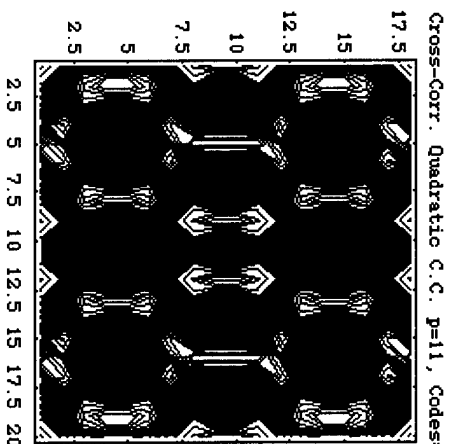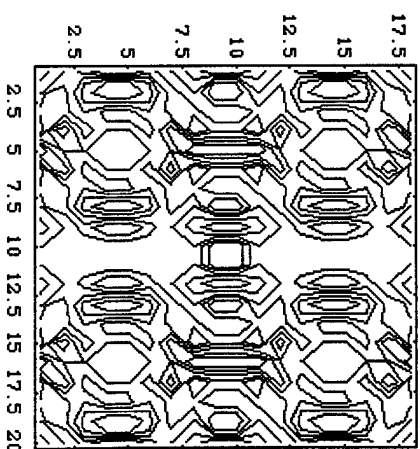
C.

Fig. 6.7
A. Cross-correlation of Quadratic Congruence Code, $p = 11$, Codes #1 and #2 using a 2D- Fourier Transform (double cylindrical lens) and inverse Fourier Transform.
B. Same data as A, but viewed from above as a contour plot with shading.
C. Same data as A and B, but viewed from above as a contourplot without shading.

A.

B.

C.
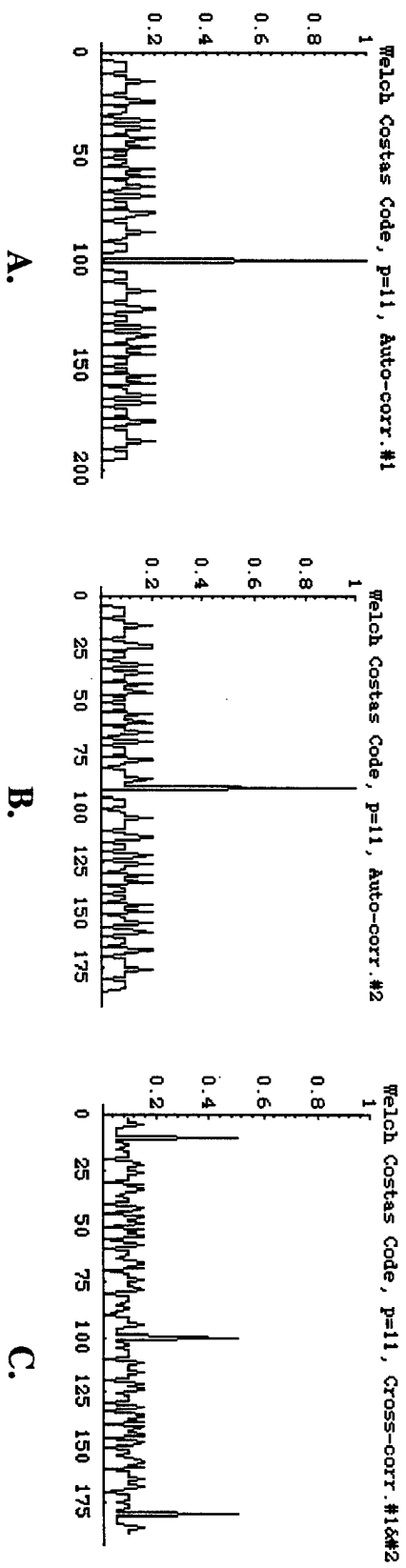
Fig. 6.8 A. Auto-correlation of Welch-Costas Code, $p = 11$, Code #1 using a wedge Fourier Transform and inverse Fourier Transform.
B. Auto-correlation of Welch-Costas Code, $p = 11$, Code #2 using a wedge Fourier Transform and inverse Fourier Transform.
C. Cross-correlation of Welch-Costas Code, $p = 11$, Codes #1 & #2 using a wedge Fourier Transform and inverse Fourier Transform.

Auto-Corr.Welch-Costas C.p=11, Codes#1&2

A.

B.

C.
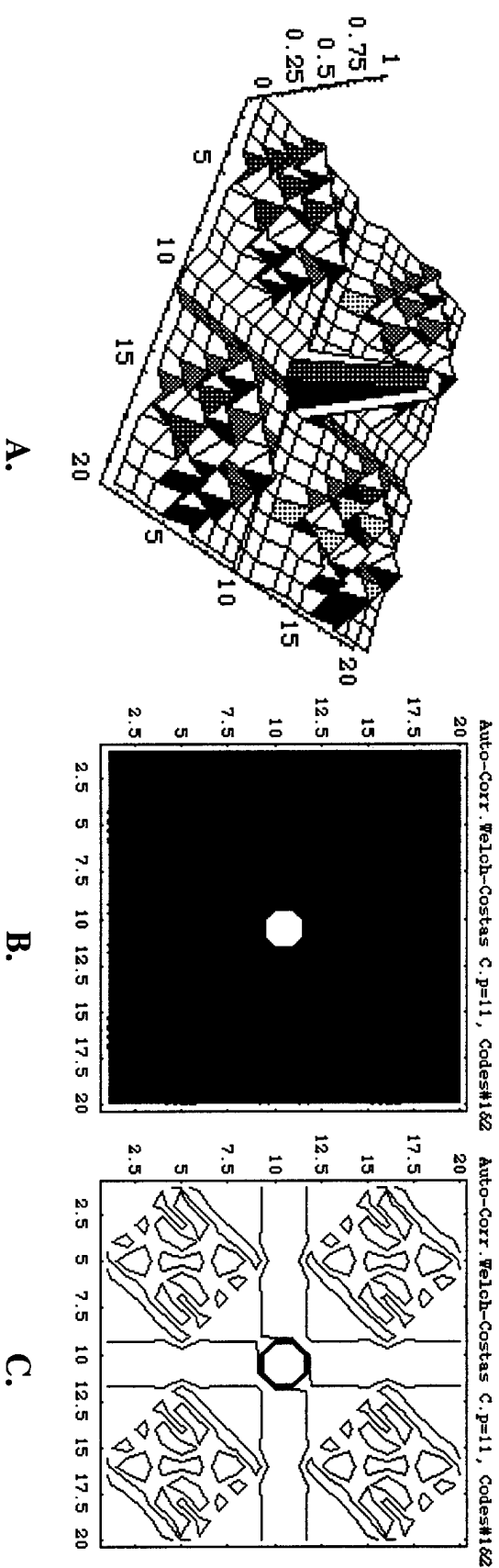
Fig. 6.9
A. Auto-correlation of Welch-Costas Code, $p$ = 11, Code #1 using a 2D- Fourier Transform (double cylindrical lens) and inverse Fourier Transform.
B. Same data as A, but viewed from above as a contour plot with shading.
C. Same data as A and B, but viewed from above as a contourplot without shading.

Cross-Corr.Welch-Costas C.p=11, Codes#1&2



**A.**

Cross-Corr.Welch-Costas C.p=11, Codes#1&2



**B.**

Cross-Corr.Welch-Costas C.p=11, Codes#1&2
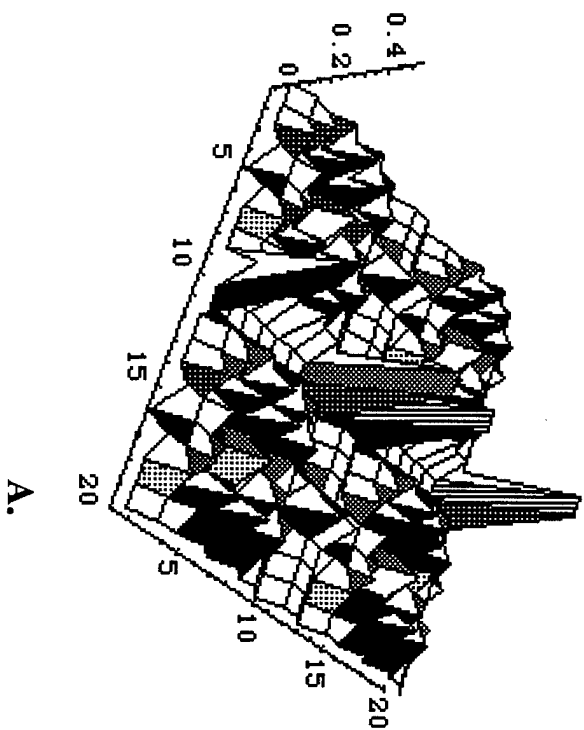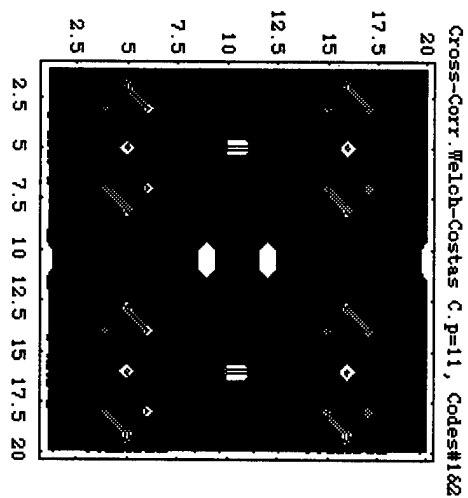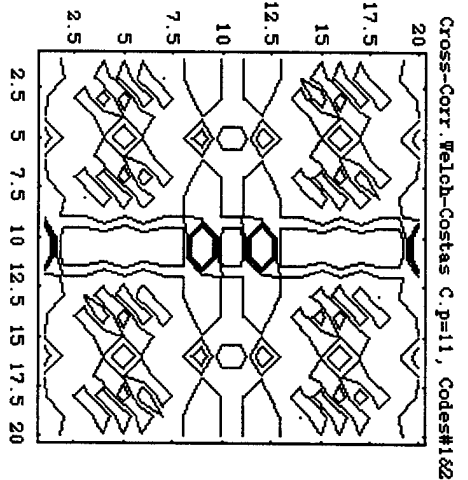


**C.**

Fig. 6.10
A. Cross-correlation of Welch-Costas Code, $p = 11$, Codes #1 and #2 using a 2D-Fourier Transform (double cylindrical lens) and inverse Fourier Transform.
B. Same data as A, but viewed from above as a contour plot with shading.
C. Same data as A and B, but viewed from above as a contourplot without shading.

# 7. Bit Error Rate Analysis

High data rate transmission is dependent not only on the use of coding schemes but on optimum system components. The system components are subject to figure-of-merit constraints defined by variables of the system. The following is the commencement of an analysis which examines the derivation of the most important variables and the relationship of such variables to state-of-the-art components.
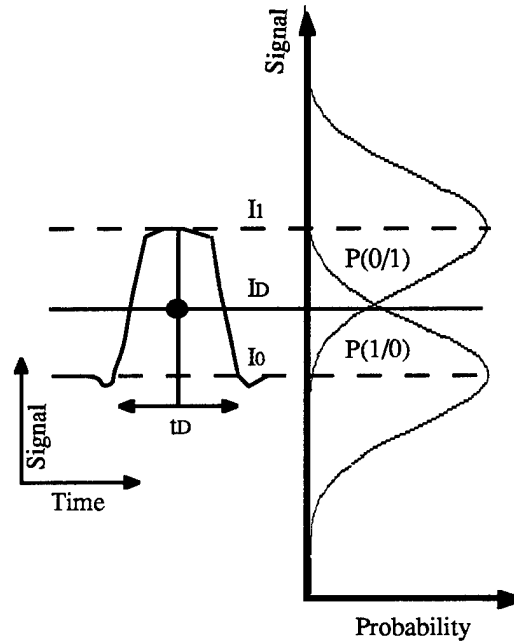


Fig. 7.1 Left: Time-dependent fluctuating signal generated in the receiver in response to a digital PCM bit stream. Signal is sampled at the instant $t_D$ by decision circuit and compared with a threshold level $I_D$. Right: Gaussian probability distributions centered at the average signal level $I_1$ and $I_0$. Dashed region shows the probability of incorrect identification when $I_1$ falls below $I_D$ or $I_0$ exceeds $I_D$. From[9].

The Bit Error Rate (BER) or probability of error is defined as:

$$BER = p(1)P(0/1) + p(0)P(1/0),$$

(see Fig. 7.1) where $p(1)$ and $p(0)$ are the probabilities of receiving a "1" or a "0", respectively, $P(0/1)$ is the probability of the receiver deciding "0" when "1" is received, and $P(1/0)$ is the probability of the receiver deciding "1" when "0" is received. In a pulse-code modulated bit stream, "1" and "0" are equally likely to occur, so $p(1) = p(0) = 0.5$. The BER is thus:

$$BER = 0.5 \left[ P(0/1) + P(1/0) \right].$$

---

[9] Koch, T. A. & Kaminow, I. P. (Ed.s) *Optical Fiber Telecommunications*, Academic, New York, 1997, Vol.s III.

Now the shot noise, $i_s$, of avalanche photodiodes (APDs) is not described by a simple analytic probability density function[10]. An approximation is to treat $i_s$ as a Gaussian random variable but with an adapted variance $\sigma_s^2$. The thermal noise, on the other hand, is well described by Gaussian statistics with zero mean and variance $\sigma_T^2$. Therefore, the sampled value, I, has a Gaussian probability density function with variance $\sigma^2 = \sigma_s^2 + \sigma_T^2$, but the average and variances are different for bit "1" and bit "0", resulting in the conditional probabilities:

$$P(0/1) = \frac{1}{\sigma_1\sqrt{2\pi}}\int_{-\infty}^{I_D}\exp\left[-\frac{(I-I_1)^2}{2\sigma_1^2}\right]dI = \frac{1}{2}erfc\left(\frac{I_1-I_D}{\sigma_1\sqrt{2}}\right),$$

$$P(1/0) = \frac{1}{\sigma_0\sqrt{2\pi}}\int_{I_D}^{\infty}\exp\left[-\frac{(I-I_0)^2}{2\sigma_0^2}\right]dI = \frac{1}{2}erfc\left(\frac{I_D-I_1}{\sigma_1\sqrt{2}}\right),$$

where erfc is the complimentary error function[11]:

$$erfc(x) = \frac{2}{\sqrt{\pi}}\int_{x}^{\infty}\exp\left[-y^2\right]dy.$$

Substitution gives:

$$BER = \frac{1}{4}\left[erfc\left(\frac{I_1-I_D}{\sigma_1\sqrt{2}}\right)+erfc\left(\frac{I_D-I_0}{\sigma_0\sqrt{2}}\right)\right],$$

indicating that the BER depends on the decision threshold $I_D$. Therefore, $I_D$ is minimized to optimize the BER. A minimum occurs when $I_D$ satisfies:

$$\frac{(I_1-I_D)}{\sigma_1} = \frac{(I_D-I_0)}{\sigma_0} = Q.$$

As

$$I_D = \frac{\sigma_0 I_1 + \sigma_1 I_0}{\sigma_0 + \sigma_1}, \qquad (A)$$

if $\sigma_1 = \sigma_0$, $I_D = (I_1 + I_0)/2$, which occurs when the decision threshold is set at midpoint. However, in the case of APD receivers, the shot noise is larger for bit "1" than bit "0", since $\sigma_s^2$ varies linearly with the current. Therefore, the BER for APD receivers can be minimized by setting the decision threshold in accordance with Eq. (A).

[10] McIntyre, R.J., *IEEE Trans. Electron. Dev.*, ED-13, 164, 1966;
Webb, P.P., McIntyre, R.J. & Conradi, J., *RCA Rev.*, 35, 235, 1974;
McIntyre, R.J., *IEEE Trans. Electron. Dev.*, ED-19, 703, 1972;
Balaban, P., *Bell System Tech. J.*, 55, 745, 1976;
Personick, S.D., Balaban, P., Bobsin, J.H. & Kumar, P.R., *IEEE Trans. Commun.*, COM-25, 541, 1977.
[11] Ambramowitz, M. & Stegun, I.A., Eds., *Handbook of Mathematical Functions*, Dover, New York, 1970.

The BER with optimum setting of the decision threshold is then:

$$BER = \frac{1}{2} erfc\left(\frac{Q}{\sqrt{2}}\right) \approx \frac{\exp\left[-Q^2/2\right]}{Q\sqrt{2\pi}},$$

with $Q$ defined as:

$$Q = \frac{I_1 - I_0}{\sigma_1 + \sigma_0}.$$

Fig 7.2 shows the variation of BER as a function of $Q$. For $Q = 6$, the BER is $10^{-9}$; and for $Q > 7$, the BER $< 10^{-12}$.

**Bit Error Rate**
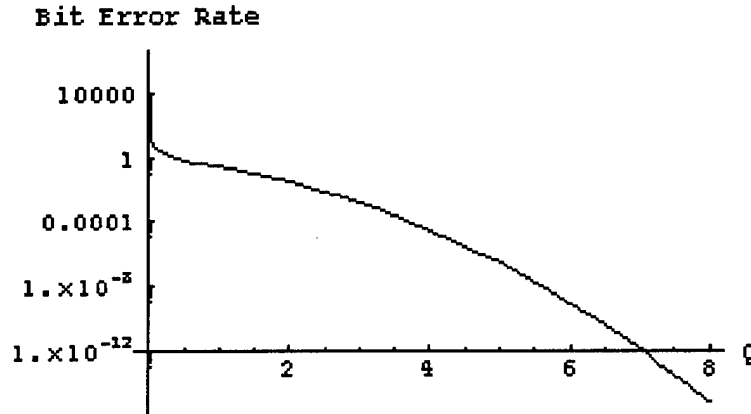


Fig. 7.2 BER versus the $Q$ parameter.

*Extinction Ratio:*

If $P_0$ is the "off" state power and $P_1$ is the "on" state power, then the extinction ratio is:

$$r_{ex} = P_0 / P_1$$

$P_0$ is not zero as some power is emitted by most transmitters even in the "off" state due to the "off" state power depending on bias current and threshold current. In fact, $P_0$ can be a significant fraction of $P_1$ if the laser is biased close to, or above, threshold.

Using the definition of receiver sensitivity:

$$\overline{P}_{rec} = \frac{(P_1 + P_0)}{2},$$

the parameter $Q$ is:

$$Q = \frac{1 - r_{ex}}{1 + r_{ex}} \frac{2R\overline{P}_{rec}}{\sigma_1 + \sigma_0},$$

where $R$ is the receiver responsivity.

The receiver sensitivity is then defined:

$$\overline{P}_{rec}(r_{ex}) = \frac{1 + r_{ex}}{1 - r_{ex}} \frac{\sigma_T Q}{R},$$

where $\sigma_T$ is the square root of the variation in the current due to thermal fluctuations. This result indicates that the receiver sensitivity increases, when the extinction ratio is not equal to zero. The minimum average optical power required by a receiver increases because of nonideal conditions, this increases being called the *power penalty*, defined:

$$\delta_{ex} = \frac{\overline{P}_{rec}(r_{ex})}{\overline{P}_{rec}(0)},$$

or, in decibels:

$$\delta_{ex} = 10 \log_{10}\left(\frac{\overline{P}_{rec}(r_{ex})}{\overline{P}_{rec}(0)}\right) = 10 \log_{10}\left(\frac{1 + r_{ex}}{1 - r_{ex}}\right).$$

Fig. 7.3 shows the power penalty increasing with an increasing extinction ratio. It can be seen that the power penalty is significant if the laser is biased above threshold.
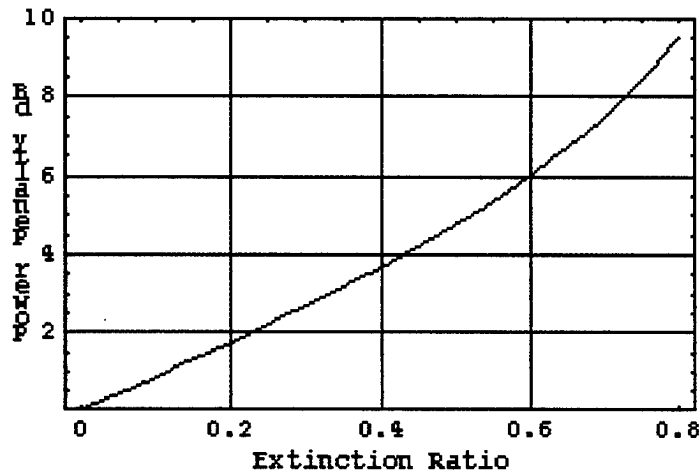


Fig. 7.3 Power penalty versus extinction ratio.

*Intensity Noise:*

Fluctuations in light emitted by the transmitter is called intensity noise. The optical receiver converts power fluctuations into current fluctuations which add to those resulting from shot noise and thermal noise. This results in a degradation of the SNR.

The total current variance is then

$$\sigma^2 = \sigma_s^2 + \sigma_T^2 + \sigma_I^2,$$

where

$$\sigma_I = R\langle\Delta P_{in}^2\rangle^{1/2} = RP_{in}r_I.$$

The parameter, $r_I$, is a measure of the noise level of the incident optical signal, and defined:

$$r = \frac{\langle\Delta P_{in}^2\rangle^{1/2}}{P_{in}}.$$

It is related to the relative intensity noise (RIN) of the transmitter by:

$$r_I^2 = \frac{1}{2\pi}\int_{-\infty}^{\infty} RIN(\omega)d\omega.$$

Thus, $r_I$ is simply the inverse of the SNR of light emitted by the transmitter. Normally, the transmitter SNR is better than 20 dB, so $r_I < 0.01$.

The parameter, $Q$, is reduced in the presence of intensity noise, and the receiver sensitivity becomes:

$$\overline{P}_{rec}(r_I) = \frac{Q\sigma_T + q\Delta fQ^2}{R(1 - r_I^2Q^2)}.$$

The power penalty defining an increase in the receiver sensitivity when the intensity noise parameter is greater than zero, is then:

$$\delta_I = 10\log_{10}\left[\overline{P}_{rec}(r_I)/\overline{P}_{rec}(0)\right] = -10\log_{10}\left(1 - r_I^2Q^2\right).$$

Fig. 7.4 shows that the power penalty as a function of the intensity noise parameter for maintaining $Q = 6$ (i.e., a BER of $10^{-9}$) is negligible for $r_I < 0.01$ (as $\delta_I$ is below 0.02 dB).[9] The power penalty only becomes a limiting factor if $r_I$ exceeds 0.1 (when the power penalty becomes almost 2 dB).
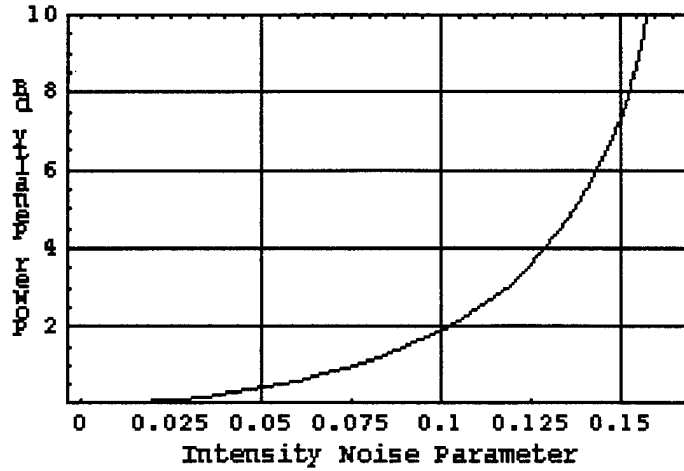
Fig. 7.4 Power penalty versus the intensity noise parameter, $r_I$.

## Timing Jitter:

The decision instant for signal reception shown in Fig. 1 is dependent on the clock-recovery circuit. If the input to the clock-recovery circuit is noisy, the sampling time fluctuates around its mean value set at the bit center. These fluctuations are called timing jitter.

If the probability density function of the timing jitter, $\Delta t$, is assumed to be Gaussian, it is described by:

$$p(\Delta t) = \frac{1}{\tau_j \sqrt{2\pi}} \exp\left(-\frac{\Delta t^2}{2\tau_j^2}\right),$$

where $\tau_j$ is the standard deviation of $\Delta t$. The probability density of current fluctuation, $\Delta i_j$ is then:

$$p(\Delta i_j) = (\pi b \Delta i_j I_1)^{-1/2} \exp\left(-\frac{\Delta i_j}{b I_1}\right),$$

where

$$b = \frac{4}{3}(\pi^2 - 6)(B\tau_j)^2.$$

The receiver sensitivity is then:

$$\overline{P}_{rec}(b) = \frac{\sigma_T Q}{R} \frac{1 - b/2}{(1 - b/2)^2 - b^2 Q^2/2},$$

94

and the power penalty is:

$$\delta_j = 10\log_{10}\frac{\overline{P}_{rec}(b)}{P_{rec}(0)} = 10\log_{10}\left(\frac{1-b/2}{(1-b/2)^2 - b^2 Q^2/2}\right).$$

Fig. 7.5 plots power penalty as a function of the parameter $B\tau_j$, which is the fraction of the bit period over which the decision time fluctuates. It can be seen that a 2 dB power penalty occurs for $B\tau_j = 0.16$.
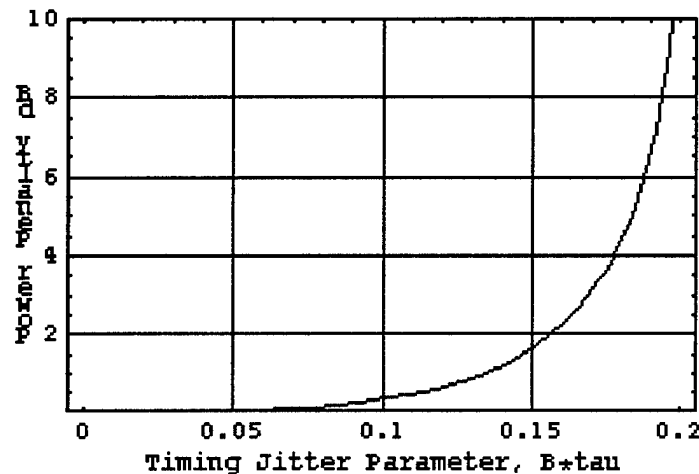


Fig. 7.5 Power penalty versus the timing jitter parameter $B\tau_j$.

## *Orthogonal Codes: Hub Systems:*

A high speed hub system is dependent on the capability of recognizing and locking-on to codes which either define a channel or define a user. Three code constructions are analyzed: the hyperbolic congruence codes (Table 7.1), the quadratic congruence codes (Table 7.2) and the Welch-Costas codes (Table 7.3) - all for $p = 11$.

Table 7.1
Hyperbolic Congruence Code, p=11, "1" Positionings

| Frame | #1 | #2 | #3 | #4 | #5 | #6 | #7 | #8 | #9 | #10 |
|-------|----|----|----|----|----|----|----|----|----|-----|
| 1 | 1 | 2 | 3 | 4 | 5 | 6 | 7 | 8 | 9 | 10 |
| 2 | 6 | 1 | 7 | 2 | 8 | 3 | 9 | 4 | 10 | 5 |
| 3 | 4 | 8 | 1 | 5 | 9 | 2 | 6 | 10 | 3 | 7 |
| 4 | 3 | 6 | 9 | 1 | 4 | 7 | 10 | 2 | 5 | 8 |
| 5 | 9 | 7 | 5 | 3 | 1 | 10 | 8 | 6 | 4 | 2 |
| 6 | 2 | 4 | 6 | 8 | 10 | 1 | 3 | 5 | 7 | 9 |
| 7 | 8 | 5 | 2 | 10 | 7 | 4 | 1 | 9 | 6 | 3 |
| 8 | 7 | 3 | 10 | 6 | 2 | 9 | 5 | 1 | 8 | 4 |
| 9 | 5 | 10 | 4 | 9 | 3 | 8 | 2 | 7 | 1 | 6 |
| 10 | 10 | 9 | 8 | 7 | 6 | 5 | 4 | 3 | 2 | 1 |

| Frame | #1 | #2 | #3 | #4 | #5 | #6 | #7 | #8 | #9 | #10 |
|---|---|---|---|---|---|---|---|---|---|---|
| | | | | Table 7.2 | | | | | | |
| | | | Quadratic Congruence Code, p=11, "1" Positionings | | | | | | | |
| 1 | 1 | 2 | 3 | 4 | 5 | 6 | 7 | 8 | 9 | 10 |
| 2 | 3 | 6 | 9 | 1 | 4 | 7 | 10 | 2 | 5 | 8 |
| 3 | 6 | 1 | 7 | 2 | 8 | 3 | 9 | 4 | 10 | 5 |
| 4 | 10 | 9 | 8 | 7 | 6 | 5 | 4 | 3 | 2 | 1 |
| 5 | 4 | 8 | 1 | 5 | 9 | 2 | 6 | 10 | 3 | 7 |
| 6 | 10 | 9 | 8 | 7 | 6 | 5 | 4 | 3 | 2 | 1 |
| 7 | 6 | 1 | 7 | 2 | 8 | 3 | 9 | 4 | 10 | 5 |
| 8 | 3 | 6 | 9 | 1 | 4 | 7 | 10 | 2 | 5 | 8 |
| 9 | 1 | 2 | 3 | 4 | 5 | 6 | 7 | 8 | 9 | 10 |

| Frame | #1 | #2 | #3 | #4 | #5 | #6 | #7 | #8 | #9 | #10 |
|---|---|---|---|---|---|---|---|---|---|---|
| | | | | Table 7.3 | | | | | | |
| | | | Welch-Costas Code, p=11, "1" Positionings | | | | | | | |
| 1 | 2 | 4 | 6 | 8 | 10 | 1 | 3 | 5 | 7 | 9 |
| 2 | 4 | 8 | 1 | 5 | 9 | 2 | 6 | 10 | 3 | 7 |
| 3 | 8 | 5 | 2 | 10 | 7 | 4 | 1 | 9 | 6 | 3 |
| 4 | 5 | 10 | 4 | 9 | 3 | 8 | 2 | 7 | 1 | 6 |
| 5 | 10 | 9 | 8 | 7 | 6 | 5 | 4 | 3 | 2 | 1 |
| 6 | 9 | 7 | 5 | 3 | 1 | 10 | 8 | 6 | 4 | 2 |
| 7 | 7 | 3 | 10 | 6 | 2 | 9 | 5 | 1 | 8 | 4 |
| 8 | 3 | 6 | 9 | 1 | 4 | 7 | 10 | 2 | 5 | 8 |
| 9 | 6 | 1 | 7 | 2 | 8 | 3 | 9 | 4 | 10 | 5 |
| 10 | 1 | 2 | 3 | 4 | 5 | 6 | 7 | 8 | 9 | 10 |

Using a Fourier and inverse Fourier wedges, auto-correlations, cross-correlations and auto-correlations in the presence of another code are shown in Fig.s 7.6, 7.7 and 7.8 for the hyperbolic congruence, quadratic congruence and the Welch-Costas codes. What is shown is that the optical method performs well in the interfering presence of only one other code. The inferior cross-correlation performance of the Welch-Costas code (Fig. 7.8C) is to be expected.

Fig.s 7.9, 7.10 and 7.11 show the identification/recognition of 4 codes using 2-D Fourier, 2D-inverse Fourier and filter optics for the hyperbolic congruence, quadratic congruence and Welch-Costas codes, respectively. Again, the optics method performs well in identifying/recognizing 4 codes. However, quite a different picture is provided by the following:

Fig.s 7.12-7.16 show 2D-auto-correlations of the hyperbolic congruence code #1 with codes #1+...+#2, #1+...+#3, #1+...#4, #1+...+#5 and #1+...+#6. Fig.s show 1D-auto-correlations of the #1 code with Code #1 with codes #1+...+#2, #1+...+#3, #1+...+#4, #1+...+#5, #1+...+#6, #1+...+#7, #1+...+#8, #1+...+#9, and #1+...+#10.

These results clearly show that the decision-making capability of the optical method is finally overwhelmed by the presence of the other orthogonal codes.

The reason for this ultimately poor performance is inherent in the optical method. Fourier optics is a global method and there is no filtering prior to the performance of the identifying transformations. The optical method is a *global (in time)* matched filtering method. Better performance can be obtained with a *local (in time)* matched filtering method which screens (i.e. blocks) the presence of other nonlocal codes. Such a method would involve electronic on-off switching.
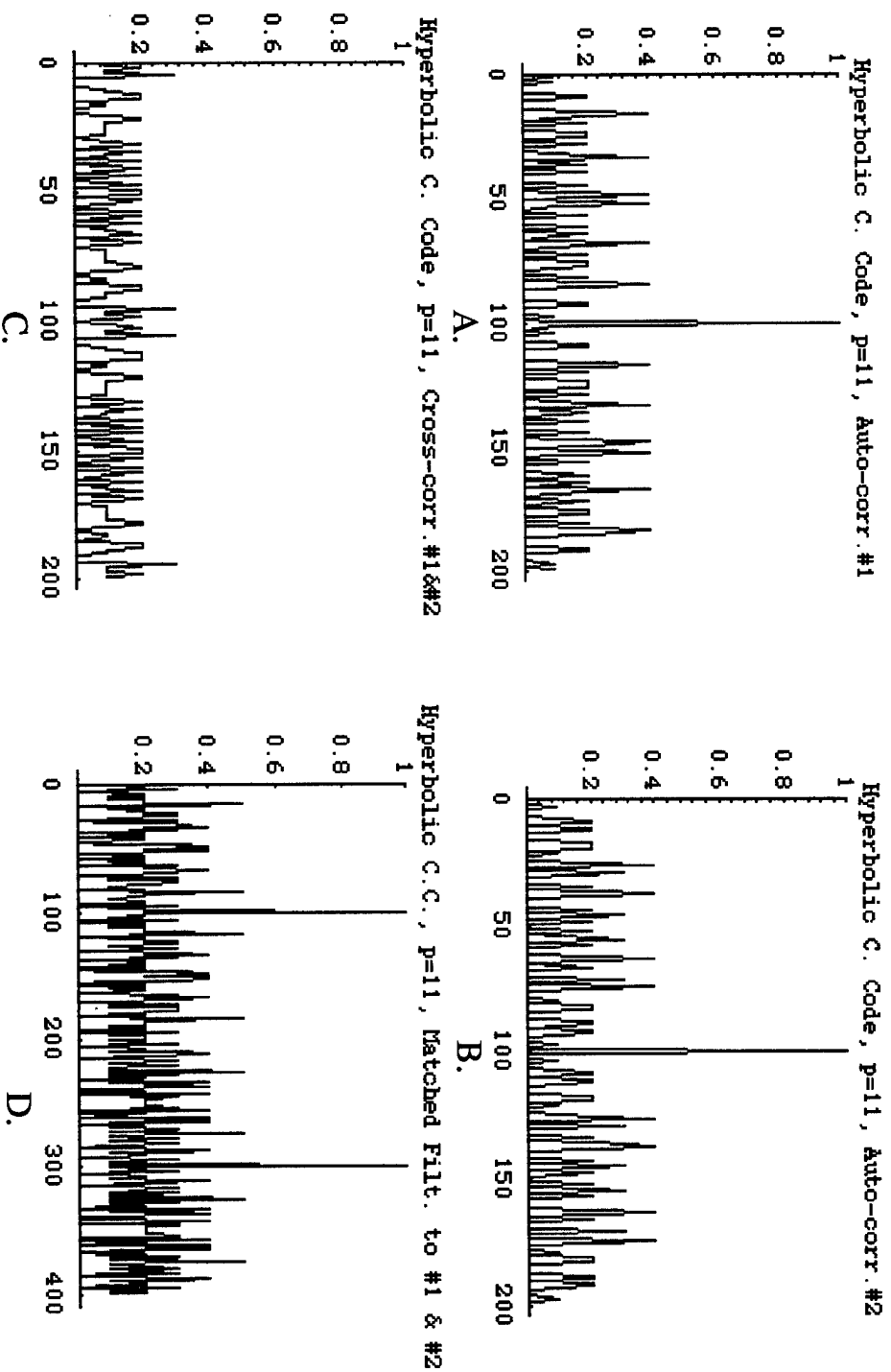
Fig. 7.6 A. Auto-correlation of Hyperbolic Congruence Code, $p = 11$, Code #1 using a wedge Fourier Transform and inverse Fourier Transform.
B. Auto-correlation of Hyperbolic Congruence Code, $p = 11$, Code #2 using a wedge Fourier Transform and inverse Fourier Transform.
C. Cross-correlation of Hyperbolic Congruence Code, $p = 11$, Codes #1 & #2 using a wedge Fourier Transform and inverse Fourier Transform.
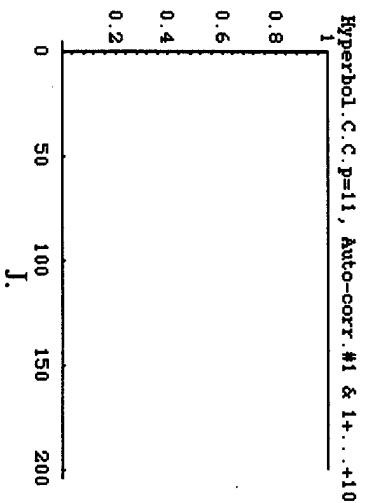D. Identification of Hyperbolic Congruence Codes #1 and #2 in noise using Fourier optics and filters.
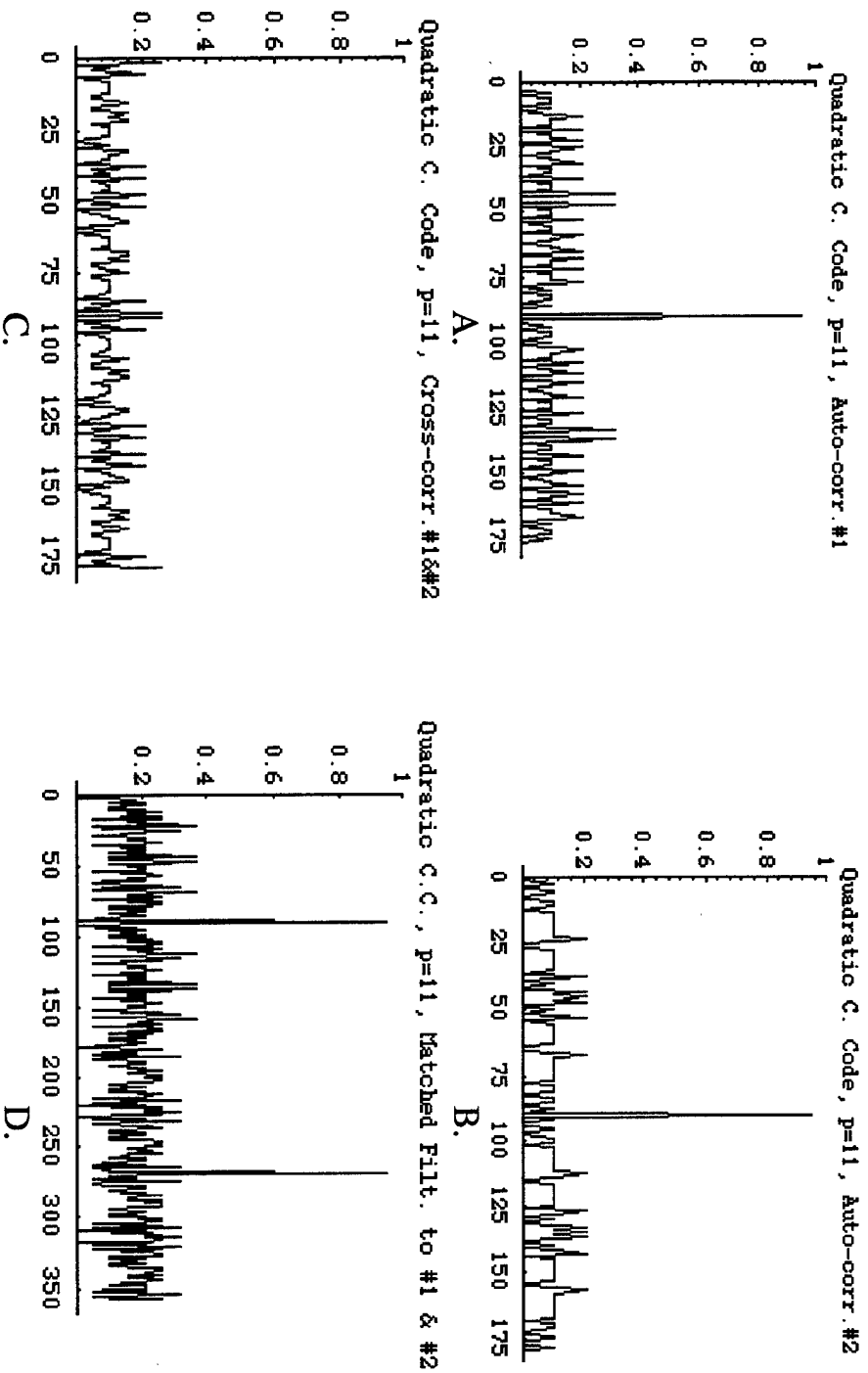
Fig. 7.7 A. Auto-correlation of Quadratic Congruence Code, $p$ = 11, Code #1 using a wedge Fourier Transform and inverse Fourier Transform.
B. Auto-correlation of Quadratic Congruence Code, $p$ = 11, Code #2 using a wedge Fourier Transform and inverse Fourier Transform.
C. Cross-correlation of Quadratic Congruence Code, $p$ = 11, Codes #1 & #2 using a wedge Fourier Transform and inverse Fourier Transform.
D. Identification of Quadratic Congruence Codes #1 and #2 in noise using Fourier optics and filters.
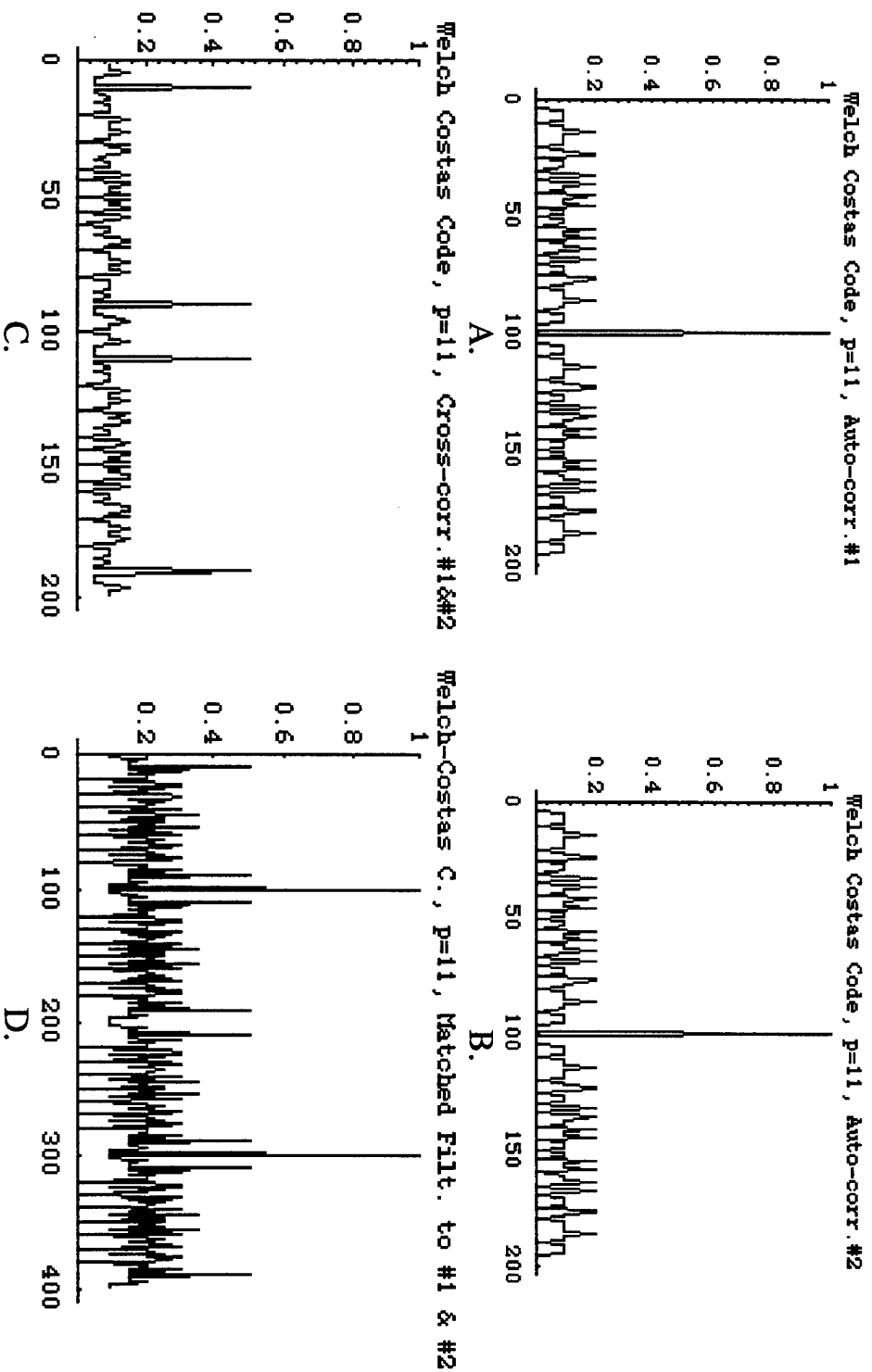
**Fig. 7.8** A. Auto-correlation of Welch-Costas Code, $p = 11$, Code #1 using a wedge Fourier Transform and inverse Fourier Transform.
B. Auto-correlation of Welch-Costas Code, $p = 11$, Code #2 using a wedge Fourier Transform and inverse Fourier Transform.
C. Cross-correlation of Welch-Costas Code, $p = 11$, Codes #1 & #2 using a wedge Fourier Transform and inverse Fourier Transform.
D. Identification of Welch-Costas Codes #1 and #2 in noise using Fourier optics and filters.
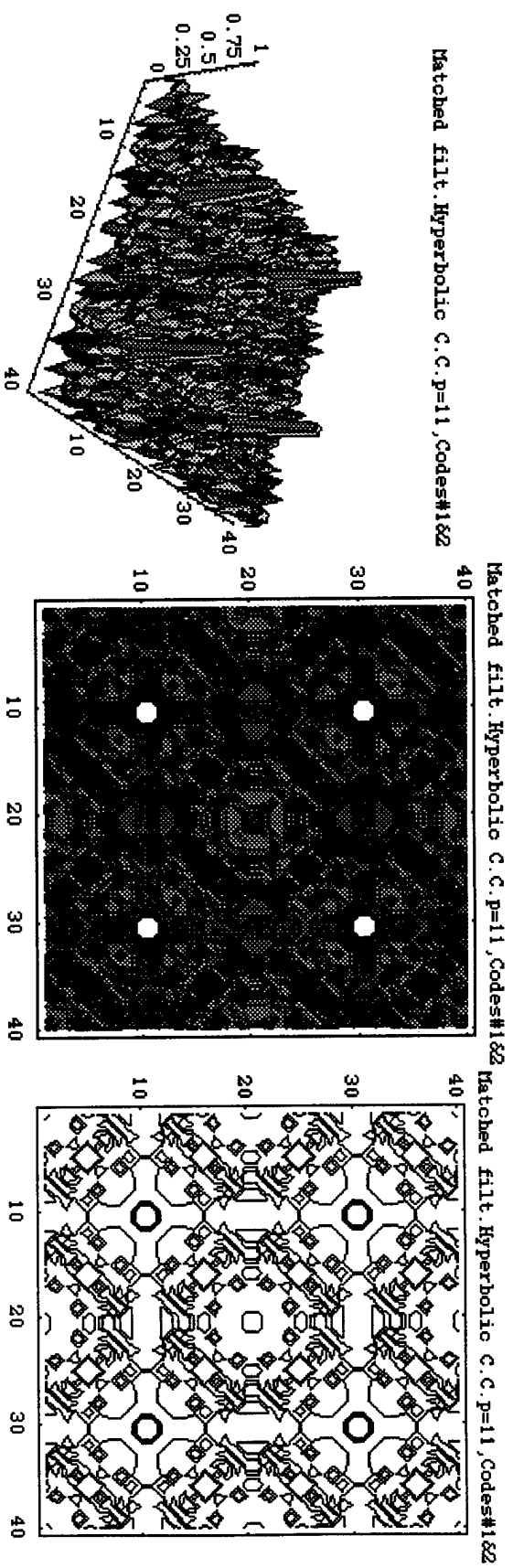
Matched filt.Hyperbolic C.C.p=11,Codes#1&2

Matched filt.Hyperbolic C.C.p=11,Codes#1&2

Matched filt.Hyperbolic C.C.p=11,Codes#1&2

Fig. 7.9

Matched filter identification of Hyperbolic Congruence Codes, $p = 11$, Codes #1, #2, #3 and #4 using a 2D-Fourier Transform (double cylindrical lens),

A. Matched filter identification of Hyperbolic Congruence Codes, $p = 11$, Codes #1, #2, #3 and #4 using a 2D-Fourier Transform (double cylindrical lens), inverse Fourier Transform and filters.

B. Same data as A, but viewed from above as a contour plot with shading.

C. Same data as A and B, but viewed from above as a contourplot without shading.

Matched filt.Quadratic C.C.p=11,Codes#1&2

Matched filt.Quadratic C.C.p=11,Codes#1&2

Matched filt.Quadratic C.C.p=11,Codes#1&2

Fig. 7.10
A. Matched filter identification of Quadratic Congruence Codes, $p$ = 11, Codes #1, #2, #3 and #4 using a 2D-Fourier Transform (double cylindrical lens), inverse Fourier Transform and filters.
B. Same data as A, but viewed from above as a contour plot with shading.
C. Same data as A and B, but viewed from above as a contourplot without shading.

Matched filt.Welch-Costas C.p=11,Codes#1&2
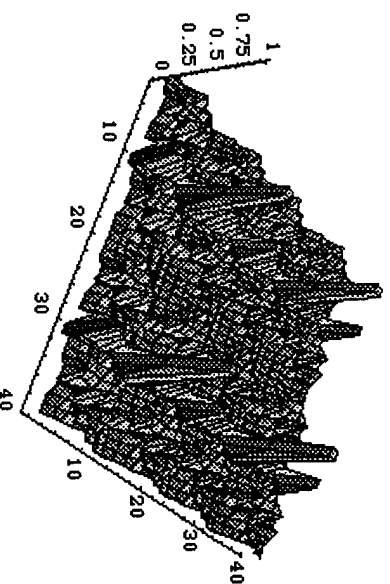
Matched filt.Welch-Costas C.p=11,Codes#1&2
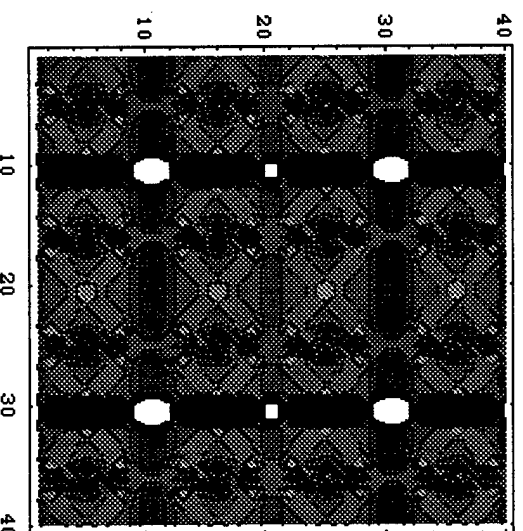
Matched filt.Welch-Costas C.p=11,Codes#1&2
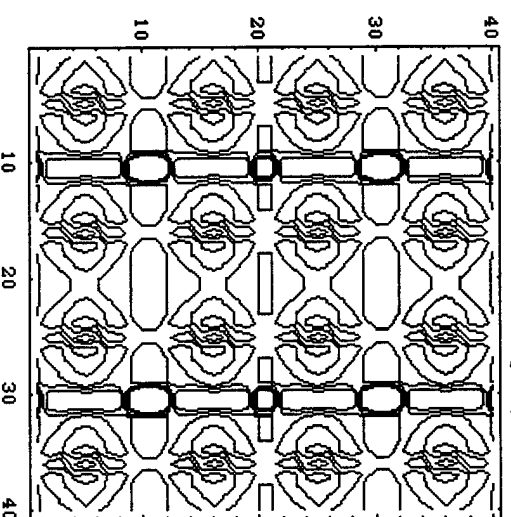
Fig. 7.11

A. Matched filter identification of Welch-Costas Codes, $p = 11$, Codes #1, #2, #3 and #4 using a 2D-Fourier Transform (double cylindrical lens), inverse Fourier Transform and filters.

B. Same data as A, but viewed from above as a contour plot with shading.

C. Same data as A and B, but viewed from above as a contourplot without shading.

Auto-Corr.Hyperbol.C.C.p=11,#1 & #1+...+#2

Auto-Corr.Hyperbol.C.C.p=11,#1 & #1+...+#2

Auto-Corr.Hyperbol.C.C.p=11,#1 & #1+...+#2
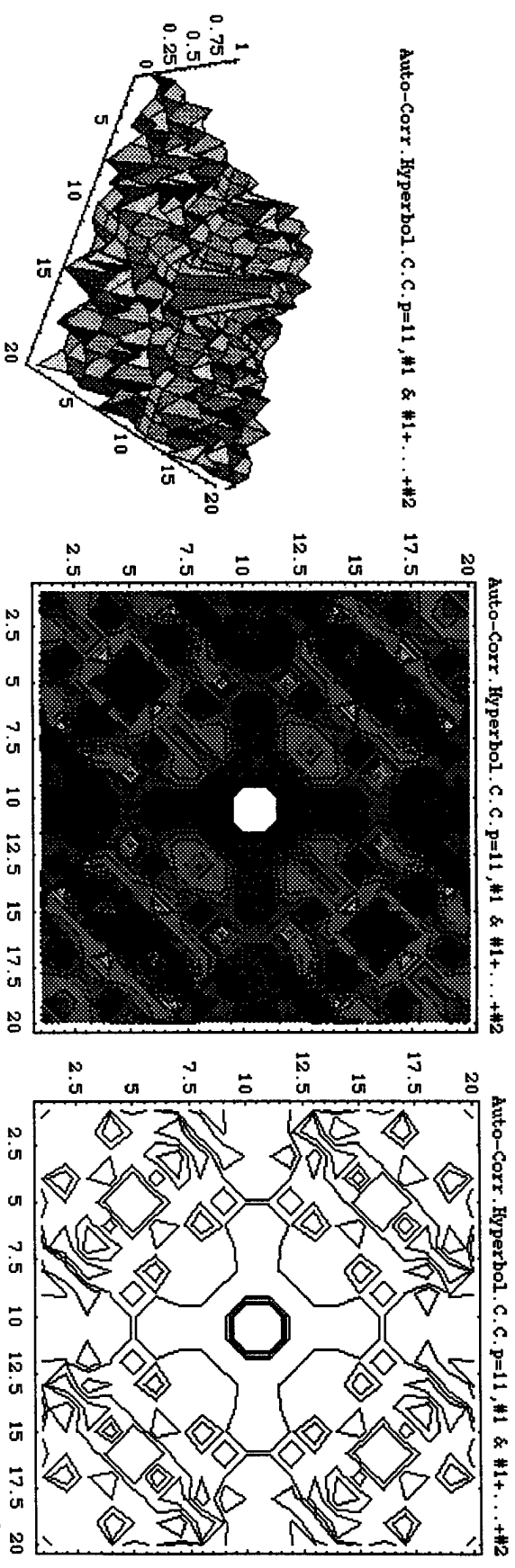
Fig. 7.12 A. Matched filter identification of Hyperbolic Congruence Code, $p = 11$, Code #1, in the presence of Codes #1...#2 using a 2D-Fourier Transform (double cylindrical lens), inverse Fourier Transform and filters.
B. Same data as A, but viewed from above as a contour plot with shading.
C. Same data as A and B, but viewed from above as a contourplot without shading.

Auto-Corr.Hyperbol.C.C.p=11,#1 & #1+...+#3



Auto-Corr.Hyperbol.C.C.p=11,#1 & #1+...+#3



Auto-Corr.Hyperbol.C.C.p=11,#1 & #1+...+#3
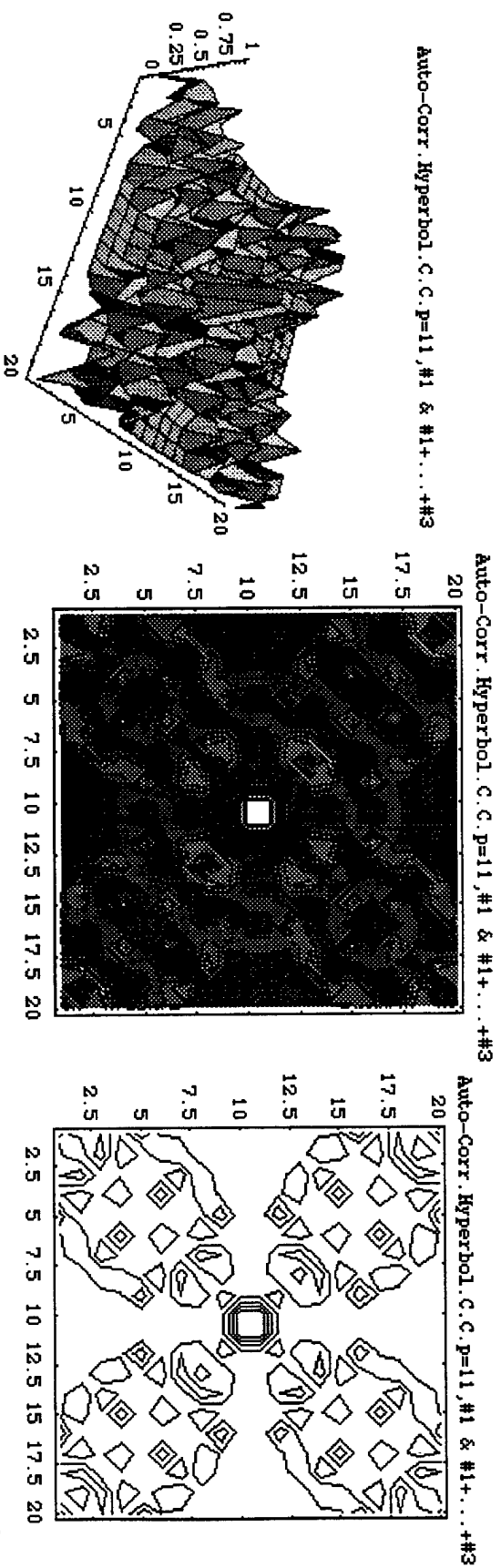


Fig. 7.13 A. Matched filter identification of Hyperbolic Congruence Code, $p = 11$, Code #1, in the presence of Codes #1....#3 using a 2D-Fourier Transform (double cylindrical lens), inverse Fourier Transform and filters.
B. Same data as A, but viewed from above as a contour plot with shading.
C. Same data as A and B, but viewed from above as a contourplot without shading.

Auto-Corr.Hyperbol.C.C.p=11,#1 & #1+...+#4



Auto-Corr.Hyperbol.C.C.p=11,#1 & #1+...+#4

Auto-Corr.Hyperbol.C.C.p=11,#1 & #1+...+#4
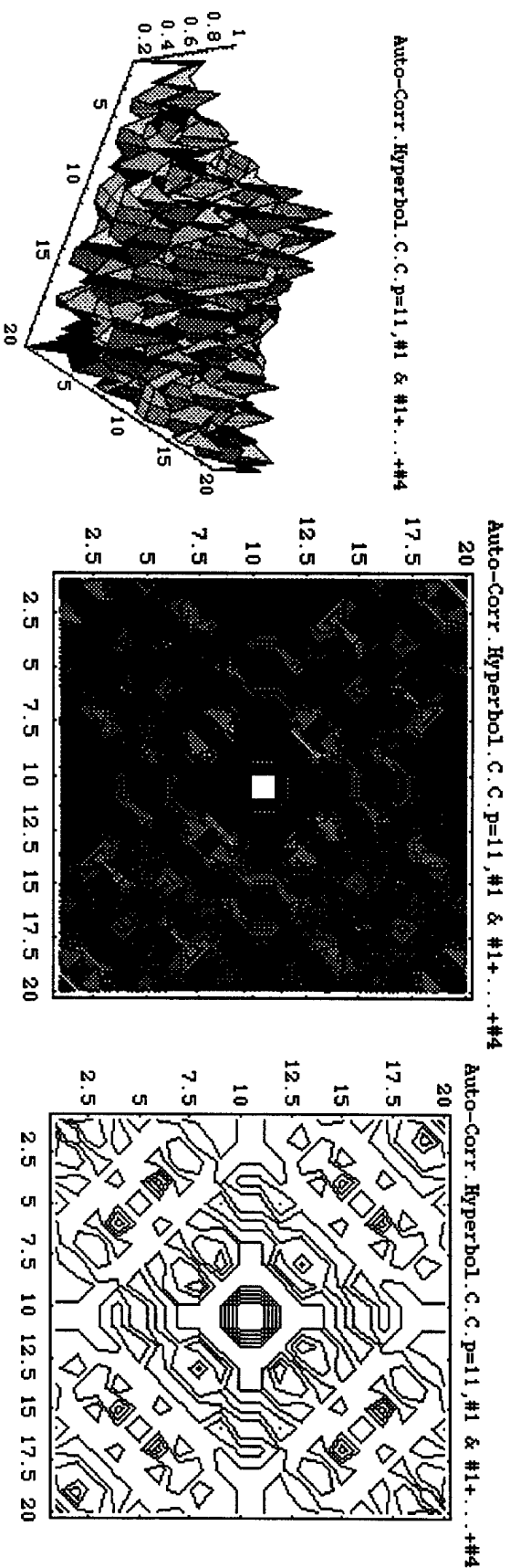
Fig. 7.14 A. Matched filter identification of Hyperbolic Congruence Code, $p = 11$, Code #1, in the presence of Codes #1....#4 using a 2D-Fourier Transform (double cylindrical lens), inverse Fourier Transform and filters.
B. Same data as A, but viewed from above as a contour plot with shading.
C. Same data as A and B, but viewed from above as a contourplot without shading.

Auto-Corr.Hyperbol.C.C.p=11,#1 & #1+...+#5

Auto-Corr.Hyperbol.C.C.p=11,#1 & #1+...+#5

Auto-Corr.Hyperbol.C.C.p=11,#1 & #1+...+#5
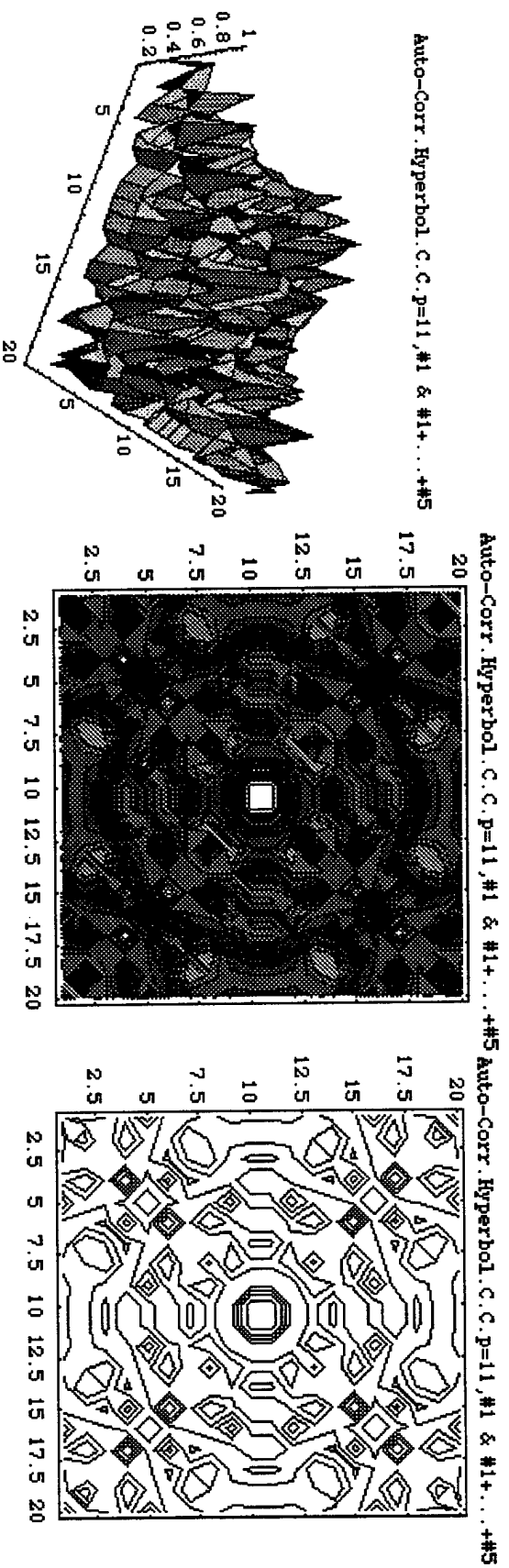
Fig. 7.15 A. Matched filter identification of Hyperbolic Congruence Code, $p = 11$, Code #1, in the presence of Codes #1....#5 using a 2D-Fourier Transform (double cylindrical lens), inverse Fourier Transform and filters.
B. Same data as A, but viewed from above as a contour plot with shading.
C. Same data as A and B, but viewed from above as a contourplot without shading.

Auto-Corr.Hyperbol.C.C.p=11,#1 & #1+...+#6

Auto-Corr.Hyperbol.C.C.p=11,#1 & #1+...+#6

Auto-Corr.Hyperbol.C.C.p=11,#1 & #1+...+#6
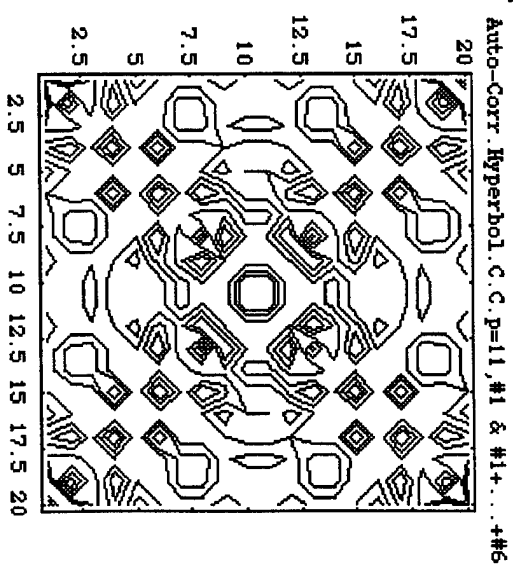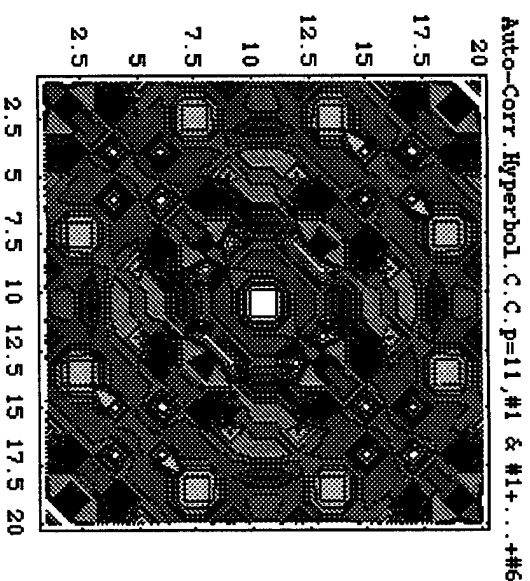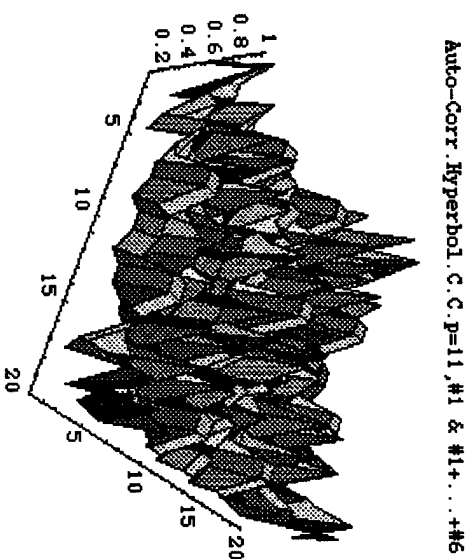
Fig. 7.16 A. Matched filter identification of Hyperbolic Congruence Code, $p$ = 11, Code #1, in the presence of Codes #1...#6 using a 2D-Fourier Transform (double cylindrical lens), inverse Fourier Transform and filters.

B. Same data as A, but viewed from above as a contour plot with shading.

C. Same data as A and B, but viewed from above as a contourplot without shading.

Hyperbol.C.C.p=11, Auto-corr.#1 & 1
A.

Hyperbol.C.C.p=11, Auto-corr.#1 & 1+2
B.

Hyperbol.C.C.p=11, Auto-corr.#1 & 1+2+3
C.

Hyperbol.C.C.p=11, Auto-corr.#1 & 1+...+4
D.

Hyperbol.C.C.p=11, Auto-corr.#1 & 1+...+5
E.

Hyperbol.C.C.p=11, Auto-corr.#1 & 1+...+6
F.

Hyperbol.C.C.p=11, Auto-corr.#1 & 1+...+7
G.

Hyperbol.C.C.p=11, Auto-corr.#1 & 1+...+8
H.

Hyperbol.C.C.p=11, Auto-corr.#1 & 1+...+9
I.

Hyperbol.C.C.p=11, Auto-corr.#1 & 1+...+10

1
0.8
0.6
0.4
0.2
0

0    50    100    150    200

J.
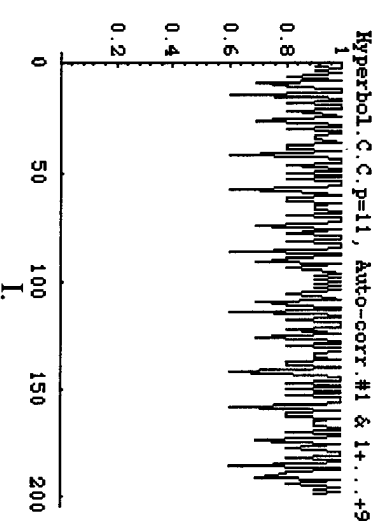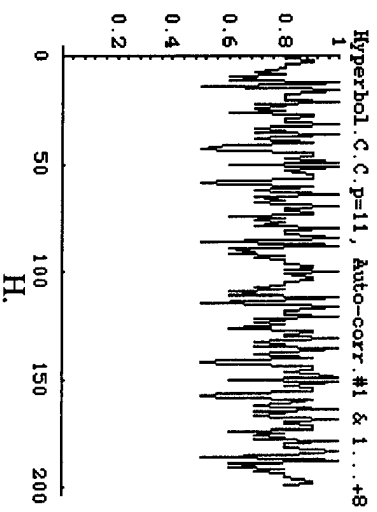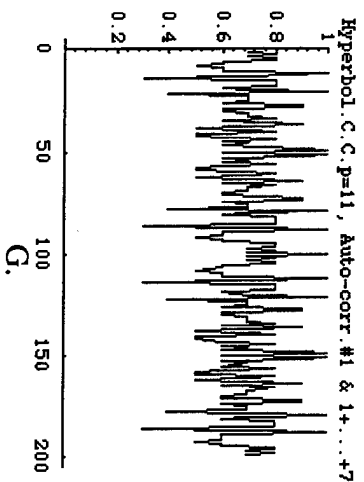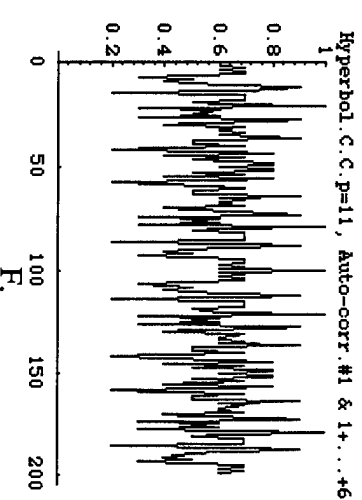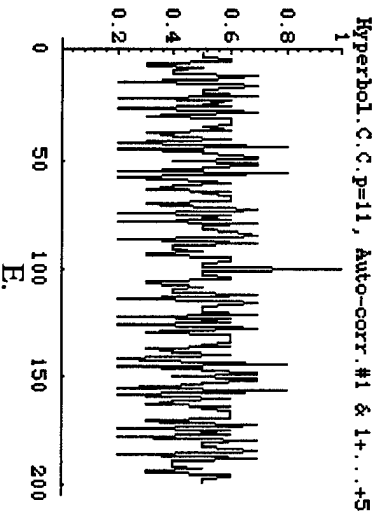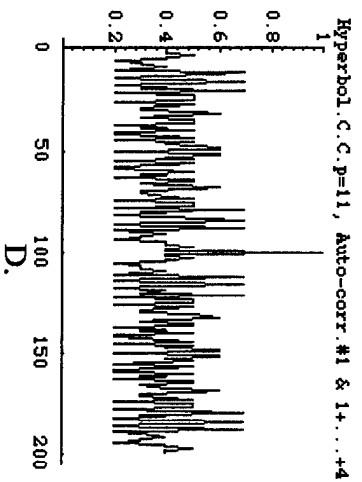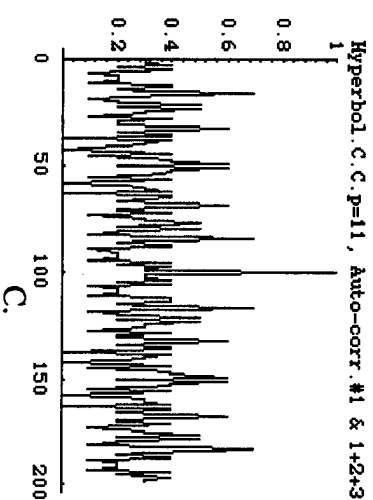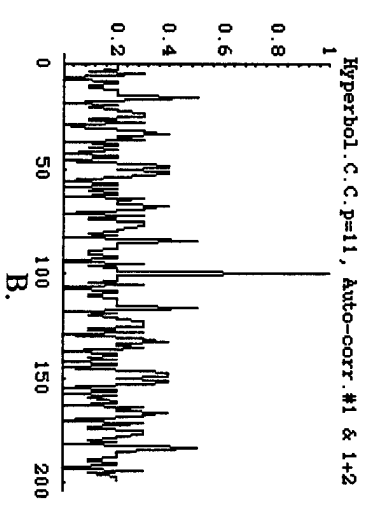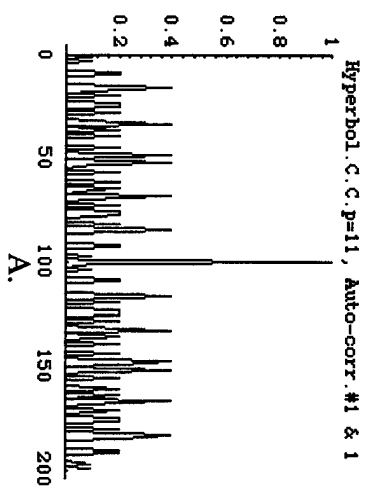
Fig. 7.17 A. Auto-correlation of Hyperbolic Congruence Code, $p = 11$, Code #1 using a wedge Fourier Transform and inverse Fourier Transform against itself, Code #1.

B. Auto-correlation of Hyperbolic Congruence Code, $p = 11$, Code #1 against Codes #1+...+#2.

C. Auto-correlation of Hyperbolic Congruence Code, $p = 11$, Code #1 against Codes #1+...+#3.

D. Auto-correlation of Hyperbolic Congruence Code, $p = 11$, Code #1 against Codes #1+...+#4.

E. Auto-correlation of Hyperbolic Congruence Code, $p = 11$, Code #1 against Codes #1+...+#5.

F. Auto-correlation of Hyperbolic Congruence Code, $p = 11$, Code #1 against Codes #1+...+#6.

G. Auto-correlation of Hyperbolic Congruence Code, $p = 11$, Code #1 against Codes #1+...+#7.

H. Auto-correlation of Hyperbolic Congruence Code, $p = 11$, Code #1 against Codes #1+...+#8.

I. Auto-correlation of Hyperbolic Congruence Code, $p = 11$, Code #1 against Codes #1+...+#9.

J. Auto-correlation of Hyperbolic Congruence Code, $p = 11$, Code #1 against Codes #1+...+#10.

## 8.0 Shannon's Theorem Constraints

Shannon's channel capacity theorem gives the relation:

$$\frac{C}{B} = \log_2\left(1 + \frac{RE_b}{N_0 B}\right),$$

where $E_b$ is the energy per bit: $E_b = S/R$, $S$ is the average power, $R$ is the data rate in information bits per second, $N_0$ is noise in Watts/Hertz and $N = N_0 B$. $B$ is general bandwidth.

Shannon's theorem also requires:

$$\frac{R}{B} < \frac{C}{B}.$$

For maximum data rate, we seek the maximum spectral bit rate, $r$, in bits per second per Hertz:

$$r = \frac{R}{W},$$

commensurate with an acceptable BER, which means, applying Shannon's theorem, that:

$$r < \log_2\left(1 + r\frac{E_b}{N_0}\right) \quad or \quad \frac{E_b}{N_0} > \frac{2^r - 1}{r}.$$

Now in the case of (1) a WDM channel or (2) multibit pulses or packets, the analogy of optical fiber transmissions to RF communications is close. If the fiber has a maximum bandwidth $B$, then a decision must be made concerning whether that bandwidth is used by multibit packets - we call that a "parallel" bandwidth, $B_p$ - or by different WDM channels - we call that "sequential" bandwidth, $B_s$. (An analogous procedure is overseen by the Federal Communications Commission in allocating blocks of RF bandwidth to individual users.)

Therefore, if there is less energy per bit, then $B_p$ is high. This case may be contrasted with that of less delay per bit, which means that the sampling bandwidth, $B_s$, is high. But there is a finite bandwidth, $B$, and the allocated bandwidth $B_p$ must not encroach on the allocated $B_s$ bandwidth. The general bandwidth, $B$, is thus related to the "WDM bandwidth" and the "multibit packet bandwidth", by:

$$B = B_s + B_p.$$

The trades that can be made - up to the Shannon capacity boundary limit, $R = C$, are shown in Fig. 1. Given a constant general bandwidth $B$, there is a constant condition represented by:

$$\frac{R}{B} \cdot \frac{N_0}{E_b} = const.,$$

which in the case of WDM channels with multibit packets, is:

$$\frac{R}{\left(B_p + B_s\right)} \cdot \frac{N_0}{E_b} = \text{const.}$$

The following is thus indicated:

The spectral bit rate, $r$, can be increased to approach a maximum set by the Shannon limit (i.e., a maximum with an acceptable BER). Given a constant general bandwidth $B$, with allocation to either WDM usage, or, multibit packet usage, or both, such that $B = B_p + B_s$, then:

(1) The data rate, $R$, can be increased, but, in compensation, $N_0/E_b$ must be decreased (i.e., $E_b/N_0$ must be increased).

Alternatively, the following method gives better BER, but pays a price in spectral data rate:

(2) $N_0/E_b$ can be increased (i.e., $E_b/N_0$ can be decreased), but, in compensation, the data rate, $R$, must be decreased.

As the objective is high data rate, method (1) is preferred.

## Bandwidth Efficiency
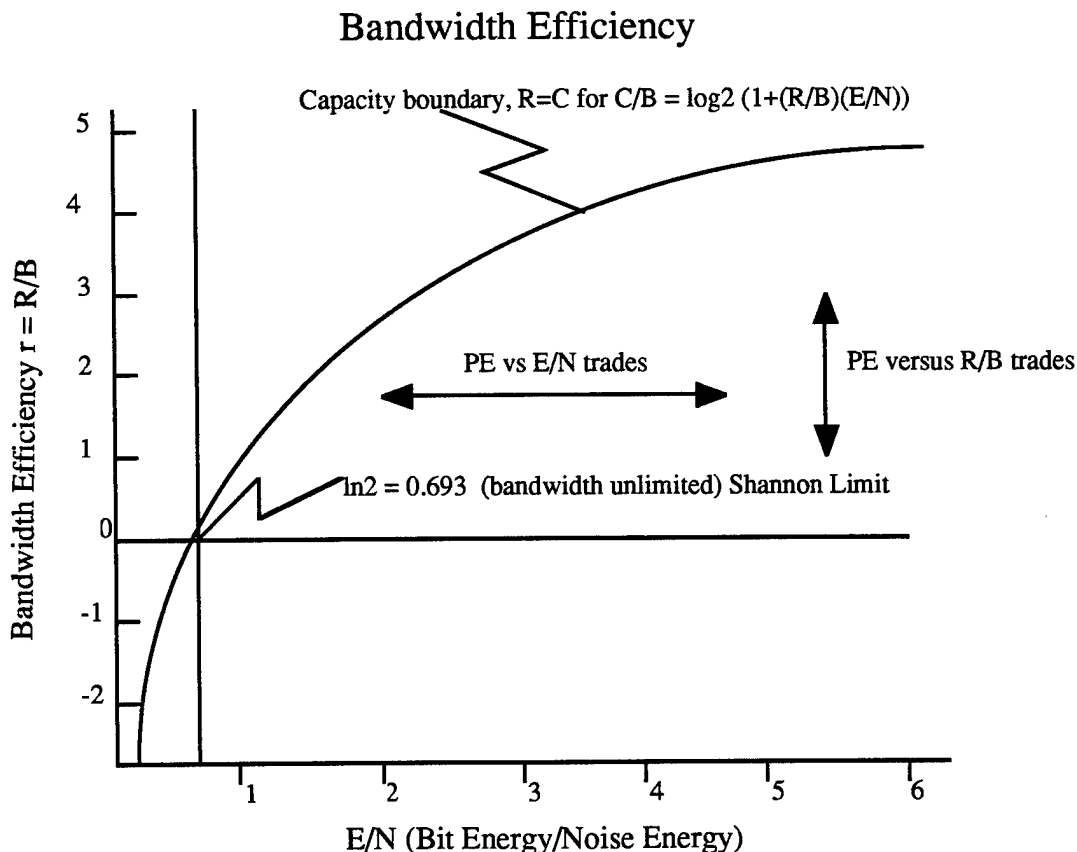


Fig.8.1

$B = \text{Bandwidth} = B_p + B_s$,

$B_p = $ parallel bandwidth or bandwidth per packet for multibit packets,

$B_s = $ sequential bandwidth or WDM bandwidth,

$N = $ noise energy,

112

$$R = \text{bit rate},$$
$$r = \text{bandwidth efficiency} = R/B,$$
$$C = \text{channel capacity}.$$

The objective is to maximize $r$ under the $R = C$ constraint The optimizing conditions are:

$$\frac{R}{B} \cdot \frac{N}{E} = \frac{R}{\left(B_p + B_s\right)} \cdot \frac{N}{E} = \text{const.}$$

## Avalanche Photodiode Receivers

Avalanche photodiode (APD) receivers provide a higher SNR for the same incident power due to an internal gain which increases the photocurrent by a multiplication factor, $M$:

$$I_p = MRP_{in},$$

where $I_p$ is the photocurrent, $P_{in}$ is the incident optical power, $R$ is the responsivity of the photodetector ($= h\nu/q \times$ the quantum efficiency) and $M$ is a multiplication factor. In the case of APD receivers, besides the shot noise from the generation of primary electron-hole pairs, there is also that associated with the generation of secondary electron-hole pairs.

The total shot noise variance for an APD is:

$$\sigma_s^2 = 2qM^2 F_A\left(RP_{in} + I_d\right)\Delta f,$$

where $I_d$ is the dark current, $\Delta f$ is bandwidth and $F_A$ is the excess noise factor of the APD:

$$F_A(M) = k_A M + (1 - k_A)(2 - 1/M).$$

In this last equation, $k_A = \alpha_h/\alpha_e$ if $\alpha_h < \alpha_e$, but $k_A = \alpha_e/\alpha_h$ when $\alpha_h > \alpha_e$, where $\alpha_e$ and $\alpha_h$ are defined by the electron current and the hole current:

$$\frac{di_e}{dx} = \alpha_e i_e + \alpha_h i_h,$$

$$-\frac{di_h}{dx} = \alpha_e i_e + \alpha_h i_h$$

The following Fig. 8.2 shows the dependence of the excess noise factor, $F_A$, as a function of the APD gain, $M$, and of the dimensionless parameter, $k_A$.[12] This Figure shows that for the minimum excess noise factor, the ratio $k_A$ should be as small as possible.

---

[12] Webb, P.P., McIntyre, R.J. & Conradi, J., *RCA Rev.*, 35, 235, 1974.
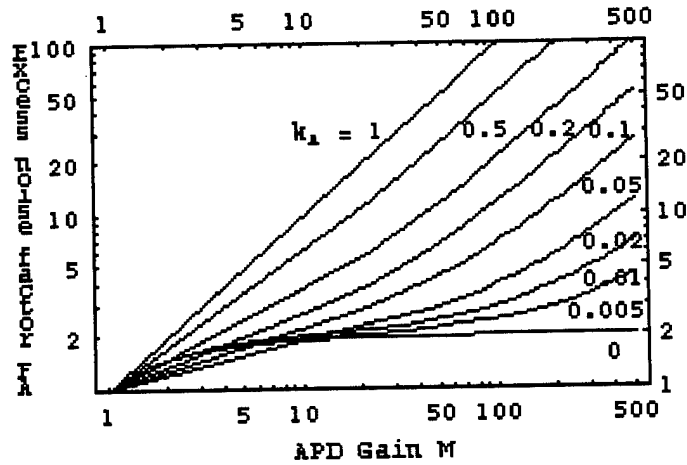
Fig. 8.2 Excess noise factor $F_A$ as a function of the average APD gain M for the following values of the ionization-coefficient ratio $k_A$ (top to bottom): 1, 0.5, 0.2, 0.1, 0.05, 0.02, 0.01, 0.005 and 0.

The SNR for APD receivers is optimum for an optimum, $M_{opt}$, of the APD gain M defined:

$$M_{opt} \approx \left( \frac{4k_B T F_n}{k_A q R_L (R P_{in} + I_d)} \right)^{1/3} .$$

The following Fig. 8.3 shows that $M_{opt}$ decreases with a decrease in $P_{in}$ and is also sensitive to the coefficient ratio, $k_A$.[13] This Figure was constructed for $R_L = 1$ kohm, $F_n = 2$, $R = 1$ A/W and $I_d = 2$ nA and for a 1.55 µm InGaAs receiver.
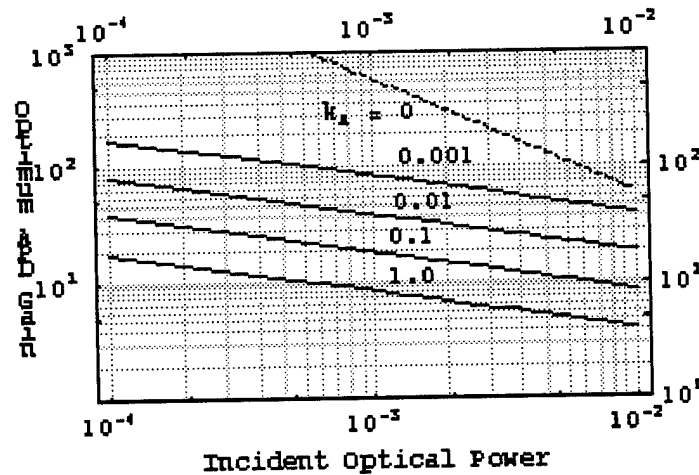


Fig. 8.3 Optimum APD gain $M_{opt}$ as a function of the incident optical power $P_{in}$ for several values of $k_A$: 0 (dashed), 0.001, 0.01, 0.1 and 1.0 (bottom). Parameter values corresponding to a typical 1.55 µm InGaAs APD receiver were used.

---

[13] Agrawal, G.P., *Fibver-Optic Communication Systems*, 2nd Edition, Wiley, NY, 1997.

## Bit Error Rate and Q

The bit error rate (BER) in the Gaussian approximation is:

$$BER = \frac{1}{2} erfc\left(\frac{Q}{\sqrt{2}}\right) \approx \frac{\exp(-Q^2/2)}{Q\sqrt{2\pi}},$$

where Q, for "1" and "0" bits is:

$$Q = \frac{I_1 + I_2}{\sigma_1 + \sigma_2}.$$

The following Fig. 8.4 shows the variation of the BER as a function of the $Q$ parameter.
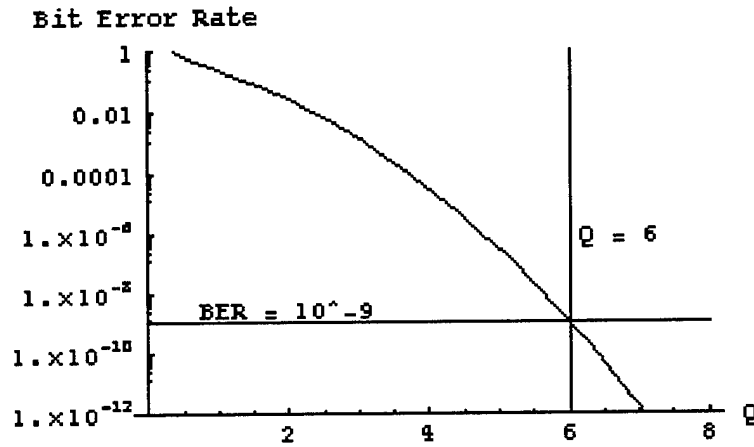
**Bit Error Rate**



Fig. 8.4 Bit-error rate versus the $Q$ parameter. Line at BE = $10^{-9}$ intersects curve at $Q = 6$.

## 8.1 Power Penalties

### 8.1.1

Semiconductor lasers still emit power, $P_0$, in the off state, resulting in a power penalty. If $P_1$ is the on-state power, then an *extinction ratio* is defined as:

$$r_{ex} = P_0/P_1.$$

A definition of receiver sensitivity is:

$$\overline{P}_{rec} = \frac{P_1 + P_0}{2},$$

which permits a definition of the power penalty:

$$\delta_{ex} = 10\log_{10}\left(\frac{\overline{P}_{rec}(r_{ex})}{\overline{P}_{rec}(0)}\right) = 10\log_{10}\left(\frac{1 + r_{ex}}{1 - r_{ex}}\right).$$

The following Fig. 8.1.1 shows the dependence of the power penalty on the extinction ratio. Typically, $r_{ex}$ is below 0.05 and the power penalty is negligible (< 0.4 dB). However, the power penalty can becomes significant if the semiconductor laser is biased above threshold.
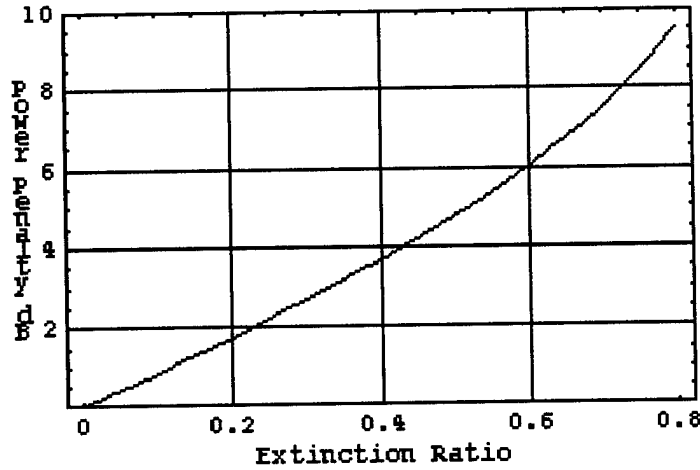


Fig. 8.1.1 Power penalty versus the extinction ratio $r_{ex}$.

## 8.1.2

Light emitted by any transmitter exhibits power fluctuations known as intensity noise. The optical receiver converts power fluctuations into current fluctuations which add to those resulting from shot noise and thermal noise. One approach to an analysis of the composite noise influences on the receiver is to add the variances:

$$\sigma^2 = \sigma_s^2 + \sigma_T^2 + \sigma_I^2,$$

where

$$\sigma_I = R\langle\left(P_{in}^2\right)\rangle^{1/2} = RP_{in}r_I,$$

and

$$r_{in} = \langle\left(\Delta P_{in}^2\right)\rangle^{1/2} / P_{in}$$

is a measure of the noise level of the incident optical signal.

The power penalty, which is the increase in $\overline{P}_{rec}$ when $r_I \neq 0$ is:

$$\delta_I = 10\log_{10}\left[\overline{P}_{rec}(r_I)/\overline{P}_{rec}(0)\right] = -10\log_{10}(1 - r_I^2 Q^2).$$

The following Fig. 8.1.2 shows the power penalty as a function of intensity noise parameter for maintaining $Q = 6$ (i.e., BER = $10^{-9}$).[14] For most optical transmitters $r_I < 0.01$, so the power penalty is negligible (< 0.02 dB). Only if the BER is saturated above the $10^{-9}$ level does the power penalty become substantial, and even infinite.

---

[14] Agrawal, G.P. & Shen, T.M., *Electron. Lett.*, 22, 450, 1986.
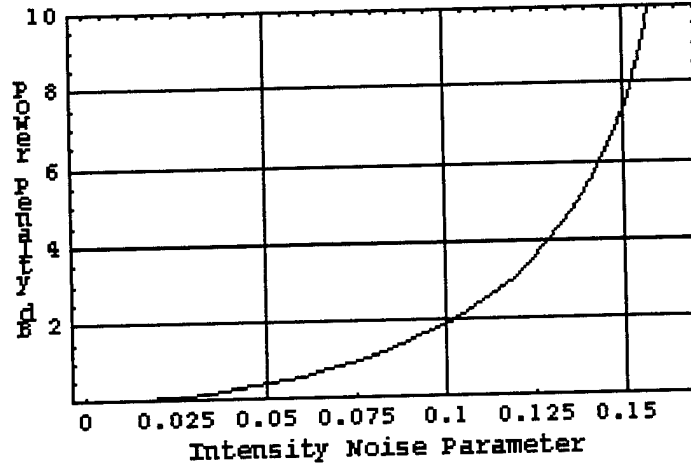
Fig. 8.1.2 Power penalty versus the intensity noise parameter $r_I$.

### 8.1.3

The SNR is also affected by time fluctuations called timing jitter. The SNR is reduced by such fluctuations but can be maintained by increasing the received optical power. This increase is the power penalty induced by the timing jitter.

The current fluctuation induced by the timing jitter is defined as:

$$\Delta i_j = \left(\frac{2\pi^2}{3} - 4\right)(B\Delta t)^2 I_1,$$

where $\Delta i_j$ is the current induced by the timing jitter $\Delta t$ and $B$ is the bit rate. The probability density of the current fluctuations is:

$$p(\Delta i_j) = \frac{1}{\sqrt{\pi b \Delta i_j I_1}} \exp\left(-\frac{\Delta i_j}{b I_1}\right),$$

where

$$b = \left(\frac{4\pi^2}{3} - 8\right)(B\tau_j)^2,$$

and $\tau_j$ is the RMS value, or standard deviation, of $\Delta t$. The receiver sensitivity is then:

$$\overline{P}_{rec}(b) = \left(\frac{\sigma_T Q}{R}\right)\frac{1 - b/2}{(1 - b/2)^2 - b^2 Q^2/2}$$

and the power penalty is given by:

117

$$\delta_j = 10\log_{10}\left(\frac{\overline{P}_{rec}(b)}{\overline{P}_{rec}(0)}\right) = 10\log_{10}\left(\frac{1-b/2}{(1-b/2)^2 - b^2 Q^2/2}\right).$$

The following Fig.8.1.3 shows how the power penalty due to jitter varies with the fraction of the bit period over which the decision time fluctuates - $B\tau_j$.[15] The jitter becomes infinite beyond $B\tau_j$ = 0.2. This analysis assumes Gaussian statistics for the receiver current, but jitter-induced current fluctuations are not Gaussian. More accurate calculations show that a Gaussian approximation underestimates the power penalty due to jitter.
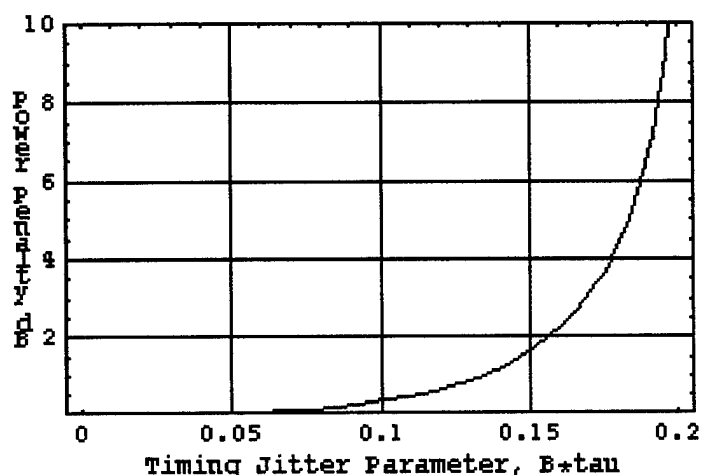


Fig. 8.1.3 Power penalty versus the timing jitter parameter $B\tau_j$.

### 8.1.4

The average optical power corresponding to a BER of $10^{-9}$ is a measure of receiver sensitivity. In the following Fig. 8.1.4 the theoretical quantum limit at the two wavelengths of $\lambda$ = 1.3 $\mu$m and $\lambda$ = 1.55 $\mu$m over bit rates from 100 Mhz to 10 GHz.[16] (Real receivers are expected to be worse by 20 db as compared with the quantum limit.) The Figure shows that as

[15] O'Reilly, J.J., DaRocha, J.R.F. & Schumacher, K., IEE Proc. 132, Pt. J., 309, 1985;

Schumacher, K. & O'Reilly, J.J., Electron. Lett., 23, 718, 1987;

Shen, T.M., Electron. Lett., 22, 1043, 1986;

Lee, T.P., Burrus, C.A., Dentai, A.G. & Ogawa, Electron. Lett., 16, 155, 1980.

[16] Smith, D.R., Hooper, R.C., Smyth, P.P. & Wake, D., Electron Lett., 18, 453, 1982;

Yamada, J., Kawana, A., Miya, T., Nagai, H. & Kimura, T., IEEE J. Quantum Electron. 18, 1537, 1982;

Brain, M.C., Smyth, P.P., Smith, D.R., White, B.R. & Chidghey, P.J., Electron. Lett., 20, 894, 1984;

Snodgrass, M.L. & Klinman, R., J. Lightwave Technol., 2, 968, 1984;

Walker, S.D. & Blank, L.C., Electron. Lett., 20, 808, 1984;

Chen, C.Y., Kasper, B.L., Cox, H.M. & Plourde, J.K., Appl. Phys. Lett., 46, 379, 1985;

Kasper, B.L., Campbell, J.C., Gnauck, A.H., Dentai, A.G. & Talman, J.R., Electron. Lett., 21, 982, 1985;

Kasper, B.L., Campbell, J.C., Talman, J.R., Gnauck, A.H., Bowers, J.E. & Holden, W.S., J. Lightwave Technol., 5, 344, 1987;

Heidemann, R., Scholz, U. & Wedding, B. Electron. Lett., 23, 1030, 1987;

Shikada, M., Fujita, S., Henmi, N., Takano, I., Mito, I., Taguchi, K. & Minemura, K., J. Lightwave Technol., 5, 1488, 1987;

Fujita, S., Kitamura, M., Torika, T., Henmi, N., Yamada, H., Suzaki, T., Takano, I. & Shikada, M., Electron Lett., 25, 702, 1989;

Kitamura, K., Ito, K., Matsuda, H., Kaneko, T. & Haneda, M., Electron Lett., 27, 1435, 1991.

bit rate increases, receiver sensitivity declines. Therefore, in order to obtain a measure of receiver sensitivity performance, test must be conducted over multiple wavelengths.
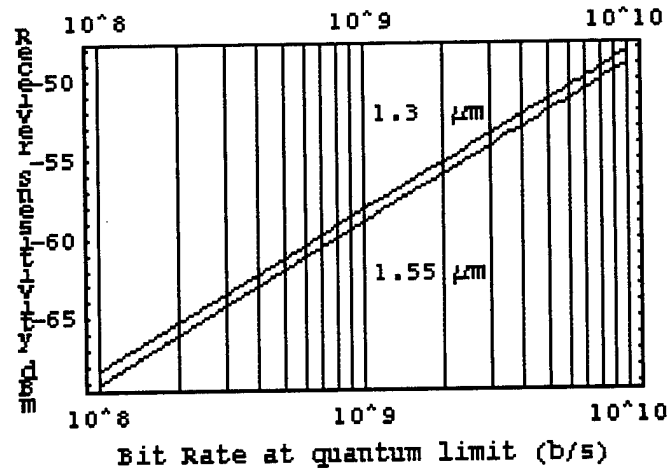


Fig. 8.1.4  The quantum limit of receiver sensitivity for $\lambda = 1.3$ $\mu$m (top) and $\lambda = 1.55$ $\mu$m (bottom). (The quantum limit is defined as BER = $10^{-9}$ or the average number of photons contained within the "1" bit = 20.) Real receivers are expected to be worse by 20 db or more with respect to the quantum limit.

Fig.s 8.1.5 and 8.1.6 illustrate that a demand for a higher BER at constant bit rate must result in a less sensitive receiver. Fig. 8.1.4 compared with Fig.8.1.6 illustrates that a higher bit rate results also in a decline in receiver sensitivity.
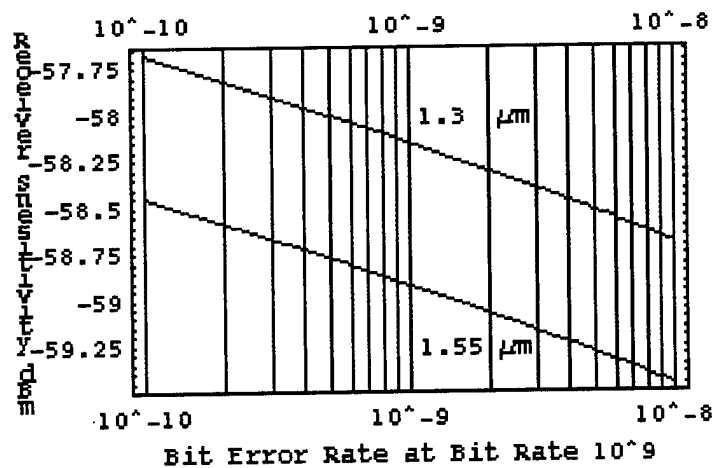


Fig. 8.1.5 Receiver sensitivity at the quantum limit as a function of BER at a bit rate of $10^9$ for $\lambda = 1.3$ $\mu$m (top) and $\lambda = 1.55$ $\mu$m (bottom). The better the BER (to the left), the higher the average photon count within the "1" bit, and the lower the sensitivity.

119
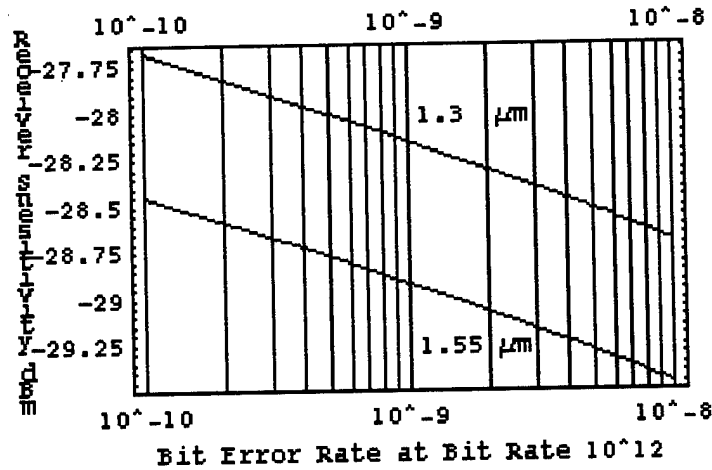
Fig. 8.1.6 Receiver sensitivity at the quantum limit as a function of BER at a bit rate of $10^{12}$ for $\lambda = 1.3$ μm (top) and $\lambda = 1.55$ μm (bottom). Sensitivity degradation has decreased by 30 dB in comparison with the lower bit rate (Fig. 9).

This point is illustrated again in Fig. 8.1.7. This figure shows a decline in the receiver sensitivity at a constant BER (the quantum limit of $10^{-9}$) as a function of increasing bit rate.
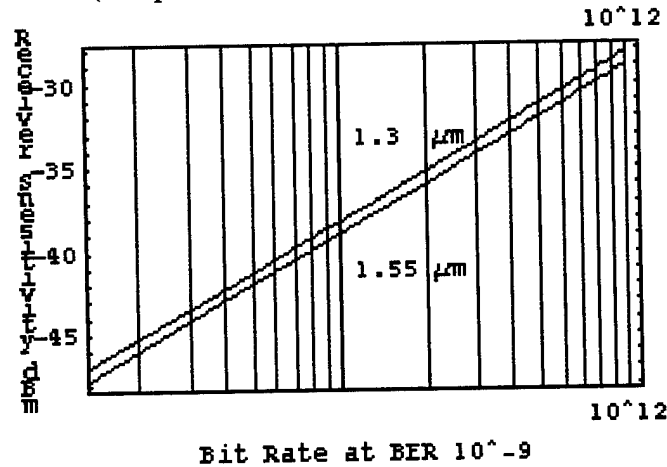


Fig. 8.1.7. Receiver sensitivity at the quantum limit as a function of bit rate at a BER $10^{-9}$ for $\lambda = 1.3$ μm (top) and $\lambda = 1.55$ μm (bottom). Sensitivity degradation decreases as bit rate increases.

## 8.1.5

One result of dispersion-induced pulse broadening is that the pulse energy within the bit slot is reduced when the optical pulse broadens reducing the SNR at the decision circuit and resulting in a disperion-induced power penalty. This penalty is the increase (in dB) in the received power compensating for the peak-power and defined by:

$$\delta_d = -5\log_{10}[1 - (4BLD\sigma_\lambda)^2] ,$$

where $B$ is the bit rate, $D$ is the dispersion parameter, $L$ is length and $\sigma_\lambda$ is the RMS width of the source spectrum (assumed Gaussian). The following Fig. 8.1.5.1 shows the the power penalty as a function of $BLD$ $\sigma_\lambda.^2$ The power penalty becomes infinite when $BLD$ $\sigma_\lambda$

= 0.25, indicating that the BL product is the limiting factor. Typically, $BLD\ \sigma_\lambda < 0$, so the dispersion parameter is below 2 dB.
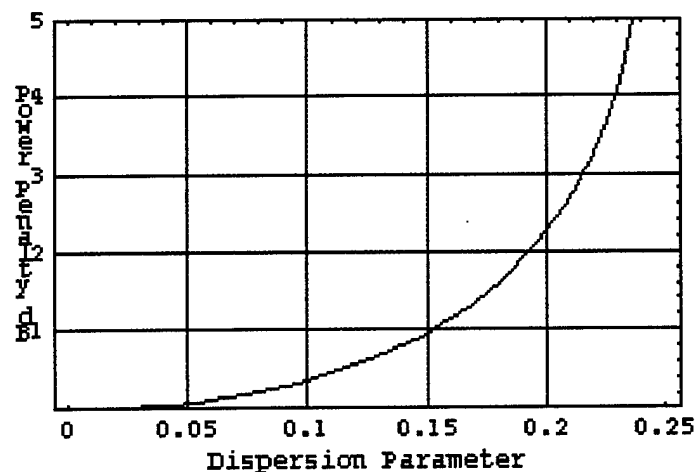


Fig. 8.1.5.1 Dispersion-induced power penalty for a Gaussian pulse as a function of $BLD\sigma_\lambda$. Source spectrum is also assumed to be Gaussian, with an RMS width of $\sigma_\lambda$.

## 8.1.6

Mode-partition noise occurs because of anticorrelation among pairs of longitudinal modes. For multimode semiconductor lasers, the power peanlty is given by:

$$\delta_{mpn} = -5\log_{10}(1 - Q^2 r_{mpn}^2),$$

where $r_{mpn}$ is the relative noise level of the received power in the presence of mode-partition noise. Assuming that the average mode power is distributed according to a Gaussian distribution, the relative noise level is:

$$r_{mpn} = \frac{k}{\sqrt{2}}\left(1 - \exp\left[-(\pi BLD\sigma_\lambda)^2\right]\right),$$

where $k$ is the mode partition coefficient. Fig. 8.1.6.1 below shows the power penalty at a BER of $10^{-9}$ ($Q = 6$) as a function of the normalized dispersion parameter, $BLD\sigma_\lambda$, and values of the mode partition coefficient, $k$.[17] The power penalty can be reduced to a negligible level ($\delta_{mpn} < 0.5$ dB) by designing the system so that $BLD\sigma_\lambda < 0.1$.

[17] Cheng, W.-H. & Chu, A.-K., Chu, *IEEE Photon Technol. Lett.*, 8, 611, 1996;
Anderson, T.B. & Clarke, B.R., *IEEE J. Quantum Electron.*, 29, 3, 1993;
Valle, A., Colet, P., Pesquera & San Miguel, M., *IEE Proc.*, 140 Pt. J, 237, 1993;
Wu, H. & Chang, H., *IEEE J. Quantum Electron.*, 29, 2154, 1993;
Valle, A., Mirasso, C.R. & Pesquera, L., *IEEE J. Quantum Electron.*, 31, 876, 1995.
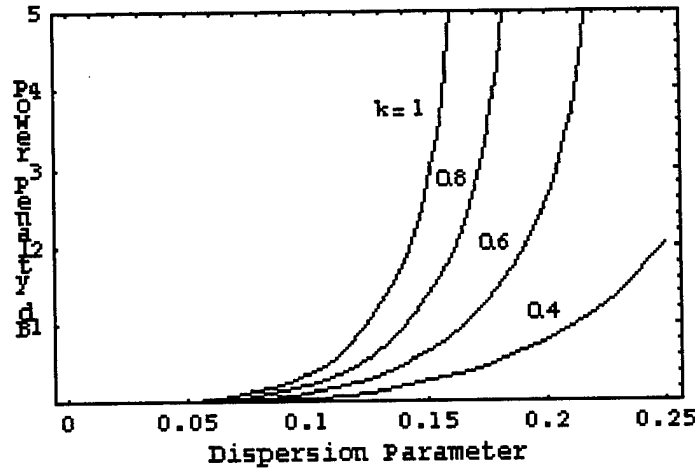
Fig. 8.1.6.1 MPN-induced power penalty versus $BLD\sigma_\lambda$ for a multimode semiconductor laser of RMS spectral width $\sigma_\lambda$ for BER $= 10^{-9}$ ($Q = 6$). Different curves correspond to different values of the mode-partition coefficient $k$.

**8.1.7**

The single-mode nature of distributed feedback (DFB) lasers described by the mode-suppression ratio (MSR), defined as the ratio of the main-power $P_m$ to the power $P_s$ of the most dominant side mode. The effect of mode-partition noise (MPN) depends on MSR.

The MPN-induced power penalty in the presence of receiver noise is obtained by adding an additional noise term accounting for side-mode fluctuations. For a $p$-$i$-$n$ receiver the BER is:

$$BER = \frac{1}{2} erfc\left(\frac{Q}{\sqrt{2}}\right) + \exp\left(-\frac{R_{ms}}{2} + \frac{R_{ms}^2}{4Q^2}\right)\left[1 - \frac{1}{2}erfc\left(\frac{Q}{\sqrt{2}} - \frac{R_{ms}}{Q\sqrt{2}}\right)\right],$$

where

$$R_{ms} = \frac{\overline{P}_m}{\overline{P}_s}$$

is the MSR. The BER exceeds $10^{-9}$ when MSR $< 42$. The following Fig. 8.1.7.1 shows the BER as a function of the power penalty at a BER of $10^{-9}$ as a function of MSR.[18] The power penalty becomes infinite for MSR values below 42, since the $10^{-9}$ BER cannot be realized irrespective of the power received. On the other hand, the penalty is negligible ($<$ 0.1 dB) for MSR values in excess of 100 (20 dB).

[18] Cartledge, J.C., *J. Lightwave Technol.*, 6, 626, 1988.
Henmi, N., Koizumi, Y., Yamaguchi, M., Shikada, M. & Mito, I., *J. Lightwave Technol.*, 6, 636, 1988;
Fishman, D.A., *J. Lightwave Technol.*, 8, 634, 1990;
Anderson, T.B. & Clarke, B.R., *IEEE J. Quantum Electron.*, 29, 3, 1993.

**BER vs Increase in received power**
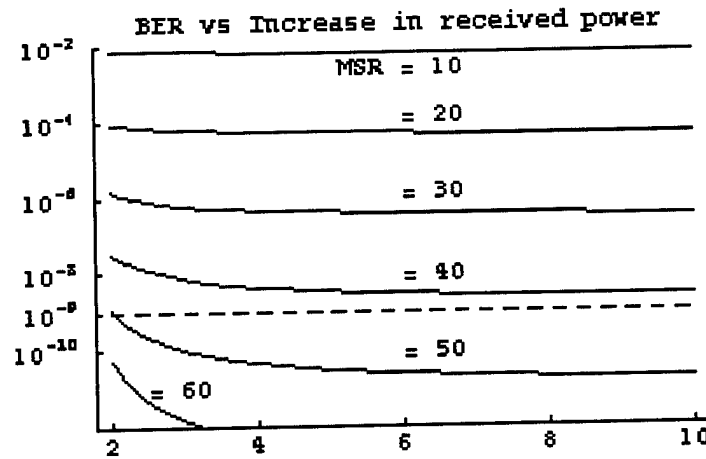


Fig. 8.1.7.1 Effect of MPN on bit-error rate of DFB laseres for several values of mode-suppresssion ratio (MSR): 10, 20, 30, 40, 50, 60 (top to bottom). Intersection of the BER = $10^{-9}$ line with the curves provides MPN-induced power penalty.

## 8.1.8

Frequency chirping also limits performance. (Optical pulses with a time-dependent phase shift are called chirped.) The power penalty due to chirping is:

$$\delta_c = -20\log_{10}\left\{1-\left(\frac{4\pi^2}{3}-8\right)B^2 L_D \Delta\lambda_c t_c\left[1+\left(\frac{2B}{3}\right)(LD\Delta\lambda_c - t_c)\right]\right\},$$

where $\Delta\lambda_c$ is the spectral shift associated with frequency chirping and $t_c$ is the chirp duration and the receiver is assumed to contain a $p$-$i$-$n$ photodiode. The following Fig. 8.1.8.1 shows the power penalty as a function of parameter combination $BLD\Delta\lambda_c$ and for several values of $Bt_c$, a measure of the fraction of the bit period over which chirping occurs[19]. The power penalty can be kept below 1 dB if the system is designed such that $BLD\Delta\lambda_c < 0.1$ and $Bt_c < 0.2$.

[19] Koch, T.L. & Bowers, J.E., *Electron. Lett.*, 20, 1038, 1984;
Gnauck, A.H. et al, *J. Lightwave Technol.*, 3, 1032, 1985;
Agrawal, G.P. & Potasek, M.J., *Opt. Lett.*, 11, 318, 1986.
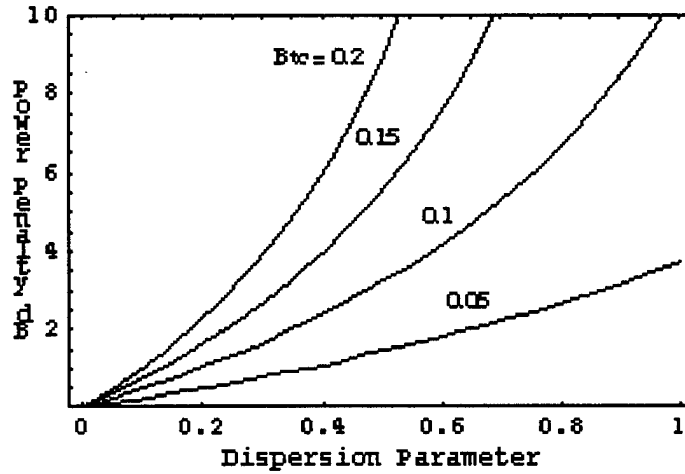
Fig. 8.1.8.1 Chirp-induced power penalty as a function of $BLD\Delta\lambda_c$ for several values of the parameter $Bt_c$. $\Delta\lambda_c$ is the wavelength shift occurring because of frequency chirp and $t_c$ is the duration of such a wavelength shift.

## 8.1.9

In the case of lightwave systems operating at high bit rates ($B > 2$ Gb/s), the bit duration is generally shorter than the total duration $2t_c$ over which chirping occurs. In that case, the frequency chirp increases almost linearly over the entire pulse width (or bit slot). Assuming a Gaussian optical pulse linearly chirped over its entire width, the power penalty is then:

$$\delta_c = 5\log_{10}\left[\left(1 + 8C\beta_2 B^2 L\right)^2 + \left(8\beta_2 B^2 L\right)^2\right]$$

where the group velocity dispersion (GVD) coefficient $\beta_2$ is related to the dispersion, $D$, by:

$$D = \frac{d}{d\lambda}\left(\frac{1}{v_g}\right) = -\frac{2\pi c}{\lambda^2}\beta_2.$$

Fig.8.1.9.1 below shows the chirp-induced power penalty as a function of $|\beta_2|B^2L$ for several values of the chirp parameter, $C$. [13] The power penalty is negligible ($< 0.1$ dB) if $|\beta_2|B^2L < 0.05$. However, the panlty can exceed 5 dB if the pulses transmitted are chirped at $C = -6$. To keep the penalty below 0.1 dB, the system should be designed with $|\beta_2|B^2L < 0.002$. Performance is improved for positive values of $C$, as shown in the Figure, because the pulse goes through an initial compression phase. When the power penalty becomes negative at positive values of $C$, the frequencu chirping combats the effects of dispersion.
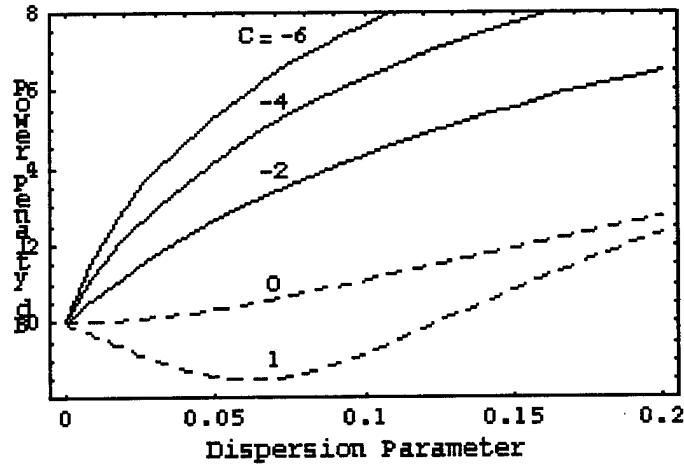
Fig. 8.1.9.1 Chirp-induced power penalty as a function of $|\beta_2|B^2L$ for several values of the chirp parameter $C$. The Gaussian optical pulse is assumed to be linearly chirped over its entire width.

## 8.1.10

Optical feedback can increase the noise intensity. The relative intensity noise (RIN) of a semiconductor laser can be enhanced by external optical feedback. The resulting power penalty is:

$$\delta_{ref} = -10\log_{10}\left(1 - r_{eff}^2 Q^2\right),$$

where $r_{eff}$ is the effective intensity noise over the receiver bandwidth $\Delta f$:

$$r_{eff}^2 \approx r_I^2 + \frac{N}{(MSR)^2},$$

where $r_I$ is the relative noise level in the absence of reflection feedback, $N$ is the number of external cavity modes and MSR is the factor by which the external-cavity modes remain suppressed.

The following Fig. 8.1.10.1 shows the reflection-noise power penalty as a function of MSR for $r_I = 0.01$ at several values of $N$.[20] In the absence of feedback ($N = 0$), the penalty is negligible. However, refelection can degrade the system performance to the extent that the system cannot achieve the desired BER despite and indefinite increase in the power received.

[20] Olsson, N.A., Tsang, W.T., Temkin, H., Dutta, N.K. & Logan, R.A., *J. Lightwave Technol.*, 3, 215, 1985;
Ho, K.-P., Walker, J.D. & Kahn, J.M., *IEEE Photon Technol. Lett.*, 5, 892, 1993.
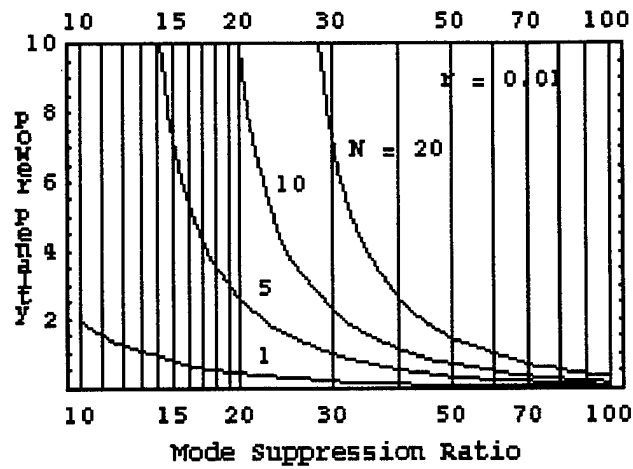
Fig. 8.1.10.1 Feedback-induced power penalty as a function of *MSR* for several values of *N* and $r_l = 0.01$. Reflection feedback into the laser is assumed to generate *N* side bands of the same amplitude.

## 9.0 Probability Density Functions and Moment Generating Functions

There are a number of approaches to the problem determining performance limits on optical communications systems in the presence of both Poisson and Gaussian noise influences. Traditionally the model for detection of the inherently stochastic optical signal is a simple realistic model of a filtered Poisson process in which randomly excited detected photons excite a bandlimited filter. However, there are further stochastic disturbances, e.g., additive Gaussian colored noise introduced by post-detection signal processing circuits. As has been pointed out by O'Reilly and others, the result is a superposition of marked (compound) and filtered process with a colored Gaussian process. This is the mixed compound Poisson plus Gaussian regime. In the following, we use moment generating function methods to calculate those influences on receiver performance. We find that although the additive influence do influence optical receivers with no gain, influences on receivers with substantial gain are negligible. In the latter case, although compound influences are present, there appears no real need to take them into consideration.

In most cases, it is impractical to derive the probability density function. However, recent developments have shown the way to using generator functions to obtain an accurate characterization[21]. This is because the mapping from characteristic functions to probability density functions is an isomorphism.

In the case of an ideal receiver (i.e., one with no thermal noise, no dark current, shot noise variance close to zero, and 100% quantum efficiency), the decision threshold could be set close to the 0-level signal. In such an unlikely situation, Poisson statistics would be used for shot-noise statistics. If $N_p$ is the average number of photons in each 1 bit, the probability of generating $m$ electron-hole pairs is then:

$$P_m = \frac{\exp[-N_p]N_p^m}{m!},$$

which is a Poisson distribution for a nonhomogeneous process. The performance of an optical detection system can be described by:

$$I(t) = q\sum_i g_i h(t - t_i),$$

where $q$ is the electronic charge, $\{t_i\}$ are the generation times resulting from the received optical signal and are Poisson distributed in any interval with a mean determined by the driving process rate; $g_i$ are random gains corresponding to the number of pairs resulting from primary carrier generation at times $t_i$; $h(t)$ is the filter impulse response. As it is not generally possible to derive a tractable closed form expression for the probability distribution for $I$, a generation function description was sought and found.

This was achieved by segmenting the time axis into elementary intervals and writing the contribution to the output current at time instant $t$ as due to carriers generated with an interval $\Delta t$ centered on $t_n$:

$$I_{t_n}(t) = q\sum_i^N g_i h(t - t_i),$$

---

[21] Cattermole. K.W. & O'Reilly, J.J. (Ed.s) *Mathematical Topics in Telecommunications. Volume 2. Problems of Randomness in Communication Engineering*, Wiley. New York, 1984.

where $N$ is the number of detection events with $\Delta t$ centered on $t_n$ and is Poisson distribution with mean:

$$E\{N\} = \lambda(t_n)\Delta t,$$

and

$$\lambda(t) = \eta\frac{P_{in}(t)}{hv} = \frac{I_p}{q}$$

is the instantaneous mean creation rate, $P_{in}(t)$ is the incident optical power, $\eta$ is the quantum efficiency and $I_p$ is the photocurrent.

A *conditional* moment generating function for $I_{t_n}$ is[22]:

$$\left\{M_{t_n}(s) \mid N = N_1\right\} = E\left\{\exp[sI_{t_n}]\right\} = E\left\{\exp\left[sq\sum_{i=1}^{N_1}g_ih(t-t_n)\right]\right\}$$

$$= \prod_{i=1}^{N_1}E\left\{\exp[sqgh(t-t_nv)]\right\}$$

where $g$ represents the gain random variable with moment generating function:

$$M_g(s) = E\left\{\exp[sg]\right\}.$$

Therefore the conditional moment generating function for $I_{t_n}$ can be written:

$$\left\{M_{t_n}(s) \mid N = N_1\right\} = \left[M_g(sqh(t-t_n))\right]^{N_1}$$

By averaging over $N$ the conditioning can be removed with respect to the number of detection events in the time interval $\Delta t$. As $N$ is Poisson distributed, the unconditional moment generating function is:

$$M_{t_n}(s) = \exp[-\lambda(t_n)\Delta t]\sum_{i=1}^{\infty}\frac{1}{i!}(\lambda(t_n))^N\left[M_g(sqh(t-t_n))\right]^N = \exp[\lambda(t_n)\Delta t\{M_g(sqh(t-t_n))-1\}]$$

Because with respect to different time intervals:
• the number of detection events are independent, and
• the avalanche gain associated with a given event is independent of the gain associated with other events,

*the moment generating function for the random variable I(t) corresponding to the sum of the contributions from the various intervals is given by the product of the elementary contributory moment generating functions, i.e.:*

[22] O'Reilly, J.J., Generating functions, bounds and approximations in optical communications. pp. 119-133, in Cattermole. K.W. & O'Reilly, J.J. (Ed.s) *Mathematical Topics in Telecommunications. Volume 2. Problems of Randomness in Communication Engineering*, Wiley. New York, 1984.

$$M_I(s) \cong \prod_n M_{I_n}(s) = \prod_n \exp\left[\lambda(t_n)\Delta t\left\{M_g\left(sqh(t-t_n)\right)-1\right\}\right] = \exp\left[\sum_n \lambda(t_n)\Delta t\left\{M_g\left(sqh(t-t_n)\right)-1\right\}\right]$$

In the $\Delta t \rightarrow 0$ limit,

$$M_I(s) = \exp\left[\int_{-\infty}^{\infty}\lambda(\tau)\left[M_g\left(sqh(t-\tau)\right)-1\right]d\tau\right]$$

which, although not analytic, can substitute for the probability density function. If a gain moment generating function is chosen of the form:

$$M_g(s) = \exp[s],$$

there is a further simplification of the moment generating function of the Poisson process to:

$$M_I(s) = \exp\left[\int_{-\infty}^{\infty}\lambda(t)\left\{\exp[sqh(t-\tau)]-1\right\}d\tau\right]$$

Furthermore, Gaussian noise is additive and independent of the signal and gain processes. *As addition of independent random variables gives rise to a multiplication of their generating functions*, the output process:

$$I_0(t) = I(t) + I_n(t)$$

has the moment generating function:

$$M_{I_0}(s) = M_I(s)M_{I_n}(s)$$

where

$$M_{I_N} = \exp\left[\frac{\sigma_n^2}{2}s^2\right]$$

is the moment generating function for a zero-mean Gaussian process with variance $\sigma_n^2$.

## Chernoff Bound

The moment generating function of the random variable $X$ is defined as:

$$M(s) = E[\exp(sX)] = \int_{-\infty}^{\infty}\exp(sx)dF(x),$$

for all real $s$ for which the integral is finite, where $F(x)$ is the distribution function of $X$. Let $P[\ ]$ denote the probability of the event in the brackets. For all non-negative $s$,

$$P[X \geq 0] = \int_0^\infty dF(x) \leq \int_0^\infty \exp(sx)dF(x).$$

From a comparison of the previous two equations, it can be concluded that:

$$P[X \geq 0] \leq M(s), \quad 0 \leq s < s_l$$

where $s_l$ is the upper limit of the interval in which $M(s)$ is defined. In order to make the bound as tight as possible, a value of $s$ is chosen that minimizes $M(s)$. Therefore[23],

$$P[X \geq 0] \leq \min_{0 \leq s < s_l} M(s).$$

The right hand side of this inequality is the *Chernoff bound*.
If it can be assumed that:

$$E(X) < 0, \quad P(X > 0) > 0,$$

then

$$P[X \geq 0] \leq \frac{1}{2} \min_{0 \leq s < s_l} M(s).$$

## Modified Chernoff Bound

Prabhu[24] derived a modified Chernoff bound (MCB) applicable to binary pulse amplitude modulation systems corrupted by additive interference and independent zero-mean Gaussian noise. This MCB requires the evaluation of the moment generating function for the interference, which may be independent zero mean Gaussian noise. Da Rocha & O'Reilly extended the MCB model to direct-detection optical communications[25].

Essentially, the extension to optical communications is achieved by modeling the signal as a signal conditioned marked and filtered Poisson process with mean value corresponding to the message waveform, by employing a conditional generating function description and by using principles of analytic continuation and contour integration. The extended MCB accommodates the inherent stochastic character of the signal, together with Gaussian noise and both optical and electrical intersymbol interference. The tightness of the MCB for optical communication is assessed by comparing it with the standard Chernoff bound (CB).

For non-avalanche gain receivers the MCB is found to be considerably tighter than the CB for all cases of practical interest. For an avalanche photodiode receiver, the MCB is tighter than the CB for modest gains, but the performance of the MCB deteriorates as the gain increases.

The analysis commences from the point of view of the decision stage of the error probability:

[23] Torrieri, D.J., *Principles of Secure Communication Systems*, 2nd Edition, Artech, 1992, pp. 66-69;
Billingsley, P., *Probability and Measure*, 2nd Edition, New York, 1986;
Jacobs, I.M., Probabiluty of error bounds for binary transmission on slowly fading Rician channel, *IEEE Trans. Inform. Theory*, IT-12, 431, 1966.
[24] Prabhu, V.K., Modified Chernoff bound for PAM systems with noise and interference. *IEEE Trans.*, IT-28, 95-100, 1982.
[25] Da Rocha, J.R.F. & O'Reilly, J.J., Modified Chernoff bound for binary optical communication. *Electronics Letters*, 18, 708-710, 1982.

$$BER = \frac{1}{2}(P(0/1) + P(1/0)),$$

where $P(0/1)$ and $P(1/0)$ are conditional error probabilities. For a decision threshold $I_D$, these conditional probabilities are:

$$P(0/1) = \int_{I_D}^{\infty} P_{I_0}(I/1)dI$$

$$= \frac{1}{2\pi}\int_{I_D}^{\infty} dI \int_{-\infty}^{\infty} \exp[-i\omega I]C_{I_0}(\omega)d\omega$$

and

$$P(1/0) = \int_{I_D}^{\infty} P_{I_0}(I/0)dI$$

$$= \frac{1}{2\pi}\int_{-\infty}^{I_D} dI \int_{-\infty}^{\infty} \exp[-i\omega I]C_{I_1}(\omega)d\omega$$

where $P_{I_i}$ is the conditional probability density function and $C_{I_i}$ the conditional characteristic function for the signal and noise process at the input to the decision device when $i$' is being received.

Next, the characteristic function is extended into the complex plane by way of analytic continuation. This allows the conditional probabilities to be obtained by contour integration:

$$P(0/1 \ or \ 1/0) = \frac{(-1)^i}{2\pi i} \int_{C_i} \frac{1}{z} \exp(-iIz)C_{I_i}(z)dz,$$

where $i = 0,1$, and $C_0$, $C_1$ are contours chosen to be parallel to the real axis in the lower and upper halfplanes, respectively.

The following substitutions are made for $z$:

$$z = u - i s_0; \quad s_0 > 0, \quad i = 0$$
$$z = u + i s_1; \quad s_1 > 0, \quad i = 1$$

and the conditional probabilities are bounded giving:

$$P(0/1) \leq \frac{1}{\sqrt{(2\pi)}s_0\sigma} \exp\left(-I_D s_0 + \sigma^2 s_0^2/2\right)M_{I_0}(s_0)$$

$$P(1/0) \leq \frac{1}{\sqrt{(2\pi)}s_1\sigma} \exp\left(I_D s_1 + \sigma^2 s_1^2/2\right)M_{I_1}(-s_1)$$

where $M_{I_0}$, $M_{I_1}$ represent conditional moment-generating functions relating to the signal process and $\sigma$ is the additive Gaussian noise variance.

By substitution an upper bound for the *BER* is obtained as:

$$BER = \frac{1}{2\sqrt{(2\pi)}s\sigma}\left\{M_{I_0}(s)\exp\left(-I_D s + \sigma^2 s^2/2\right) + M_{I_1}(-s)\exp\left(I_D s + \sigma^2 s^2/2\right)\right\}, \quad (A)$$

where

$$M_{I_0} = \frac{1}{2^N}\exp\left[H_{\lambda_0}(s,P)\right]\prod_{i=n_1}^{n_2}\left\{1 + \exp\left[H_i(s,P)\right]\right\},$$

$$M_{I_1} = \frac{1}{2^N}\exp\left[H_\Delta(s,P)\right]\prod_{i=n_1}^{n_2}\left\{1 + \exp\left[H_i(s,P)\right]\right\},$$

$N = |n_1| + n_2$ *is the number of interferers,*

$$H_\Delta(s,P) = K\int_{-\infty}^{\infty}h_\Delta(M_g(sP) - 1)d\tau,$$

$$H_i(s,P) = K\int_{-\infty}^{\infty}h_i(M_g(sP) - 1)d\tau,$$

$$H_{\lambda_0}(s,P) = \int_{-\infty}^{\infty}\lambda_0(M_g(sP) - 1)d\tau,$$

$$h_\Delta \approx h(\tau) + \lambda_0/K,$$

$$h_i \approx h(\tau - iT),$$

$$P \approx P(t - \tau),$$

with $h(t)$ the received optical pulse shape, $\lambda_0$ the photodiode dark current intensity, $K$ the optoelectronic conversion factor, $M_g(s)$ the moment-generating function for the photodiode avalanche gain and $P(t)$ the impulse response of the receiver filter following amplification and equalization for front-end bandlimiting.

Eq. (A) is applied utilizing an optimum value for $s$ which minimizes the BER, i.e., provides an upper bound to the probability of error. The results are shown in Fig.s $9.1$[26]. The modified Chernoff bound (MCB) provides a tighter bound than the Chernoff bound. However, comparing Fig. 9.1A and Fig. 9.1B, it may be seen that the difference between the two bound estimations is much less significant with receiver gain. In fact, Fig. 9.1C shows that the difference is almost negligible for a gain of 40.

---

[26] Da Rocha, J.R.F. & O'Reilly, J.J., Modified Chernoff bound for binary optical communication. *Electronics Letters*, 18, 708-710, 1982;
O'Reilly, J.J., Generating functions, bounds and approximations in optical communications. pp. 119-133, in Cattermole. K.W. & O'Reilly, J.J. (Ed.s) *Mathematical Topics in Telecommunications. Volume 2. Problems of Randomness in Communication Engineering*, Wiley. New York, 1984.

Fig.s   9.2-9.7  compare receiver characteristics using a BER based on Gaussian statistics and a BER based on mixed Poisson-Gaussian statistics. It can readily be seen that for most purposes, the difference is negligible.
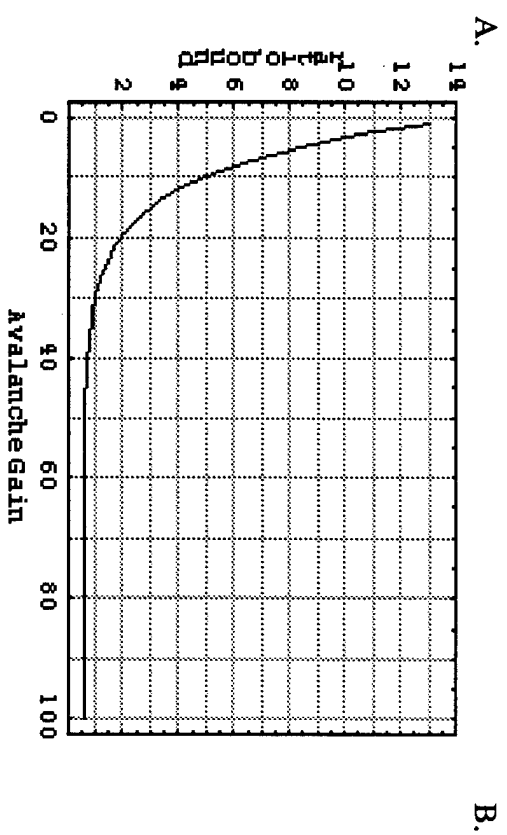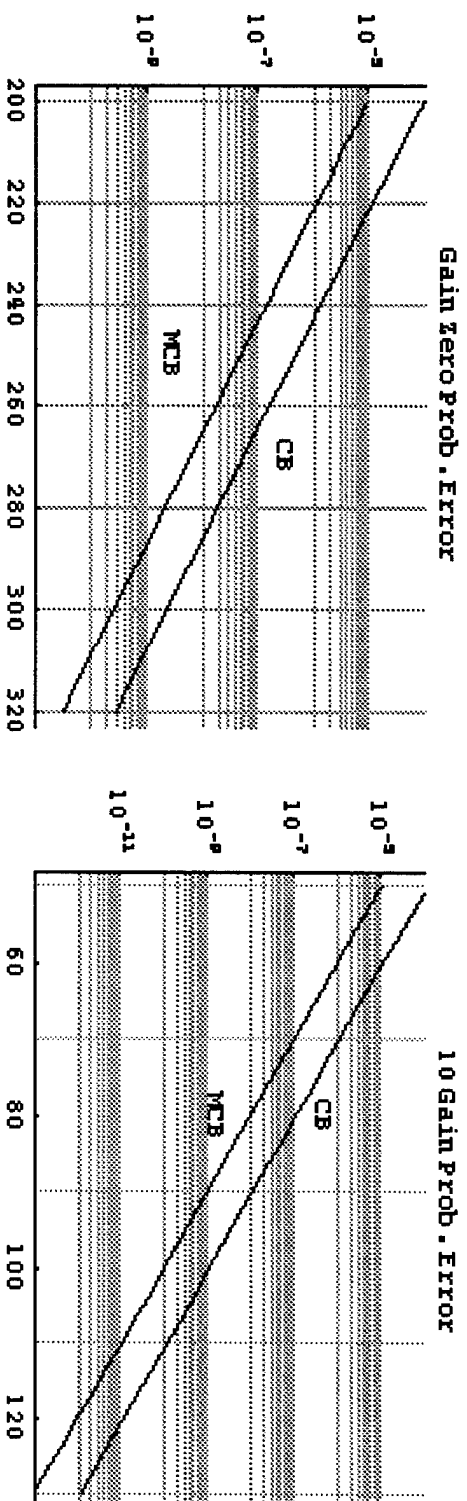
Fig. 9.1. Comparison of Chernoff and modified bound as a function of signal level. A: No gain; B: Avalanche gain = 1; C. Influence of the avalanche gain on bound tightness measured by the bound ratio. From J.R.F. Da Rocha & J.J. O'Reilly, *Electronics Letters*, 18, 708-710, 1982.
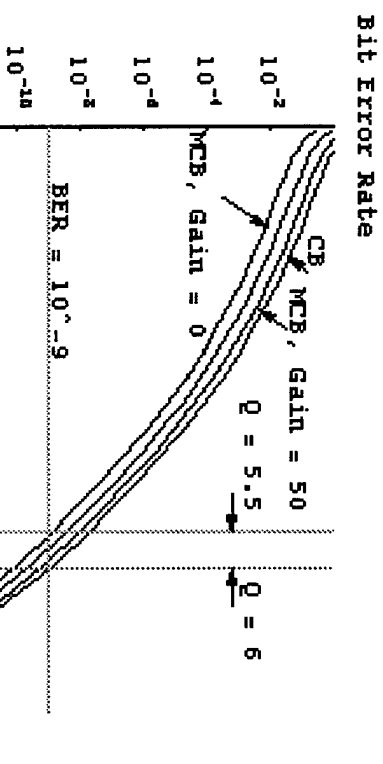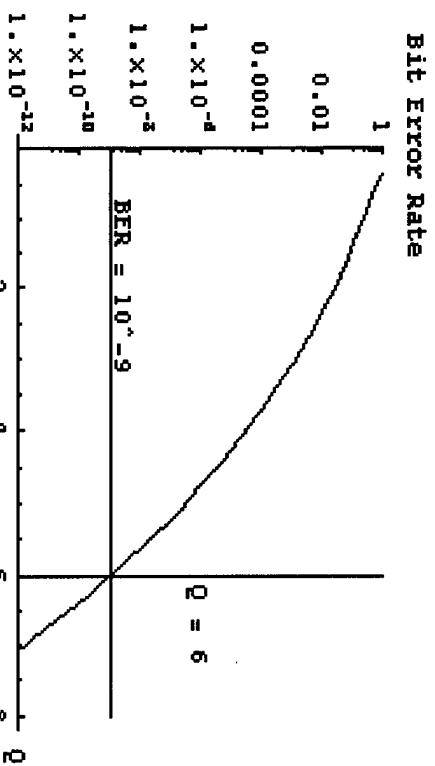
Fig. 9.2 Bit-error rate versus the $Q$ parameter. Line at BER = $10^{-9}$ intersects curve at $Q = 6$. Left: Gaussian statistics; Right: Mixed Gaussian-Poisson.
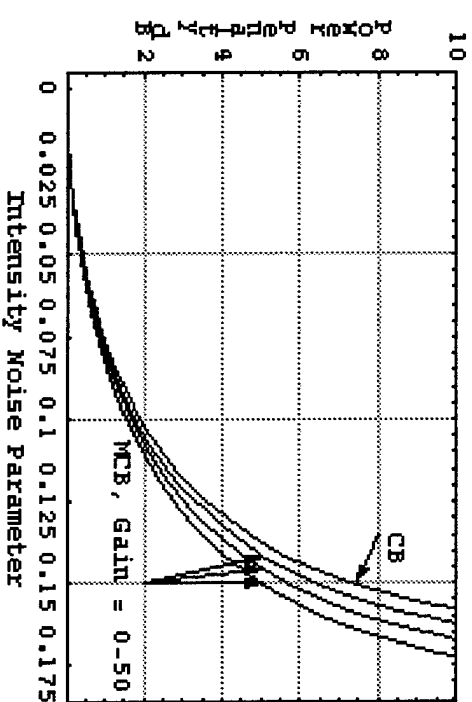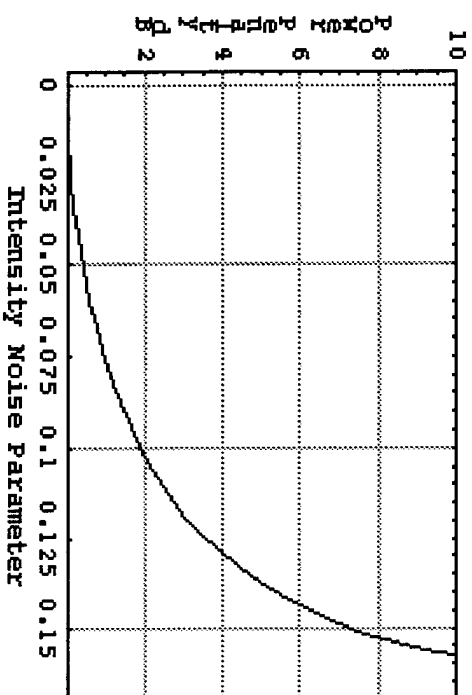


Fig. 9.3. Power penalty versus the intensity noise parameter $r$. Left: Gaussian statistics; Right: Mixed Gaussian-Poisson.
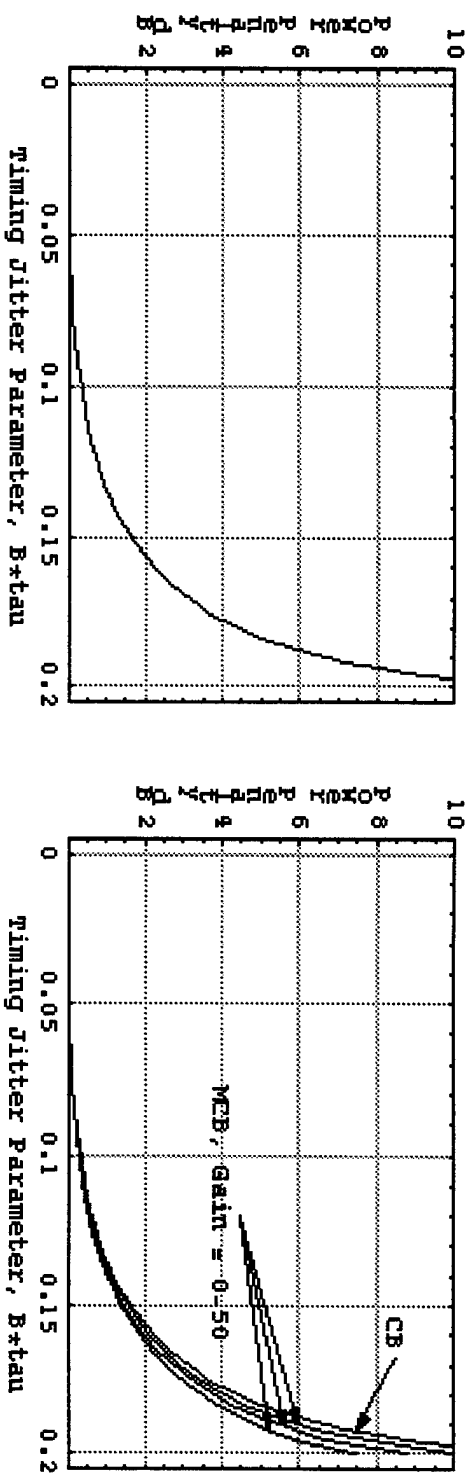
Fig. 9.4. Power penalty versus the timing jitter parameter $B\tau_j$. Left: Gaussian statistics; Right: Mixed Gaussian-Poisson.
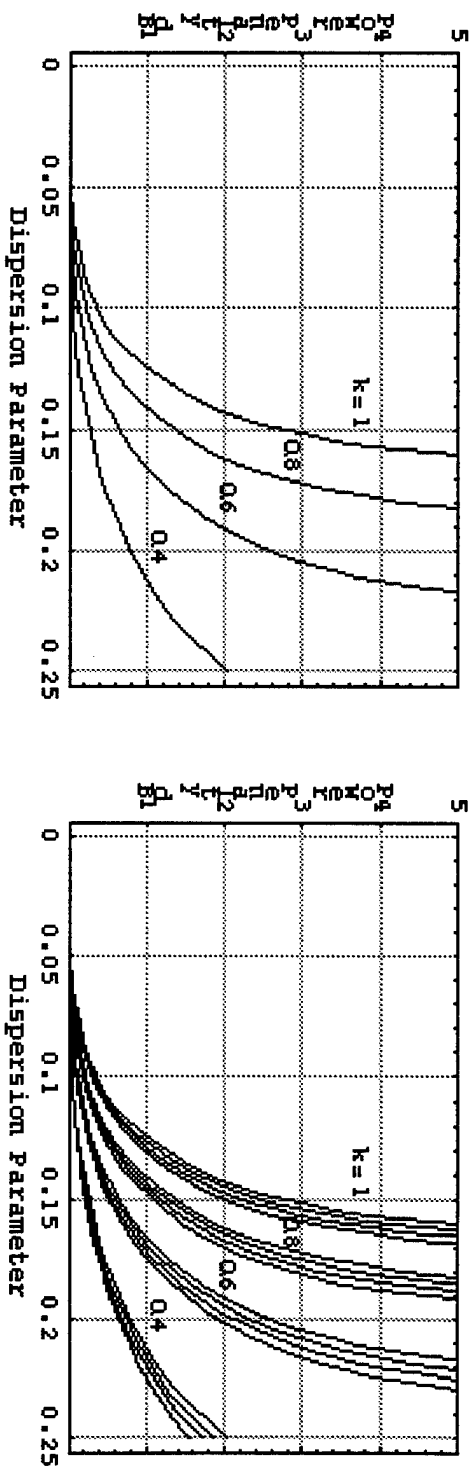


Fig. 9.5. MPN-induced power penalty versus BLD$\sigma$, for a multimode semiconductor laser of RMS spectral width $\sigma_\lambda$, for BER = $10^{-9}$ ($Q = 6$). Different curves correspond to different values of the mode-partition coefficient $k$. Left: Gaussian statistics; Right: Mixed Gaussian-Poisson.
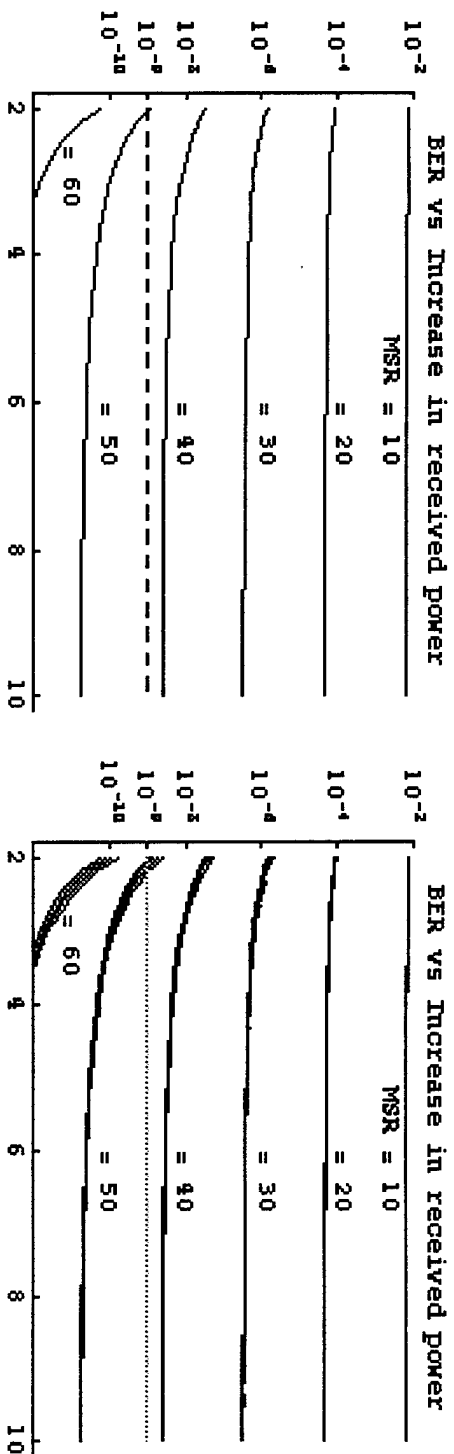
Fig. 9.6. Effect of MPN on bit-error rate of DFB laseres for several values of mode-supresssion ratio (MSR): 10, 20, 30, 40, 50, 60 (top to bottom). Intersection of the BER = $10^{-9}$ line with the curves provides MPN-induced power penalty. Left: Gaussian statistics; Right: Mixed Gaussian-Poisson.
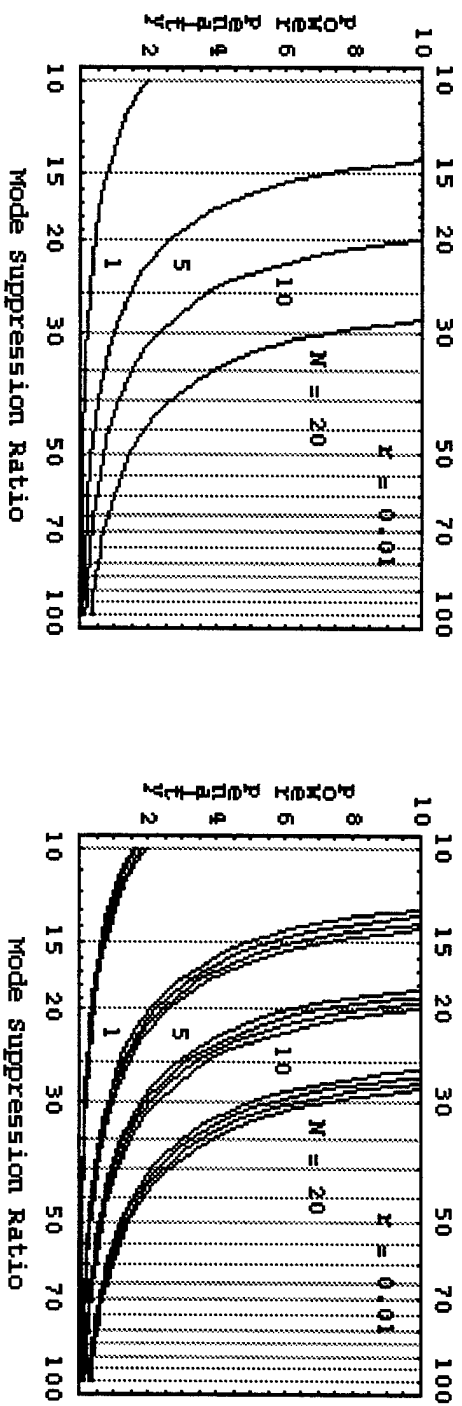
Fig. 9.7. Feedback-induced power penalty as a function of *MSR* for several values of $N$ and $r_f = 0.01$. Reflection feedback into the laser is assumed to generate $N$ side bands of the same amplitude. Left: Gaussian statistics; Right: Mixed Gaussian-Poisson.

## 10. Device Capability: Chirped Gaussian Pulses & Solitons.

We examine here the impact on data rate and bit error rate of chirped Gaussian pulses, dispersion, modulation formats, preamplification and use of soliton pulses. The interaction between dispersion and pulse chirping is examined; the optimal operation of lightwave systems is modeled near the zero-dispersion wavelength of a fiber and by using optical sources with a relatively narrow spectral width; the effect on bit error rate of various modulation formats is modeled; and the effect on receiver sensitivity of filter bandwidth at various levels of the noise figure is modeled showing that amplifiers with small noise figure must be used and performance can also be improved by reducing the optical filter bandwidth. As bit rate can also be increased by the use of very short pulses, solitons are modeled with respect to pulse evolution according to the order of the soliton. Other evolutions modeled are: to a "sech" pulse from a Gaussian input and from a "sech" input of varying order; dark solitons; soliton pairs; and chirped solitons.

### *Chirped Gaussian Pulses:*

If each frequency component of the optical field propagates in a single mode fiber as :

$$E(r,\omega) = \hat{x}F(x,y)B(0,\omega)\exp[i\beta z],$$

where $\hat{x}$ is the polarization unit vector, $F(x,y)$ is the field distribution of the fundamental fiber mode, $B(0,\omega)$ is the initial amplitude and $\beta$ is the propagation constant; and if the frequency dependence of $\beta$ is:

$$\beta(\omega) = n(\omega)\frac{\omega}{c} \approx \beta_0 + \beta_1(\Delta\omega) + \frac{1}{2}\beta_2(\Delta\omega)^2 + \frac{1}{6}\beta_3(\Delta\omega)^3,$$

where $\Delta\omega = \omega - \omega_0$, $\beta_m = \left(d^m\beta/d\omega^m\right)_{\omega=\omega_0}$, $\beta_1 = 1/v_g$, $v_g$ is the group velocity, $\beta_2$ is related to the dispersion parameter[27], and $\beta_3$ is related to the dispersion slope[28], then the basic propagation equation is[29]:

$$\frac{\partial A}{\partial z} + \beta_1\frac{\partial A}{\partial t} + \frac{i}{2}\beta_2\frac{\partial^2 A}{\partial t^2} - \frac{1}{6}\beta_3\frac{\partial^3 A}{\partial t^3} = 0, \quad (10.1)$$

where $A(z,t)$ is a slowly varying amplitude. By making the transformation to a reference frame moving with the pulse by introducing the new coordinates,

$$t' = t - \beta_1 z, \qquad z' = z,$$

---

[27] The dispersion parameter is $D = \dfrac{d}{d\lambda}\left(\dfrac{1}{v_g}\right) = -\dfrac{2\pi c}{\lambda^2}\beta_2.$

[28] The dispersion slope is $S = \dfrac{dD}{d\lambda} = \left(\dfrac{2\pi c}{\lambda^2}\right)^2 \beta_3 + \left(\dfrac{4\pi c}{\lambda^3}\right)\beta_2$ and $\beta_3 = \dfrac{d\beta_2}{d\omega} = \dfrac{d^3\beta}{d\omega^3}$ .

[29] Agrawal, G.P., *Fiber-Optic Communication Systems*, Second Edition, Wiley, 1997.

we obtain:

$$\frac{\partial A}{\partial z'} + \frac{i}{2}\beta_2 \frac{\partial^2 A}{\partial t'^2} - \frac{1}{6}\beta_3 \frac{\partial^3}{\partial t'^3} = 0$$

If the initial pulse amplitude is:

$$A(0,t) = A_0 \exp\left[-\frac{1+iC}{2}\left(\frac{t}{T_0}\right)^2\right],$$

where the parameter $T_0$ represents the half-width at the $1/e$ intensity point and the parameter $C$ governs the linear frequency chirp imposed on the pulse, then on propagation, the pulse width changes as:

$$\frac{T_1}{T_0} = \left[\left(1+\frac{C\beta_2 z}{T_0^2}\right)^2 + \left(\frac{\beta_2 z}{T_0^2}\right)^2\right]^{1/2},$$

where $T_1$ is the half-width of the pulse at the $1/e$ intensity point of the introduced pulse. The following Fig. 10.1 shows the variation of the broadening factor $T_1/T_0$ with propagation distance for a chirped Gaussian input pulse, where the dispersion length is given by:

$$L_D = \frac{T_0^2}{|\beta_2|}$$
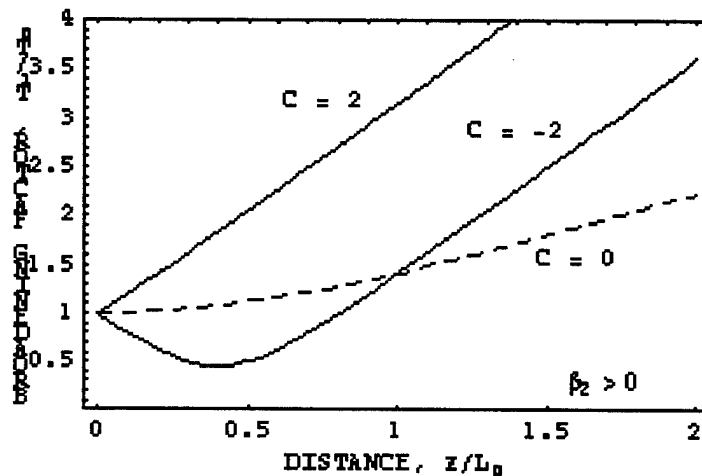


Fig. 10.1. Variation of the broadening factor with propagated distance for a chirped Gaussian input pulse. The Dashed curve corresponds to the case of an unchirped Gaussian pulse. After Ref[29].

A chirped pulse may broaden or compress depending on whether $\beta_2$ and $C$ have the same or opposite signs.

### Effect of Dispersion:

Limitations on the bit rate can be assessed as follows. The condition:

$$BL|D|\sigma_\lambda \leq 1/4, \qquad\qquad \text{(A)}$$

where $B$ is the bit rate, $L$ is length, $D$ is the dispersion parameter and $\sigma_\lambda$ is the RMS source spectral width in wavelength units, holds when the spectral width is wide to average. The condition:

$$B\sqrt{|\beta_2|L} \leq 1/4 \qquad\qquad \text{(B)}$$

is valid in the case of optical sources with small spectral width. In the case of the limit of zero dispersion, the condition is:

$$B\left(|\beta_3|L\right)^{1/3} \leq 0.324. \qquad\qquad \text{(C)}$$

Based on Eq.s (A), (B) and (C), the following Fig. 10.2. shows the limiting rate of single mode fibers as a function of the fiber length. Eq. (A) was used for the $D = 16$, $\sigma_\lambda = 1$ nm and 5 nm cases; Eq. (B) was used for the $D = 16$, $\sigma_\lambda = 0$ nm; and (C) Eq. (C) was used for the $D = 0$ case.
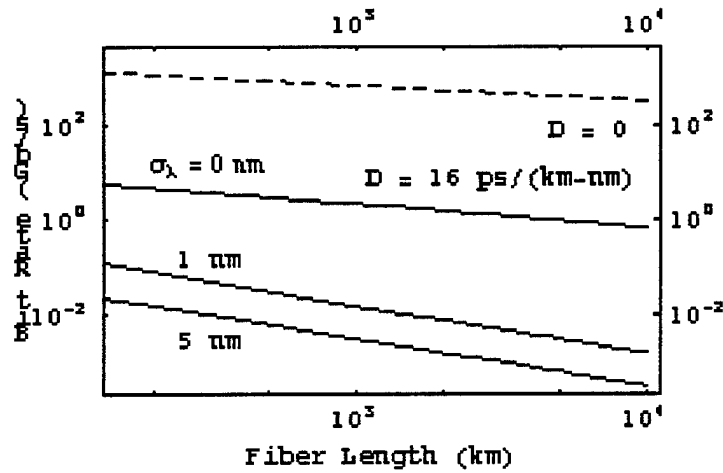


Fig. 10.2. Limiting bit rate of single mode fibers as a function of the fiber length for $\sigma_\lambda = 0$, 1, and 5 nm. The case $\sigma_\lambda = 0$ corresponds to the case of an optical source whose spectral width is much smaller than the bit rate. After Ref[29].

Fig. 10.2 shows that lightwave systems operate optimally near the zero-dispersion wavelength of a fiber and by using optical sources with a relatively narrow spectral width.

## Modulation Formats:

The bit-error rate also varies across modulation formats. The bit error rate for various modulation formats is shown in Table 10.1 and Fig. 10.3.

<table>
<tr><td colspan="2" align="center">Table 10.1. Receiver BERs</td></tr>
<tr><td align="center">Receiver</td><td align="center">BER§</td></tr>
<tr><td>(1) Synchronous PSK homodyne receiver</td><td>$BER = \frac{1}{2}erfc\left(\sqrt{2\eta N_p}\right)$</td></tr>
<tr><td>(2) Synchronous PSK heterodyne receiver</td><td>$BER = \frac{1}{2}erfc\left(\sqrt{\eta N_p}\right)$</td></tr>
<tr><td>(3) Asynchronous DPSK receiver</td><td>$BER = \frac{1}{2}\exp\left[-\eta N_p\right]$</td></tr>
<tr><td>(4) Synchronous FSK heterodyne receiver</td><td>$BER = \frac{1}{2}erfc\left(\sqrt{\frac{\eta N_p}{2}}\right)$</td></tr>
<tr><td>(5) Asynchronous FSK receiver</td><td>$BER = \frac{1}{2}\exp\left[-\frac{\eta N_p}{2}\right]$</td></tr>
<tr><td>(6) Synchronous ASK heterodyne receiver</td><td>$BER = \frac{1}{2}erfc\left(\sqrt{\frac{\eta N_p}{4}}\right)$</td></tr>
<tr><td>(7) Asynchronous ASK receiver</td><td>$BER = \frac{1}{2}\exp\left[-\frac{\eta N_p}{4}\right]$</td></tr>
</table>

§ $\eta$ is the quantum efficiency; $N_p$ is e number of photons in the "1" bit.
ASK - amplitude-shift keying
PSK - phase-shift keying
DPSK - differential phase-shift keying
FSK - frequency-shift keying
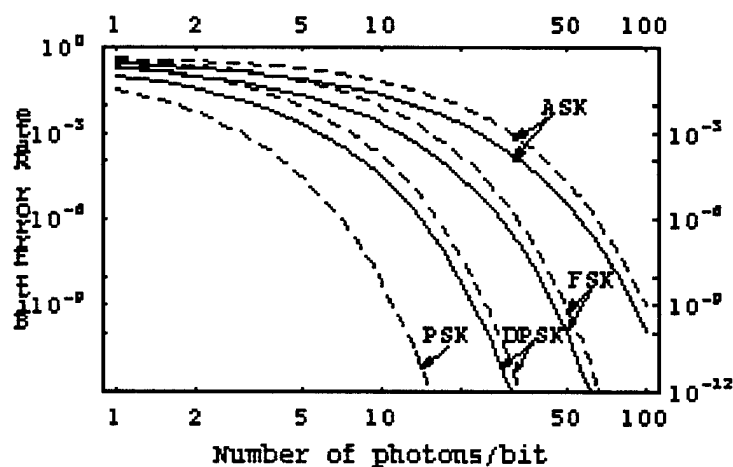


Fig. 10.3 Bit-error curves for various modulation formats. The solid and the dashed lines correspond to the cases of synchronous and asynchronous demodulation, respectively. After Ref[29]. Referring to Table 1, these curves were generated by using Eq.s (1)-(7) consecutively.

142

Fig. 10.3 shows that in all cases the BER is larger for the asynchronous case for the same value of $\eta N_p$, but the difference is so small that the receiver sensitivity at a BER of $10^{-9}$ is degraded by only about 0.5 dB.

## Preamplification:

Receiver sensitivity can be improved 10-20 dB by using an EDFA as a preamplifier[30]. However, the use of optical preamplifiers results in the contamination of the amplified signal by spontaneous emission. Because of the incoherent nature of the spontaneous emission, the amplified signal is noisier than the input signal. Using an optical preamplifier, the average number of photons/bit can be described by:

$$\overline{N}_p = \frac{1}{2}F_n\left[Q^2 + Q\left(\frac{2\Delta v_{opt}}{B}\right)^{1/2}\right],$$

where $Q = \dfrac{I_1 + I_0}{\sigma_1 + \sigma_0}$, $F_n$ is a noise figure and $\Delta v_{opt}$ is the optical filter bandwidth. The following Fig. 10.4 shows the effect on receiver sensitivity of filter bandwidth at various levels of the noise figure at $Q = 6$. The figure shows that amplifiers with small noise figure must be used. The performance can also be improved by reducing $\Delta v_{opt}$. Typically, $\overline{N}_p$ is greater than 1000 for p-i-n receivers without optical amplifiers. However, $\Delta v_{opt}$ can be less than 100 when optical amplifiers are used to preamplify the signal, despite spontaneous emission degradation.
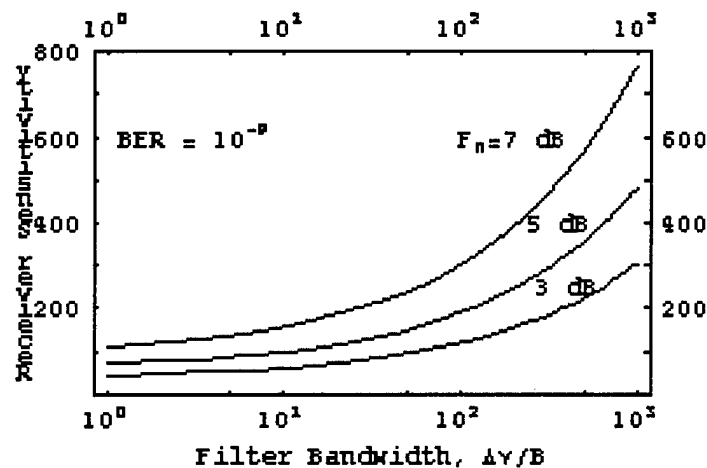


Fig. 10.4. Receiver sensitivity versus optical-filter bandwidth for several values of the noise figure $F_n$ when an optical amplifier is used for preamplification of the received signal.

[30] Smyth. P.P., Wyatt, R., Fidler, A., Eradley, P., Sayles, A. & Craig-Ryan, S., *Electron. Lett.*, 26, 1604, 1990;
Steele, R.C> & Walker, G.R., *IEEE Photon. Technol. Lett.*, 2, 753, 1990;
Blair, T.L. & Nakano, H., *Electron. Lett.*, 27, 835, 1991;
Saito, T., Sunohara, Y., Fukagai, K., Ishikawa, S., Henmi, N., Fujita, S. & Aoki, Y., *IEEE Photon. Technol. Lett.*, 3, 551, 1991;
Gnauck, A.H. & Giles, C.R., *IEEE Photon Technol. Lett.*, 4, 80, 1992;
Röhl, F.F. & Ayre, R.W., *IEEE Photon. Technol. Lett.*, 5, 358, 1993.

143

## Use of Soliton Pulses:

Bit rate can also be increased by the use of very short pulses known as solitons, which are the resultant pulses when the input signal is matched to fiber characteristics so that a balance is achieved between group-velocity dispersion (GDV) and self-phase modulation (SPM). In fact, Fig. 10.1, above, shows that group-velocity dispersion broadens optical pulses during their propagation inside the fiber except when the pulse is initially chirped correctly. Self-phase modulation results from the intensity dependence of the refractive index and imposes a chirp on the optical pulse. In order to obtain a soliton, GVD and SPM must match so that the SPM-induced chirp is canceled by the GVD-broadening of the pulse.

The wave equation in a dispersive nonlinear medium is required to describe soliton pulses. By taking Eq. (10.1), above, the effects of SPM can be included by adding a nonlinear term on the right side of the equation, which gives:

$$\frac{\partial A}{\partial z} + \beta_1 \frac{\partial A}{\partial t} + \frac{i}{2} \beta_2 \frac{\partial^2 A}{\partial t^2} - \frac{1}{6} \beta_3 \frac{\partial^3 A}{\partial t^3} = i\gamma |A|^2 A - \frac{\alpha}{2} A, \quad (10.2)$$

where $\alpha$ is a loss term and $\gamma$ is the nonlinearity parameter defined:

$$\gamma = \frac{2\pi n_2}{\lambda A_{eff}},$$

$n_2$ is the nonlinear refractive index coefficient and $A_{eff}$ is the effective core area. $\beta_2$ and $\gamma$ govern the effects of GVD and SPM, respectively.

Eq.10.1. is written in normalized form using:

$$\tau = \frac{t - \beta_1 z}{T_0}, \qquad \xi = \frac{z}{L_D}, \qquad U = \frac{A}{\sqrt{P_0}}$$

where $T_0$ is a measure of pulse width, $P_0$ is the peak power of the pulse and the dispersion length is:

$$L_D = \frac{T_0^2}{|\beta^2|}.$$

This normalized form is the *nonlinear Schrödinger equation* (NSE):

$$i\frac{\partial U}{\partial \xi} - \text{sgn}(\beta_2)\frac{1}{2}\frac{\partial^2 U}{\partial \tau^2} + N^2 |U|^2 U = 0 \quad (10.3) \text{ NSE}$$

where $\text{sgn}(\beta_2) = +1$ or $-1$, depending on whether $\beta_2$ is positive (normal GVD) or negative (anomalous GVD). The parameter $N$, represents *a dimensionless combination of the pulse and fiber parameters*:

$$N^2 = \gamma P_0 L_D = \frac{\gamma P_0 T_0^2}{|\beta_2|}.$$

Pulse like soliton solutions are found for the case of anomalous dispersion ($\beta_2 < 0$) and dark soliton solutions are found for the case of normal dispersion ($\beta_2 > 0$).

If the definition $u = NU$ is introduced as a renormalized amplitude, the canonical form of the NSE is obtained (with $\beta_2 < 0$):

$$i\frac{\partial u}{\partial \xi} + \frac{1}{2}\frac{\partial^2 u}{\partial \tau^2} + |u|^2 u = 0.$$

If an input pulse with an initial amplitude:

$$u(0,\tau) = N\sec h(\tau)$$

is introduced into the fiber, its shape remains unchanged when $N = 1$, but follows a periodic pattern when $N > 1$, but with its shape recovered at intervals.

For $N = 1$ (the fundamental soliton), the soliton is remarkably stable, but at other values of $N$ (higher-order solitons) chirping occurs (Fig. 10.5). On the other hand, if $N = 1$, the pulse evolves toward a sech pulse even if the input is Gaussian (Fig. 10.6). This evolution toward the "sech" pulse occurs for values of $N$ in the range 0.5 - 1.5 (Fig. 10.7).

In the case of normal dispersion, the intensity profile of the resulting solution is a dip in a uniform background which remains unchanged during propagation inside the fiber. The general solution for a dark soliton is:

$$u_d(\xi,\tau) = (\eta\tanh\varsigma - i\kappa)\exp[iu_0^2\xi],$$

where

$$\varsigma = \eta(\tau - \kappa\xi), \quad \eta = u_0\cos\phi, \quad \kappa = u_0\sin\phi \quad ,$$

for which $u_0$ is the amplitude of the background, $\phi$ is an internal phase angle, and $\eta$ and $\kappa$ are the amplitude and velocity of the dark soliton. The phase of a soliton changes across its width, as is shown in Fig. 10.8.

As each soliton pulse occupies only a fraction of a bit slot, the presence of pulses in neighboring bits can perturb a soliton because the combined optical field is not a solution of NSE. Therefore soliton interaction results. In order to model this effects, the NSE can be solved with a soliton pair as the input:

$$u(0,\tau) = \sec h(\tau - q_0) + r\sec h[r(\tau + q_0)]\exp[i\theta]$$

where $r$ is the relative amplitude of the two solitons, $\theta$ is the relative phase and $2q_0$ is the initial (normalized) separation. Fig. 10.9. shows the evolution of a soliton pair with

separation $q_0 = 3.5$ and for several values of the parameters $r$ and $\theta$. Soliton interaction depends on the relative phase $\theta$ and the amplitude ratio $r$.

Fig. 10 shows the evolution of a chirped pulse soliton with an input amplitude:

$$u(0,\tau) = N \sec h(\tau)\exp[-iC\tau^2/2],$$

where $C$ is the chirp parameter. The pulse is initially compressed mainly due to the positive chirp; the pulse then broadens but is then compressed a second time with tails gradually separating from the main peak. The main peak evolves into a soliton over a propagation distance $\xi > 15$. Only 83% of the energy is converted into a soliton for the case $C = 0.5$ shown in Fig. 10.10. For $C = 0.8$, the fraction reduces to 62%.
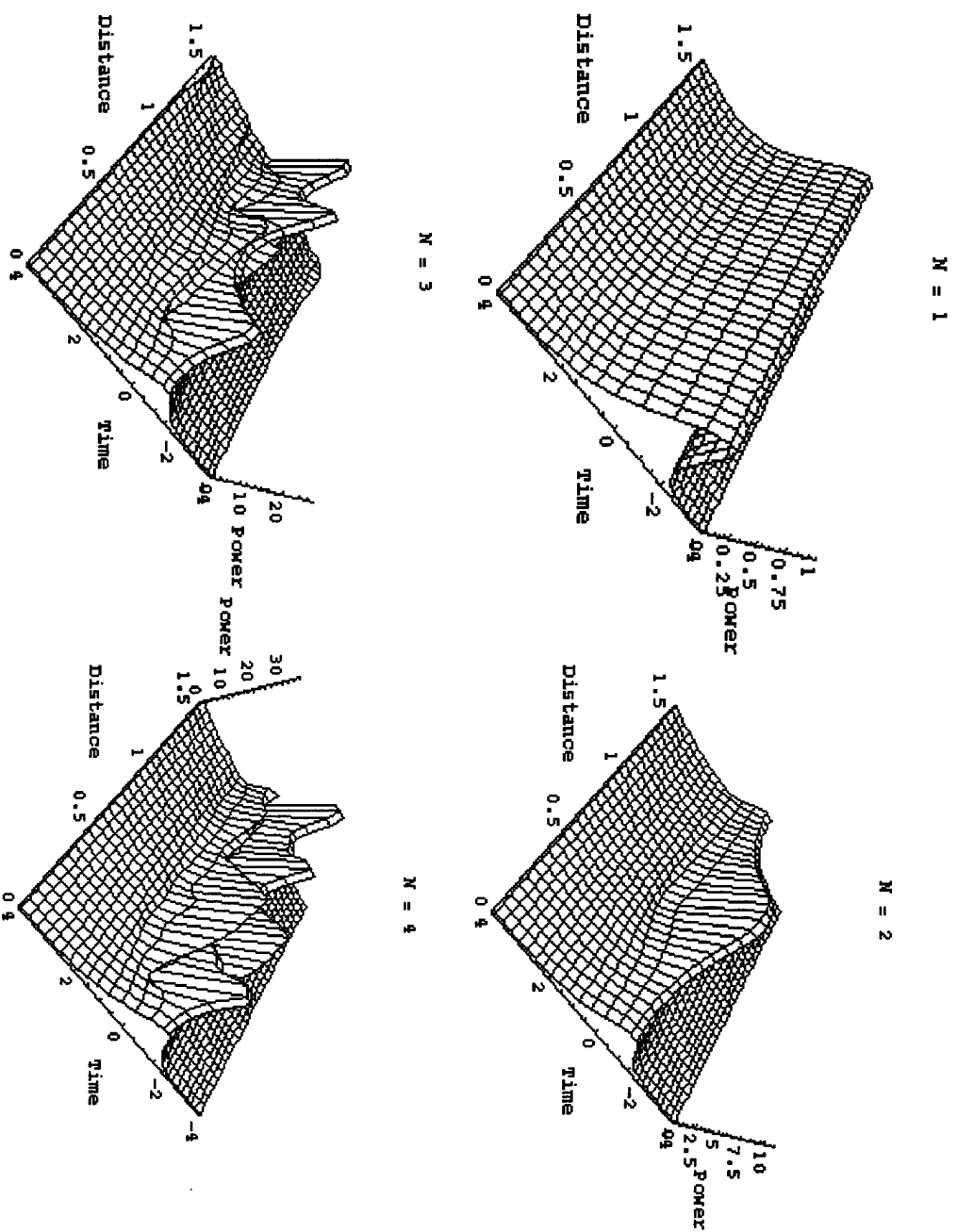
Fig. 10.5. Evolution of the first, second, third and fourth order solitons over one soliton period with $u(0, \tau) = N \sec h(\tau)$ as input.
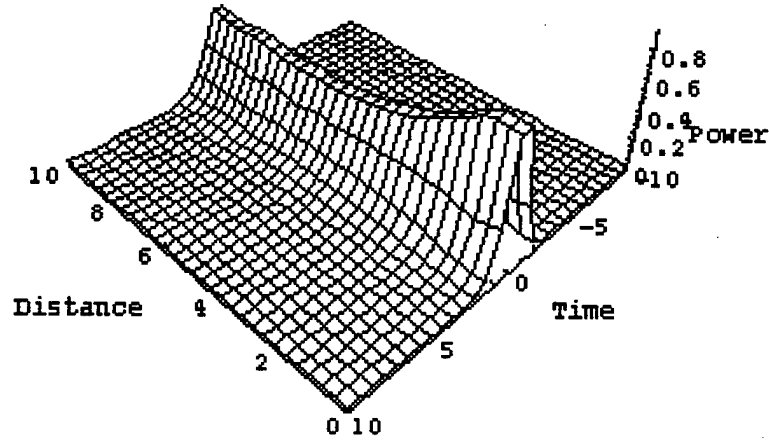
Fig. 10.6. Evolution of a Gaussian pulse with $N = 1$ over the range $\xi = 0\text{-}10$. Although the input is $u(0,\tau) = \exp[-\tau^2 / 2]$ there is an adjustment of the shape, width and peak power as the pulse evolves to the fundamental soliton.
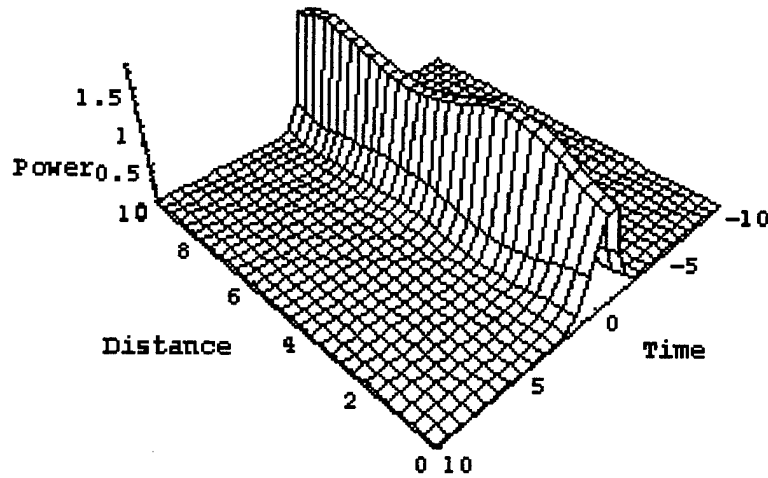
Fig. 10.7. Pulse evolution for a "sech" pulse with $N = 1.2$ over the range $\xi = 0 \text{ - } 10$. Although the input is $u(0,\tau) = 1.2 \sec h(\tau)$, i.e., $N = 1.2$, the pulse evolves toward the fundamental soliton, $N = 1$, by adjusting its width and peak power.

**A.**



**B.**
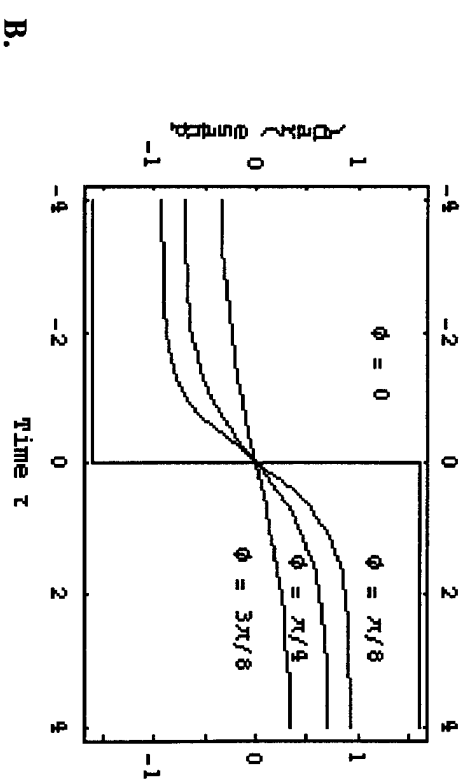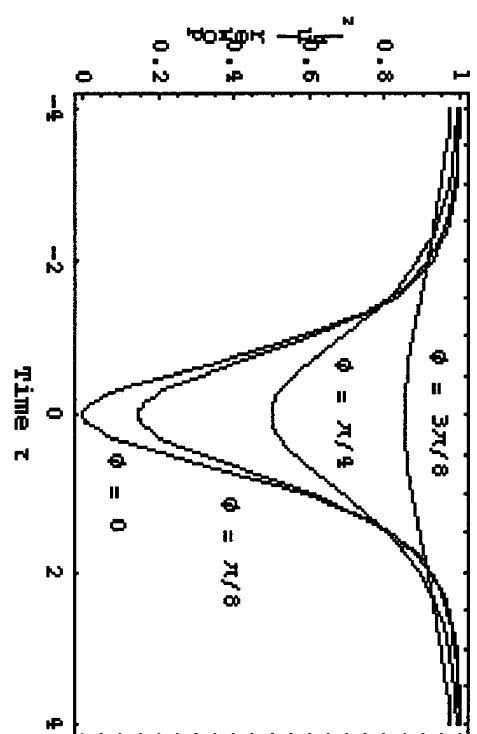
Fig. 10.8. (a) Intensity and (b) phase profiles of dark solitons for several values of the internal phase φ.

Θ = 0, r = 1.0

A(1)



Θ = 0, r = 1.0

A(2)

150

$\Theta = \pi/4, \; r = 1.0$

B(1)



$\Theta = \pi/4, \; r = 1.0$

B(2)

$\theta = \pi/2$, $\Upsilon = 1.0$

C(1)



$\theta = \pi/2$, $\Upsilon = 1.0$

C(2)

**D(1)**
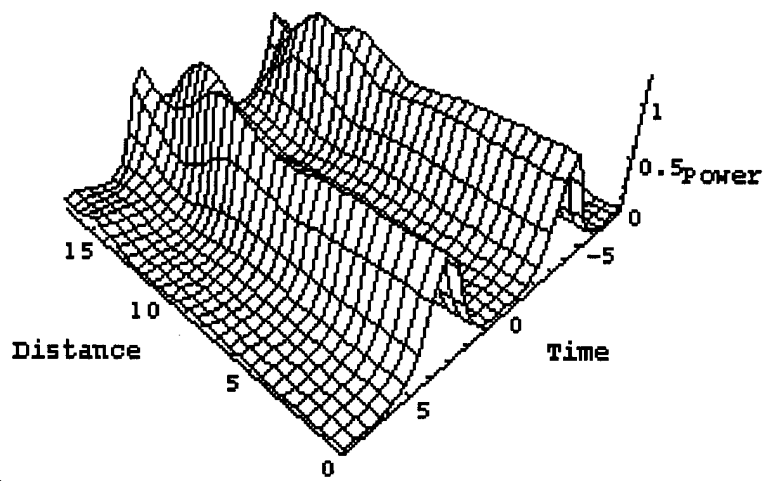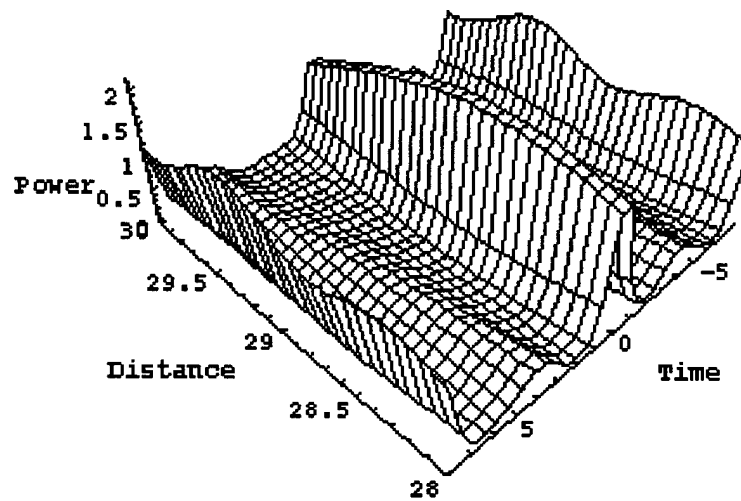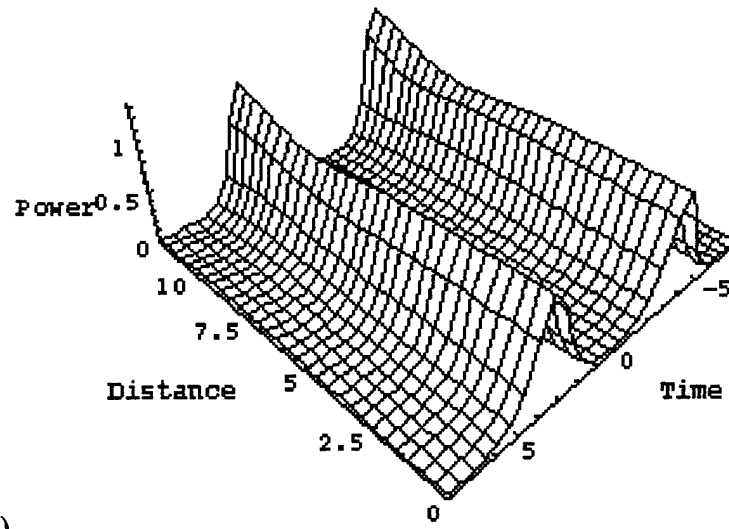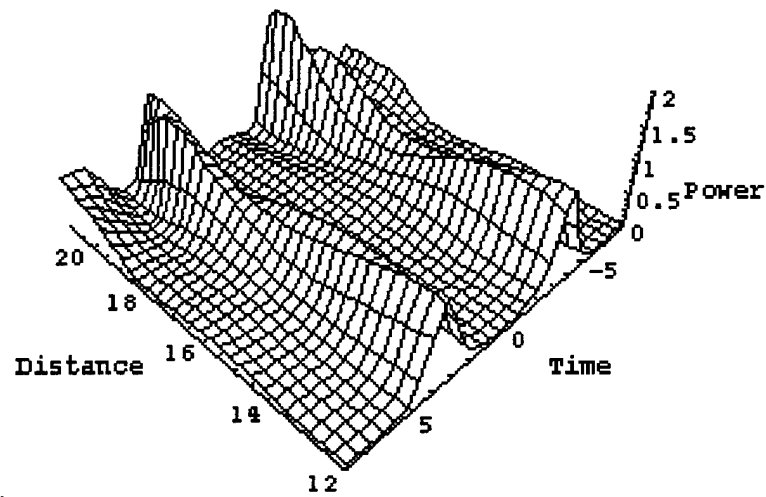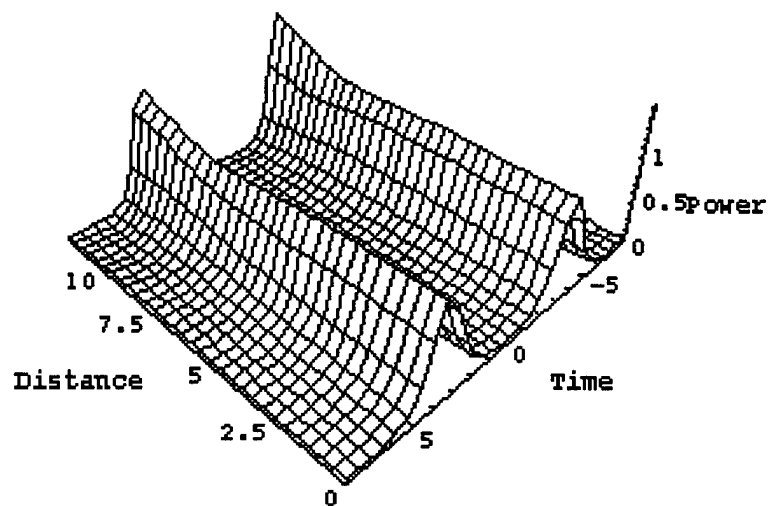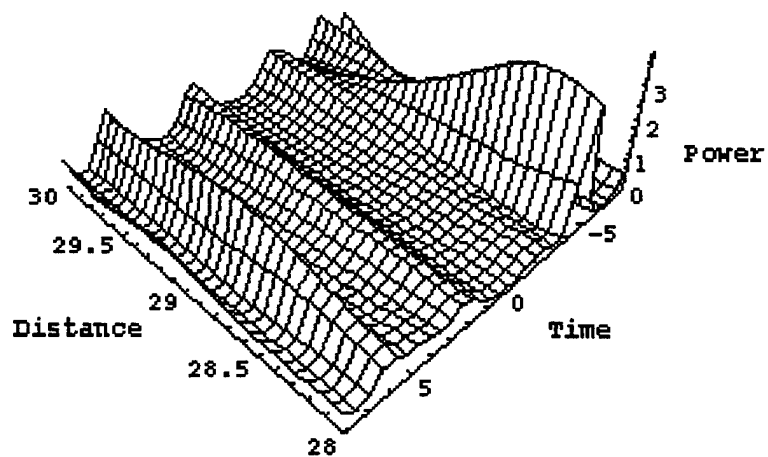
**D(2)**
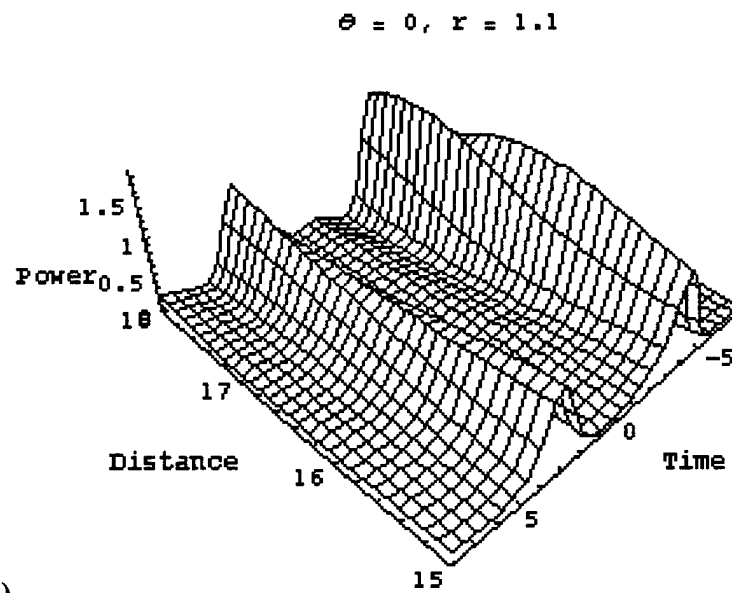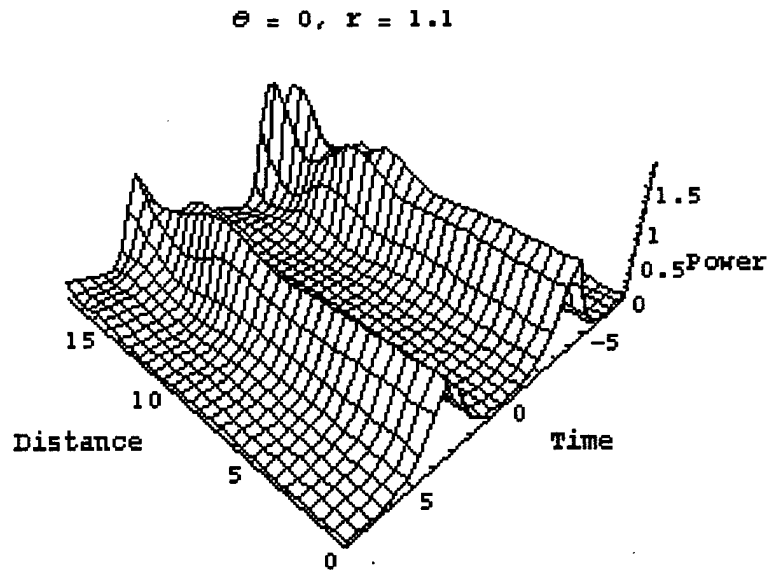
Fig. 10.9. Evolution of a soliton pair over a variety of dispersion lengths showing the effects of soliton interaction for different choices of amplitude ratio $r$ and relative phase $\theta$ and initial spacing $q_0$. Input amplitude: $u(0, \tau) = \sec h(\tau - q_0) + \tau \sec h[r(\tau + q_0)] \exp[i\theta]$.

A.
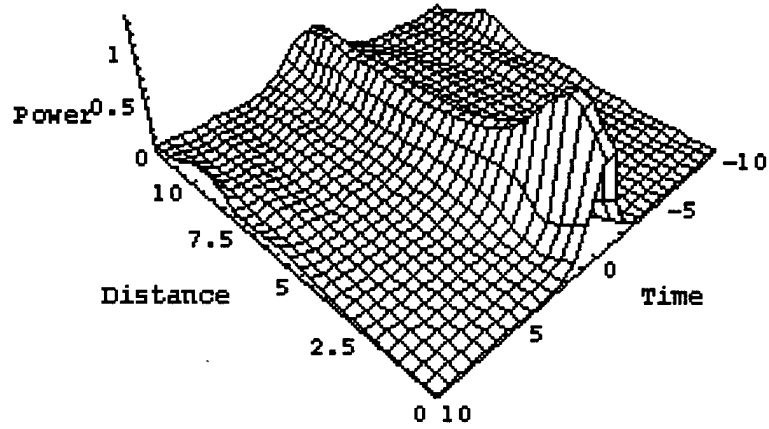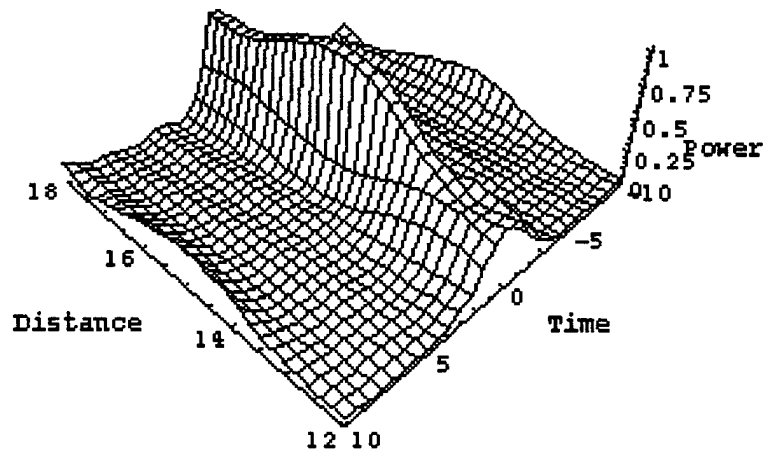
B.

Fig. 10.10. Evolution of a chirped optical pulse for $N = 1$, $C = 0.5$; A. $\xi = 0 - 12$; B. $\xi = 12 - 18$, with input $u(0, \tau) = N \sec h(\tau)\exp[-iC\tau^2 / 2]$.

## 11. Underlying Group Structure of Orthogonal Codes.

In this section we address the underlying group structure of the orthogonal codes: the hyperbolic congruence, the quadratic congruence, and the Welch-Costas codes. Achievement of the highest data rate optical communications - given a defined subcomponent performance - is dependent on achieving orthogonal codes with both excellent auto- and cross-correlation properties. Excellent performance in the case of one attribute, e.g., auto-correlation, is sometimes associated with poor performance in the other attribute, e.g., cross-correlation. To determine the group structure determining performance on both attributes, we initiated a study of the relative incidence of sequence occurrence across codes based on different prime numbers, and for sequences of 2,...., 6. We report the Mathematica algorithms in an Appendix and demonstrate the differences in group structure between the three types of orthogonal codes. The superiority of the hyperbolic and quadratic congruence codes in both auto- and cross-correlation properties, as compared with the superiority of the Welch-Costas codes in auto-correlation properties, but poor performance in cross-correlation properties, is mirrored in the lack of symmetry shown by the Welch-Costas codes in the analysis offered here.

### Introduction:

Orthogonal codes have one occurrence per frame and the sequence of occurrences across a superframe can be represented by a series of numbers which indicate the slot position for an occurrence in each frame of the superframe. Each code family is based on a prime number, $p$, and there are $p - 1$ codes generated per prime number. Therefore, there are 2 codes generated for $p = 3$, 4 codes for $p = 5$, 6 codes for $p = 7$ and 10 codes for $p = 11$, etc.

We constructed algorithms that permitted the generation of the codes in terms of the slot position of the code's occurrence in the frame for the three families of orthogonal codes: hyperbolic congruence, quadratic congruence and Welch-Costas codes. This permitted a visualization of each code's underlying group structure and the analyses to follow are based on this form of representation.

The following are the hyperbolic congruence codes for codes #1 - #10 for $p = 1$, 3, 5, 7 and 11:

$$
\begin{pmatrix}
\{1\} \\
\{1,\ 2\} \\
\{1,\ 3,\ 2,\ 4\} \\
\{1,\ 4,\ 5,\ 2,\ 3,\ 6\} \\
\{1,\ 6,\ 4,\ 3,\ 9,\ 2,\ 8,\ 7,\ 5,\ 10\}
\end{pmatrix}
$$

$$
\begin{pmatrix}
\{2,\ 1\} \\
\{2,\ 1,\ 4,\ 3\} \\
\{2,\ 1,\ 3,\ 4,\ 6,\ 5\} \\
\{2,\ 1,\ 8,\ 6,\ 7,\ 4,\ 5,\ 3,\ 10,\ 9\}
\end{pmatrix}
$$

$$
\begin{pmatrix}
\{3,\ 4,\ 1,\ 2\} \\
\{3,\ 5,\ 1,\ 6,\ 2,\ 4\} \\
\{3,\ 7,\ 1,\ 9,\ 5,\ 6,\ 2,\ 10,\ 4,\ 8\}
\end{pmatrix}
$$

$$\begin{pmatrix} \{4,\ 2,\ 3,\ 1\} \\ \{4,\ 2,\ 6,\ 1,\ 5,\ 3\} \\ \{4,\ 2,\ 5,\ 1,\ 3,\ 8,\ 10,\ 6,\ 9,\ 7\} \end{pmatrix}$$

$$\begin{pmatrix} \{5,\ 6,\ 4,\ 3,\ 1,\ 2\} \\ \{5,\ 8,\ 9,\ 4,\ 1,\ 10,\ 7,\ 2,\ 3,\ 6\} \end{pmatrix}$$

$$\begin{pmatrix} \{6,\ 3,\ 2,\ 5,\ 4,\ 1\} \\ \{6,\ 3,\ 2,\ 7,\ 10,\ 1,\ 4,\ 9,\ 8,\ 5\} \end{pmatrix}$$

$$(7\quad 9\quad 6\quad 10\quad 8\quad 3\quad 1\quad 5\quad 2\quad 4\,)$$

$$(8\quad 4\quad 10\quad 2\quad 6\quad 5\quad 9\quad 1\quad 7\quad 3\,)$$

$$(9\quad 10\quad 3\quad 5\quad 4\quad 7\quad 6\quad 8\quad 1\quad 2\,)$$

$$(10\quad 5\quad 7\quad 8\quad 2\quad 9\quad 3\quad 4\quad 6\quad 1\,)$$

Using the algorithm reported in the Appendix, the following Fig. 11.1 shows the incidence of sequence occurrence across codes for the hyperbolic congruence codes, $p = 1$, 2, 3, 5, 7 and 11. This Fig. 11.1 should be compared with Fig.s 11.2 and 11.3 to follow.
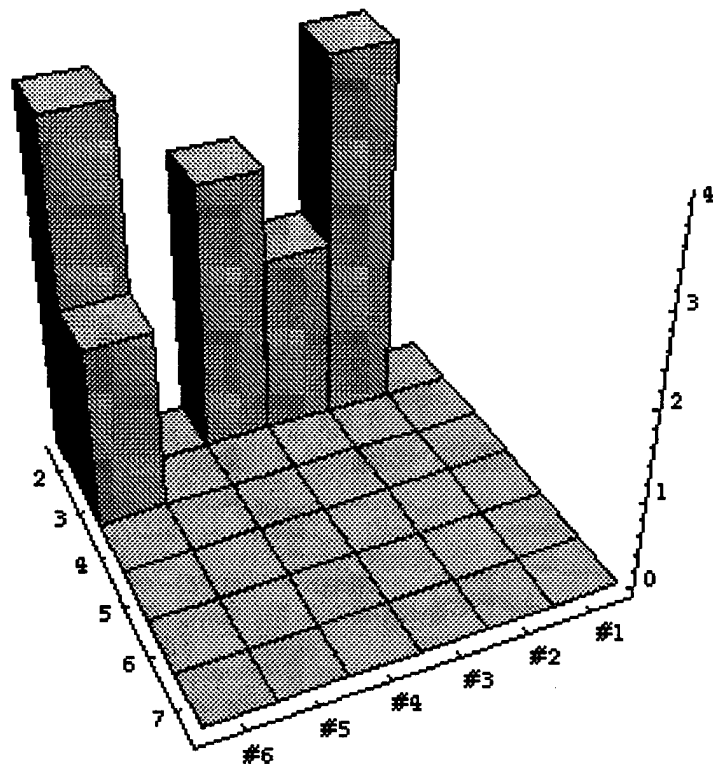
Fig. 11.1. The incidence of sequence recurrence across codes based on p = 1, 2, 3, 5, 7 and 11, and for the codes #1 - #6 and for sequences of length 2 through 7. In the case of the Hyperbolic Congruence Codes there is some recurrence at sequences of length 2 and one instance of a sequence of length 3.

The following are the quadratic congruence codes for codes #1 - #10 for $p =$
1, 3, 5, 7 and 11:

$$\begin{pmatrix} \{1\} \\ \{1,\ 2\} \\ \{1,\ 3,\ 2,\ 4\} \\ \{1,\ 4,\ 5,\ 2,\ 3,\ 6\} \\ \{1,\ 6,\ 4,\ 3,\ 9,\ 2,\ 8,\ 7,\ 5,\ 10\} \end{pmatrix}$$

$$\begin{pmatrix} \{2,\ 1\} \\ \{2,\ 1,\ 4,\ 3\} \\ \{2,\ 1,\ 3,\ 4,\ 6,\ 5\} \\ \{2,\ 1,\ 8,\ 6,\ 7,\ 4,\ 5,\ 3,\ 10,\ 9\} \end{pmatrix}$$

$$\begin{pmatrix} \{3,\ 4,\ 1,\ 2\} \\ \{3,\ 5,\ 1,\ 6,\ 2,\ 4\} \\ \{3,\ 7,\ 1,\ 9,\ 5,\ 6,\ 2,\ 10,\ 4,\ 8\} \end{pmatrix}$$

$$\begin{pmatrix} \{4,\ 2,\ 3,\ 1\} \\ \{4,\ 2,\ 6,\ 1,\ 5,\ 3\} \\ \{4,\ 2,\ 5,\ 1,\ 3,\ 8,\ 10,\ 6,\ 9,\ 7\} \end{pmatrix}$$

$$\begin{pmatrix} \{5,\ 6,\ 4,\ 3,\ 1,\ 2\} \\ \{5,\ 8,\ 9,\ 4,\ 1,\ 10,\ 7,\ 2,\ 3,\ 6\} \end{pmatrix}$$

$$\begin{pmatrix} \{6,\ 3,\ 2,\ 5,\ 4,\ 1\} \\ \{6,\ 3,\ 2,\ 7,\ 10,\ 1,\ 4,\ 9,\ 8,\ 5\} \end{pmatrix}$$

$$(\ 7\quad 9\quad 6\quad 10\quad 8\quad 3\quad 1\quad 5\quad 2\quad 4\ )$$

$$(\ 8\quad 4\quad 10\quad 2\quad 6\quad 5\quad 9\quad 1\quad 7\quad 3\ )$$

$$(\ 9\quad 10\quad 3\quad 5\quad 4\quad 7\quad 6\quad 8\quad 1\quad 2\ )$$

$$(\ 10\quad 5\quad 7\quad 8\quad 2\quad 9\quad 3\quad 4\quad 6\quad 1\ )$$

Using the algorithm reported in the Appendix, the following Fig. 11.2 shows the incidence of sequence occurrence across codes for the quadratic congruence codes, $p = 1$, 2, 3, 5, 7 and 11. This Fig. 11.2 should be compared with Fig. 11.1, above, and Fig. 11.3 to follow.



Quadratic Congruence Codes
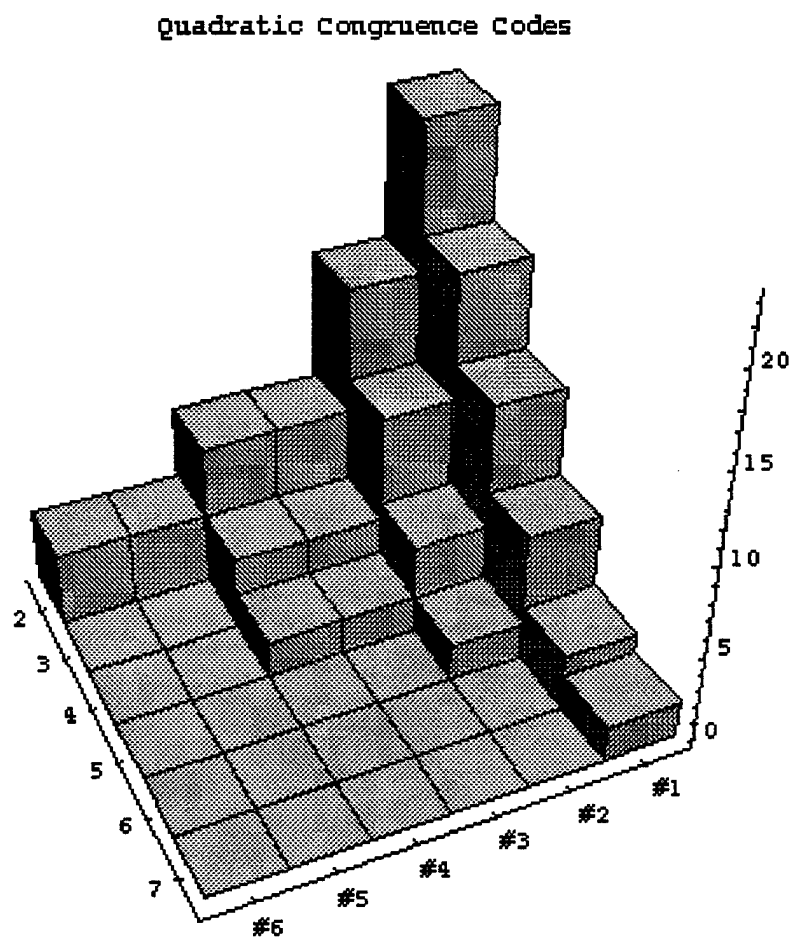
Fig. 11.2. The incidence of sequence recurrence across codes based on p = 1, 2, 3, 5, 7 and 11, and for the codes #1 - #6 and for sequences of length 2 through 7. In the case of the Quadratic Congruence Codes there is maximum recurrence at sequences of length 2 for code #1. The incidence of recurrence diminishes across codes #1 - #6. Recurrences at other sequence lengths is also maximum for code #1 and there is diminishing recurrence across codes #1 - #6.

159

The following are the Welch-Costas codes for codes #1 - #10 for $p = 1, 3, 5, 7$ and 11:

$$
\begin{pmatrix}
\{2, 1\} \\
\{2, 4, 3, 1\} \\
\{2, 4, 1, 2, 4, 1\} \\
\{2, 4, 8, 5, 10, 9, 7, 3, 6, 1\}
\end{pmatrix}
$$

$$
\begin{pmatrix}
\{1, 2\} \\
\{4, 3, 1, 2\} \\
\{4, 1, 2, 4, 1, 2\} \\
\{4, 8, 5, 10, 9, 7, 3, 6, 1, 2\}
\end{pmatrix}
$$

$$
\begin{pmatrix}
\{1, 2, 4, 3\} \\
\{6, 5, 3, 6, 5, 3\} \\
\{6, 1, 2, 4, 8, 5, 10, 9, 7, 3\}
\end{pmatrix}
$$

$$
\begin{pmatrix}
\{3, 1, 2, 4\} \\
\{1, 2, 4, 1, 2, 4\} \\
\{8, 5, 10, 9, 7, 3, 6, 1, 2, 4\}
\end{pmatrix}
$$

$$
\begin{pmatrix}
\{3, 6, 5, 3, 6, 5\} \\
\{10, 9, 7, 3, 6, 1, 2, 4, 8, 5\}
\end{pmatrix}
$$

$$
\begin{pmatrix}
\{5, 3, 6, 5, 3, 6\} \\
\{1, 2, 4, 8, 5, 10, 9, 7, 3, 6\}
\end{pmatrix}
$$

$$( \; 3 \quad 6 \quad 1 \quad 2 \quad 4 \quad 8 \quad 5 \quad 10 \quad 9 \quad 7 \; )$$

$$( \; 5 \quad 10 \quad 9 \quad 7 \quad 3 \quad 6 \quad 1 \quad 2 \quad 4 \quad 8 \; )$$

$$( \; 7 \quad 3 \quad 6 \quad 1 \quad 2 \quad 4 \quad 8 \quad 5 \quad 10 \quad 9 \; )$$

$$( \; 9 \quad 7 \quad 3 \quad 6 \quad 1 \quad 2 \quad 4 \quad 8 \quad 5 \quad 10 \; )$$

Using the algorithm reported in the Appendix, the following Fig. 11.3 shows the incidence of sequence occurrence across codes for the Welch-Costas codes, $p$ = 1, 2, 3, 5, 7 and 11. This Fig. 11.3 should be compared with Fig.s 11.1, and 11.2 above.
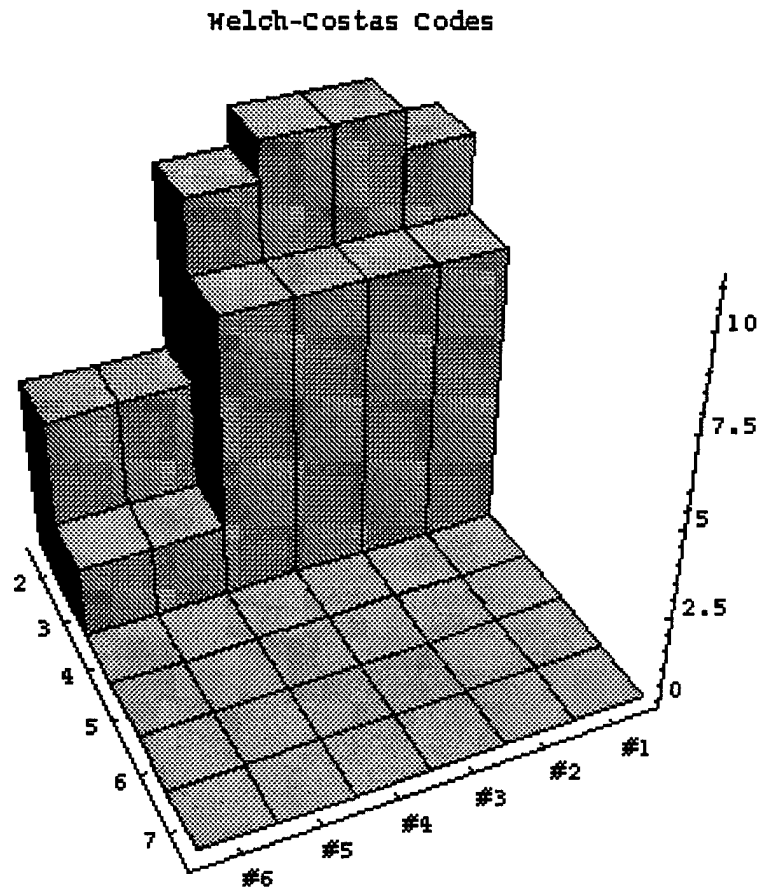


Welch-Costas Codes

Fig. 11.3. The incidence of sequence recurrence across codes based on p = 1, 2, 3, 5, 7 and 11, and for the codes #1 - #6 and for sequences of length 2 through 7. In the case of the Welch Costas Codes there is maximum recurrence at sequences of length 2 across all codes #1 - #6. There is also recurrence at sequence of length 3, and again across all codes #1 - #6.

Fig. s 11.1-11.3, together with Fig.s 11.4-11.9, indicate that the superiority of the hyperbolic and quadratic congruence codes in both auto- and cross-correlation properties, as compared with the superiority of the Welch-Costas codes in auto-correlation properties, but poor performance in cross-correlation properties, is mirrored in the lack of symmetry shown by the Welch-Costas codes in the analysis offered by Fig.s 11.8 and 11.9. This approach will be pursued in the future.

161

Hyperbolic Congruence Codes, p = 1-19, #1
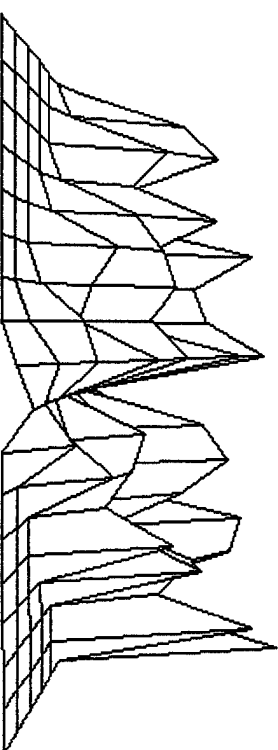
Hyperbolic Congruence Codes, p = 1-19, #2
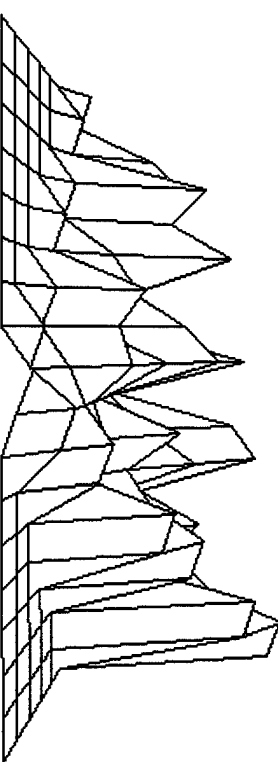
Hyperbolic Congruence Codes, p = 1-19, #3
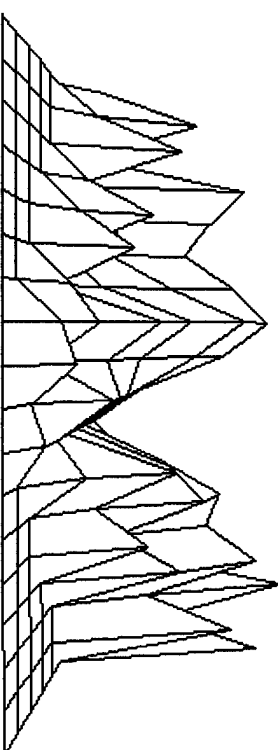
Hyperbolic Congruence Codes, p = 1-19, #4
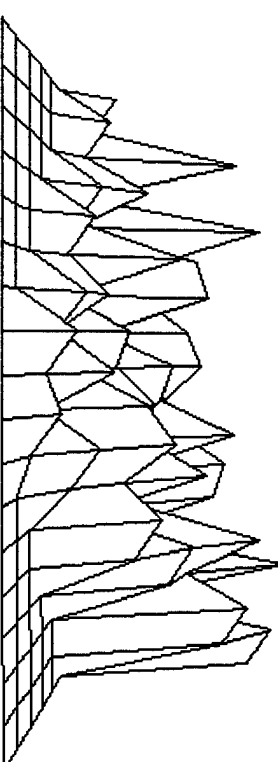
Hyperbolic Congruence Codes, p = 1-19, #5
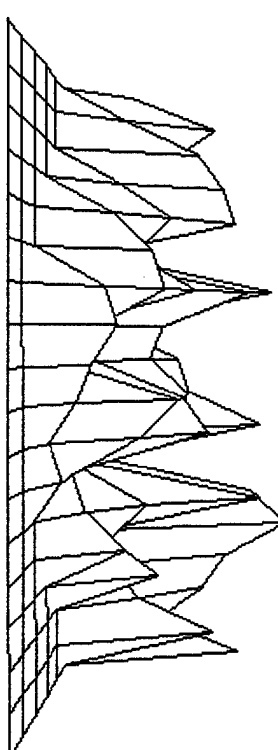
Fig. 11.4. Hyperbolic Congruence Codes, p = 1 - 19, Codes #1 - #5.

Fig. 11.5. Hyperbolic Congruence Codes, p = 1- 19, Codes #1 - #5.
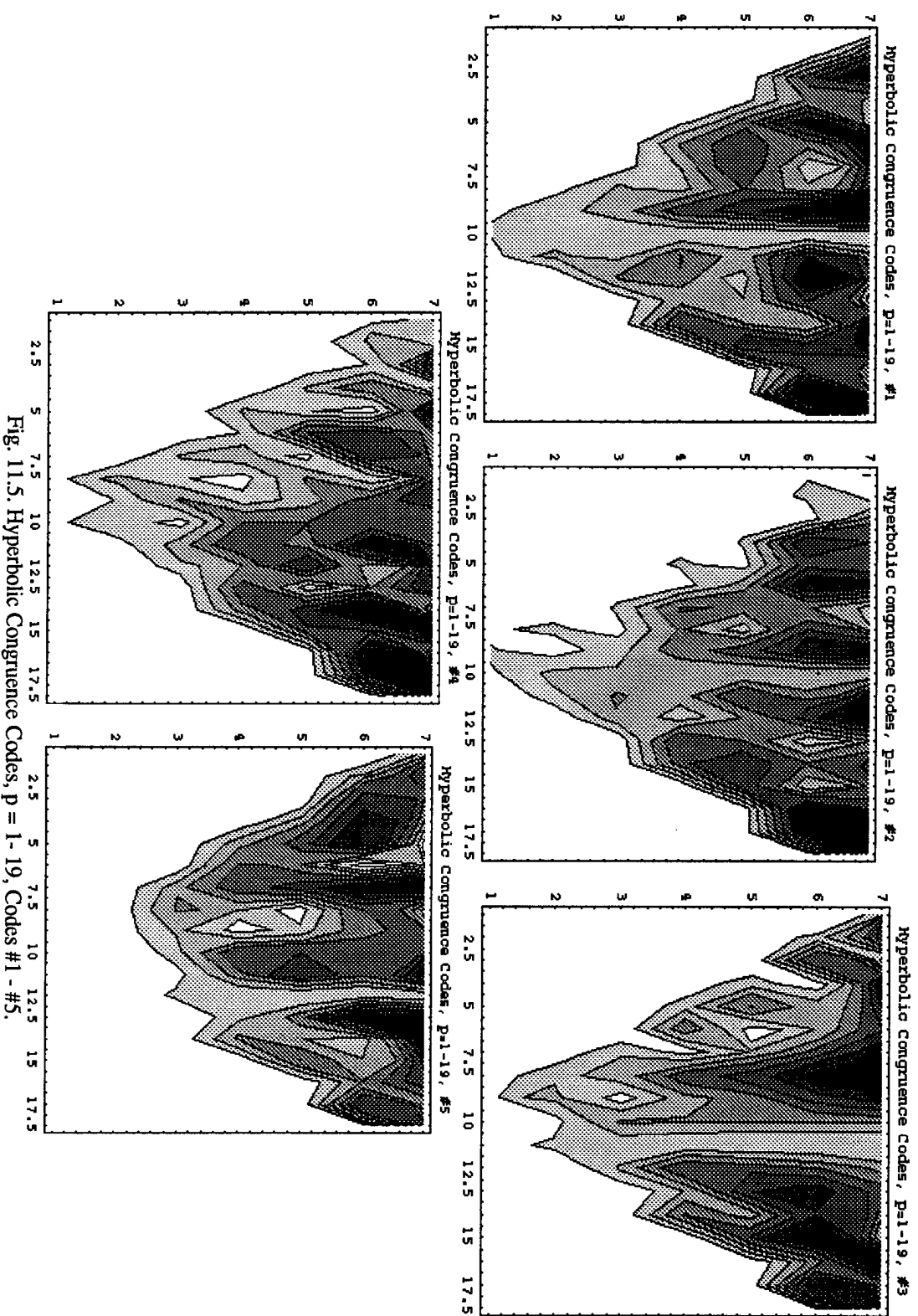
Quadratic Congruence Codes, p = 1-19, #1
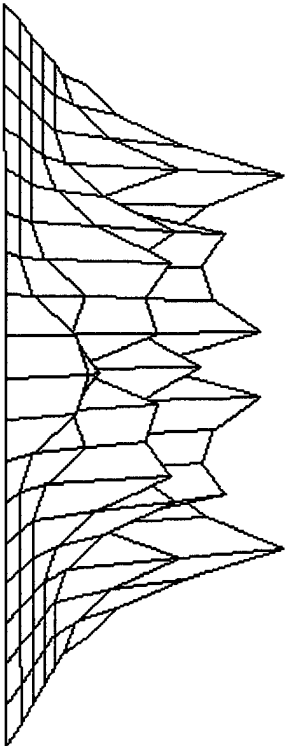
Quadratic Congruence Codes, p = 1-19, #2

Quadratic Congruence Codes, p = 1-19, #3
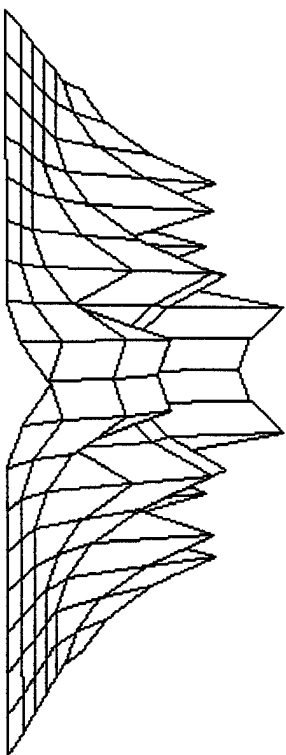
Quadratic Congruence Codes, p = 1-19, #4
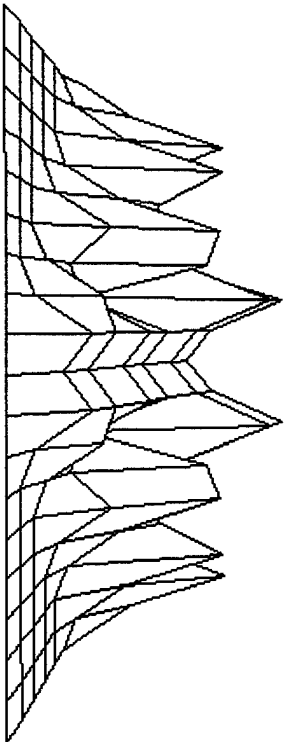
Quadratic Congruence Codes, p = 1-19, #5
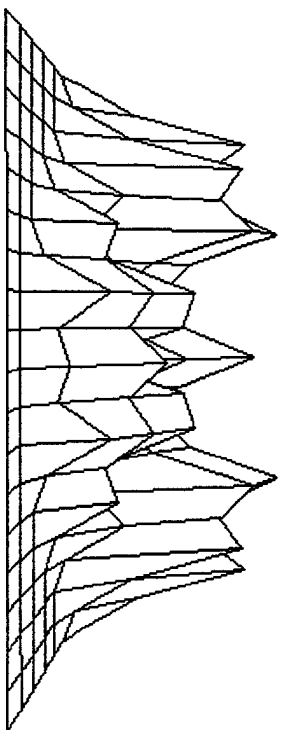
Fig. 11.6. Quadratic Congruence Codes, p = 1 - 19, Codes #1 - #5.
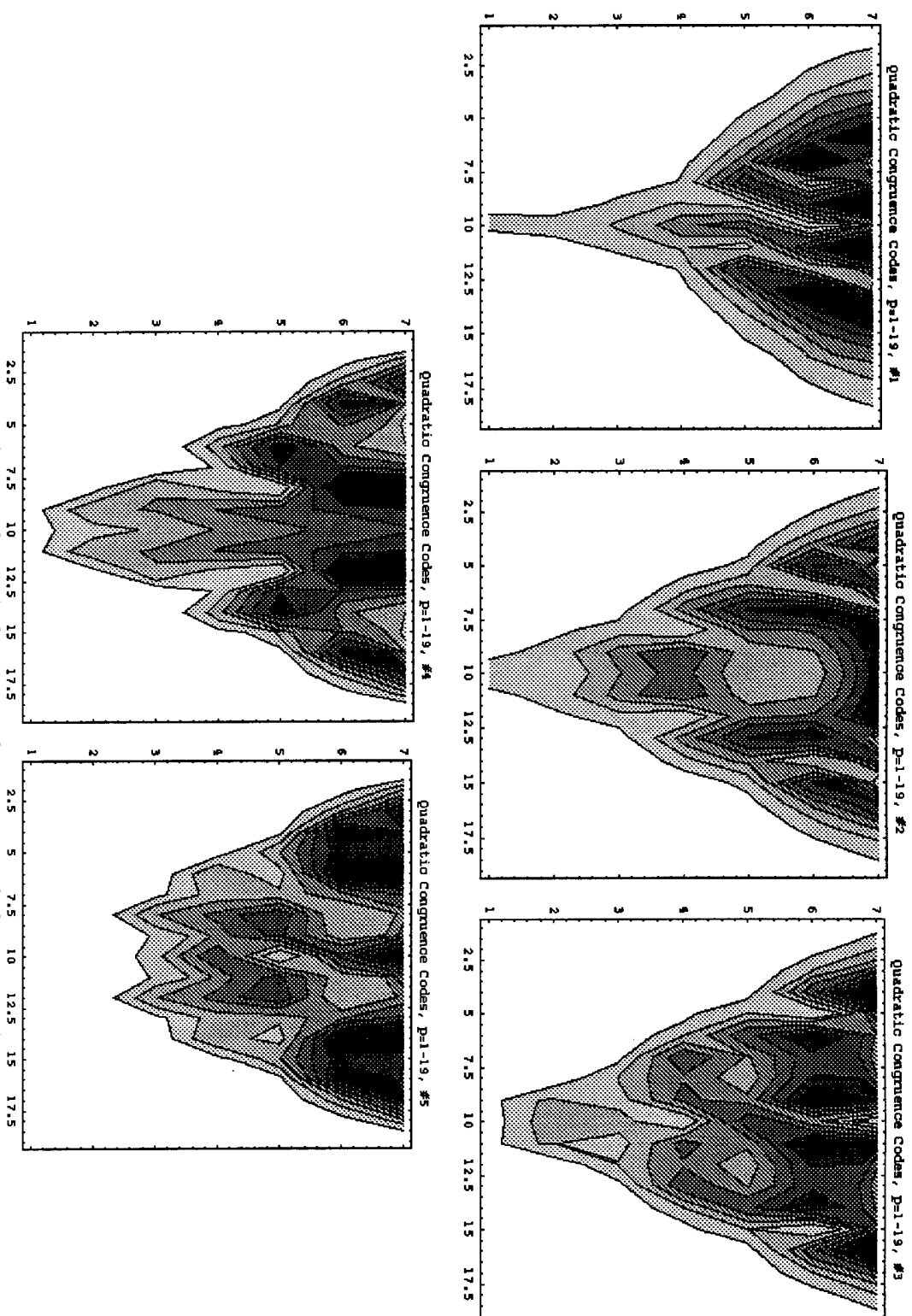
Fig. 11.7. Quadratic Congruence Codes, p = 1 - 19, Codes #1 - #5.

Welch-Costas Codes, p = 1-19, #1
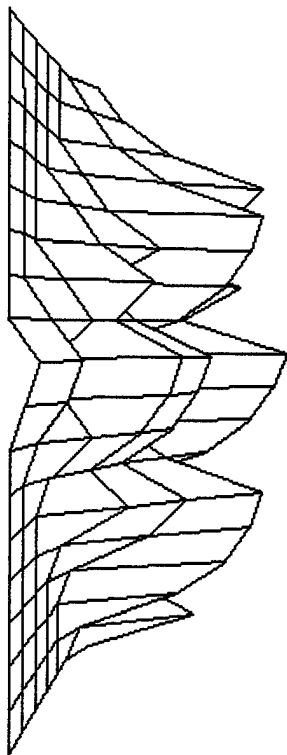
Welch-Costas Codes, p = 1-19, #2
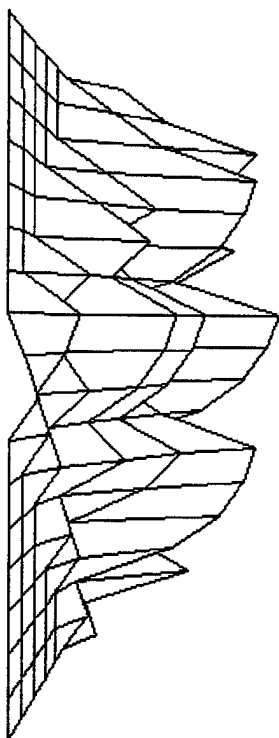
Welch-Costas Codes, p = 1-19, #3
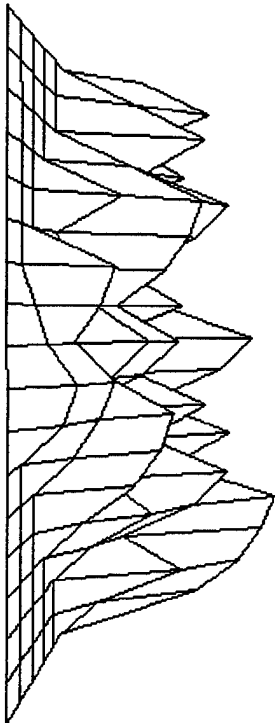
Welch-Costas Codes, p = 1-19, #4
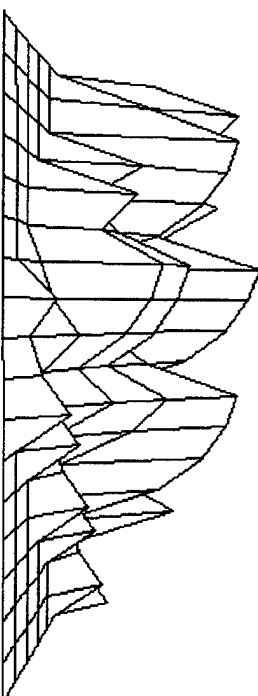
Welch-Costas Codes, p = 1-19, #5
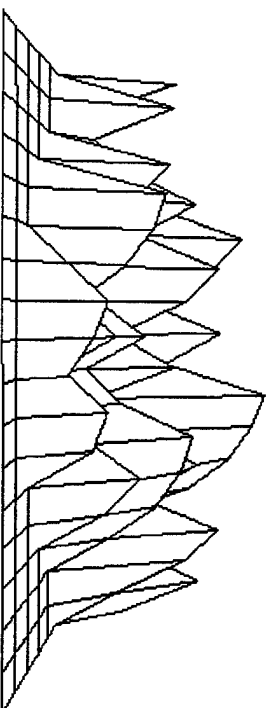
Fig. 118. Welch-Costas Codes, p = 1 - 19, Codes #1 - #5.
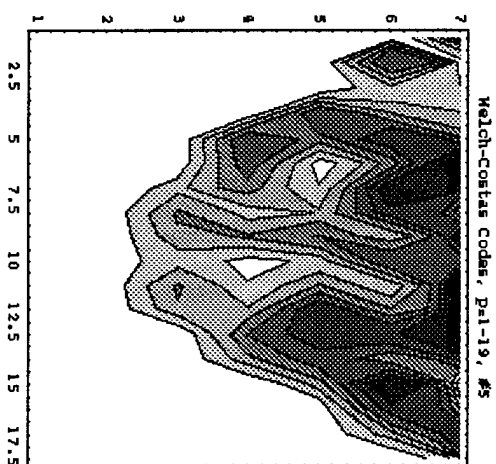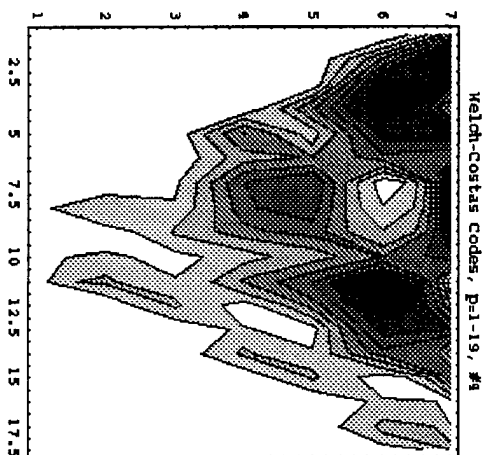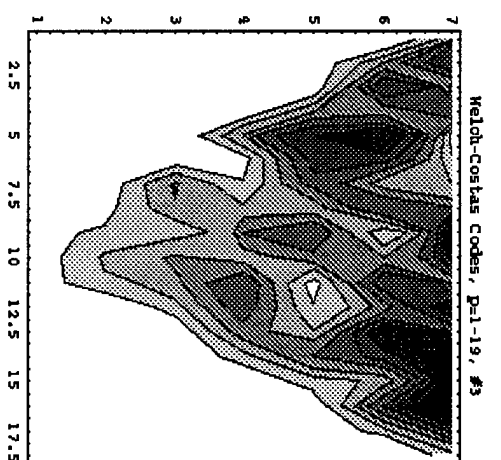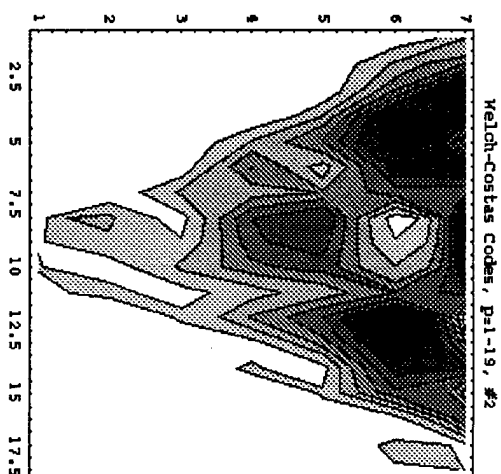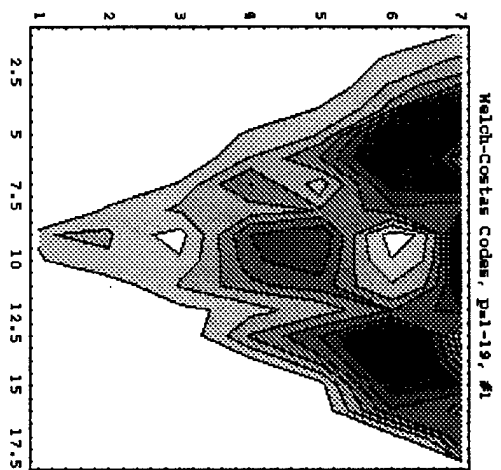
Fig. 11.9. Welch-Costas Codes, p = 1 - 19, Codes #1 - #5.

# Appendix 11.1

(1) Sequence determination for **hyperbolic congruence codes**, p = 1, 2, 3, 5, 7 and 11, for sequences 2,....., 6.

```
p=11;
q=1;
oneStepA[s_,q_]:=Table[Extract[Position[
                    Transpose[Table[
    If[(Mod[q-n*r,s])==0,1,0],
    {n,1,s-1},{r,1,s-1}]],1],
                    {x,2}],{x,1,s-1}];
ZZZ[x_]:=DeleteCases[Table[If[PrimeQ[i] && i>q,oneStepA[i,q]],{i,1,x}],
                    Null];
AR1=ZZZ[p];
Howmany=Length[AR1];
z={};
Do[AppendTo[z,AR1[[i]]],{i,1,Howmany}];
z=Flatten[z];
Howlong=Length[z];
For[n=2,n<(Howlong-1),n++,
  Do[excerpt=Take[z,{x+1,x+n}];
     remainder=Drop[z,{x+1,x+n}];
  If[MatchQ[remainder,{___,Sequence@@
  excerpt,___}],Print[excerpt],Continue[] ],
  {x,0,Howlong-n}]]
```

(2) Sequence determination for **quadratic congruence codes**, p = 1, 2, 3, 5, 7 and 11, for sequences 2,....., 6.

```
p=11;
q=1;
oneStepA[s_,q_]:=Table[Extract[Position[
                    Transpose[Table[
    If[(Mod[n-(q*0.5*(r*(r+1))),s])==0,1,0],
    {n,0,s-1},{r,0,s-1}]],1],
                    {x,2}],{x,1,s}];
ZZZ[x_]:=DeleteCases[Table[If[PrimeQ[i] && i>q,oneStepA[i,q]],{i,1,x}],
                    Null];
AR1=ZZZ[p];
Howmany=Length[AR1];
z={};
Do[AppendTo[z,AR1[[i]]],{i,1,Howmany}];
z=Flatten[z];
Howlong=Length[z];
For[n=2,n<(Howlong-1),n++,
  Do[excerpt=Take[z,{x+1,x+n}];
     remainder=Drop[z,{x+1,x+n}];
  If[MatchQ[remainder,{___,Sequence@@
  excerpt,___}],Print[excerpt],Continue[] ],
  {x,0,Howlong-n}]]
```

(3) Sequence determination for **Welch-Costas codes**, p = 1, 2, 3, 5, 7 and 11, for sequences 2,....., 6.

```
p=11;
q=1;
oneStepA[s_,q_]:=Table[Extract[Position[
                    Transpose[Table[
                    If[(Mod[n-q*(2^r),s])==0,1,0],
          {n,1,s-1},{r,1,s-1}]],1],
                    {x,2}],{x,1,s-1}];
ZZZ[x_]:=DeleteCases[Table[If[PrimeQ[i] && i>q,oneStepA[i,q]],{i,3,x}],
                    Null];
AR1=ZZZ[p];
Howmany=Length[AR1];
z={};
Do[AppendTo[z,AR1[[i]]],{i,1,Howmany}];
z=Flatten[z];
Howlong=Length[z];
For[n=2,n<(Howlong-1),n++,
   Do[excerpt=Take[z,{x+1,x+n}];
      remainder=Drop[z,{x+1,x+n}];
   If[MatchQ[remainder,{___,Sequence@@
   excerpt,___}],Print[excerpt],Continue[] ],
          {x,0,Howlong-n}]]
```

## 12.0 Bit Parallel Wavelength Division (BPWD).

### 12.1 Pulse Alignment.

In this section we address the possibility of increasing data rate in optical fiber communications by using the method of bit parallel wavelength division (BPWD) which utilizes, among other techniques, the "shepherding pulse" to maintain pulse alignment. Both method and technique are due to Yeh & Bergman. The shepherding technique relies on the cross-phase modulation effect. Simulation of this technique involves the numerical evaluation of simultaneous coupled nonlinear Schrödinger equations. Yeh & Bergman used the split-Fourier method. We are able to solve the coupled equations using approximation methods. Although limitations in computer memory precluded our simulating over optical fiber distances greater than 10 km, we are able to confirm that a shepherding pulse will (1) decrease the bandwidth and heighten the amplitude of shepherded pulses; and (2) align to a time slot shepherded pulses propagating before and after that time slot. We also show that the effect is due to the greater amplitude of the shepherding pulse. These results are obtained within an analysis of the more general relations of dispersive effects, the nonlinear Schrödinger equation and cross-phase modulation.


*Dispersive Relations:*

The dispersive properties of optical fibers are characterized as follows. It is well known that the group velocity, $v_g$, is: $v_g = \dfrac{d\omega}{dk}$ and the phase velocity, $v_0$, is: $v_0 = \dfrac{\omega}{k} = const.$, so that:

$$v_g = \frac{d(kv_0)}{dk} = v_0 + k\frac{dv_0}{dk}.$$

In the case of a linear dispersive transmission line, the equation of motion is:

$$\frac{\partial^2 A}{\partial t^2} - v_0^2 \frac{\partial^2 A}{\partial x^2} + \omega_0^2 A = 0,$$

with dispersion relation:

$$\omega = \sqrt{\omega_0^2 + v_0^2 k^2}.$$

The phase velocity, $v$, and the group velocity, $v_g$, are:

$$v(k) = \frac{\omega}{k} = \frac{1}{k}\sqrt{\omega_0^2 + v_0^2 k^2},$$

$$v_g(k) = \frac{d\omega}{dk} = \frac{v_0^2 k}{\sqrt{\omega_0^2 + v_0^2 k^2}}.$$

Fig. 12.1.1 shows the phase velocity and the group velocity as function of $k$ and various values of $\omega_0$.
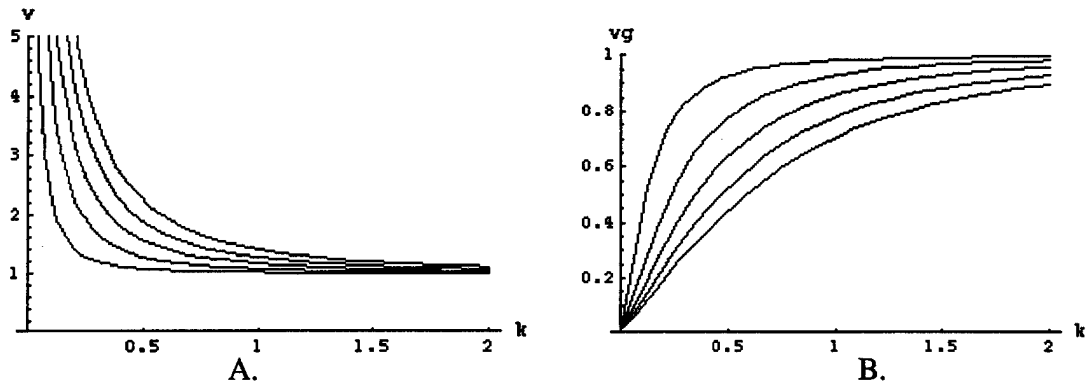
Fig. 12.1.1. A. Phase velocity and B. group velocity as a function of $k$ and various values of $\omega_0$.
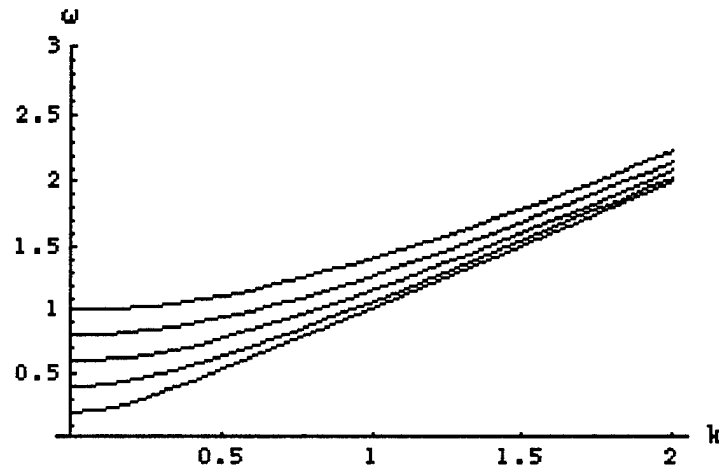


Fig. 12.1.2. The dispersion relation as a function of k and various values of $\omega_0$.

## Nonlinear Schrödinger Equation:

The nonlinear Schrödinger equation (NLS) describing soliton propagation in optical fibers in one form is:

$$i\frac{\partial A}{\partial t}+\frac{1}{2}\frac{\partial^2 A}{\partial x^2}+|A|^2 A = 0.$$

By setting $A = G/F$, where $F$ is a real function, and using the Hirota special bilinear operators defined:

$$D_t^m(a.b) = \left(\frac{\partial}{\partial t}-\frac{\partial}{\partial t'}\right)^m a(x,t)b(x,t'), \quad at\ t' = t;$$

$$D_x^n(a.b) = \left(\frac{\partial}{\partial x}-\frac{\partial}{\partial x'}\right)^n a(x,t)b(x,t'), \quad at\ x' = x,$$

where $m$ and $n$ are positive integers, the following is obtained[1]:

$$i\frac{D_t G.F}{F^2} + \frac{1}{2}\left\{\frac{D_x^2 G.F}{F^2} - \frac{G}{F}\frac{D_x^2 F.F}{F^2}\right\} + \frac{G}{F}\frac{GG*}{F^2} = 0.$$

Therefore, F and G will be solutions if they are chosen to satisfy:

$$\left(iD_t + \frac{1}{2}D_x^2\right)G.F = 0, \quad D_x^2 F.F = 0.$$

A solution is found by expanding $F$ and $G$ as a power series which self-truncates resulting in an exact two-soliton solution:

$$A(x,t) = \frac{G}{F} = 4Exp\left[\frac{it}{2}\right]\frac{\cosh[3x] + 3\exp[4it]\cosh[x]}{\cosh[4x] + 4\cosh[2x] + 3\cosh[4t]}$$

After some manipulation this can be simplified to[2]:

$$A(x,t) = -12\frac{3 + 4\cosh(2x - 8t) + \cosh(4x - 64t)}{\{3\cosh(x - 28t) + \cosh(3x - 36t)\}^2}$$

Fig. 12.1.3 shows the two soliton solution at various time intervals in which a larger amplitude wave catches a smaller amplitude wave, coalesces to form a single wave and then moves away from the smaller wave.



A



B

---
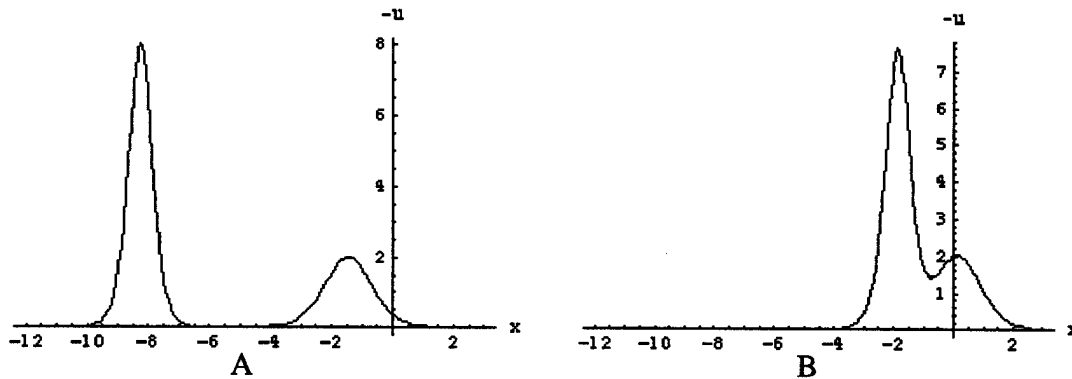
[1] cf. Remoissenet, M., *Waves Called Solitons: Concepts and Experiments*, Springer, New York, 1994, p. 223.

[2] Drazin, P.G. & Johnson, R.S., *Solitons: An Introduction*, Cambridge U. Press, 1989.

172

-u

6
5
4
3
2
1

-6   -4   -2        2   4   6   x

C

-u

7
6
5
4
3
2
1

-4   -2        2   4   6   8   10   x

D

-u

8

6

4

2

-2        2   4   6   8   10   12   x

E
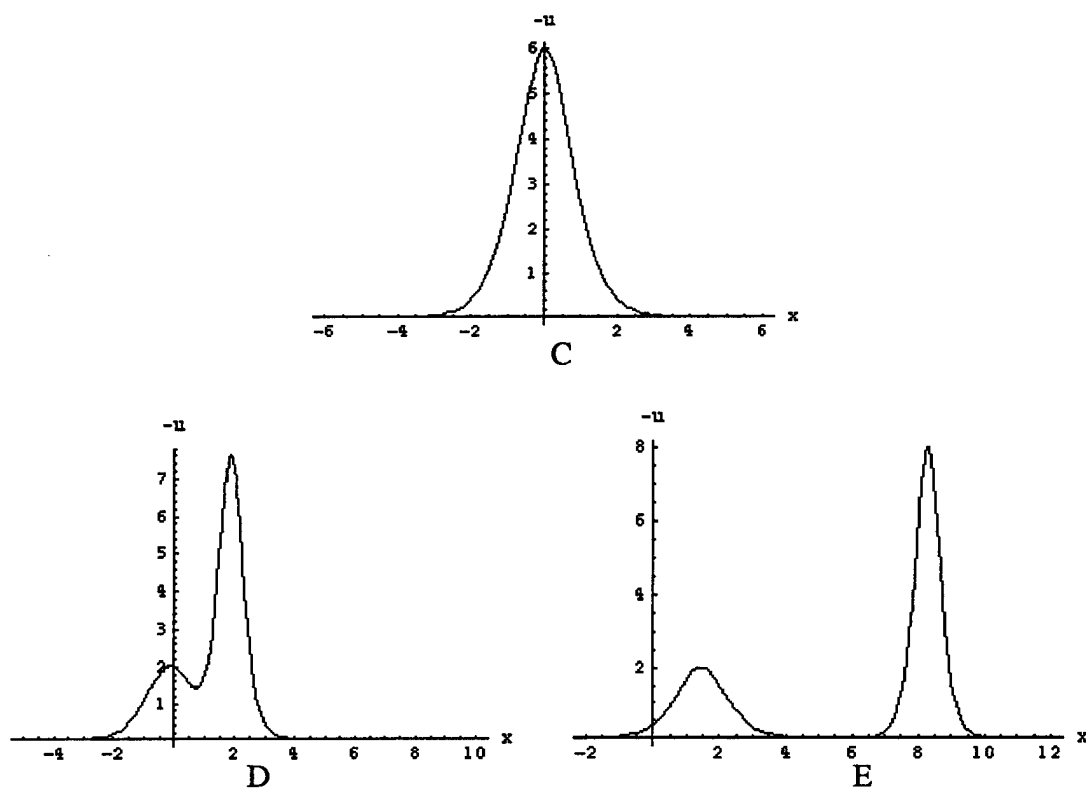
Fig. 12.1.3 Two-soliton solution in which a larger amplitude wave catches a smaller amplitude wave (A and B), coalesces (C), and then moves away from the smaller amplitude wave (D, E).

The N-soliton solution is[3]:

$$A(x,t) \approx -2\sum_{n=1}^{N} n^2 \sec h^2\left\{n(x - 4n^2 t) \mp x_n\right\}$$

-A

12
10
8
6
4
2

-2        2   4   6   x

A

-A

17.5

15

12.5

10

7.5

5

2.5

-2        2   4   6   x

B
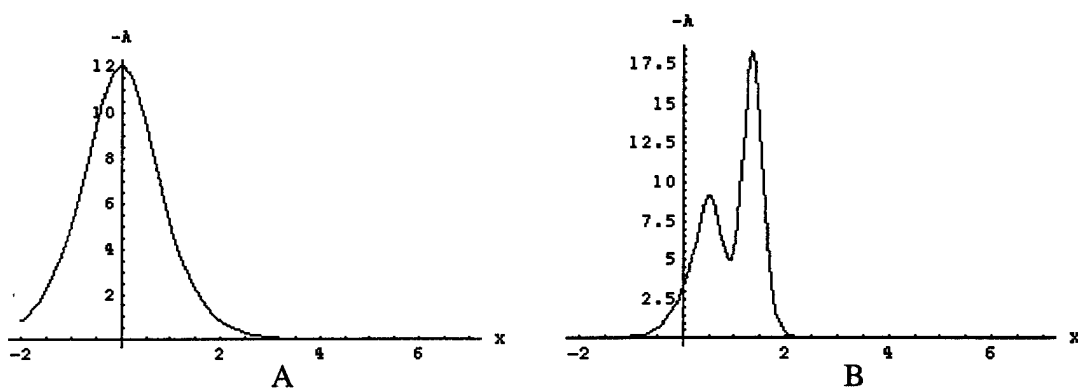
[3] Drazin, P.G. & Johnson, R.S., *Solitons: An Introduction*, Cambridge U. Press, 1989, p. 79.
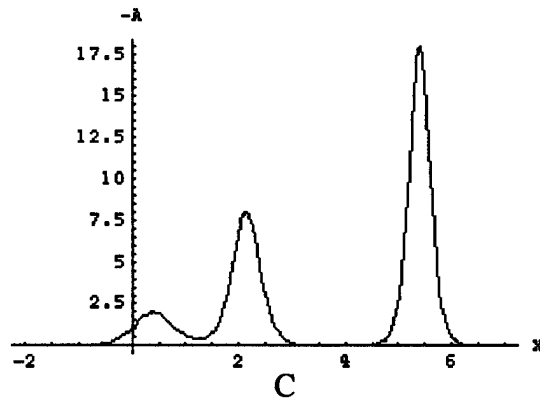
Fig. 12.1.4. Three soliton solution with (A) $A(x,0) = -12\ sech^2\ x$; (B) $t = 0.05$; (C) $t = 0.2$.

The interaction of two solitons is shown in Fig. 12.1.5, in which $|A(x,t)|$ satisfies the NLS:

$$iA_t + A_{xx} + A|A|^2 = 0,$$

and with:

$$A(x,0) = \sqrt{2}\left\{\exp\left[i\left(\frac{x-5}{2}\right)\right]\sec h(x-5) + \exp\left[-i\left(\frac{x-15}{2}\right)\right]\sec h(x-15)\right\}.$$

174
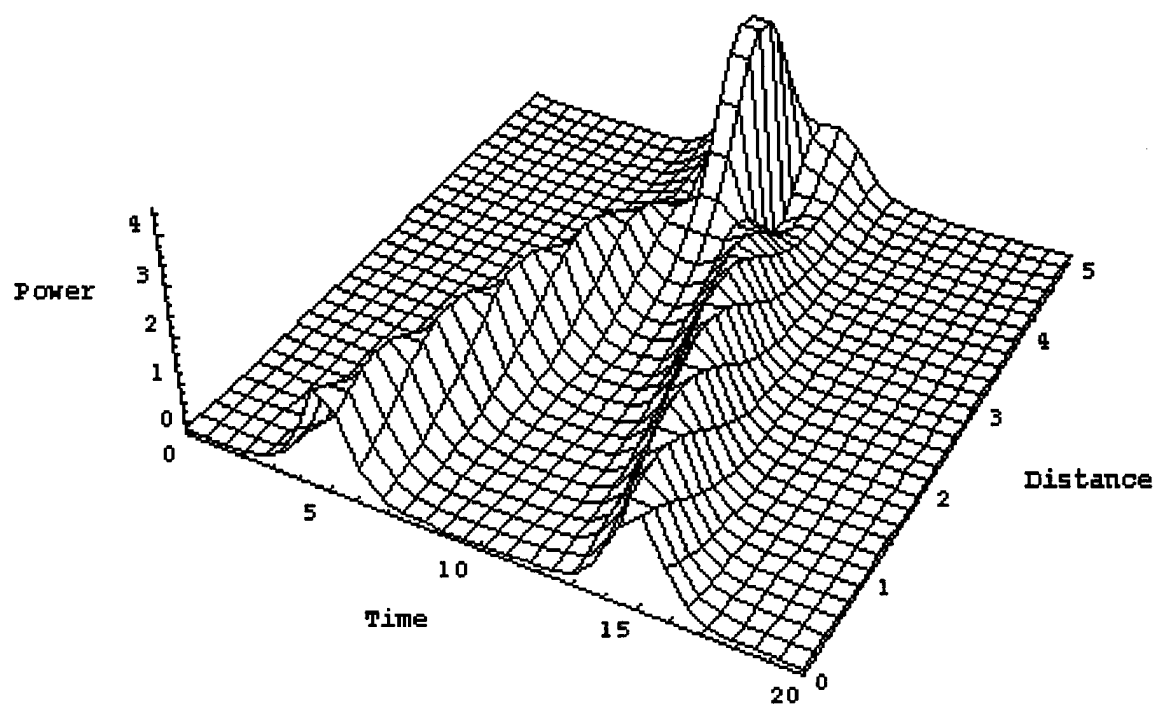
Fig. 12.1.5A Interaction of 2 solitons: distance 0-5.
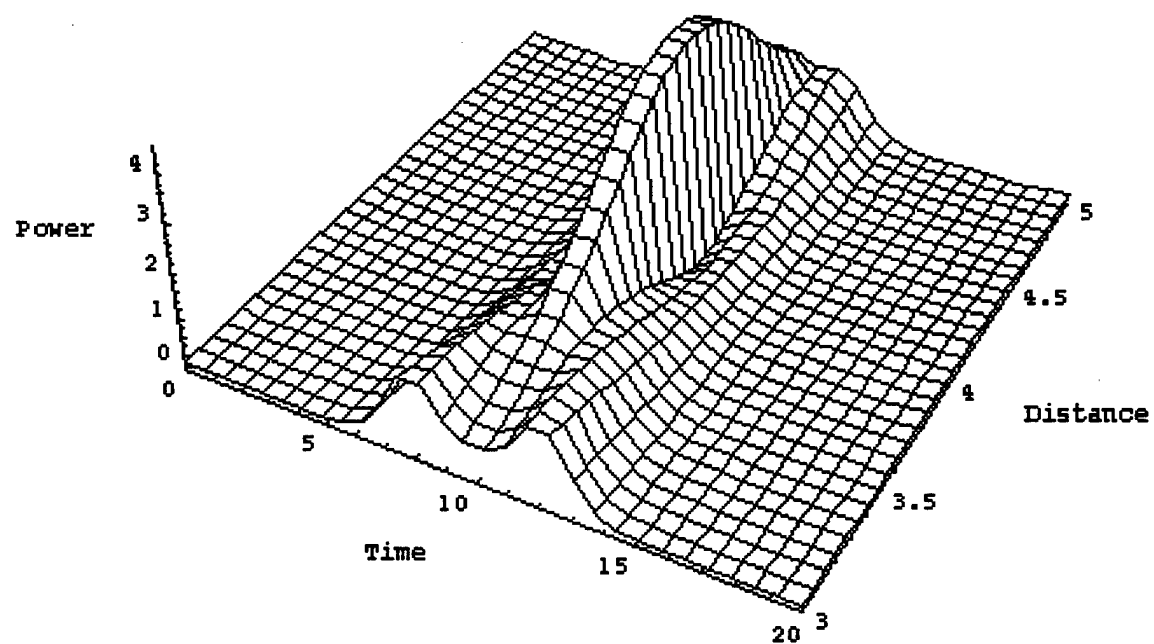
Fig. 12.1.5B Interaction of 2 solitons: distance 3-5.
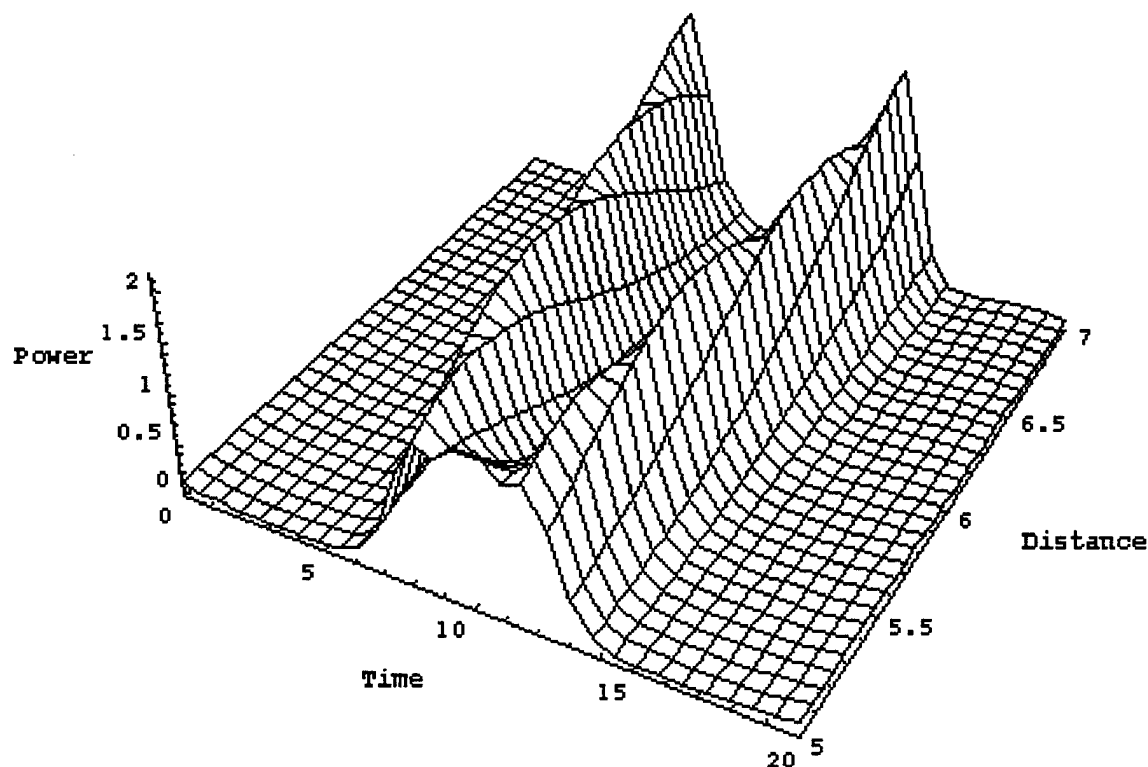
Fig. 12.1.5C Interaction of 2 solitons: distance 5-7.

## Cross-Phase Modulation:

The coupled nonlinear Schrödinger equations which described the cross-phase modulation effect are[4]:

$$\frac{\partial A_j}{\partial z}+\frac{1}{v_{gj}}\frac{\partial A_j}{\partial t}+\frac{1}{2}\alpha_j A_j = \frac{1}{2}\beta_{2j}\frac{\partial^2 A_j}{\partial t^2}-\gamma\left(\left|A_j\right|^2+2\sum_{m\neq j}^{M}\left|A_m\right|^2\right)A_j \qquad j=1,2,3,...,M$$

where

$A_j(z,t)$ is the slowly varying amplitude of the $j$'th wave;

$v_{gj}$ is the group velocity;

$\beta_{2j}$ is the dispersion coefficient;

$\alpha_j$ is the absorption coefficient;

$\gamma_j = \dfrac{n_2\omega_j}{cA_{eff}}$ is the nonlinear index coefficient;

$A_{eff}$ is the effective core area;

---

[4] Agrawal, G.P., *Phys. Rev. Lett.*, 59, 880, 1987.

$n_2 = 3.2 \times 10^{-16}$ cm$^2$/W for silica fibers;

$\omega_j$ is the carrier frequency of the $j$'th wave;

$c$ is the speed of light; and

$z$ is the direction of propagation along the fiber.

By using the normalization coefficients:

$$\tau = \frac{t - \left(\dfrac{z}{v_{g1}}\right)}{T_0},$$

$$d_{1j} = \frac{\left(v_{g1} - v_{gj}\right)}{v_{g1} v_{gj}}$$

$$\xi = \frac{z}{L_{D1}}$$

$$L_{D1} = \frac{T_0^2}{\left|\beta_{2j}\right|}$$

and setting:

$$u_j(\tau, \xi) = \left(\frac{A_j(z,t)}{\sqrt{P_{0j}}}\right) \times \exp\left[\frac{\alpha_j L_{D1} \xi}{2}\right]$$

$$L_{NLj} = \frac{1}{\left(\lambda_j P_{0j}\right)}$$

$$L_{Dj} = \frac{T_0^2}{\left|\beta_{2j}\right|}$$

gives[5]:

$$i\frac{\partial u_j}{\partial \xi} = \frac{\mathrm{sgn}\left(\beta_{2j}\right) L_{D1}}{2 L_{Dj}} \frac{\partial^2 u_j}{\partial \tau^2} - i\frac{d_{1j}}{T_0} L_{D1} \frac{\partial u_j}{\partial \tau} - \frac{L_{D1}}{L_{NLj}}\left[\exp\left(-\alpha_j L_{D1}\xi\right)\left|u_j\right|^2 + 2\sum_{m \neq j}^{M} \exp\left(-\alpha_m L_{D1}\xi\right)\left|u_m\right|^2\right] u_j$$

where

$T_0$ is the pulse width,

$P_{oj}$ is the incident optical power of the $j$th beam,

$d_{1j}$ is the walk-off parameter between beam 1 and beam $j$ and describes how fast a given pulse in beam $j$ passes through the pulse in beam 1.

[5] Yeh, C. & Bergman, L., Pulse shepherding in nonlinear fiber optics. *J. Appl. Phys.*, 80, 3174-3178, 1996;

Yeh, C. & Bergman, L., Enhanced pulse compression in nonlinear fiber by a WDM optical pulse. Phys. Rev. E., to appear February, 1998.

The walk-off length

$$L_{W(1j)} = \frac{T_0}{|d_{ij}|}$$

is the distance for which the faster moving pulse (e.g., in beam $j$) walks through the slower moving pulse in beam 1. The nonlinear interaction between the two pulses occurs over this length.

Fig.s 12.1.6A-E show cross-phase modulation with $\dfrac{\text{sgn}(\beta_{2j})L_{D1}}{2L_{Dj}}$ for beam $k$ 16 × that for beam $y$; and with $\dfrac{L_{D1}}{L_{NLj}}$ for beam $k$ 16 × that for beam $y$. The reduction of the bandwidth and the heightening of the shepherded pulses #1 and #2 is clearly seen in Fig.s 12.1.6D and 12.1.6E.

Fig.s 12.1.7A-D show cross-phase modulation with $\dfrac{\text{sgn}(\beta_{2j})L_{D1}}{2L_{Dj}}$ for beam $k$ 4 × that for beam $y$; $\dfrac{L_{D1}}{L_{NLj}}$ for beam $k$ 4 × that for beam $y$ and k is 2 × amplitude of pulses #1 and #2. The "shepherding" of the pulses #1 and #2 toward alignment in Fig.s 12.1.7C and 12.1.7D is clearly seen. It should be realized that computer memory restrictions limited the simulation only to 10 km distances. Further alignment is to be expected over longer distances.

Fig.s 12.1.8A-D show cross-phase modulation with $\dfrac{\text{sgn}(\beta_{2j})L_{D1}}{2L_{Dj}}$ for beam $k$ = that for beam $y$; $\dfrac{L_{D1}}{L_{NLj}}$ for beam $k$ = that for beam $y$ and k is 2 × amplitude of pulses #1 and #2. Again, the "shepherding" of the pulses #1 and #2 toward alignment in Fig.s 12.1.8C and 12.1.8D is clearly seen. Further alignment is to be expected over longer distances.

As the simulations represented in Fig.s 12.1.8 showed the shepherding effect with only a difference in amplitude between the shepherding and the shepherded pulses, we attribute control of the effect to that parameter.

Shepherd Pulse
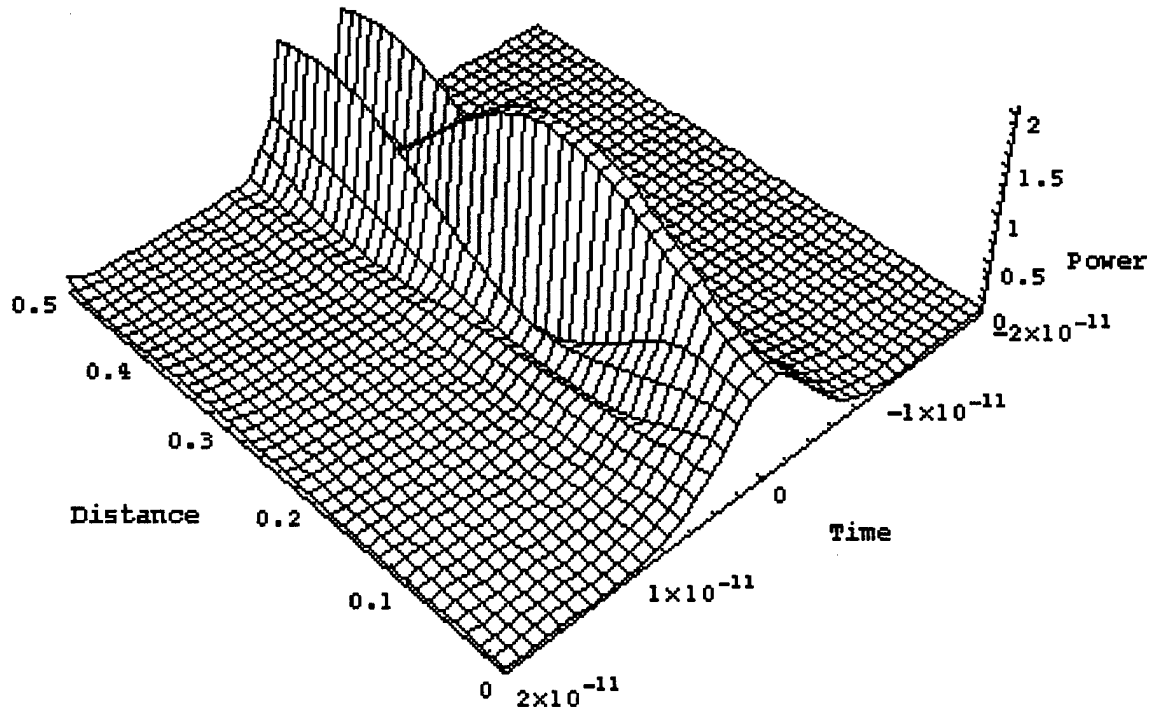


Fig. 12.1.6A. Shepherd pulse with $\dfrac{\mathrm{sgn}\left(\beta_{2j}\right)L_{D1}}{2L_{Dj}}$ for beam $k$ is 16 × that for beam $y$; and $\dfrac{L_{D1}}{L_{NLj}}$ for beam $k$ is 16 × that for beam $y$. Distance in km.

**Shepherd Pulse: 0 and 0.2 km**
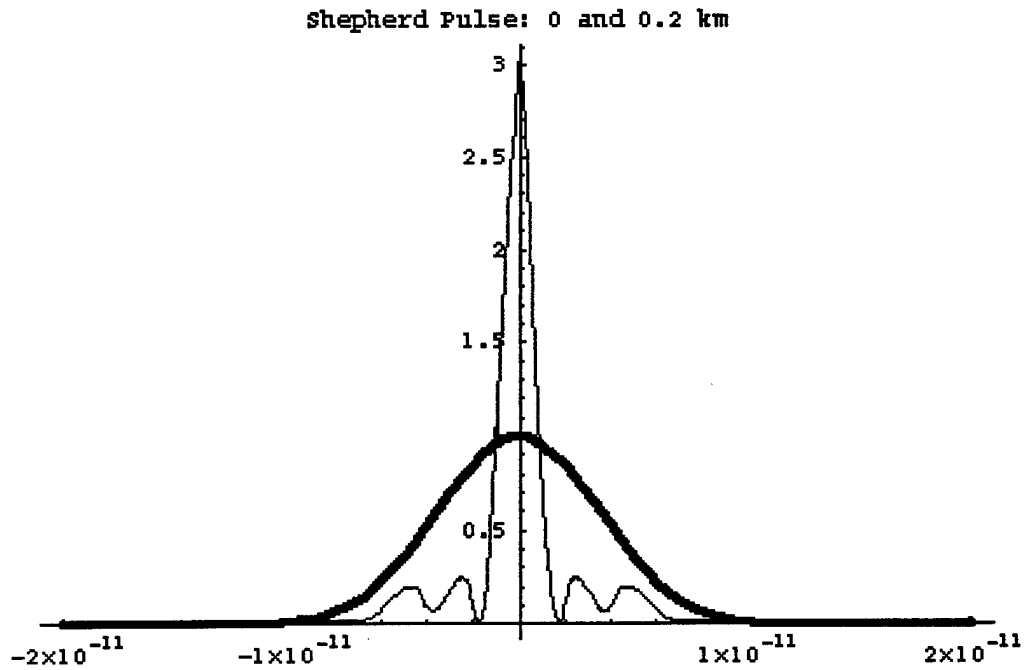
Fig. 12.1.6B. Shepherd pulse with $\dfrac{\mathrm{sgn}(\beta_{2j})L_{D1}}{2L_{Dj}}$ for beam $k$ is 16 × that for beam $y$; and $\dfrac{L_{D1}}{L_{NLj}}$ for beam $k$ is 16 × that for beam $y$. Thicker line shows the commencing pulse.



**Shepherd Pulse: 0 and 0.5 km**
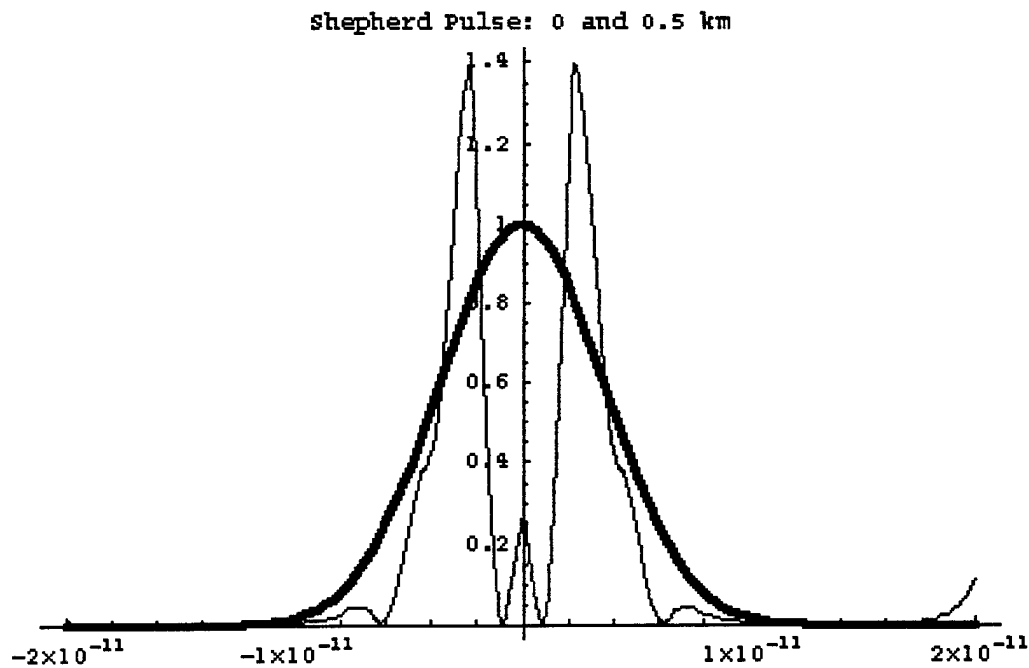
Fig. 12.1.6C. Shepherd pulse with $\dfrac{\mathrm{sgn}(\beta_{2j})L_{D1}}{2L_{Dj}}$ for beam $k$ is 16 × that for beam $y$; and $\dfrac{L_{D1}}{L_{NLj}}$ for beam $k$ is 16 × that for beam $y$. Thicker line shows the commencing pulse.

181

Pulse#1: 0 and 5 km
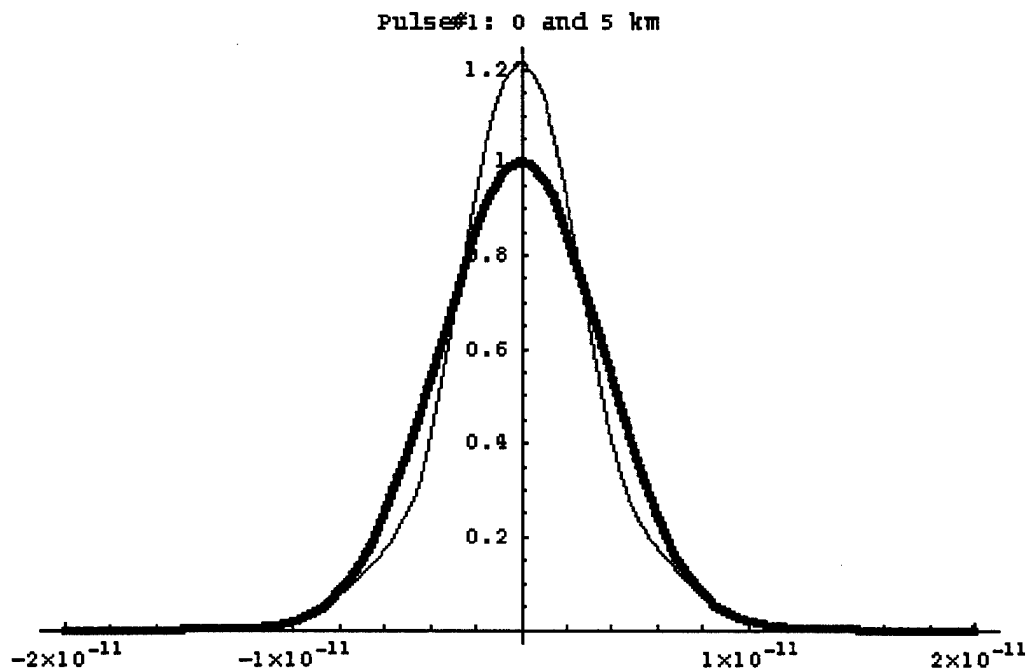
Fig. 12.1.6D. Pulse #1 with $\dfrac{\mathrm{sgn}\!\left(\beta_{2j}\right)L_{D1}}{2L_{Dj}}$ for beam $k$ is 16 × that for beam $y$; and $\dfrac{L_{D1}}{L_{NLj}}$ for beam $k$ is 16 × that for beam $y$. Thicker line shows the commencing pulse.



Pulse#2: 0 and 5 km
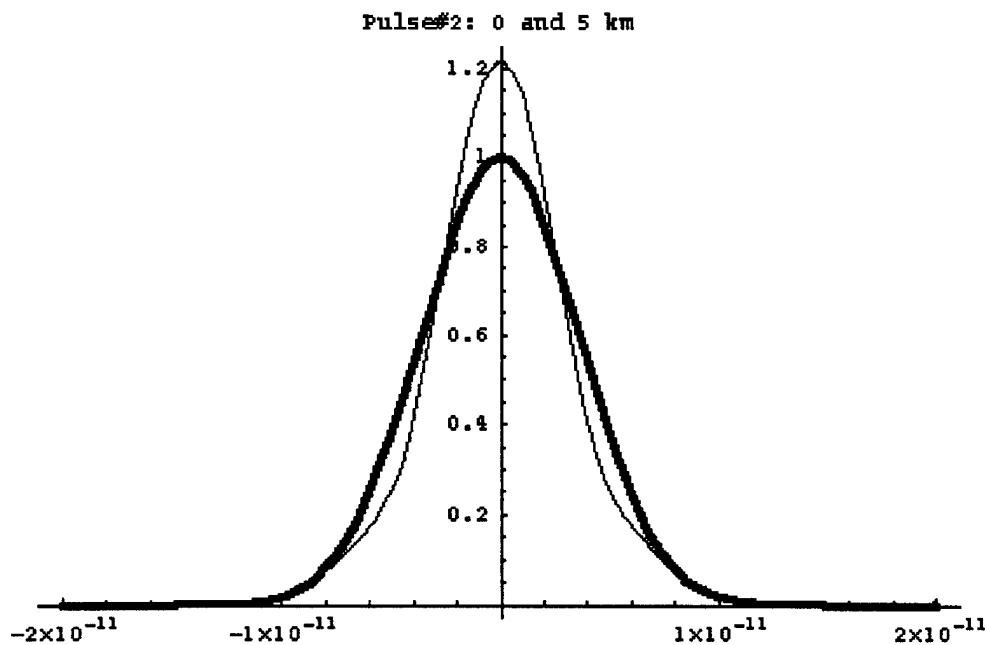
Fig. 12.1.6E. Pulse #2 with $\dfrac{\mathrm{sgn}\!\left(\beta_{2j}\right)L_{D1}}{2L_{Dj}}$ for beam $k$ is 16 × that for beam $y$; and $\dfrac{L_{D1}}{L_{NLj}}$ for beam $k$ is 16 × that for beam $y$. Thicker line shows the commencing pulse.

182

Fig. 12.1.7A. Shepherd pulse with $\dfrac{\mathrm{sgn}\left(\beta_{2j}\right)L_{D1}}{2L_{Dj}}$ for beam $k$ is $4 \times$ that for beam $y$; $\dfrac{L_{D1}}{L_{NLj}}$ for beam $k$ is $4 \times$ that for beam $y$ and k is $2 \times$ amplitude of pulses #1 and #2. Distance in km.

183

Shepherd Pulse: 0 and 3 km
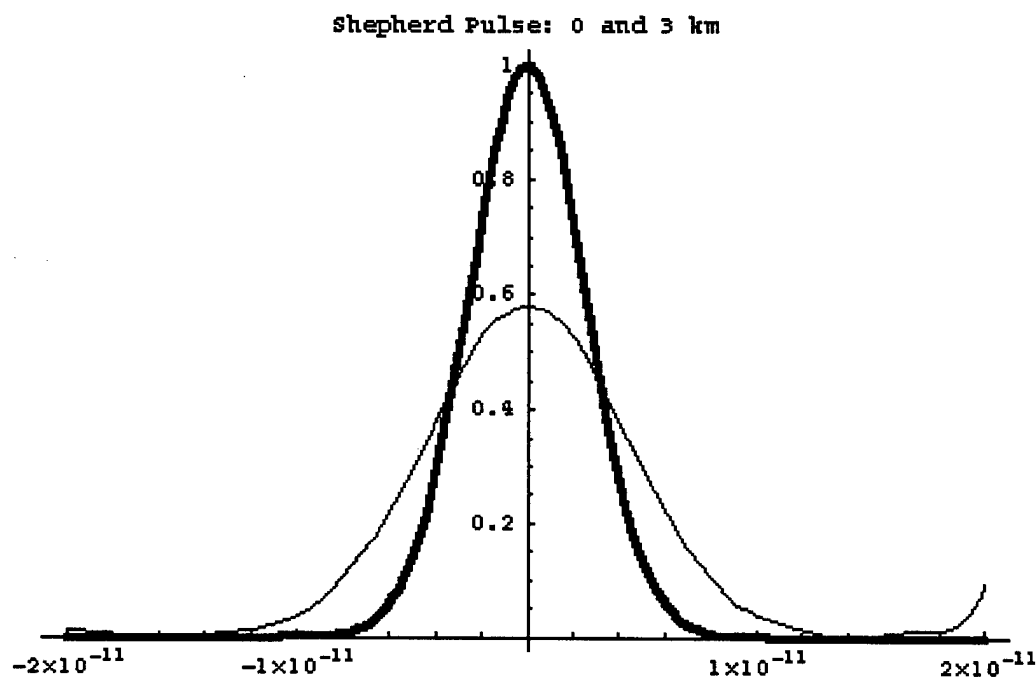
Fig. 12.1.7B. Shepherd pulse with $\dfrac{\operatorname{sgn}\!\left(\beta_{2j}\right)L_{D1}}{2L_{Dj}}$ for beam $k$ is 4 × that for beam $y$; $\dfrac{L_{D1}}{L_{NLj}}$ for beam $k$ is 4 × that for beam $y$ and k is 2 × amplitude of pulses #1 and #2. Thicker line shows the commencing pulse.



Pulse #1: 0 and 10 km
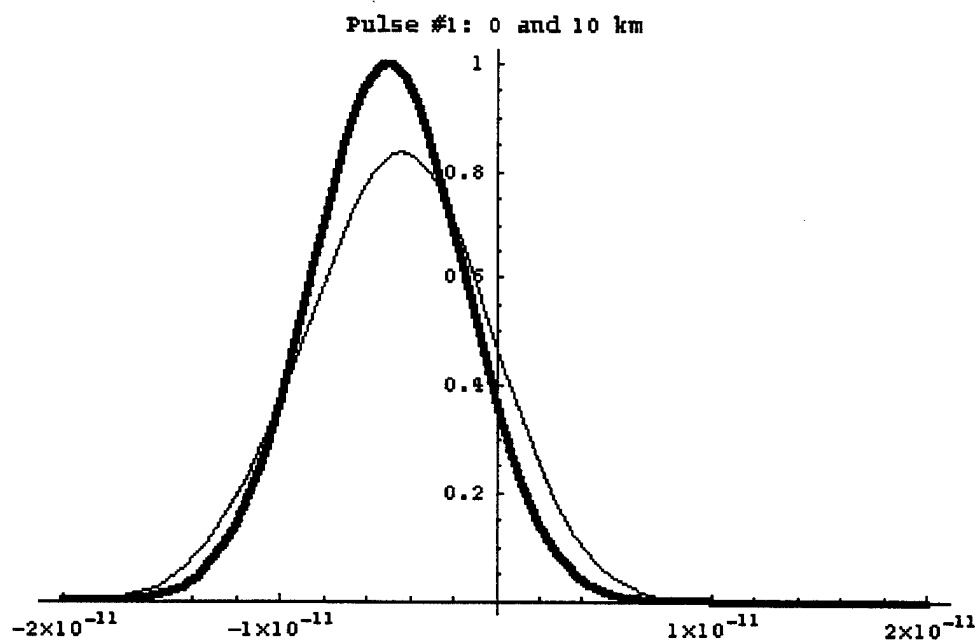
Fig. 12.1.7C. Pulse #1 with $\dfrac{\operatorname{sgn}\!\left(\beta_{2j}\right)L_{D1}}{2L_{Dj}}$ for beam $k$ is 4 × that for beam $y$; $\dfrac{L_{D1}}{L_{NLj}}$ for beam $k$ is 4 × that for beam $y$ and k is 2 × amplitude of pulses #1 and #2. Thicker line shows the commencing pulse.

184

Pulse #2: 0 and 10 km
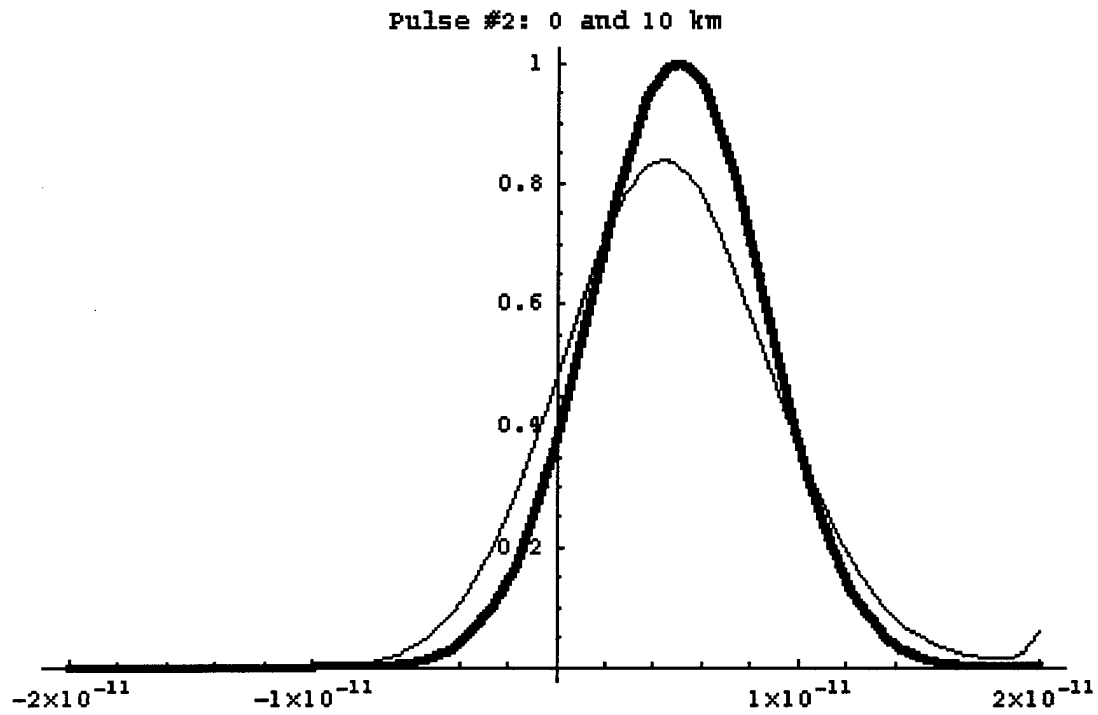
Fig. 12.1.7D. Pulse #2 with $\dfrac{\mathrm{sgn}\!\left(\beta_{2j}\right)L_{D1}}{2L_{Dj}}$ for beam $k$ is 4 × that for beam $y$; $\dfrac{L_{D1}}{L_{NLj}}$ for beam $k$ is 4 × that for beam $y$ and k is 2 × amplitude of pulses #1 and #2. Thicker line shows the commencing pulse.

Fig. 12.1.8A. Shepherd pulse with $\dfrac{\mathrm{sgn}\!\left(\beta_{2j}\right)L_{D1}}{2L_{Dj}}$ for beam $k$ = that for beam $y$; $\dfrac{L_{D1}}{L_{NLj}}$ for beam $k$ = that for beam $y$ and k is 2 × amplitude of pulses #1 and #2. Distance in km.

Shepherd Pulse: 0 and 10 km
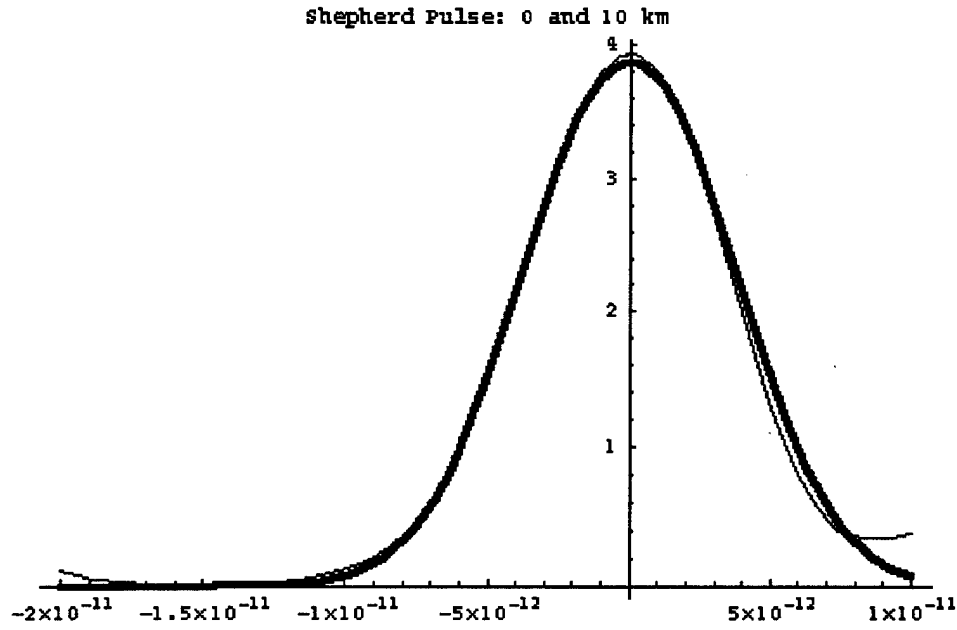
Fig. 12.1.8B. Shepherd pulse with $\dfrac{\text{sgn}\left(\beta_{2j}\right)L_{D1}}{2L_{Dj}}$ for beam $k$ = that for beam $y$; $\dfrac{L_{D1}}{L_{NLj}}$ for beam $k$ = that for beam $y$ and k is 2 × amplitude of pulses #1 and #2. Thicker line shows the commencing pulse.



Pulse #1: 0 and 10 km
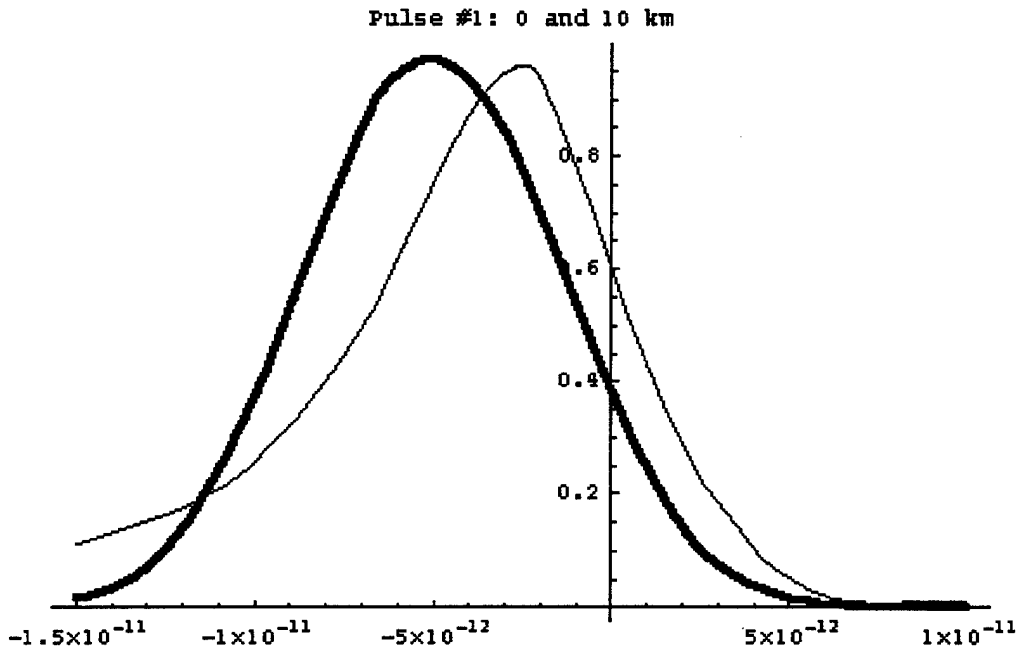
Fig. 12.1.8C. Pulse #1 with $\dfrac{\text{sgn}\left(\beta_{2j}\right)L_{D1}}{2L_{Dj}}$ for beam $k$ = that for beam $y$; $\dfrac{L_{D1}}{L_{NLj}}$ for beam $k$ = that for beam $y$ and k is 2 × amplitude of pulses #1 and #2. Thicker line shows the commencing pulse.

187

**Pulse #2: 0 and 10 km**
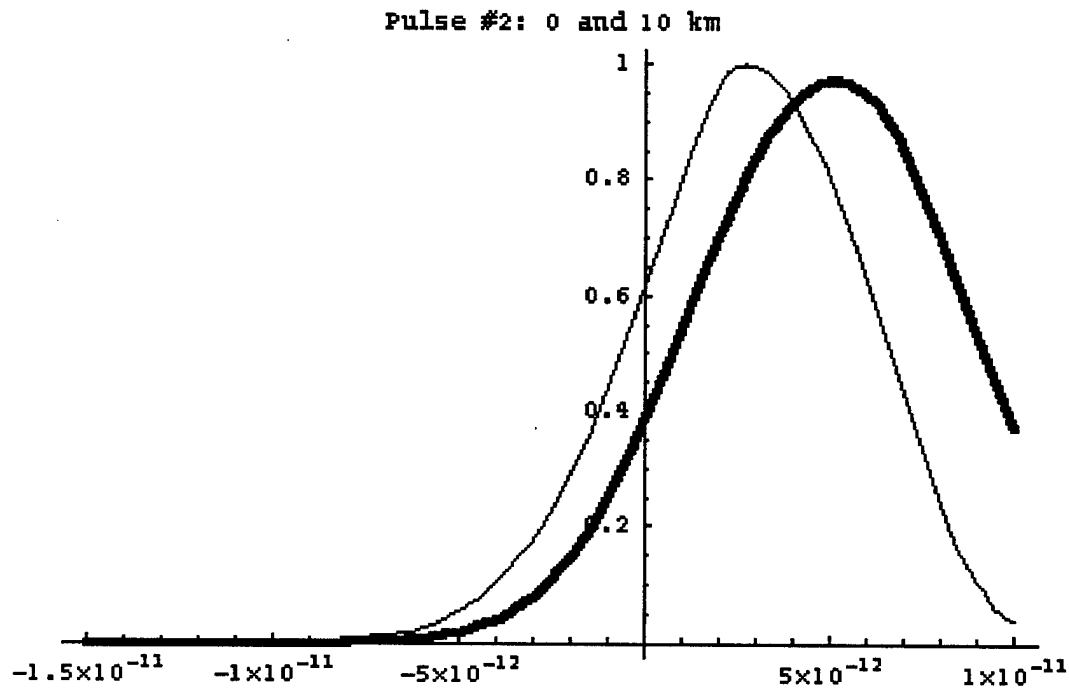
Fig. 12.1.8D. Pulse #2 with $\dfrac{\mathrm{sgn}\left(\beta_{2j}\right)L_{D1}}{2L_{Dj}}$ for beam $k$ = that for beam $y$; $\dfrac{L_{D1}}{L_{NLj}}$ for beam $k$ = that for beam $y$ and k is 2 × amplitude of pulses #1 and #2. Thicker line shows the commencing pulse.

188

## 12.2 Pulse Compression Effects.

In this section we confirm that: (1) a shepherd pulse, although energy will not be exchanged between the beams, will enhance the compression of co-propagating beams at different wavelengths if those beams are in the anomalous dispersion region; (2) unlike SPM and GVD, in the case of CPM, in the presence of a shepherding pulse compression will occur for soliton orders << 1; (3) if the primary pulse is in the normal dispersion region, a dark soliton is generated rather than pulse compression; (4) time-alignment of copropagating beams. Successful generation of time-aligned pulses on BPWD beams is crucial to the realization of ultra-high data rate BPWD single fiber systems.

### Cross-Phase Modulation[6]:

Cross-Phase modulation (CPM) effects are caused by the intensity dependence of optical fiber's refractive index. The mechanism of CPM pulse compression can be compared and contrasted with that of soliton compression, which involves higher-order solitons resulting from self-phase modulation (SPM) and anomalous group-velocity dispersion (GVD)[7]. CPM compression takes place for pulses on *different* wavelength beams.

The coupled nonlinear Schrödinger equations which described the cross-phase modulation effect are[8]:

$$\frac{\partial A_j}{\partial z} + \frac{1}{v_{gj}}\frac{\partial A_j}{\partial t} + \frac{1}{2}\alpha_j A_j = \frac{1}{2}\beta_{2j}\frac{\partial^2 A_j}{\partial t^2} - \gamma\left(\left|A_j\right|^2 + 2\sum_{m\neq j}^{M}\left|A_m\right|^2\right)A_j \qquad j = 1,2,3,...,M$$

where

$A_j(z,t)$ is the slowly varying amplitude of the $j$'th wave;

$v_{gj}$ is the group velocity;

$\beta_{2j}$ is the dispersion coefficient;

$\alpha_j$ is the absorption coefficient;

$\gamma_j = \dfrac{n_2\omega_j}{cA_{eff}}$ is the nonlinear index coefficient;

$A_{eff}$ is the effective core area;

$n_2 = 3.2 \times 10^{-16}$ cm$^2$/W for silica fibers;

$\omega_j$ is the carrier frequency of the $j$'th wave;

$c$ is the speed of light; and

$z$ is the direction of propagation along the fiber.

By using the normalization coefficients:

---

[6] Agrawal, G.P., Modulation instability induced by cross-phase modulation. *Phys. Rev. Lett.*, 59, 880-883, 1987.

[7] Mollenauer, L.F. Stolen, R.H., Gordon, J.P. & Tomlinson, W.J., *Opt. Lett.*, 8, 289, 1983;
Nakatsuka, H., Grischkowsky, D. & Balant, A.C., *Phys. Rev. Lett.*, 47, 910, 1981;
Tomlinson, W.J., Stolen, R.H. & Shank, C.V., *J. Opt. Soc. Am.*, B1, 139, 1984;
Tomlinson, W.J. & Knox, W.H., *J. Opt. Soc. Am.*, B4, 1404, 1987.

[8] Agrawal, G.P., Modulation instability induced by cross-phase modulation. *Phys. Rev. Lett.*, 59, 880-883, 1987.

$$\tau = \frac{t - \left(\dfrac{z}{v_{g1}}\right)}{T_0},$$

$$d_{1j} = \frac{\left(v_{g1} - v_{gj}\right)}{v_{g1} v_{gj}}$$

$$\xi = \frac{z}{L_{D1}}$$

$$L_{D1} = \frac{T_0^2}{|\beta_{2j}|}$$

and setting:

$$u_j(\tau, \xi) = \left(\frac{A_j(z,t)}{\sqrt{P_{0j}}}\right) \times \exp\left[\frac{\alpha_j L_{D1} \xi}{2}\right]$$

$$L_{NLj} = \frac{1}{\left(\lambda_j P_{0j}\right)}$$

$$L_{Dj} = \frac{T_0^2}{|\beta_{2j}|}$$

gives[9]:

$$i\frac{\partial u_j}{\partial \xi} = \frac{\text{sgn}(\beta_{2j})L_{D1}}{2L_{Dj}}\frac{\partial^2 u_j}{\partial \tau^2} - i\frac{d_{1j}}{T_0}L_{D1}\frac{\partial u_j}{\partial \tau} - \frac{L_{D1}}{L_{NLj}}\left[\exp\left(-\alpha_j L_{D1}\xi\right)|u_j|^2 + 2\sum_{m \neq j}^{M}\exp\left(-\alpha_m L_{D1}\xi\right)|u_m|^2\right]u_j$$

where

$T_0$ is the pulse width,
$P_{oj}$ is the incident optical power of the $j$th beam,
$d_{1j}$ is the walk-off parameter between beam 1 and beam $j$ and describes how fast a given
  pulse in beam $j$ passes through the pulse in beam 1.

The walk-off length

$$L_{W(1j)} = \frac{T_0}{|d_{ij}|}$$

---

[9] Yeh, C. & Bergman, L., Pulse shepherding in nonlinear fiber optics. *J. Appl. Phys.*, 80, 3174-3178,
  1996;
  Yeh, C. & Bergman, L., Enhanced pulse compression in nonlinear fiber by a WDM optical pulse. *Phys.
  Rev. E.*, to appear February, 1998.

is the distance for which the faster moving pulse (e.g., in beam $j$) walks through the slower moving pulse in beam 1. The nonlinear interaction between the two pulses occurs over this length. Furthermore, for CPM to be significant, the group velocity mismatch between the beams must be near zero.

In the case of SPM and GVD, pulse compression will occur when the soliton order, $N$, is larger than 1 but not less than 1.[10] However, in the case of CPM, in the presence of a shepherding pulse compression will occur for $N \ll 1$. When the shepherding pulse order, $N_s$, is greater than the primary pulse order, $N_p$, there is even greater compression (see Fig. 8).

The following Fig.s 12.2.1-4 are based on a shepherd pulse of 20 psec. and 2 other pulses of 60 psec. duration. The amplitude of the shepherd pulse is 3 and that of the two other pulses is 0.1. The Figures 12.2.1-4 then only differ in the sign of the dispersion coefficient. It should be noted for positive dispersion (i.e., normal dispersion region or positive GVD region) in the case of the primary pulse (Fig.s 12.2.2, 12.2.4, 12.2.5, 12.2.10 and 12.2.13) a black soliton results. For pulse compression to occur, the primary compressed pulses must be in the negative dispersion (i.e., anomalous dispersion region or negative GVD region). Figures 12.2.1, 12.2.3, 12.2.6, 12.2.7, 12.2.8, 12.2.9, 12.2.11 and 12.2.12 exhibited such compression for primary pulses in the anomalous dispersion region.

[10] Agrawal, G.P., *Nonlinear Fiber Optics*, Academic Press, NY, 1989.

Pulse #1 (-,-,+)
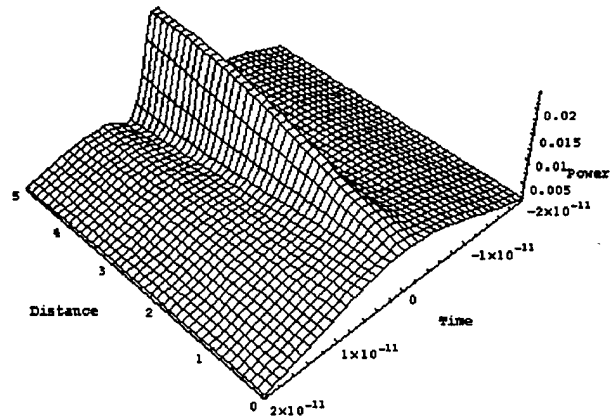


**1A.**

Pulse #2 (-,-,+)



**1B**

Shepherd Pulse (-,-,+)



**1C.**

192

Pulse #1 (-,-,+)



**1D.**

Pulse #2 (-,-,+)



**1E.**

Shepherd Pulse (-,-,+), 0 & 5 km



**1F.**
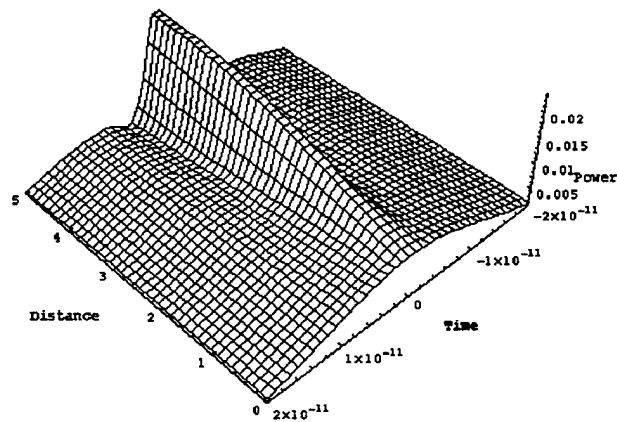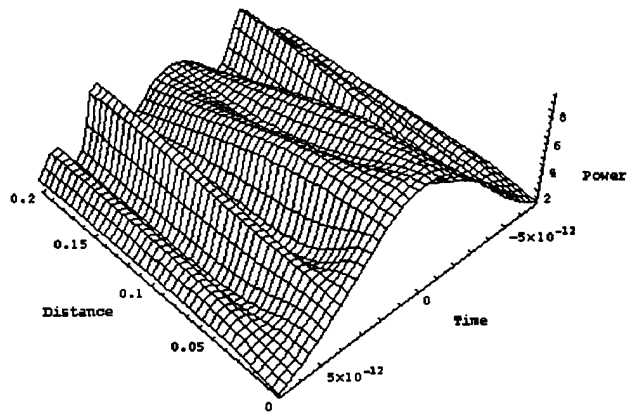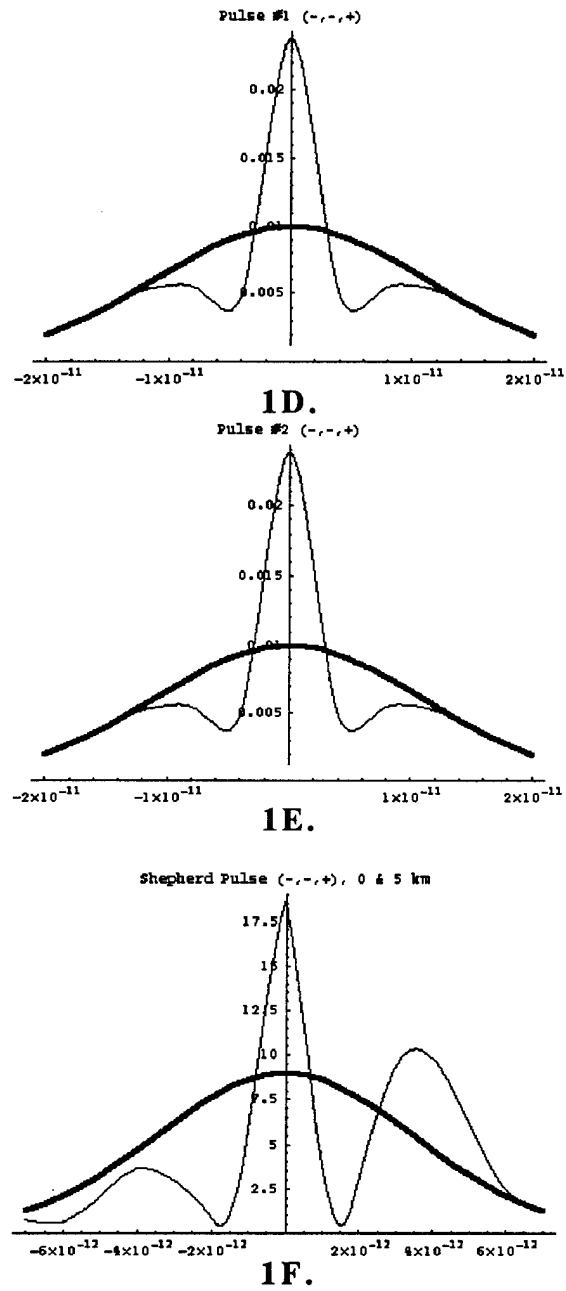
Fig. 12.2.1. A & D: Pulse #1, B & E: Pulse #2, C &F. Shepherd Pulse. Parameters for Pulse #1 and #2: Amplitude: 0.1, dispersion coefficient $\beta_2$ = -2. Parameters for Shepherd Pulse: Amplitude 3, dispersion coefficient $\beta_2$= +2. After Ref[11], Fig. 1.

---

[11] Yeh, C., Bergman, L., Morookian, J. & Monacos, S., Generation of time-aligned pulses on wavelength division multiplexed beams in a nonlinear fiber. Manuscript, 1998.

193

Pulse#1 (+,+,-)



2A.

Pulse#2 (+,+,-)



Fig. 2B.

Shepherd Pulse (+,+,-)



Fig. 2C.

194

Pulse#1 (+,+,-), 0 & 5 km

0.012
0.01
0.008
0.006
0.004
0.002

-2x10⁻¹¹   -1x10⁻¹¹   1x10⁻¹¹   2x10⁻¹¹

**Fig. 2D.**

Pulse#2 (+,+,-), 0 & 5 km

0.012
0.01
0.008
0.006
0.004
0.002

-2x10⁻¹¹   -1x10⁻¹¹   1x10⁻¹¹   2x10⁻¹¹

**Fig. 2E.**

Shepherd Pulse (+,+,-), 0 & 0.2 km

17.5
15
12.5
10
7.5
5
2.5

-6x10⁻¹² -4x10⁻¹² -2x10⁻¹²   2x10⁻¹² 4x10⁻¹² 6x10⁻¹²
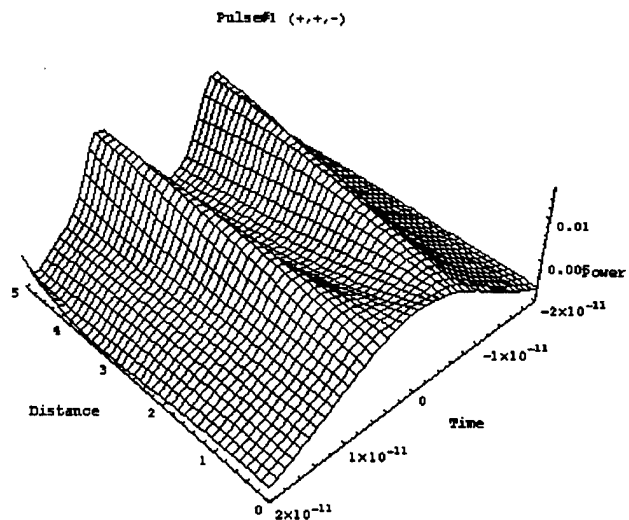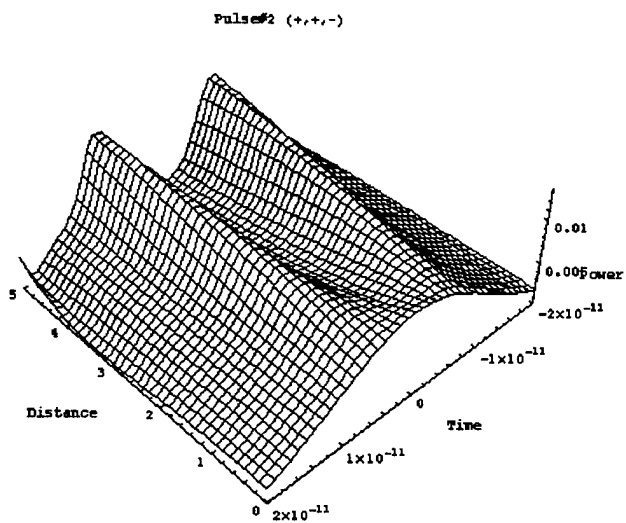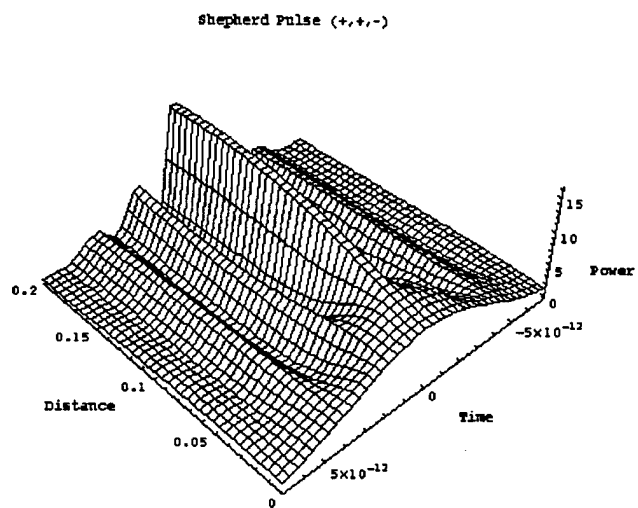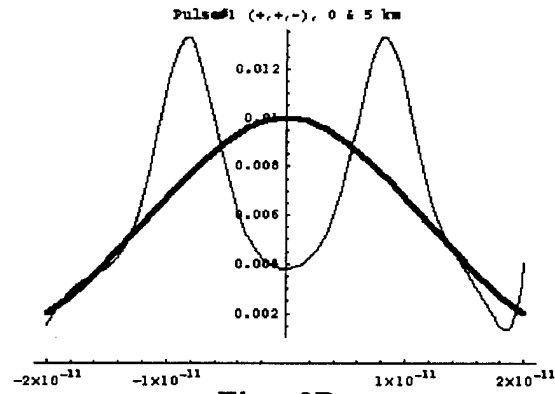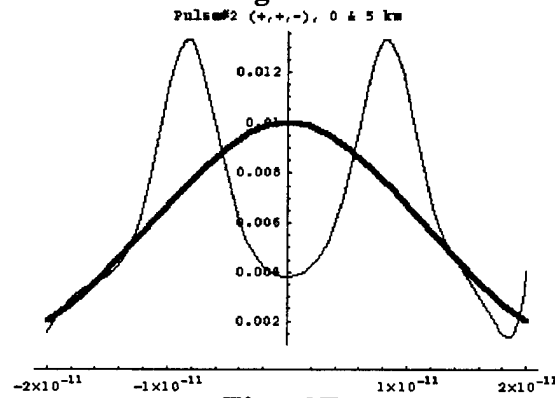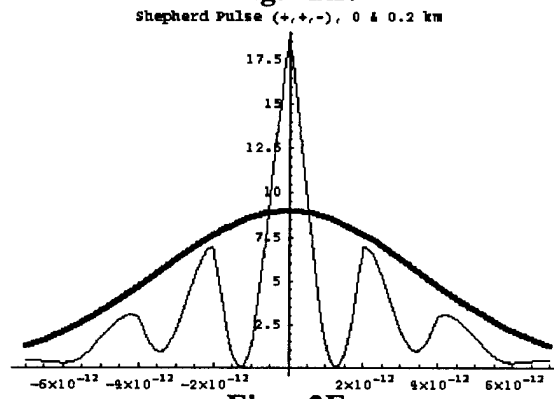
**Fig. 2F.**

Fig 12.2.2. A & D: Pulse #1, B & E: Pulse #2, C &F. Shepherd Pulse. Parameters for Pulse #1 and #2: Amplitude: 0.1, dispersion coefficient $\beta_2 = +2$. Parameters for Shepherd Pulse: Amplitude 3, dispersion coefficient $\beta_2 = -2$. After Ref[11]. Fig. 1.

Pulse#1 (-,-,-)

**Fig. 3A.**



Pulse#2 (-,-,-)

**Fig. 3B.**



Shepherd Pulse (-,-,-)

**Fig. 3C.**

196

**Fig. 3D.**

Pulse#1 (-,-,-), 0 & 5 km

```
        0.02
       0.015
        0.01
       0.005
-2x10⁻¹¹   -1x10⁻¹¹      1x10⁻¹¹   2x10⁻¹¹
```

**Fig. 3E.**

Pulse#2 (-,-,-), 0 & 5 km

```
        0.02
       0.015
        0.01
       0.005
-2x10⁻¹¹   -1x10⁻¹¹      1x10⁻¹¹   2x10⁻¹¹
```

**Fig. 3F.**

Shepherd Pulse (-,-,-), 0 & 0.2 km

```
        17.5
         15
        12.5
         10
         7.5
          5
         2.5
-6x10⁻¹² -4x10⁻¹² -2x10⁻¹²      2x10⁻¹² 4x10⁻¹² 6x10⁻¹²
```
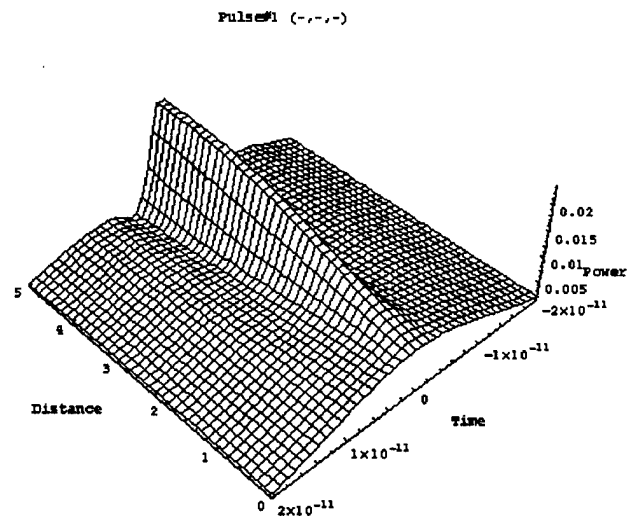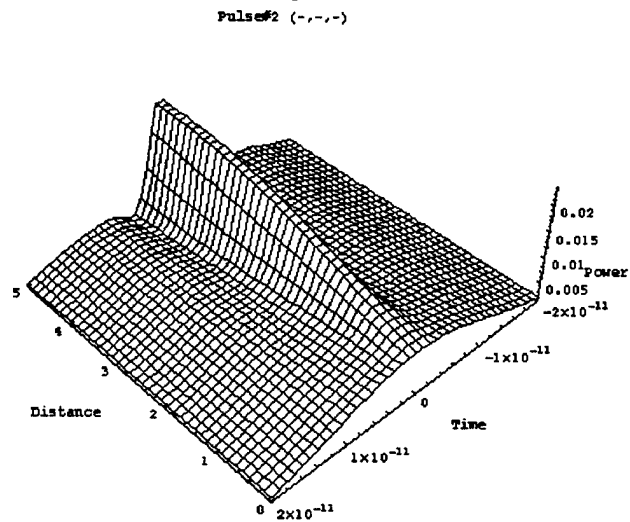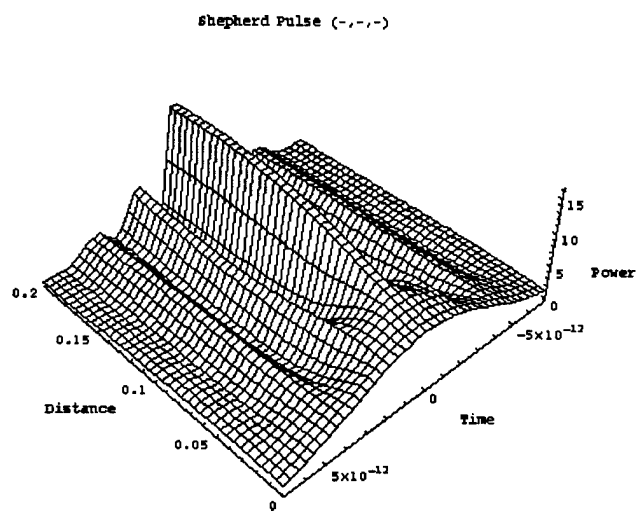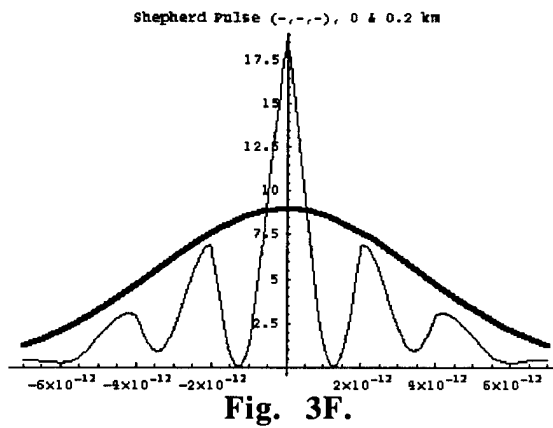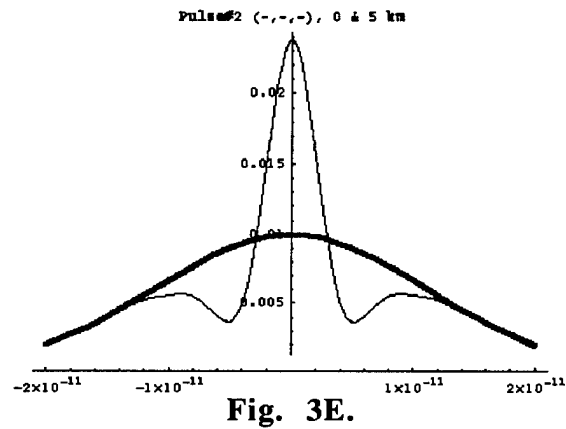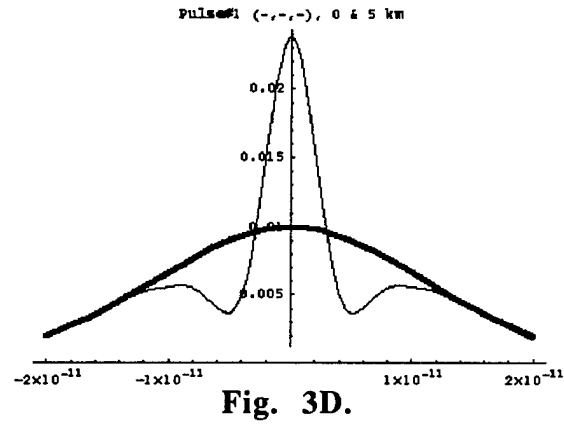
Fig.12.2.3. A & D: Pulse #1, B & E: Pulse #2, C &F. Shepherd Pulse. Parameters for Pulse #1 and #2: Amplitude: 0.1, dispersion coefficient $\beta_2$ = -2. Parameters for Shepherd Pulse: Amplitude 3, dispersion coefficient $\beta_2$= -2. After Ref[11], Fig. 1.

197

Pulse#1 (+,+,+)

Fig. 4A.


Pulse#2 (+,+,+)

Fig. 4B.


Shepherd Pulse (+,+,+)

Fig. 4C.

Fig. 4D.



Fig. 4E.



Fig. 4F.
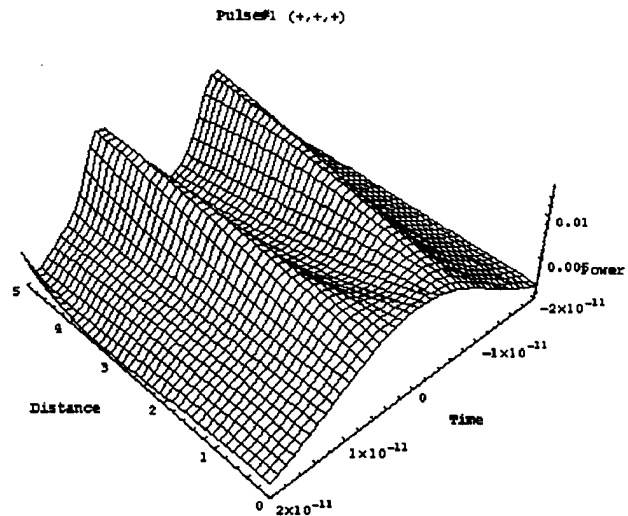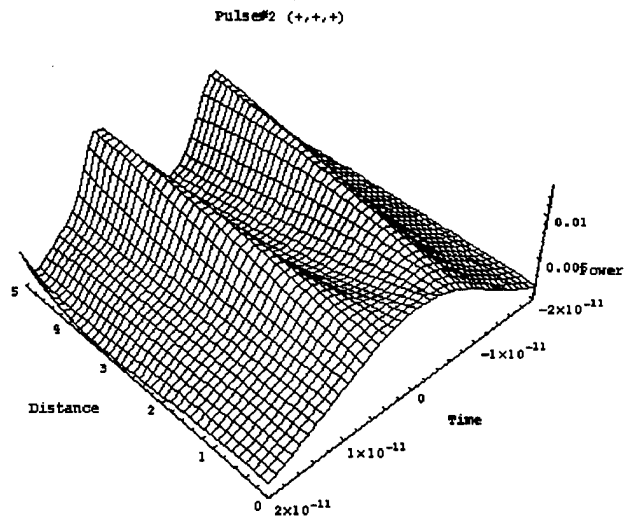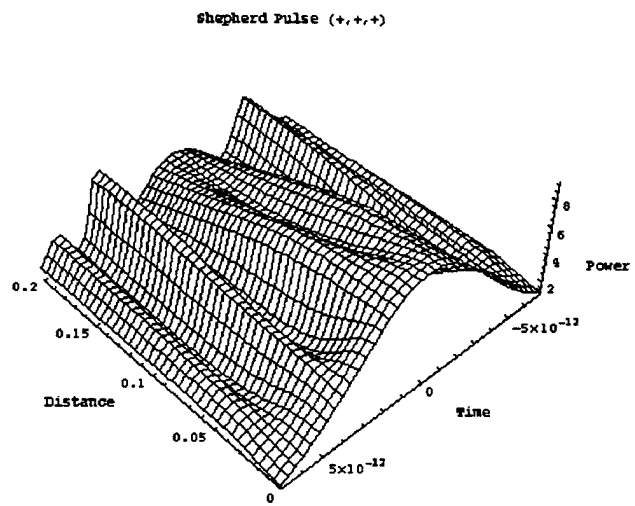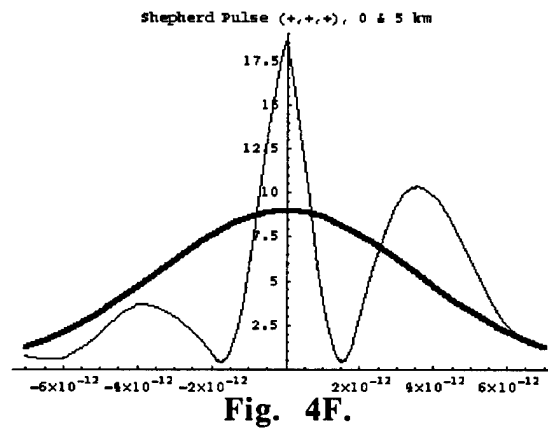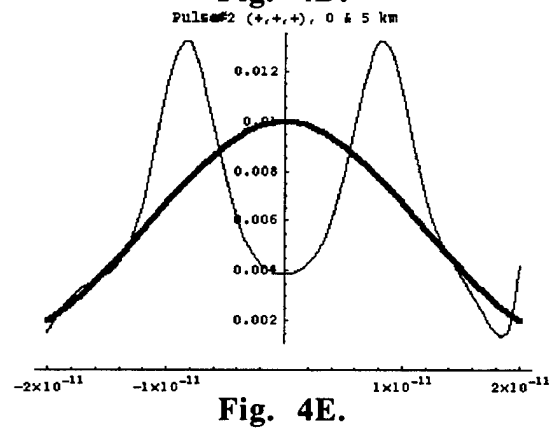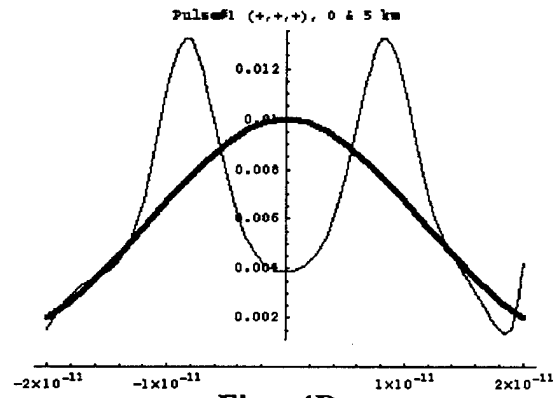
Fig. 12.2.4. A & D: Pulse #1, B & E: Pulse #2, C &F. Shepherd Pulse. Parameters for Pulse #1 and #2: Amplitude: 0.1, dispersion coefficient $\beta_2$= +2. Parameters for Shepherd Pulse: Amplitude 3, dispersion coefficient $\beta_2$= +2. After Ref[11], Fig. 1.

Generated Pulse, +2, -2
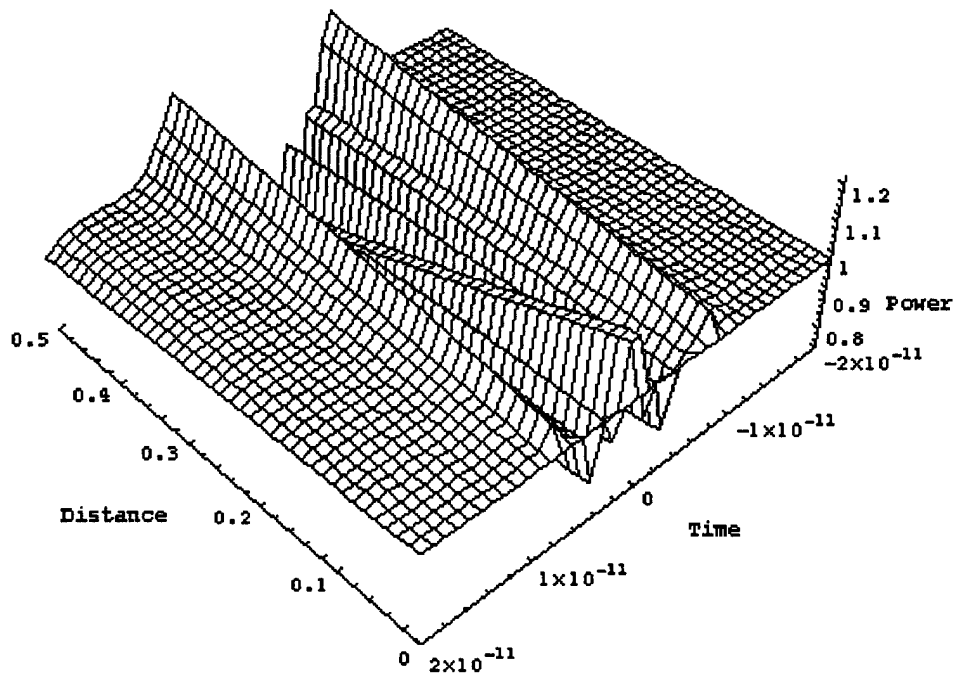


**Fig. 5A.**

Shepherd Pulse, +2, -2



**Fig. 5B.**

200

**Fig. 5C.**

Shepherd Pulse, 0.5 km, +2, -2



**Fig. 5D.**
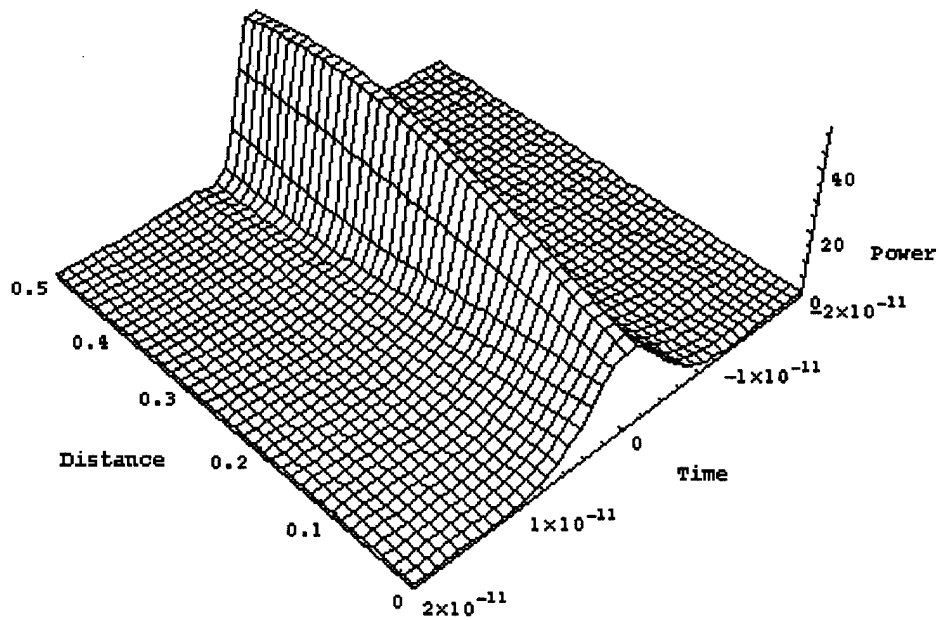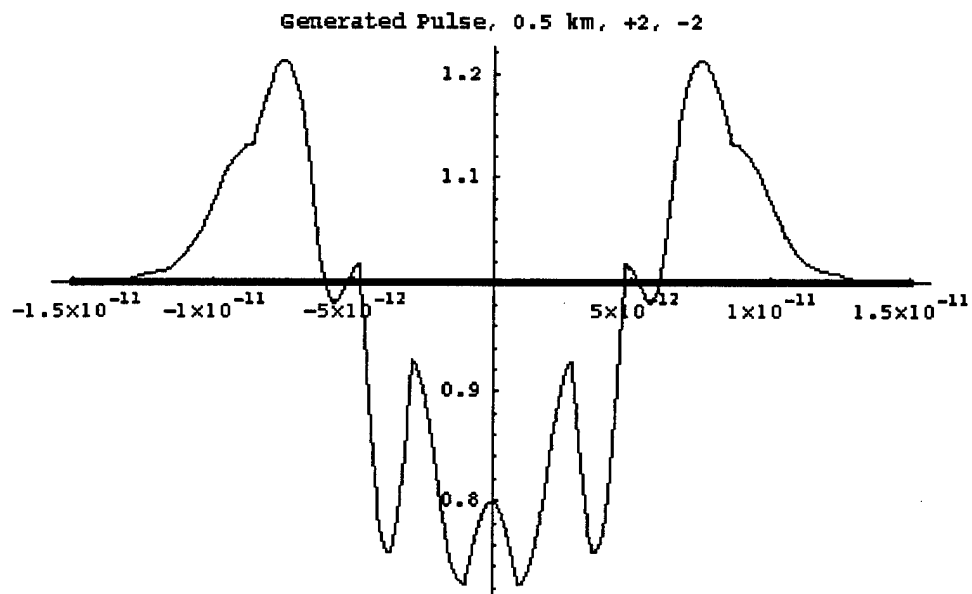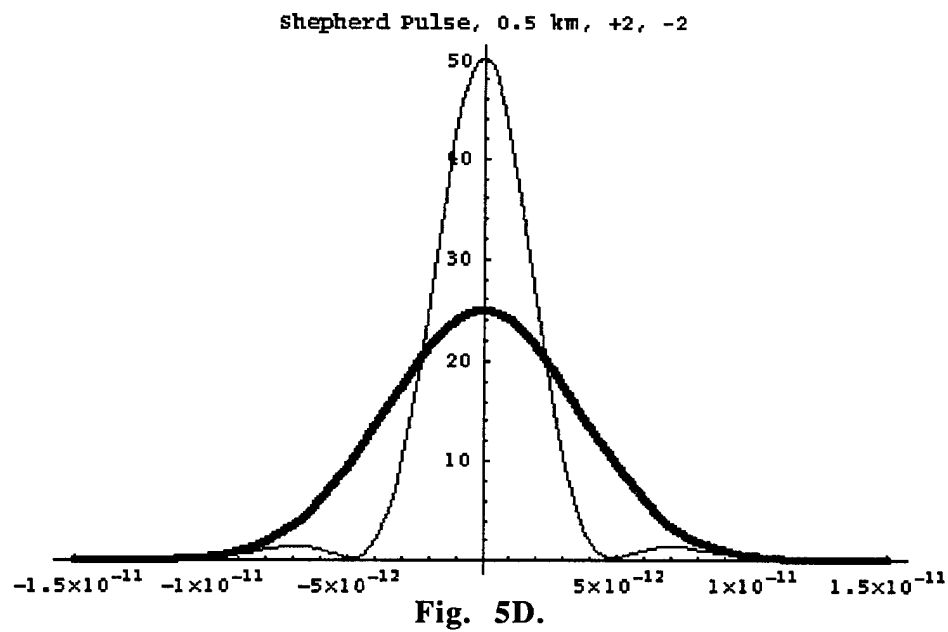
Fig. 12.2.5. A & C: Generated Pulses, $\beta_2$ = +2. B & E: Shepherd Pulse, amplitude 5 and $\beta_2$ = -2. After Ref[11], Fig. 2.

Generated Pulse, -1, -2
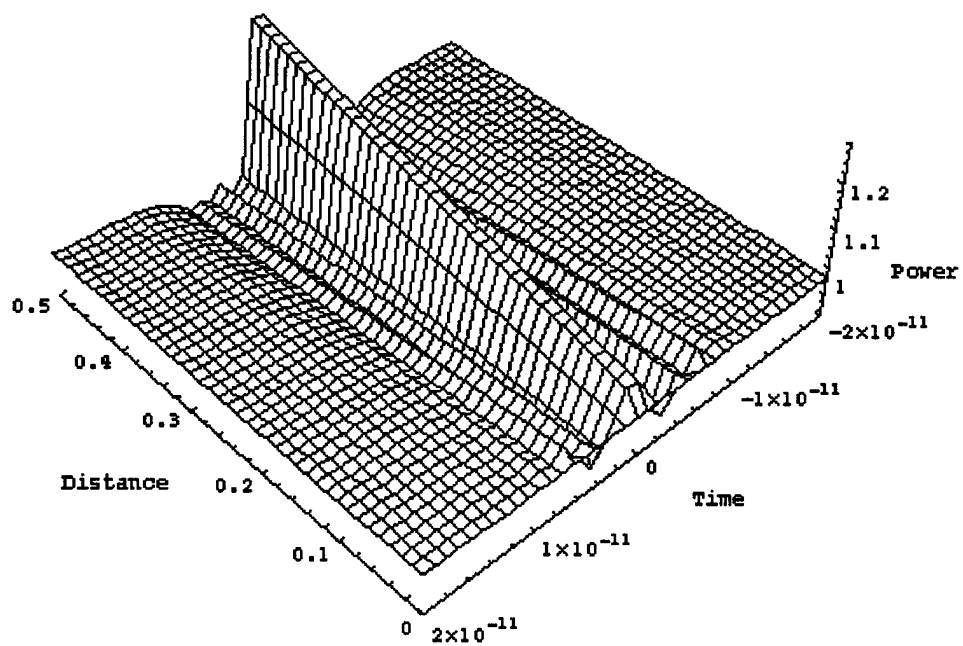


**Fig. 6A.**

Shepherd Pulse, -1, -2
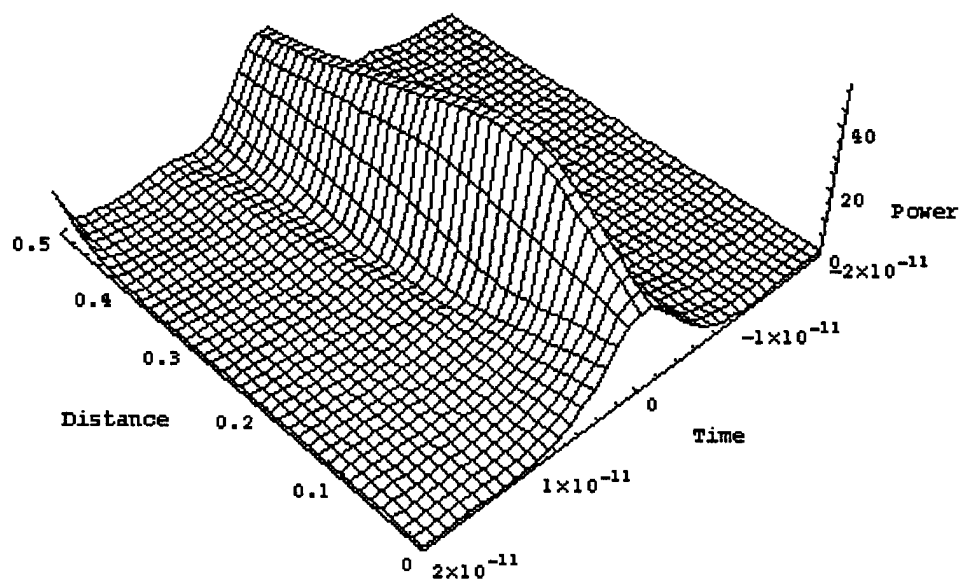


**Fig. 6B.**
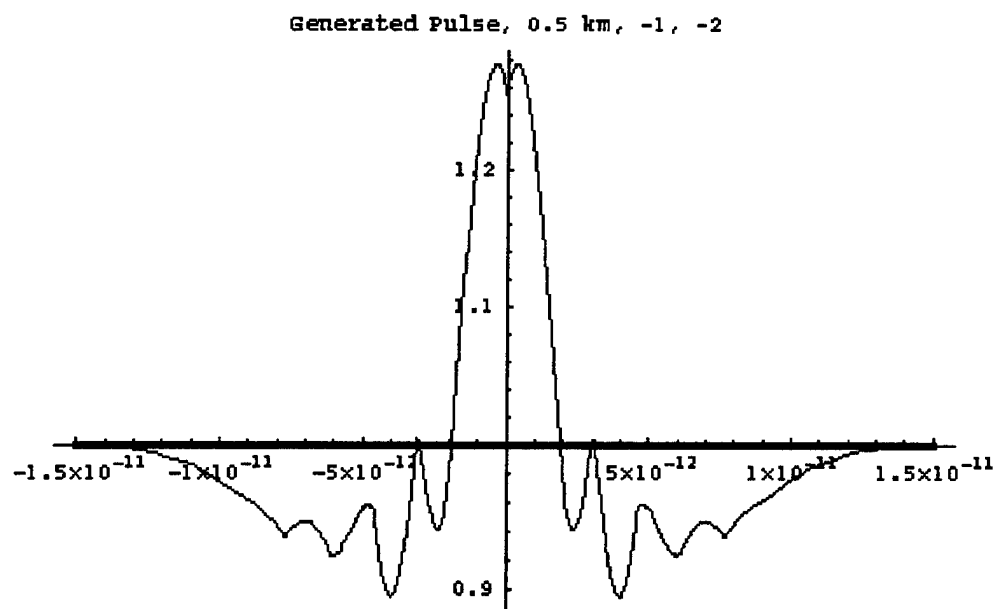
**Fig. 6C.**
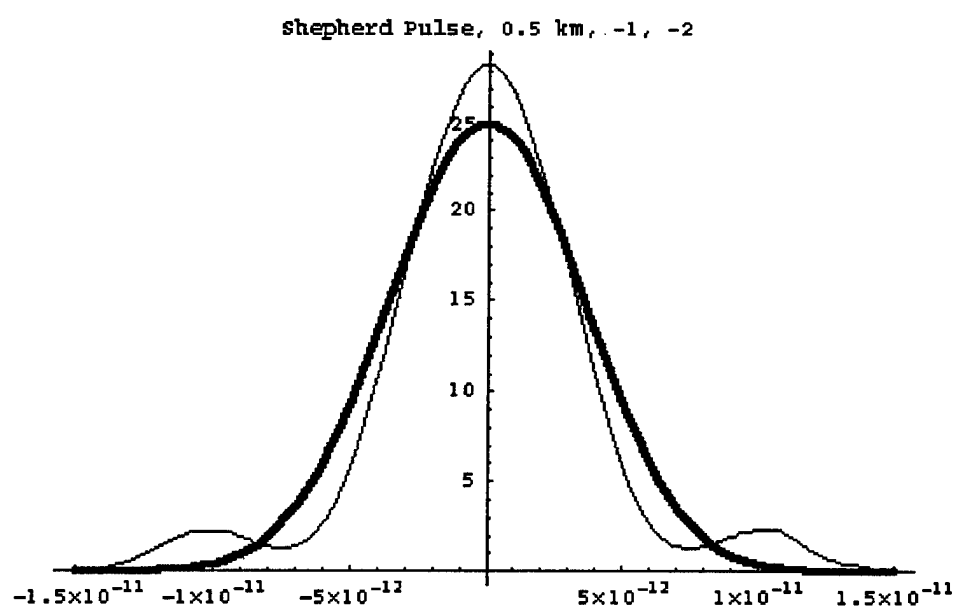
**Fig. 6D.**

Fig. 12.2.6. A & C: Generated Pulses, $\beta_2 = -1$. B & E: Shepherd Pulse, amplitude 5 and $\beta_2 = -2$. After Ref[11], Fig. 2.

Generated Pulse, -1.5, -2
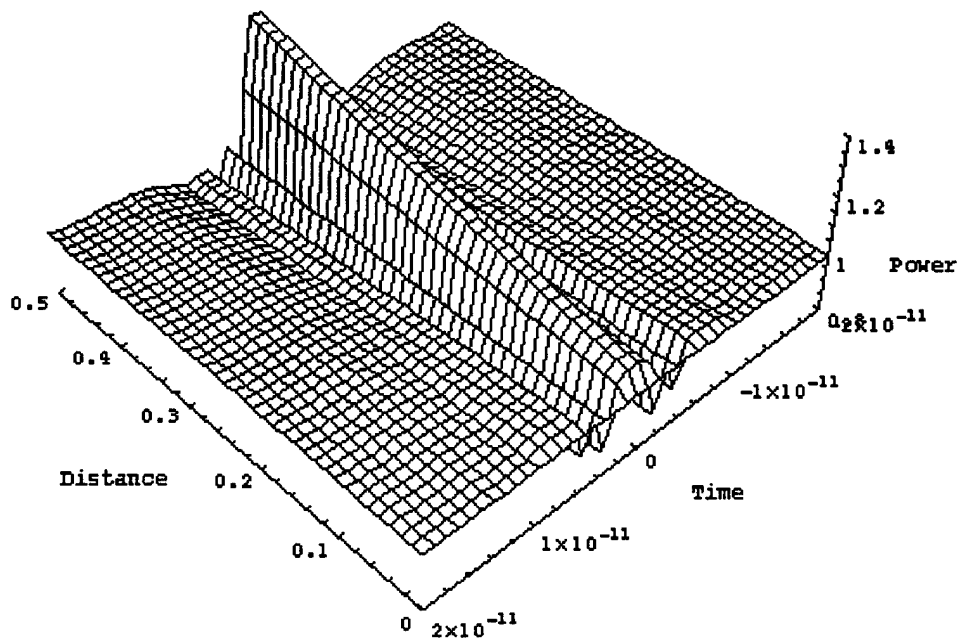


**Fig. 7A.**

Shepherd Pulse, -1.5, -2



**Fig. 7B.**

**Generated Pulse, 0.5 km, -1.5, -2**



## Fig. 7C.

**Shepherd Pulse, 0.5 km, -1.5, -2**



## Fig. 7D.
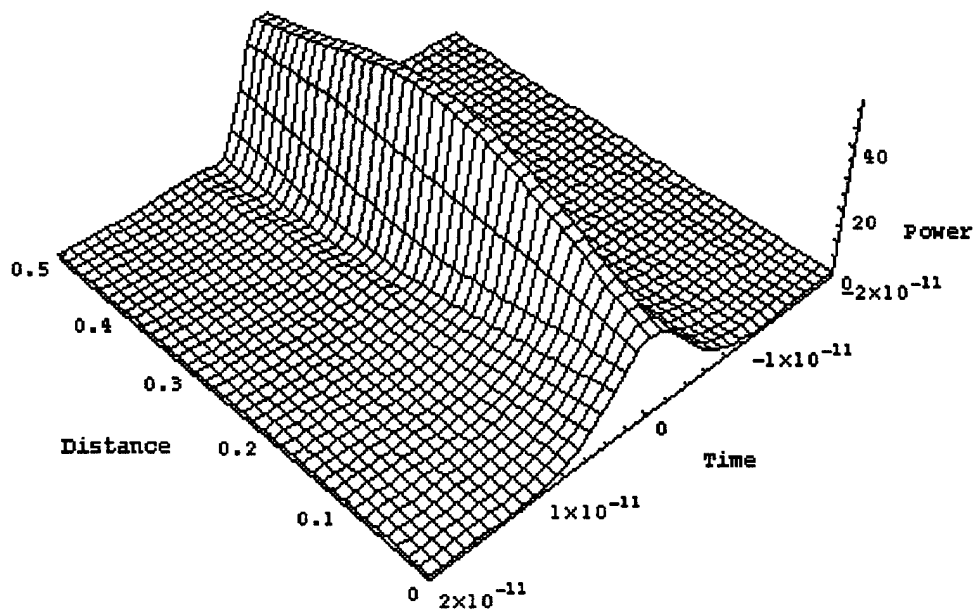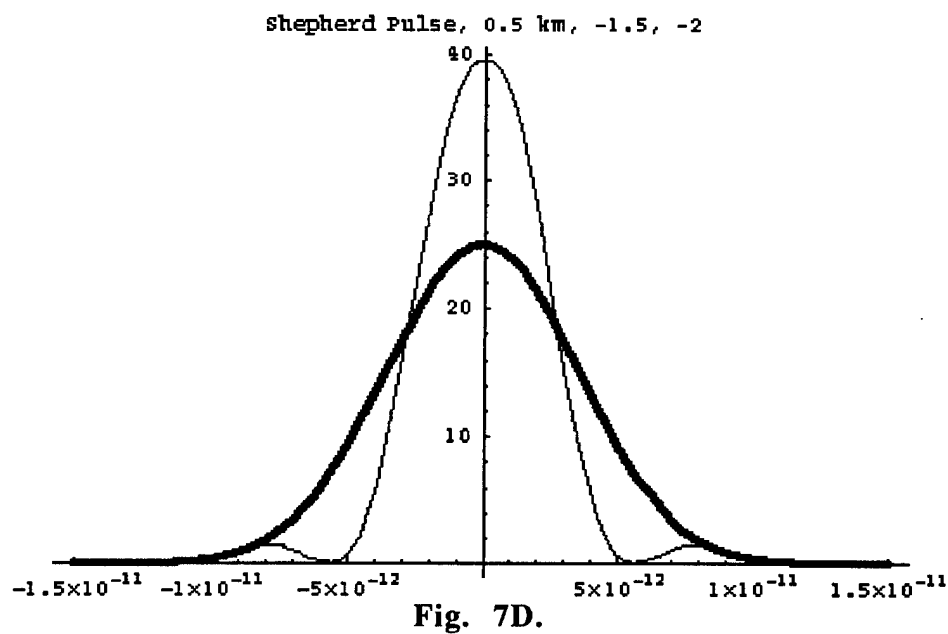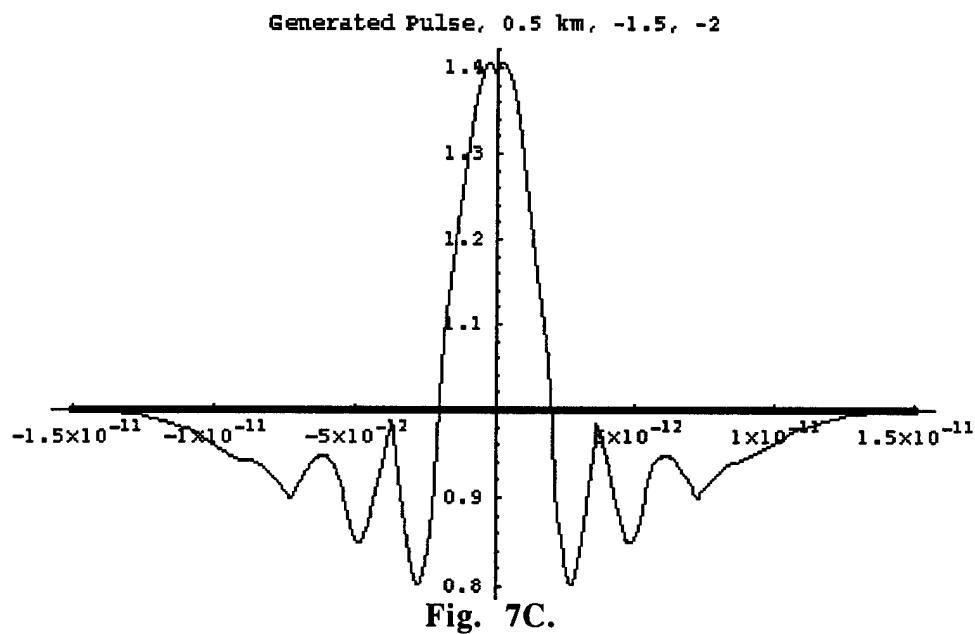
Fig. 12.2.7. A & C: Generated Pulses, $\beta_2$ = -1.5. B & E: Shepherd Pulse, amplitude 5 and $\beta_2$ = -2. After Ref[11], Fig. 2.

205
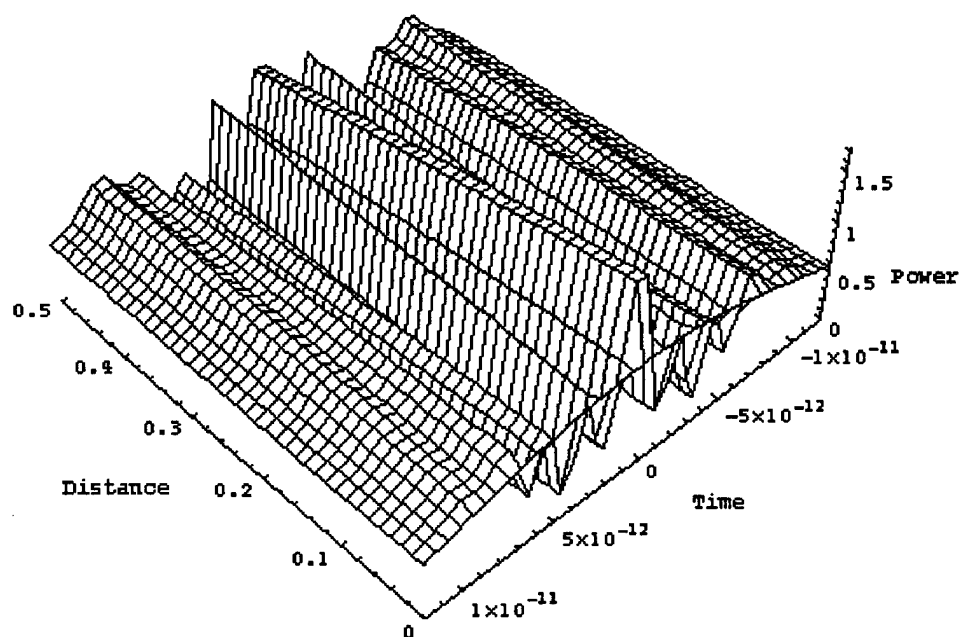
Primary Pulse (1,7) (-2,-2)



**Fig. 8A.**

Shepherd Pulse (1,7) (-2,-2)



**Fig. 8B.**

Primary Pulse (1,7),(-2,-2) 0 & 0.1 km
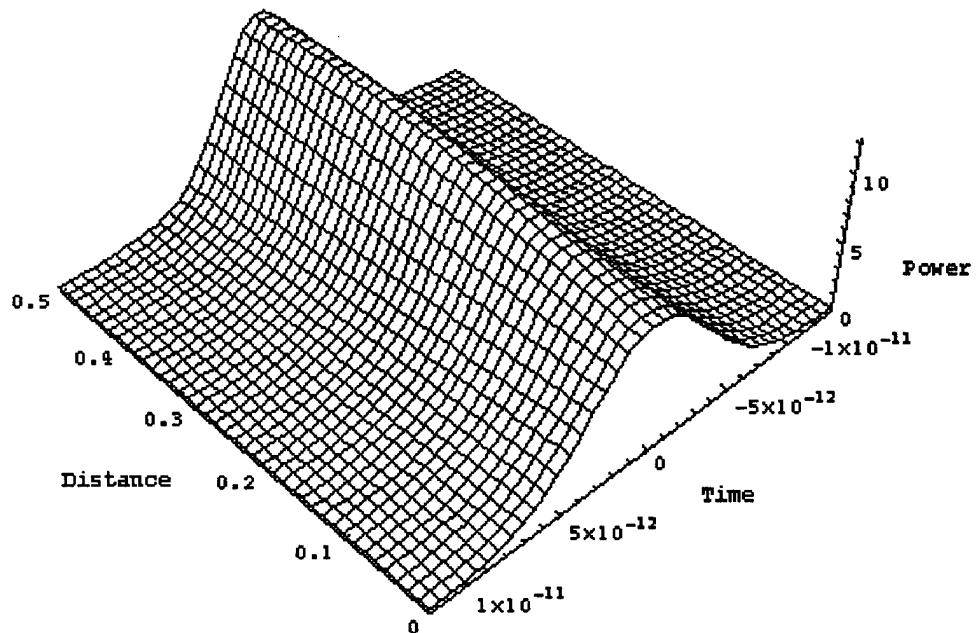


Fig. 8C.

Shepherd Pulse (1,7),(-2,-2) 0 & 0.4 km
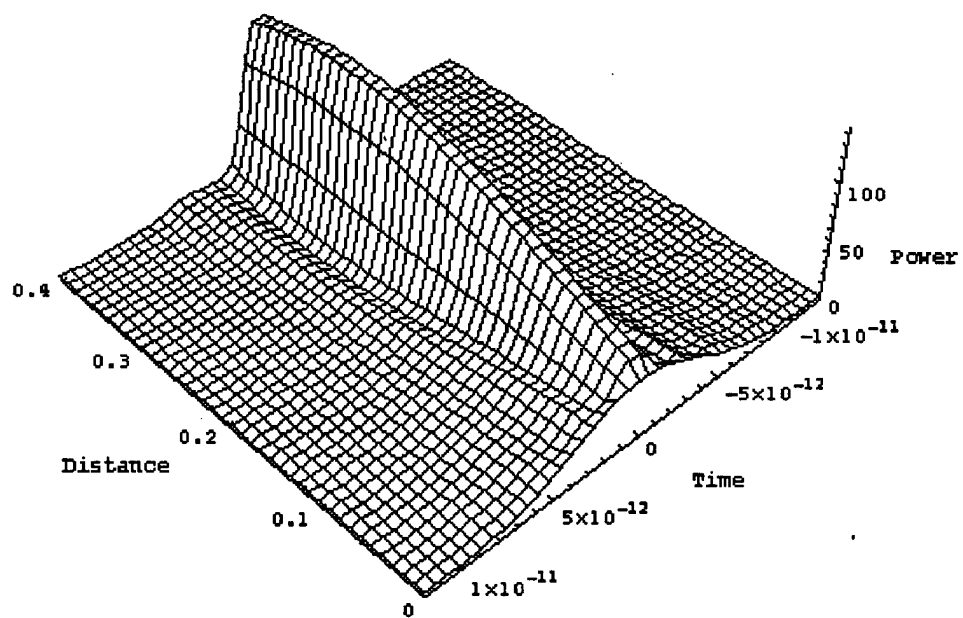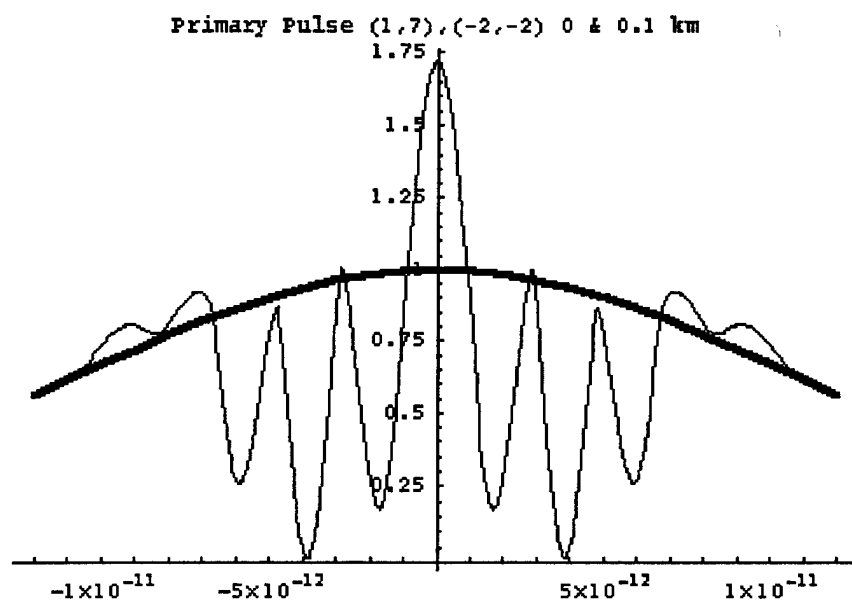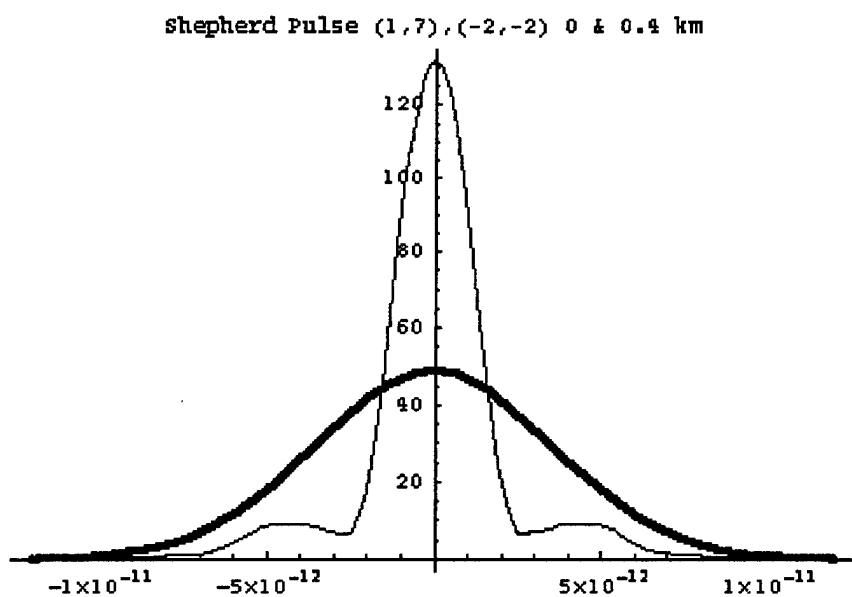


Fig. 8D.
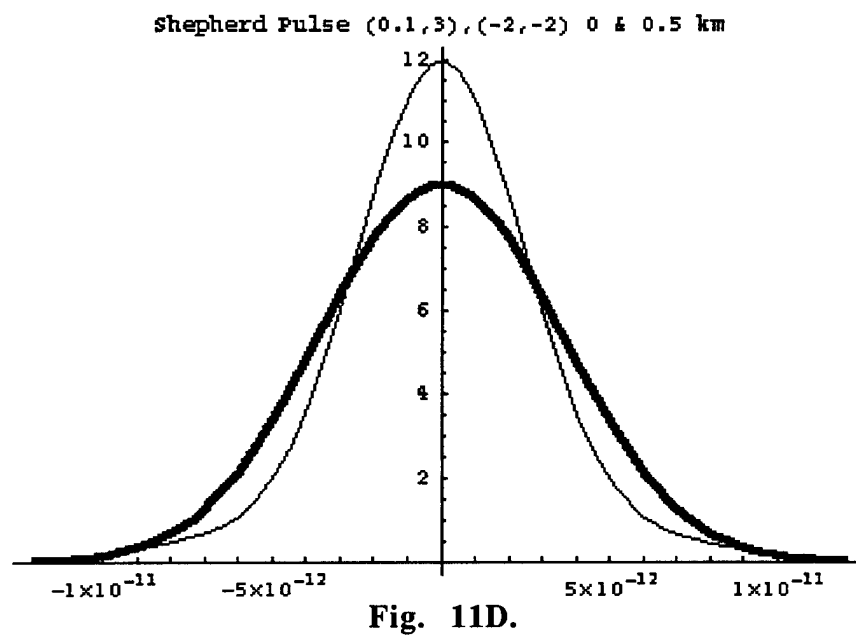
Fig. 12.2.8. A & C: Primary Pulse, Amplitude = 1, $\beta_2$ = -2. B & D: Shepherd Pulse: Amplitude = 7, $\beta_2$ = -2. After Ref[12]. Fig. 2.

---

[12] Yeh, C. & Bergman, L.A., Enhanced pulse compression in nonlinear fiber by a WDM optical pulse. *Phys. Rev.* E, to appear in the Feb. 1998 issue.

Primary Pulse (2,5) (-2,-2)
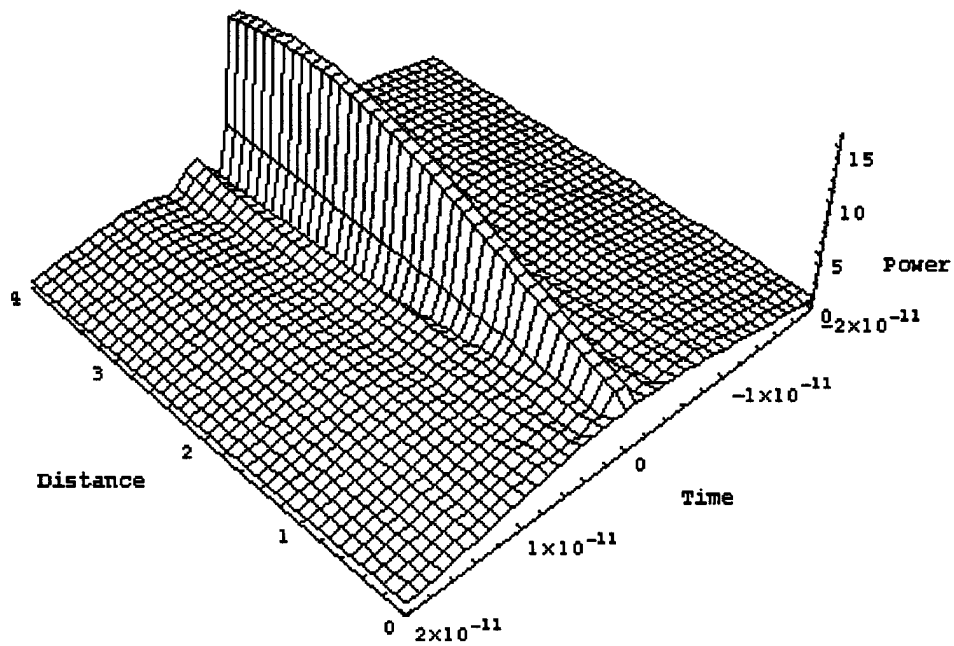


**Fig. 9A.**

Shepherd Pulse (2,5) (-2,-2)



**Fig. 9B.**
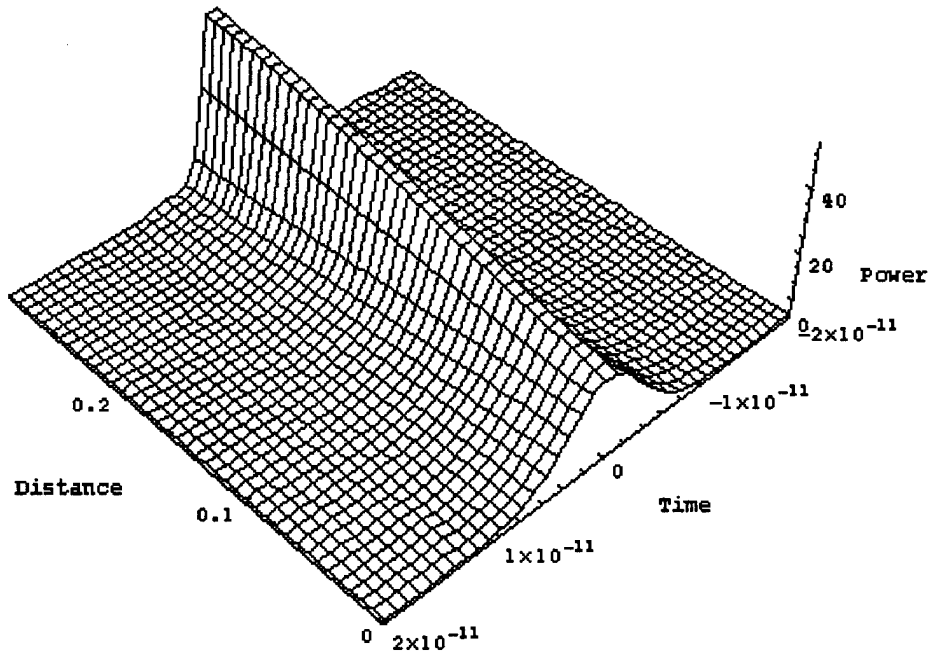
Primary Pulse (2,5),(-2,-2) 0 & 4 km
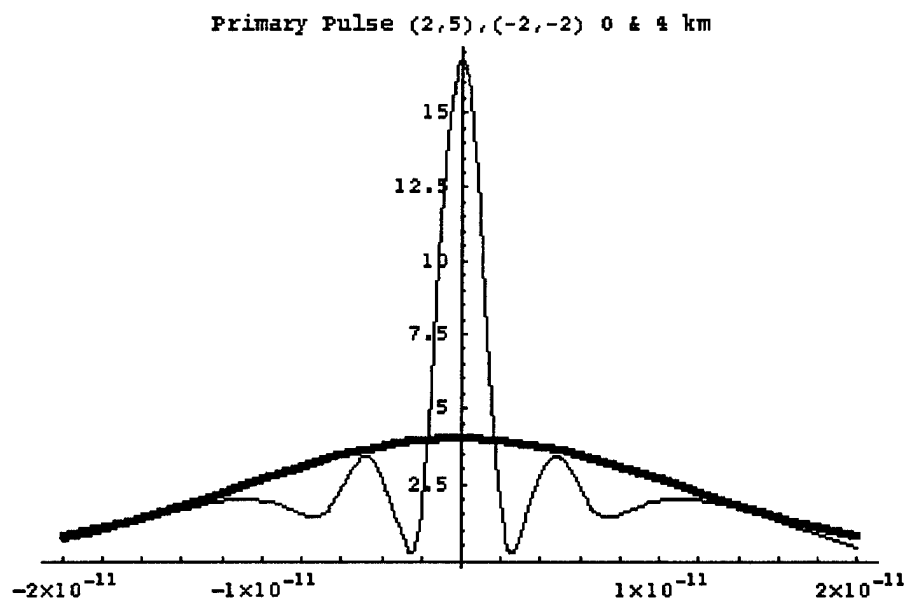
**Fig. 9C.**


Shepherd Pulse (2,5),(-2,-2) 0 & 0.3 km
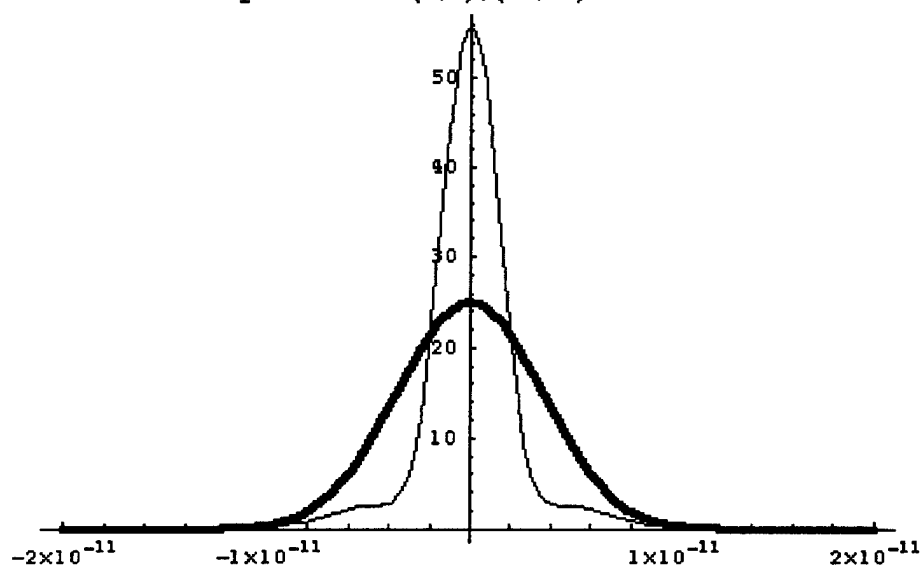
**Fig. 9D.**

Fig. 12.2.9. A & C: Primary Pulse, Amplitude = 2, $\beta_2$ = -2. B & D: Shepherd Pulse: Amplitude = 5, $\beta_2$ = -2. After Ref[12].

Primary Pulse (0.1,3) (+2,+2)
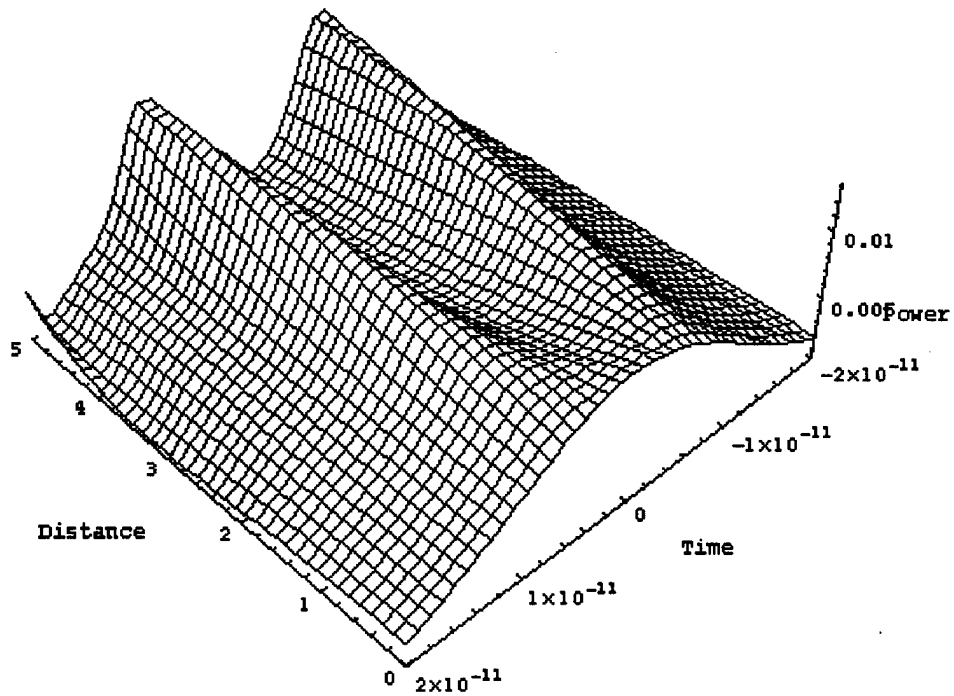


**Fig. 10A.**

Shepherd Pulse (0.1,3) (+2,+2)



**Fig. 10B.**

**Primary Pulse (0.1,3),(+2,+2) 0 & 5 km**



**Fig. 10C.**

**Shepherd Pulse (0.1,3),(+2,+2) 0 & 0.5 km**
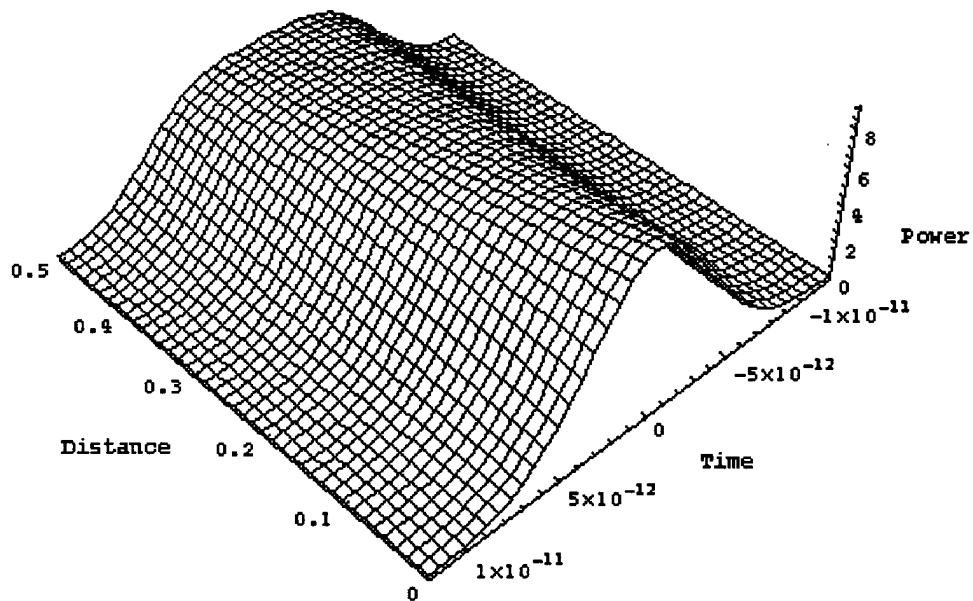


**Fig. 10E.**
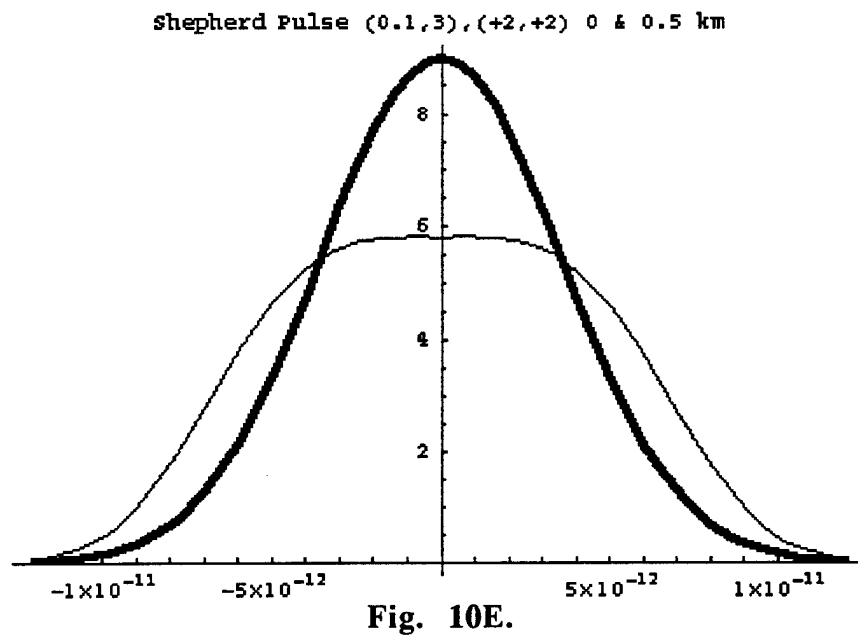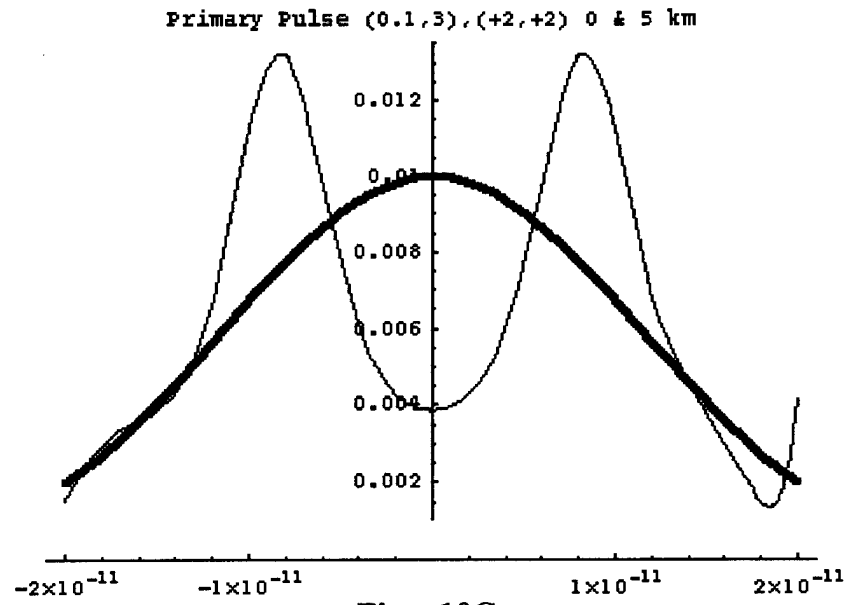
Fig. 12.2.10. A & C: Primary Pulse, Amplitude = 0.1, $\beta_2$ = +2. B & D: Shepherd Pulse: Amplitude = 3, $\beta_2$ = +2. After Ref[12]. Fig. 5.
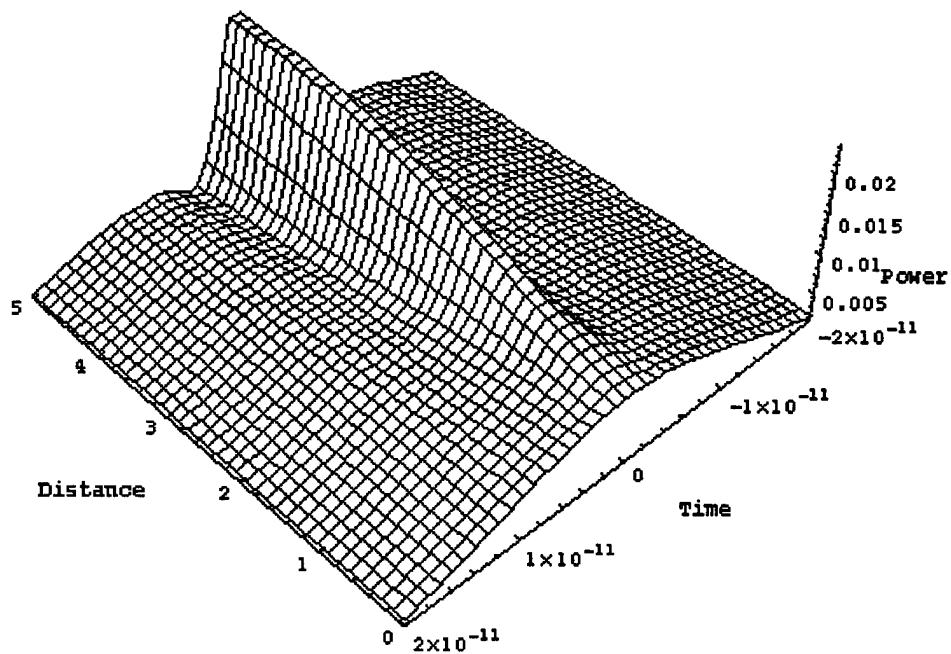
Primary Pulse (0.1,3) (-2,-2)
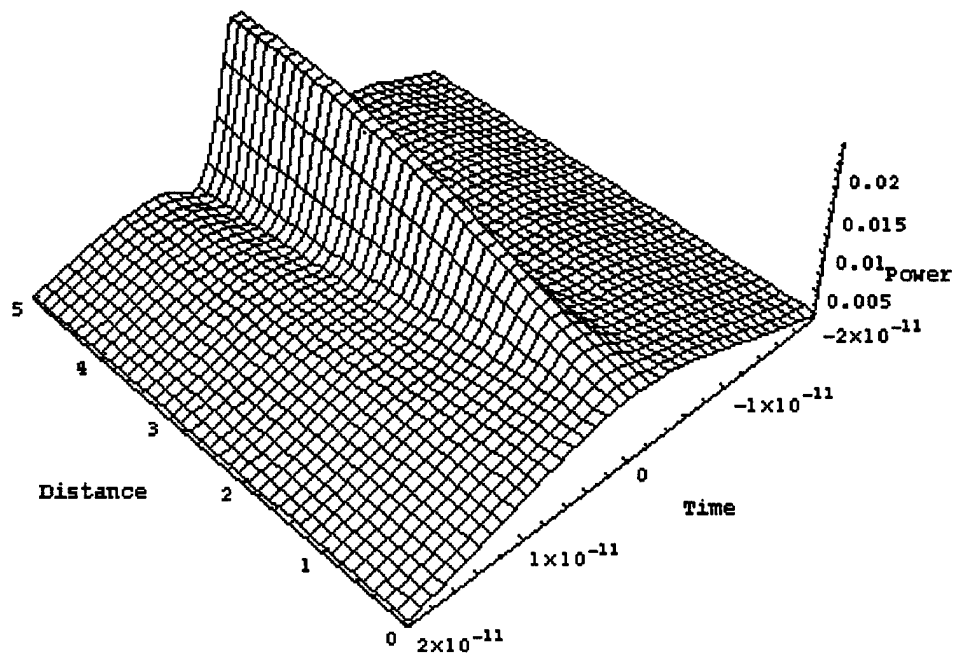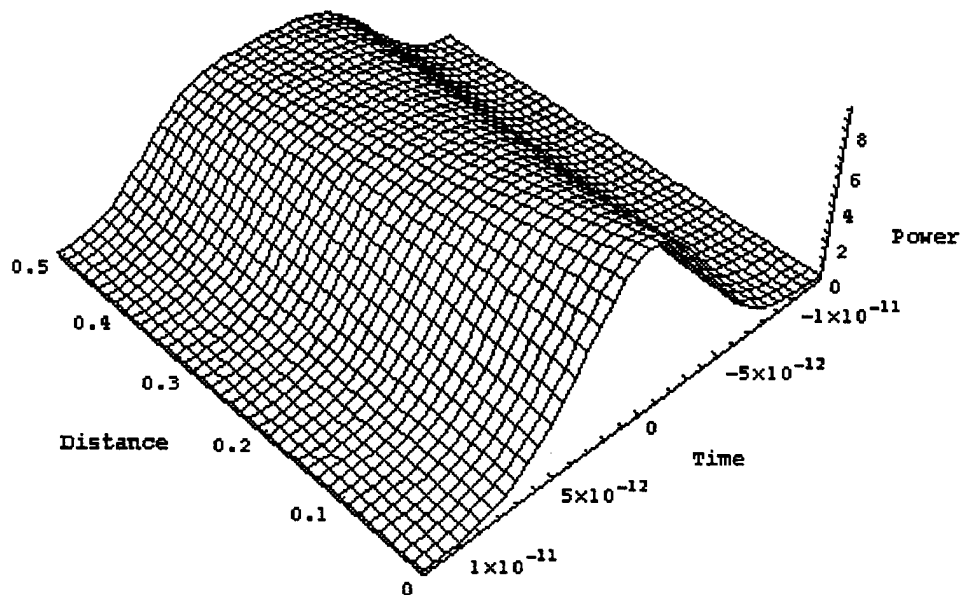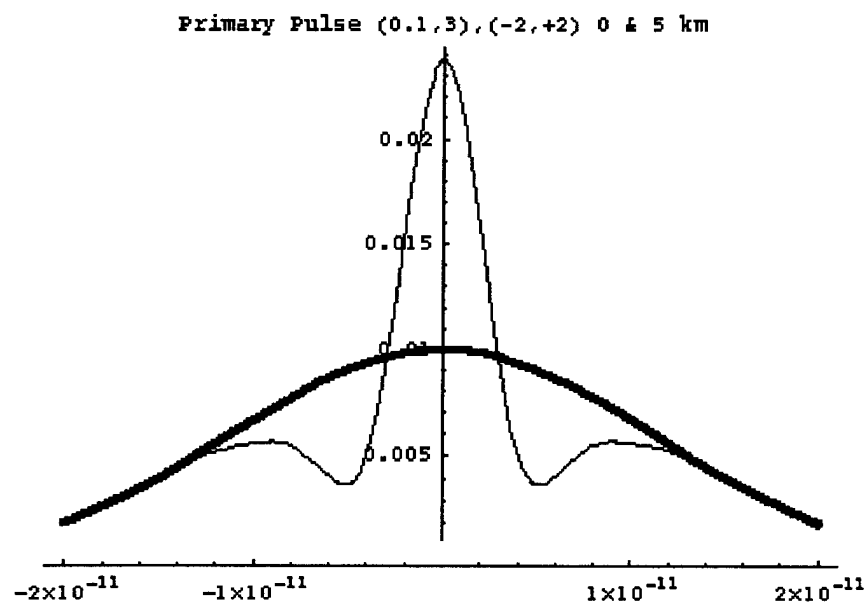


**Fig. 11A.**

Shepherd Pulse (0.1,3) (-2,-2)



**Fig. 11B.**

Fig. 11C.



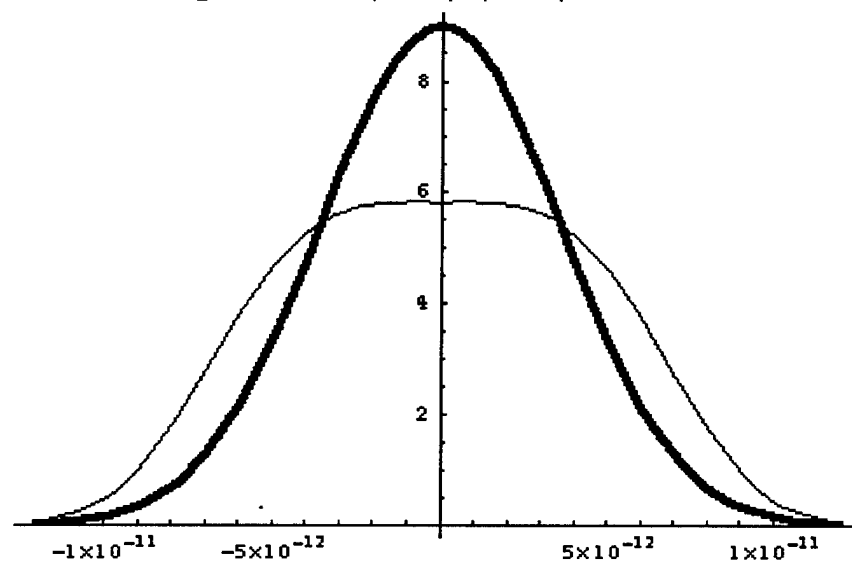Fig. 11D.
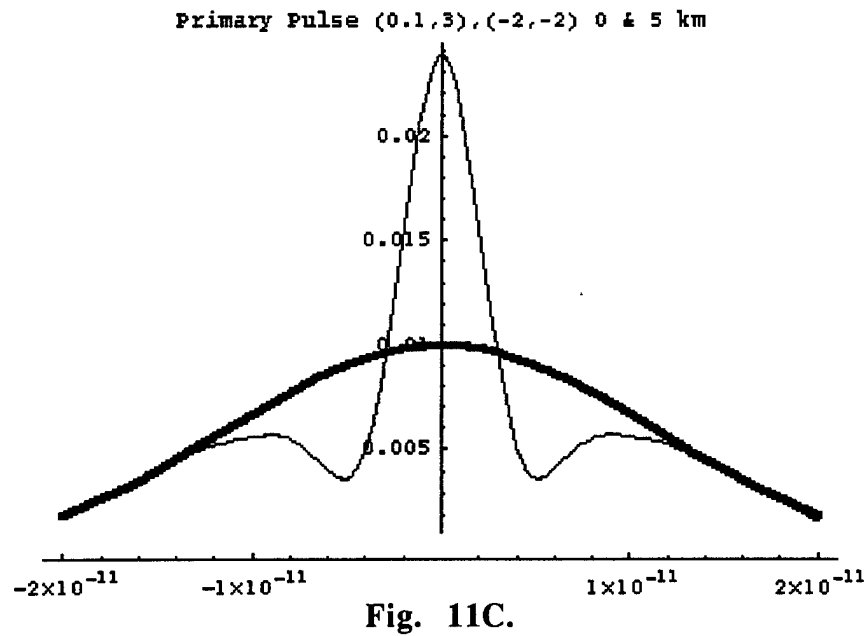
Fig. 12.2.11. A & C: Primary Pulse, Amplitude = 0.1, $\beta_2$ = -2. B & D: Shepherd Pulse: Amplitude = 3, $\beta_2$ = -2. After Ref[12]. Fig. 5.

**Fig. 12A.**

**Fig. 12B.**

Primary Pulse (0.1,3),(-2,+2) 0 & 5 km

Fig. 12C.



Shepherd Pulse (0.1,3),(-2,+2) 0 & 0.5 km

Fig. 12D.

Fig. 12.2.12 A & C: Primary Pulse, Amplitude = 0.1, $\beta_2$ = -2. B & D: Shepherd Pulse: Amplitude = 3, $\beta_2$ = +2. After Ref[12]. Fig. 5.
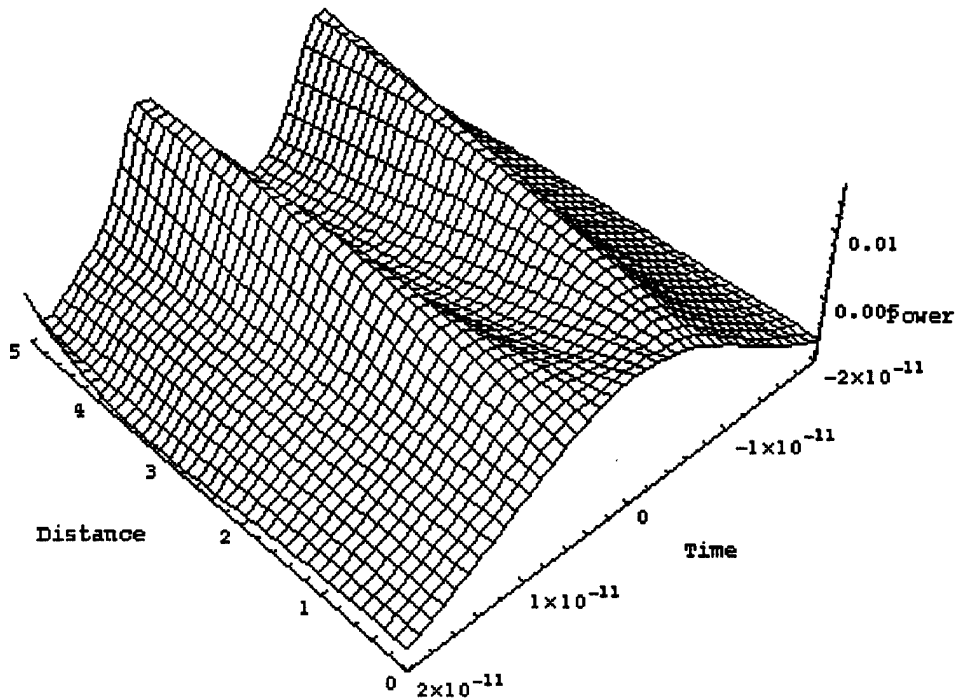
**Fig. 13A.**

**Fig. 13B.**

**Fig. 13C.**



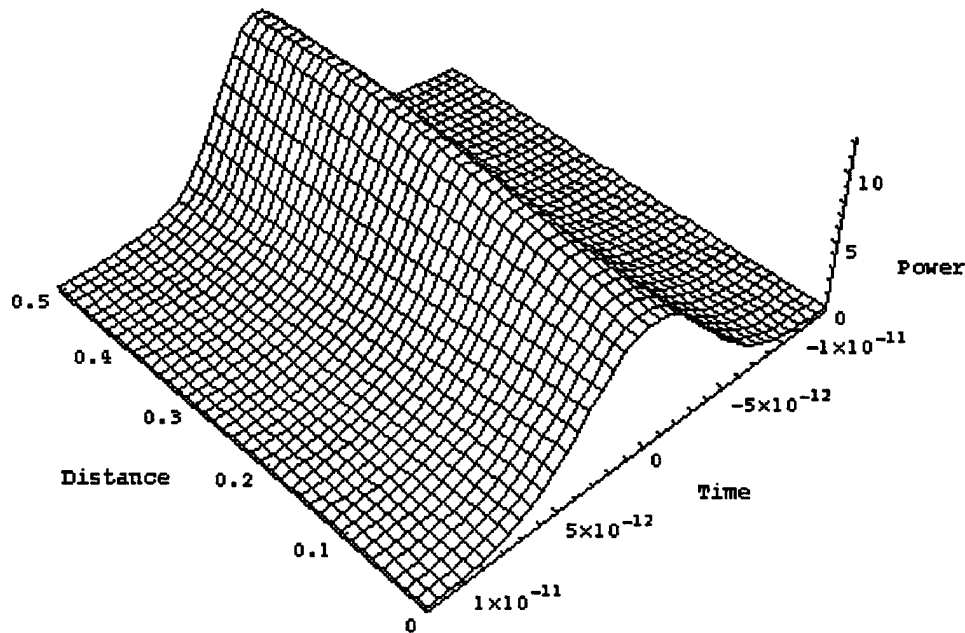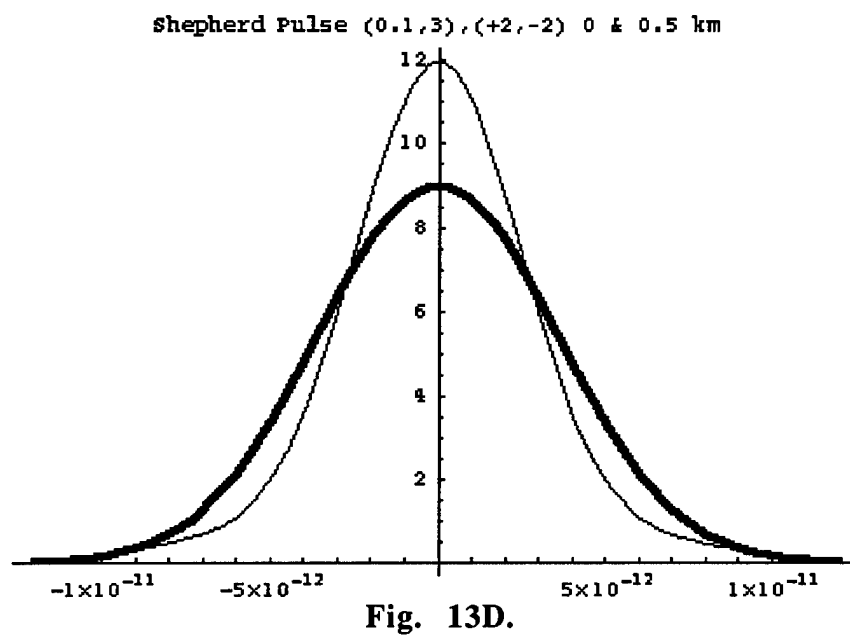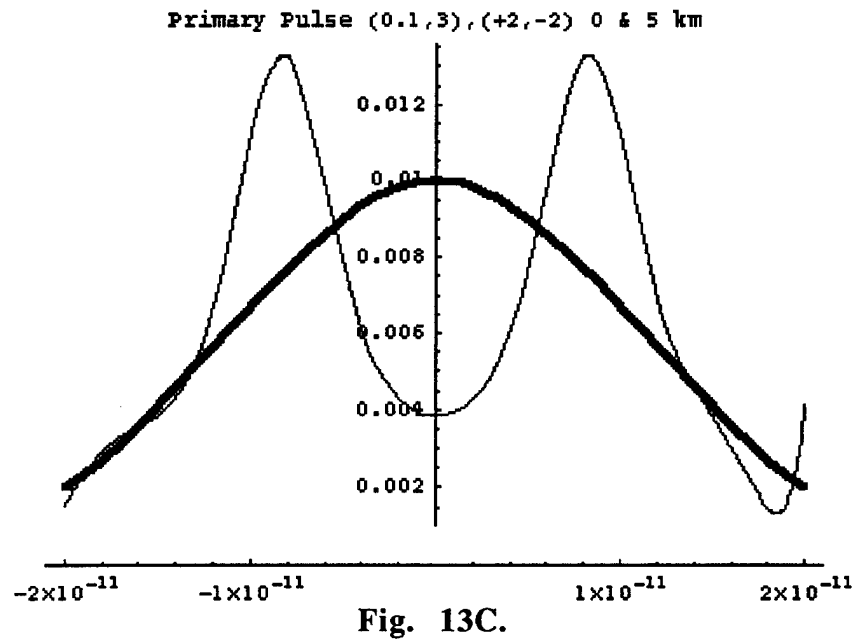**Fig. 13D.**

Fig. 12.2.13. A & C: Primary Pulse, Amplitude = 0.1, $\beta_2$ = +2. B & D: Shepherd Pulse: Amplitude = 3, $\beta_2$ = -2. After Ref[12]. Fig. 5.

## 13.0 Summary recommendations.

The major recommendations of this study are:

• The present work supports the adoption of a *two-stage hierarchy* of codes. At the first stage, *orthogonal codes* define the microchannel or user, identified by a first (temporal) matched filter. Once a code is identified by this filter, a second (temporal) matched filter identifies the BPSK or pulse-position-modulated data with error correction, hence *error-correcting codes* are required for the second stage. The recommendations of this study are that congruence codes be used as orthogonal codes (hyperbolic, quadratic, cubic and quartic) and Lexicographic codes for error correction codes.

• Besides a *hierarchical backbone topology*, a *multidimensional coding scheme* intermixing CMDA, TDMA and WDM provides the possibility of the highest data rates.

• These recommended techniques provide signal spreading techniques, but they are *spread time techniques*, as opposed to spread spectrum techniques.

• A major part of this study addressed the impact of *symmetry principles* on code design to achieve optimum properties. This study provides many examples of heretofore unknown symmetries underlying code design. Future work will address the use of symmetry in designing optimum codes.

The unique approaches taken in this study were:

(1) *spread time techniques* (as opposed to spread spectrum techniques), which permit the highest data rates with the highest S/N and exploit the availability of optical pulse technology and the recent capabilities in pulse crafting and holography;

(2) *Hierarchical* backbone communications link topologies, with *multidimensional* coding schemes;

(3) the incorporation of WDM as well as wavelet diversity with respect to scale and translation when possible;

(4) the use of *symmetry principles* for insight into optimum coding principles;

(5) *Lexicographic ordering* for perfect code generation.

(6) These techniques will be dependent on accurate pulse alignment and pulse compression capability. Bit parallel wavelength division (BPWD) and the concept of the shepherding pulse are promising techniques addressing these issues.

The results of a successful implementation of these recommendations will be:

• maximum permissible data rate transmissions permitted by the latest device technologies and multiple band optical fiber channels;

• multi-dimensional coding based on *time*, as well as *frequency, hopping* principles;

• the techniques of CDMA and TDMA linked for optimum system usage ;

• *spread time* principles, as opposed to *spread spectrum* principles, as the method of choice for the highest data rate communications.